Flow-Substrate Interactions of Submarine Mass Flows

Yan Li

Submitted in accordance with the requirements for the degree of Doctor of Philosophy (PhD)

The University of Leeds
School of Earth and Environment
May 2026

This page is intentionally left blank.

Declaration

The candidate confirms that the work submitted is their own, except where work which has formed part of jointly authored publications has been included. The contribution of the candidate and the other authors to this work has been explicitly indicated below. The candidate confirms that appropriate credit has been given within the thesis where reference has been made to the work of others.

Chapter 4 – Submitted September 2025

Li, Y., Hodgson, D. M., Peakall, J., Wu, N., Clare, M. 2026. Learning from crushing failures: changes in physical properties reveal the mechanics of submarine carbonate landslides

Author contributions:

Li, Y. – Conceptualisation, led data collection and analysis, figure and manuscript preparation.
Hodgson, D.M – Conceptualisation and detailed manuscript review.
Peakall, J. – Conceptualisation and detailed manuscript review.
Wu, N. – Detailed manuscript review.
Clare, M.A. – Detailed manuscript review.

Target Journal: *Basin Research (submitted September 2025)*

Chapter 5 – In preparation for submission

Li, Y., Hodgson, D. M., Peakall, J. 2026. Self-confining submarine debris flows: a mechanism for long run-out on gentle slopes.

Author contributions:

Li, Y. – Data collection and analysis, and figure and manuscript preparation.
Hodgson, D.M – Conceptualisation and detailed manuscript review.
Peakall, J. – Conceptualisation and detailed manuscript review.

Chapter 6 – In preparation for submission

Li, Y., Hodgson, D. M., Peakall, J., Keevil, G. M., Brown, H. C., Gao, W. 2026. Segregation and evolving substrate interaction: process insights from observation of single and successive subaqueous granular flows

Author contributions:

Li, Y. – Experimental design, data collection and analysis, and figure and manuscript preparation.
Hodgson, D.M – Conceptualisation and detailed manuscript review.
Peakall, J. – Conceptualisation and detailed manuscript review.
Keevil, G.M – Experimental design, and laboratory assistance.
Brown, H.C. – Experimental design and laboratory assistance.
Gao, W. – Laboratory assistance and detailed manuscript review.

Acknowledgements

I would like to express my sincere gratitude to my brilliant supervisors, David Hodgson and Jeff Peakall, for their outstanding support, patience, and guidance throughout this four-year research project. It is a great privilege to work under your supervision. Your knowledge, encouragement, and thoughtful suggestions have shaped not only this thesis, but also the way I think as a researcher. Under your guidance, I have become more confident and developed a much stronger understanding of the mechanisms of submarine slope instability and flow dynamics. From you, I have learned both a passion for sedimentology research and the importance of critical thinking.

I would like to acknowledge the financial support of the China Scholarship Council (CSC) and the University of Leeds, which gave me the opportunity to study in such an outstanding sedimentology research group. I am grateful to the Institute of Applied Geoscience (IAG), University of Leeds for the funding that enabled me to purchase the dataset for this research. I also thank the International Association of Sedimentologists (IAS) Postgraduate Research Grants for supporting the physical experiments.

My sincere thanks go to Adam McArthur for organising regular Sed Chat meetings, which create such a friendly and nice environment for discussion and learning from each other. I am very grateful to Gareth Keevil and Helena Brown for their powerful lab assistance in the physical experiments, to Mike Clare and Nan Wu for their thoughtful manuscript revision, and to Ben Carven for help with Petrel. I am also grateful to Nigel Mountney and Charlotte Botter for giving me the opportunity to demonstrate in their modules. My thanks also go to Mohammed Mohamed, Hager Elattar, Edward Keavney, William Taylor, Megen Davies, Carys Simpson, Saulo Alves Carreiro De Araujo, Sheng Chen, Jack Humphries, and Lydia Brown for your help and kindness, especially when I was completely new to both the group and life in UK.

Finally, I would like to thank my family and friends for their constant love, support, and encouragement throughout this journey. I am also proud of myself. This journey has not been easy, but it has made me stronger. Well done, Yan!

Abstract

Submarine landslides and debris flows are widely distributed in modern and ancient deep-water sedimentary basins, and can damage marine infrastructures and generate destructive tsunamis. However, the mechanisms that initiate slope failures and facilitate long runout of flows on gentle slopes remain poorly understand. This thesis integrates seismic reflection data and cores from Exmouth Plateau, offshore NW Australia, with subaqueous granular-flow experiments, to investigate flow-substrate interactions that account for submarine failure initiation and flow evolution processes.

The results show that large-scale submarine landslides on gentle carbonate slopes are fundamentally governed by sediment composition. Clay-capped foraminifera-rich successions lead to excess water preservation within chambered foraminifera shells, causing the formation of weak layers. Under contractive shearing, basal weak layers release pore water through crushing of foram shells, causing elevated pore pressure and generating a lubrication layer that facilitates runout of the overriding slide. The study demonstrates that submarine debris flows can become self-confined through a combination of lateral depositional relief and substrate incision. The self-confining process establishes a positive feedback, in which flow confinement drives substrate incision that in turn increases flow confinement, thereby lengthening flow runout distances even on gentle slopes.

Experimental subaqueous granular flows form coarse-enriched lateral levees and fines-enriched conduit deposits through particle segregation, like their subaerial counterparts, but are more mobile due to interstitial fluids. In subaqueous multiple-flow experiments, the presence of lateral levees increases the velocity of subsequent flows. This results in substrate erosion and downslope particle remobilisation that increases the flow volume, substrate incision, flow confinement, and runout distance.

Together, these findings provide a new process-based model for how subaqueous landslides initiate, evolve, and reach long runout distances even on gentle slopes. This thesis highlights the importance of dynamic flow-substrate interactions (i.e., lubrication, deposition, or erosion), with implications for elucidating flow dynamics and sedimentary processes and assessing submarine geohazards.

Table of Contents

List of Figures

List of Tables

Nomenclature and Abbreviations

BSS(s) = basal shear surface(s)

BSZ = basal shear zone

DEM = digital elevation model(s)

GSD(s) = grain-size distribution(s)

MTC(s) = mass transport complex(s)

MTD(s) = mass transport deposit(s)

mbsf = metres below sea floor

ODP = Ocean Drilling Program

TS(s) = top surface(s)

TWT = two way travel time

UWL = underlying weak layer

vol.% = volume percentage

WL(s) = weak layer(s)

Chapter 1 Introduction

Submarine mass gravity flows encompass a spectrum of slope failure processes, including creep, slide, slump, debris flow and associated turbidity currents (Nemec, 1990; Shanmugam et al., 1994; Posamentier and Martinsen, 2011). Creep refers to slow downslope deformation involving intergranular frictional sliding with quasi-static grain contracts, slide is coherent mass with minor internal deformation, slump is coherent mass with considerable internal deformation, debris flow is characterised by fully disaggregated sediments and turbidity current is featured by non-cohesive turbulent flow (Nemec, 1990; Haughton et al., 2009; Hodgson et al., 2026). During the evolution of the processes, mass disaggregation and lateral displacement increase (Hampton et al., 1996; Moscardelli and Wood, 2008; Wu et al., 2021; Hodgson et al., 2026). When a submarine landslide occurs, material is transported from the upstream headwall domain to the downstream toe domain, leading to the formation of extensive headwall scarps, and compressive structures (e.g., thrusts and folds) in the toewall (Bull et al., 2009; Carter et al., 2020).

Submarine landslides are widely distributed in modern and ancient deep-water sedimentary basins (Masson et al., 2006; Moscardelli and Wood, 2008). They can damage marine infrastructures (e.g., seafloor cable networks) and generate destructive tsunamis, hence posing a threat to coastal communities (Piper et al, 1999; Fine et al., 2005; Ikehara et al., 2014; White et al., 2016; Mulia et al., 2020). Catastrophic mass movement events were initially thought to be prevalent on steep (commonly >5°, locally up to 10~15°) slopes, such as in canyon heads and delta fronts (Shepard, 1955; Moore, 1961; Hampton et al., 1996). Subsequent studies have demonstrated that large-scale (>10^3 km^2) submarine landslides may occur on very gentle slopes (<2°), such as the Storegga landslide and the Trñnadjupet Slide on the Norwegian margin (~1°; Laberg and Vorren, 2000; Haflidason et al., 2004; Kvalstad et al., 2005), and the Sahara Slide and Agadir Slide on the NW African continental margin (<1°; Embley, 1982; Krastel et al., 2019). Although much prior focus has been on siliciclastic-dominated slopes, carbonate landslides are also known to be very widespread (e.g., Berger and Johnson, 1976; Mosher et al., 1993; Puga-Bernabéu et al., 2011, 2020; Hengesh et al., 2013; Lüdmann et al., 2022; Nugraha et al., 2022; Wu et al., 2023), yet the understanding of these is comparably poor.

Recent studies have shown that the formation of submarine landslides can be controlled by the presence of laterally extensive weak layers in the slope stratigraphy (e.g., Berndt et al., 2012; L'Heureux et al., 2012; Locat et al., 2014; Urlaub et al., 2015; Elger et al., 2018; Krastel et al., 2019). Weak layers can generate excess pore pressure and cause transiently reduced shear strength, leading to decreased frictional resistance to sliding (Laberg and Vorren, 2000; Trincardi et al., 2004; Masson et al., 2006; Urlaub et al., 2018; Sammartini et al., 2021; Gatter et al., 2021; Li et al., 2025). The formation and evolution processes of weak layers are closely related to the contrasts in sediment physical properties, particularly compressibility, permeability and shear strength, which control the pre-requisite conditions before failure (L'Heureux et al., 2012; Locat et al., 2014; Madhusudhan et al., 2017; Urlaub et al., 2018, 2020; Gatter et al., 2020; Gatter et al., 2021).

Flow mobility can be substantially enhanced by lateral confinement that restricts flow spreading, maintains flow thickness and sustains flow momentum downslope, thereby facilitating longer runout distances. In submarine environments, confinement is commonly imposed by pre-existing seafloor topography, including submarine canyon and channel systems (Talling et al., 2013; Krastel et al., 2016; Böttner et al., 2024; McArthur et al., 2024), pre-existing deposits (e.g., mass-transport deposits and channel-levee systems; Ward et al., 2018; Nwoko et al., 2020a, 2020b), and basin margins, structural topography and escarpments (Gee et al., 2001; Ortiz-Karpf et al., 2018; Li et al., 2020). Topographic confinement can control flow routing pathways (Talling et al., 2013; Krastel et al., 2016; McArthur et al., 2024), and has been shown to enhance erosive capacity, deepen basal shear surfaces, and promote sediment transport into deep basins (Böttner et al., 2024).

Field observations and experimental results of subaerial debris flows show that debris flows can self-confine through formation of lateral levees (Kokelaar et al., 2014). Depositional relief is generated through grain-size segregation, and can enhance confinement for subsequent flow (Major and Iverson, 1999; Gray and Kokelaar, 2010; Iverson et al., 2010; Johnson et al., 2012; Kokelaar et al., 2014). However, the equivalent work of self-confinement in subaqueous settings remain limited. In particular, how self-confining debris flows interact with erodible substrates, and how such flow-substrate feedbacks influence the self-confinement evolution and mobility processes remain poorly understood. Therefore, the analysis of self-confinement processes in subaqueous settings, is crucial for understanding the enhancement of submarine flow mobility.

Furthermore, only modest prior attention has been paid to large submarine landslides on low gradient slopes composed of carbonate ooze. Therefore, it is important to understand how large-scale submarine landslides are developed on gentle carbonate slopes, and how flow-substrate interactions influence flow mobility on such low-angle slopes. Multiple large submarine landslides on low gradient slopes composed of carbonate ooze have been identified offshore NW Australia covering more than 6000 km^2 of seafloor (Scarselli et al., 2013; Scarselli, 2020; Nugraha et al., 2022; Wu et al., 2023). Weak layers are recognized in carbonate successions with a widespread distribution (e.g., Wu et al., 2023). However, it remains relatively poorly understood how changes in physical properties influence the evolution processes of carbonate failures on gentle slopes remain poorly understood.

This thesis presents and synthesises the results from the following submarine mass movement landforms:

i. A deep-burial, large-scale submarine carbonate landslide from the Exmouth Plateau, Offshore Northwest Australia, to analyse how the changes in physical properties of carbonate sediments govern weak layer formation and the initiation and evolution of submarine landslides on low gradient slopes.
ii. A shallow-burial submarine debris flow from the Exmouth Plateau, Offshore Northwest Australia, to investigate how self-confining processes develop in submarine environments and how such processes enhance flow runout distances on gentle slopes.
iii. Scaled, subaqueous physical experiments of segregation in both single and successive granular flows, designed to explore the evolution of segregation in subaqueous settings, with particular emphasis on dynamic flow-substrate interactions.

The ambition for this thesis is to address the following research questions.

1.1 What causes instability on low gradient carbonate submarine slopes?

Rationale: The stability of submarine slopes is fundamentally controlled by the physical properties of sediments, which control both the pre-conditioning of the sedimentary pile prior to failure (Miramontes et al., 2018; Urlaub et al., 2018; Gatter et al., 2021; Wang et al., 2025), and the mechanical behaviour of flows during mass movement downslope (Iverson, 1997; Iverson et al., 2010; de Haas et al., 2015). Global compilations of seafloor sediment distribution show that carbonate ooze is the most widespread deep-sea lithology in the global ocean (Dutkiewicz et al., 2015, 2020). The physical properties of carbonate sediments, including high compressibility and water content, and the abundance of microfossils, such as foraminifera, can promote the development of weak layers within the carbonate-rich successions that cause large-scale landslides even on gentle slopes (Gatter et al., 2021; Wu et al., 2023). Geotechnical observations demonstrate that even minor proportions of foraminifera, as little as 0.47 wt%, can result in pronounced increase in porosity of carbonate-rich successions (Sawyer and Hodelka, 2016). However, most models of the initiation and evolution processes of submarine landslides have been derived from siliciclastic environments (e.g., Iverson, 1997; Gee et al., 1999; Iverson et al., 2010, 2011), resulting in a limited understanding of carbonate-rich landslides.

Large submarine landslides have been recognised on gentle carbonate slopes with gradients of less than 2°, including those on the Exmouth Plateau, offshore Australia (Scarselli et al., 2013; Scarselli, 2020; Wu et al., 2023), and those on the northern and eastern flanks of the Ontong Java Plateau (Berger and Johnson, 1976; Mosher et al., 1993). Submarine landslides exhibit strong erosive capacity and increase their volume through substrate entrainment. Recent studies show that carbonate ooze-dominated slides are more erosive than siliciclastic slides. For example, the Gorgon carbonate slide deposits have a volume up to 13 times its initial failure volume, compared to a maximum of ~7.5 times the initial failure volume in siliciclastic landslides (Nugraha et al., 2022). The dramatic volume increase in carbonate landslides occurs through bulking up along the pathway, which probably results from their passage across a highly erodible carbonate ooze substrate (Nugraha et al., 2022). Fragile foraminifera and nannofossils dominate Cenozoic carbonate oozes (Palmer-Julson and Rack, 1992; Rack et al., 1993) that are weakly cemented at their contacts during early burial. When carbonate oozes fail, their post-failure remoulded strength can decrease ten-fold relative to their initial strength, whereas siliciclastic clays typically show only two-fold reduction in strength (Gaudin and White, 2009). Such pronounced strength loss in carbonate oozes can promote greater substrate entrainment, allowing ooze-related failure to gain more volume during transport.

Consolidation tests indicate that calcareous oozes are usually underconsolidated to normally consolidated at shallow burial depths (< ~200 mbsf; Rack et al., 1993). This suggests that calcareous oozes have high compressibility and are sensitive to the overburden pressure. Additionally, carbonate sediments exhibit higher water content than siliciclastic sediments, because 'extra' volumes of pore water can be stored within the chambers of foraminifera and similar microfossils (Bachman, 1984; Rack et al., 1993). Under moderate compressive stresses, foraminifera tests within carbonate oozes are susceptible to breakage and can release the 'extra' intra-particle water, which can rapidly elevate pore pressure and reduce sediment shear strength (Rack et al., 1993). Consequently, carbonate sediments can experience rapid compaction, elevated pore pressure generation, and strength reduction during burial, increasing their susceptibility to slope failure and substrate entrainment.

The physical properties of carbonate sediments are recognised as key controls on slope failure, and have been documented either prior to (Urlaub et al., 2018; Gatter et al., 2021; Wu et al., 2023) or after (Sawyer and Hodelka, 2016) failure. However, there remains limited understanding of how physical properties (e.g., water content, porosity, permeability and composition) evolve within the same sedimentary successions from intact stratigraphy into failure. In particular, the changes in the physical properties within the underlying sensitive carbonate substrates can strongly influence flow-substrate interactions, including erosion, deposition or lubrication. Resolving this gap is critical for improving hazard assessment models, which rarely account for stratigraphic composition or the influence of sediment physical properties on flow evolution processes.

1.2 How do subaqueous flows self-confine?

Rationale: Subaqueous debris flows can achieve runout distance of tens to hundreds of kilometres on slopes of less than 1° (e.g., Gee et al., 1999). Such extraordinary mobility on gentle slopes poses a challenge to classical gravity flow models that predict rapid deceleration under low-gradient slopes. Understanding the mechanisms responsible for long runout is crucial for understanding the dynamic flow-substrate feedback on mobility, reconstructing deep-water sediment transport processes, and assessing submarine geohazards.

Several mechanisms have been proposed to explain the high mobility of subaqueous debris flows, including hydroplaning (Mohrig et al., 1998; De Blasio et al., 2004a, 2004b; Elverhøi et al., 2005, 2010; De Blasio et al., 2006; Acosta et al., 2017), and elevated pore pressure (Iverson, 1997; Gee et al., 1999; Major and Iverson, 1999; Talling et al., 2012a; Peakall et al., 2020). These processes can reduce basal friction thus enhancing flow mobility. However, subaerial experimental results show that debris flows travelling over smooth and rough beds can achieve comparable runout distances, despite flows over smooth beds moving ~30% faster (Iverson et al., 2010). This observation suggests that basal roughness alone cannot fully explain debris-flow mobility (Iverson et al., 2010, 2011). Consequently, grain-size segregation has been proposed as an important mechanism controlling levee formation in debris flows (Major, 1997; Major and Iverson, 1999; Iverson et al., 2010; Johnson et al., 2012). During segregation, coarser particles migrate upward within the flow and are advected towards the advancing front, where particles are overridden by the advancing flow along the flow axis and laterally displaces coarse particles to off-axis locations, progressively forming coarse-grained levees behind the flow head (Iverson et al., 2010; Gray and Kokelaar, 2010; Johnson et al., 2012; Kokelaar et al., 2014). These lateral levees act to confine subsequent flows, restrict lateral flow spreading, and thereby facilitating longer runout distances.

Subaqueous debris flows, analogous in many respects to terrestrial debris flows, can generate complex morphologies, including blocky and hummocky frontal morphology, lateral levees and rafted sediment blocks, at much larger scales (Prior et al., 1984; Masson et al., 1993). Examples include the up to 15 m high lateral levees observed in the Saharan debris flow (Masson et al., 1993) and the ~5 m high front relief on the

Kitimat fjord debrite (Prior et al., 1984). These levees can inhibit lateral spreading of subsequent flows and create natural topographic confinement that helps channelise flow pathways (e.g., Johnson et al., 2012; Kokelaar et al., 2014). Self-confinement may not only arise from particle segregation, but also from dynamic interaction between the flow and substrate. Subaqueous debris flows can strongly interact with the seafloor through substrate incision, particularly in highly erodible carbonate substrates (Nugraha et al., 2022). The substrate erosion by subaqueous debris flows can modify the seafloor morphology (e.g., Gee et al., 2006) and generate a confined environment. Such evolving topographic confinement, through deepening and narrowing of the flow pathway, can further restrict lateral spreading of the flow. This establishes a positive feedback whereby enhanced confinement promotes substrate incision and further increases flow confinement, thereby increasing the run-out distance on gentle slopes. Previous studies on evolution of self-confinement have focused on the formation of confining levees during segregation processes in subaerial flow settings (e.g., Deboeuf et al, 2006; Gray and Kokelaar, 2010; Iverson et al., 2010; Johnson et al., 2012; Kokelaar et al., 2014; Rocha et al., 2019). However, the formation and evolution processes of self-confining debris flows have not been documented in subaqueous environments.

A new conceptual model for the process interaction and evolution of self-confining subaqueous flows is therefore required, explicitly regarding dynamically evolving depositional topography.

1.3 How do self-confining subaqueous flows bulk-up during emplacement?

Rationale: Subaqueous debris flows can undergo substantial bulk-up during emplacement through substrate entrainment (Prior et al., 1984; Gee et al., 1999, 2006). Such bulking-up can substantially influence flow dynamics through increasing flow volume (McCoy et al., 2012; Hodgson et al., 2019; Nugraha et al., 2022; Böttner et al., 2024), thereby controlling flow momentum and mobility. Therefore, understanding the bulk-up processes in self-confining debris flows is essential for analysing the feedbacks between substrate entrainment, flow confinement, and flow mobility.

Subaerial physical experiment results demonstrate that substrate particles can be entrained by advancing debris flows and incorporated into the recirculation zone within the segregating flow heads (Johnson et al., 2012). During recirculation, flux analysis suggests that fine particles mostly leave the head at the base of the central channel, whereas coarse particles are advected away from the flow centre-plane by the transverse component of the velocity, ultimately accumulating on the lateral sides of the flow and acting as lateral levees (Johnson et al., 2012). Flow composition can substantially influence the formation of bounding levees and flow mobility. As evidenced by the subaerial granular experimental results in Kokelaar et al. (2014), the flows containing 60-70 vol% fines exhibit longer runout than other fines percentages. Field observations demonstrate that subaqueous debris flows can entrain substantial volume from substrate (e.g., Gee et al., 1999; Dakin et al., 2013). Carbonate substrate are particularly susceptible to be entrained compared with clay-rich substrates at comparable burial depth (e.g., White et al., 2013; Nugraha et al., 2022). Consequently, substrate erosion can significantly influence flow composition, volume and thickness during transport. Despite the importance of substrate erosion of flows in controlling the evolution of flow being acknowledged (McCoy et al., 2012; Hodgson et al., 2019; Nugraha et al., 2022; Böttner et al., 2024), the role of bulking up in the evolution process of self-confinement is poorly understood. Previous studies on evolution of self-confinement have focused on the formation of confining levees (e.g., Deboeuf et al, 2006; Gray and Kokelaar, 2010; Iverson et al., 2010; Kokelaar et al., 2014), on the fixed substrate in subaerial settings. It remains unknown how the dynamic flow-substrate interaction (i.e., bulking-up) influences flow composition and flow thickness, and thus influences the process of self-confining.

Addressing this gap is essential to reconstruct the evolution processes of self-confinement (particle segregation), with particular consideration to dynamic bulk-up processes, in subaqueous settings.

1.4 Aims and objectives

The main aim of this thesis is to advance understanding of how subaqueous landslides initiate, evolve, and reach long runout distances on gentle carbonate-rich slopes. To achieve this aim, this thesis seeks to analyse the dynamic feedbacks involved in the mechanics of failure initiation (i.e., how physical properties change during failure), the flow-substrate interactions (erosion, deposition, or lubrication), and the evolving depositional and erosional processes during self-confinement. Three distinct methods are used: seismic-well tie, seismic interpretation, and physical experiments. Together, this thesis strives to synthesise the findings on the morphology and distribution of subaqueous mass flow deposits, in order to understand the mechanical changes leading to submarine failures and the process-linkages between sediment failure, subsequent evolution, and flow mobility on gentle slopes.

The main aim is addressed through the research questions outlined above, and with the following chapter-specific aims and objectives. Chapter 2 reviews the key concepts of submarine landslides and submarine debris flows, and the previous research relevant to physical properties of carbonate sediments, flow-substrate interactions and physical experiments. Chapter 3 then establishes the regional geological and stratigraphic framework of the Exmouth Plateau, offshore NW Australia, providing the context for the field-based analysis in Chapters 4 and 5 and the process-based experiments in Chapter 6.

1.4.1 Chapter 4: Learning from crushing failures: Changes in physical properties reveal the mechanics of submarine carbonate landslides

The aim of Chapter 4 is to examine how the physical properties of calcareous weak layers, such as their porosity, water content, permeability, and fossil abundance, change during failure. This will be investigated by utilising ODP wells from the offshore NW Australian, where water-rich layers can be mapped from undeformed sediments into the basal shear surfaces of carbonate landslides. Examining how the physical properties of weak layers evolve during landsliding enables the process dynamics and evolution of submarine landslides to be assessed. The objectives are to:

i. Document the physical properties of the unfailed stratigraphy recognised adjacent to the landslides through seismic-well ties.
ii. Explore the physical properties of the same key stratigraphic units and surfaces after failure.
iii. Discuss the processes accounting for changes in physical properties of key horizons (i.e., weak layers) before and after failure.

Based on the results, a new mechanistic model is proposed to capture the process interactions of carbonate landslide evolution.

1.4.2 Chapter 5: Self-confining submarine debris flows: A mechanism for long run-out on gentle slopes

The aim of Chapter 5 is to document the depositional architecture of a self-confined submarine debrite using three-dimensional seismic reflection data from the Exmouth Plateau, offshore northwest Australia, where the slope gradient is less than 1°. The objectives are to:

i. Examine how depositional relief is generated.
ii. Understand the nature of substrate incision at the base of the debrite, and quantify the amount of substrate entrainment.
iii. Document the characteristics of grooves on the basal shear surface to help reconstruct the spatio-temporal patterns of submarine debrite formation.

Based on the results, a new sedimentological model is proposed to explain the evolution of a submarine debris flow with long run-out on gentle slopes, in order to examine the nature of self-confinement in submarine debris flows.

1.4.3 Chapter 6: Segregation and evolving substrate interaction: Process insights from observation of single and successive subaqueous granular flows

The aim of Chapter 6 is to understand how submarine debris flows interact with the evolving depositional relief, by analysing the process interactions between subaqueous granular flows and their deposits through physical experiments. The specific objectives are to:

i. Investigate grain-size segregation in single subaqueous granular flows with different mixtures, and to highlight the distinctive characteristics of subaqueous segregation through the comparison with subaerial counterparts.
ii. Quantify the downstream variations in levee thickness using digital elevation models (DEM), and analyse the grain-size distribution and sphericity for deposits in single events.

iii. Evaluate the role of flow-deposit interactions during multiple events on runout distances.

Based on the experimental observations of multiple subaqueous granular flows, a new self-confining model is developed that explains how particle segregation and flow-deposition interactions can increase the run-out distances of submarine debris flows.

Drawing together the main findings from Chapters 4-6, Chapter 7 provides a synthesis and outlines directions for future work. Chapter 8 presents the conclusions of the thesis.

Chapter 2 Literature review

This literature review chapter has four parts:

i. An introduction to the classification of submarine gravity flows and their transformations and deposits, with a particular focus on submarine landslides and debris flows (Section 2.1).
ii. A review of the role of physical properties of carbonate sediments and changes on burial (Section 2.2).
iii. Seismic stratigraphic expression of deep-water systems, covering the seismic expression of submarine landslides deposits (Section 2.3).
iv. A review of previous physical experiments of granular and debris flows and the limitations of existing models (Section 2.4).

2.1 Submarine gravity flows

Submarine gravity flows are gravity-driven processes that exhibit a wide range of mass movements types and behaviours (Moscardelli and Wood, 2008; Haughton et al., 2009; Wu et al., 2021). They can be classified into: (i) cohesive and coherent mass movements, such as creeping, sliding, and slumping; and (ii) sediment gravity flows, such as debris flows, turbidity currents, and their transformations to transitional flows and hybrid flows (Middleton and Hampton, 1973; Lowe, 1982; Shanmugam et al., 1994, 2020; Haughton et al., 2009; Posamentier and Martinsen, 2011; Hodgson et al., 2026; Figure 2-1). These categories reflect increasing internal deformation and mass disaggregation from coherent slope-parallel mass movement to fully disaggregated, matrix-supported flow behaviour. Submarine landslides and submarine debris flows are widely documented on global continental margins (e.g., Moscardelli and Wood, 2008, 2016; Talling et al., 2014), and usually account for large-scale long-runout (up to hundreds of km) mass movement even on gentle slopes (<1°; e.g., Gee et al., 1999; Talling et al., 2007).

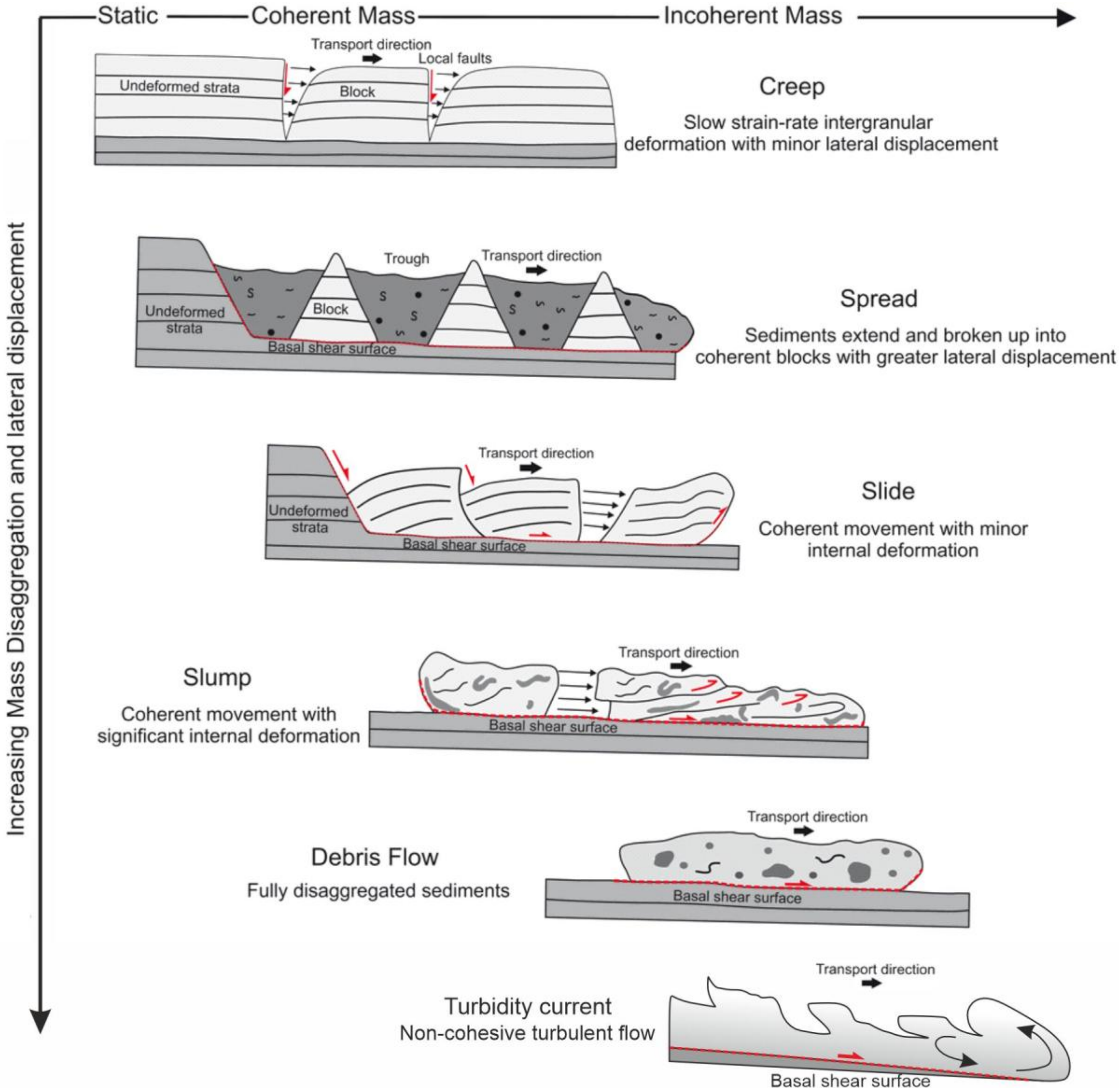

Figure 2-1: Classification of submarine slope failures from coherent mass flows to turbulent frictional sediment gravity flows (modified from Wu et al., 2021).

2.1.1 Submarine landslides

Submarine landslides are gravity-driven mass movements that can transform fully or partially from one type of sediment gravity flow to another (Piper et al, 1999; Moscardelli and Wood, 2008; Hodgson et al., 2026). Thus, submarine landslide is used as a broad, inclusive term for a wide range of submarine gravity flow types, encompassing creep (e.g., Nemec, 1990; Silva and Booth, 1984; Li et al., 2019), slides (e.g., Haflidason et al., 2004, 2005; Micallef et al., 2008; Piper et al., 2012), slumps (e.g., Couvin et al., 2024), and associated debris flows (e.g., Prior et al., 1984; Masson et al., 1997, 1998) and turbidity current processes (e.g., Clare et al., 2014; Figure 2-1 and Figure 2-2). A continuum of movement styles from creep with no basal detachment, through slide with basal detachment but limited internal deformation, to slump with basal detachment and internal deformation, reflects increasing displacement, internal deformation and disaggregation (Hampton et al., 1996; Moscardelli and Wood, 2008; Talling et al., 2012a; Wu et al., 2021; Hodgson et al., 2026).

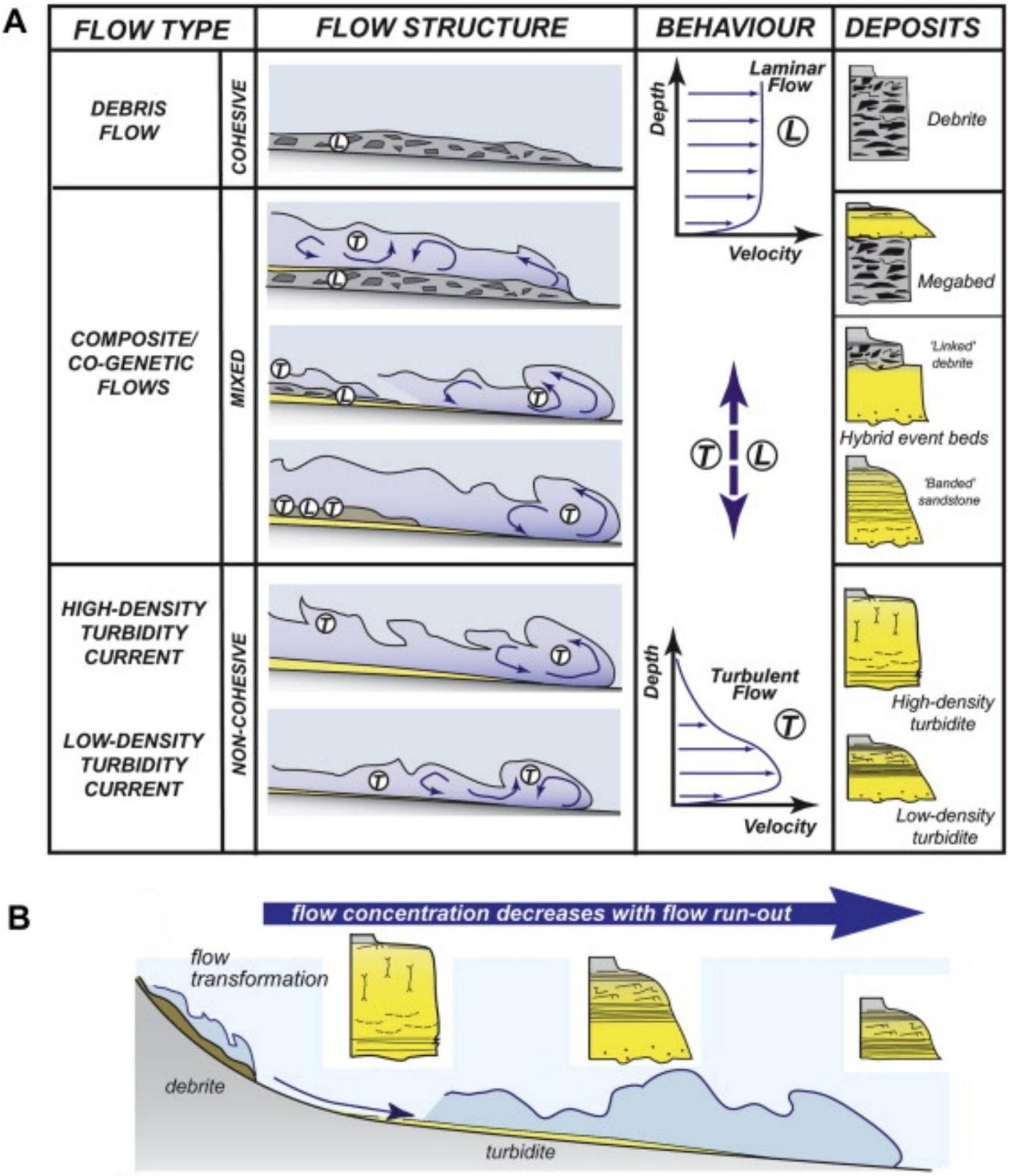

Figure 2-2: (A) Classification of subaqueous sediment gravity flows. (B) Evolution process from submarine debris flows to turbidity currents (from Haughton et al., 2009).

Submarine landslides are well known in siliciclastic depositional settings, whereas relatively few large-scale landslides, up to thousands of km^2, are documented on carbonate-dominated regions even though the slope gradient is very low (<2°). For example, on the Exmouth Plateau, offshore Northwest Australia, the submarine carbonate landslides cover an area of over 6000 km^2 on a gentle slope (Wu et al., 2023). Carbonate landslides are mainly found oceanward of the continental shelf-break in tropical or subtropical regions, such as offshore Australia (Scarselli et al., 2013, 2020; Wu et al., 2023), Ontong Java (Watson et al., 2017), the Inner Sea (Maldives) (Lüdmann et al., 2022), and the Bahamas (Tournadour et al., 2017). The global distribution of carbonate landslides is attributed to the widespread occurrence of carbonate sediments on the seafloor (Dutkiewicz et al., 2015, 2020; Figure 2-3). Carbonate sediments consist of microfossils (i.e., foraminifera and nannofossils), which exert an important role on porosity, compressibility, and shear strength (Palmer-Julson and Rack, 1992; Rack et al., 1993; Gaudin and White, 2009; Dijkstra et al., 2013; White et al., 2013). Consequently, the mechanical behaviour of carbonate-rich sedimentary successions differs fundamentally from siliciclastic settings. Most studies focus on siliciclastic submarine landslides (e.g., Sultan et al., 2004; L'Heureux et al., 2011, 2012; Vardy et al., 2012; Miramontes et al., 2018; Krastel et al., 2019), despite calcareous ooze representing the most widespread deep-sea lithology in the global ocean (Dutkiewicz et al., 2015, 2020; Figure 2-3). Given the extensive global coverage of carbonate sediment on the seafloor, understanding the mechanical behaviour of carbonate sediments is essential for evaluating submarine slope instability.

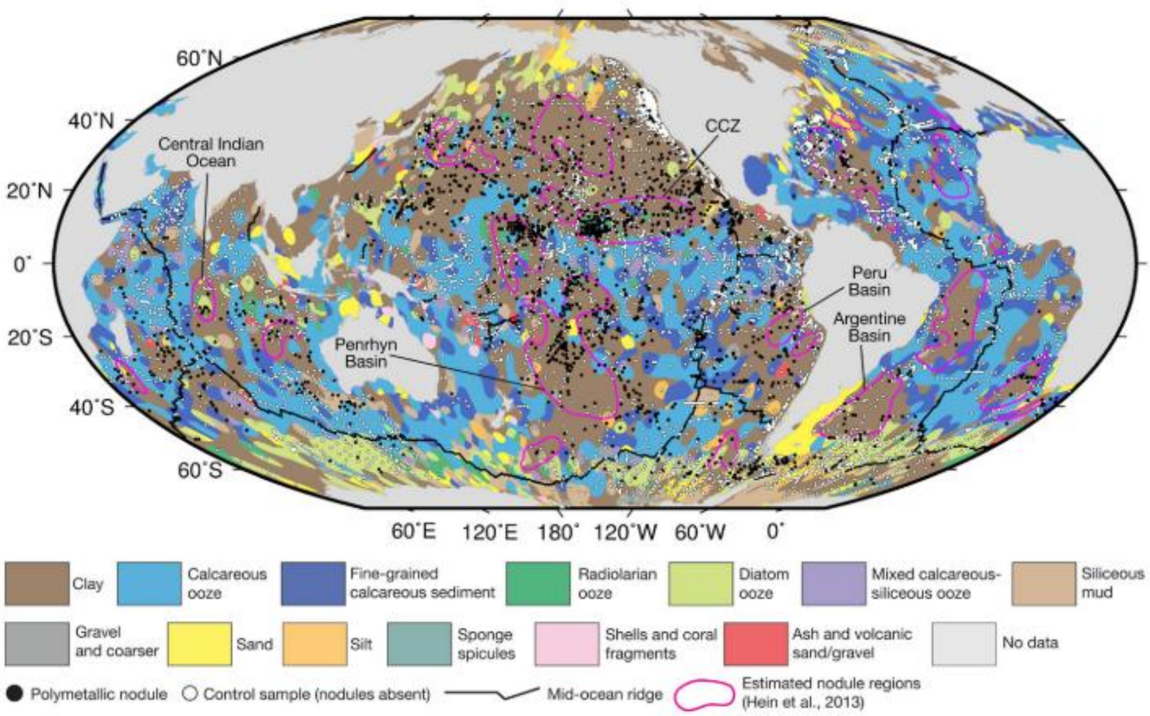

Figure 2-3: Global distribution of seafloor lithology, demonstrating that calcareous ooze is the most widespread deep-sea lithology in the global ocean (from Dutkiewicz et al., 2020).

Submarine landslide deposits are mass flow deposits and represent the preserved stratigraphic deposits of submarine slope failure events (e.g., Hampton et al., 1996; Masson et al., 2006; Micallef et al., 2008; Alsop and Marco, 2011; Hodgson et al., 2026). The volume of submarine landslide deposits can reach thousands of km^3 (Moscardelli and Wood, 2008, 2016), such as the Storegga Slide deposits offshore Norway that have a volume of approximately 2400-3200 km^3 (Haflidason et al., 2004, 2005; Bryn et al., 2005). Submarine landslide deposits play an important role in the stratigraphic architecture of sedimentary basins. In some cases, they are a substantial proportion of a basin-fill (e.g., Posamentier and Martinsen, 2011; Li et al., 2015a; Sun et al., 2018; Wu et al., 2020).

A conceptual model of submarine landslide deposits has been proposed based on seismic and outcrop observations, showing sediments from an extensional headwall region transported downslope through a transitional region, and ultimately deposited in a compressional toe region (Prior et al., 1984; Bull et al., 2009; Figure 2-4). Further details on the seismic identification of submarine landslide deposits can be seen in *Section 2.3 (Seismic stratigraphy and facies of deep-water systems)*.

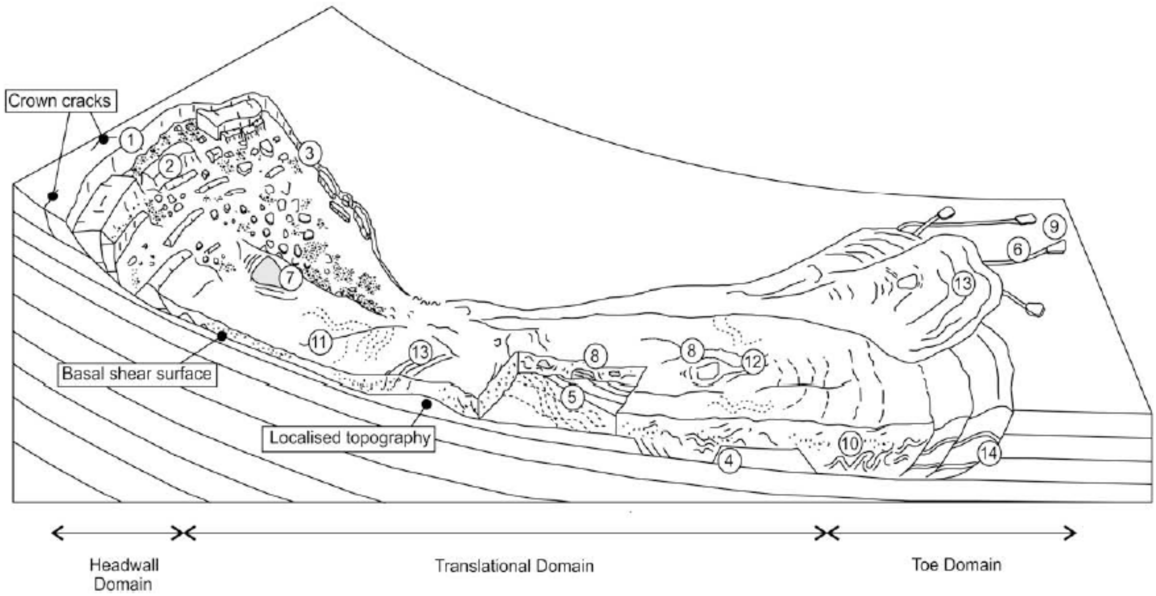

Figure 2-4: A conceptual model of a submarine landslide, consisting of three main domains, including an upstream extensive headwall region, a transitional region, and a downstream compressive toe region (from Bull et al., 2009).

2.1.2 Submarine debris flows

Submarine debris flows are a type of sediment gravity flow and are characterised by laminar, non-turbulent behaviour in which particles are supported by a combination of matrix strength, grain interaction and buoyancy (Middleton and Hampton, 1973; Coussot and Meunier, 1996; Haughton et al., 2009). Submarine debris flows are commonly matrix-supported, with cohesive forces from mud contributing to the flow rheology (Figure 2-2), and can range from high-concentration mud flows to more granular debris flows, reflecting a continuum of rheological behaviour (Talling et al., 2012a). Additionally, submarine debris flows can travel extraordinarily long (tens to hundreds of km) distances over slopes where gradients decrease to almost flat (~0°) (Prior et al., 1984; Masson et al., 1997; Gee et al., 1999; Talling et al., 2007; Tang et al., 2022). For example, the Saharan debris flow extends over 400 km downslope of the Canary Islands on a gradient that decreases to as little as 0.1° (Embley, 1976; Gee et al., 1999). The prevalence of submarine debris flows with long runout distances can catastrophically threaten deep marine engineered seafloor constructions and have a significant impact on the financial aspects of hydrocarbon exploration and deep-marine installations (Gee et al., 1999; Locat and Lee, 2002; Talling et al., 2007; Zhang et al., 2019). Submarine debris flows are characterised by a strong erosive capacity, and can gain substantial deposits through substrate entrainment (e.g., Masson et al., 1997; Gee et al., 1999; Georgiopoulou et al., 2010; Dakin et al., 2013; Hodgson et al., 2019; Krastel et al., 2019). Thus, it is important to analyse the flow-substrate interactions, especially those with long runout on gentle slopes. Further details on the flow-substrate interactions can be seen in *Section 2.2.4 (Water-rich substrates and flow processes) and Section 2.4 (Evolution of carbonate mass flows).*

The deposits of subaqueous debris flows, debrites, are formed by the *en masse* consolidation of sediment-laden gravity flows, in contrast to the incremental, size-segregating settling and layer-by-layer deposition that characterises many turbidites (Talling et al., 2012a). Subaqueous debrites are typically characterised by massive, chaotic, and poorly sorted sediments, with clasts floating within a finer-grained matrix (Embley, 1976; Prior et al., 1984; Coussot and Meunier, 1996). Based on the matrix composition and cohesive strength, subaqueous debrites can be subdivided into (i) very clean sand debrite (D_{VCS}), (ii) clean sand debrite (D_{CS}), and (iii) cohesive debrites, including lower strength muddy debrite (D_{M-1}) to higher strength muddy debrite (D_{M-2}; Talling et al., 2012a; Figure 2-5). The classification demonstrates that debris-flow behaviour forms a continuum controlled by cohesive clay fraction and matrix strength.

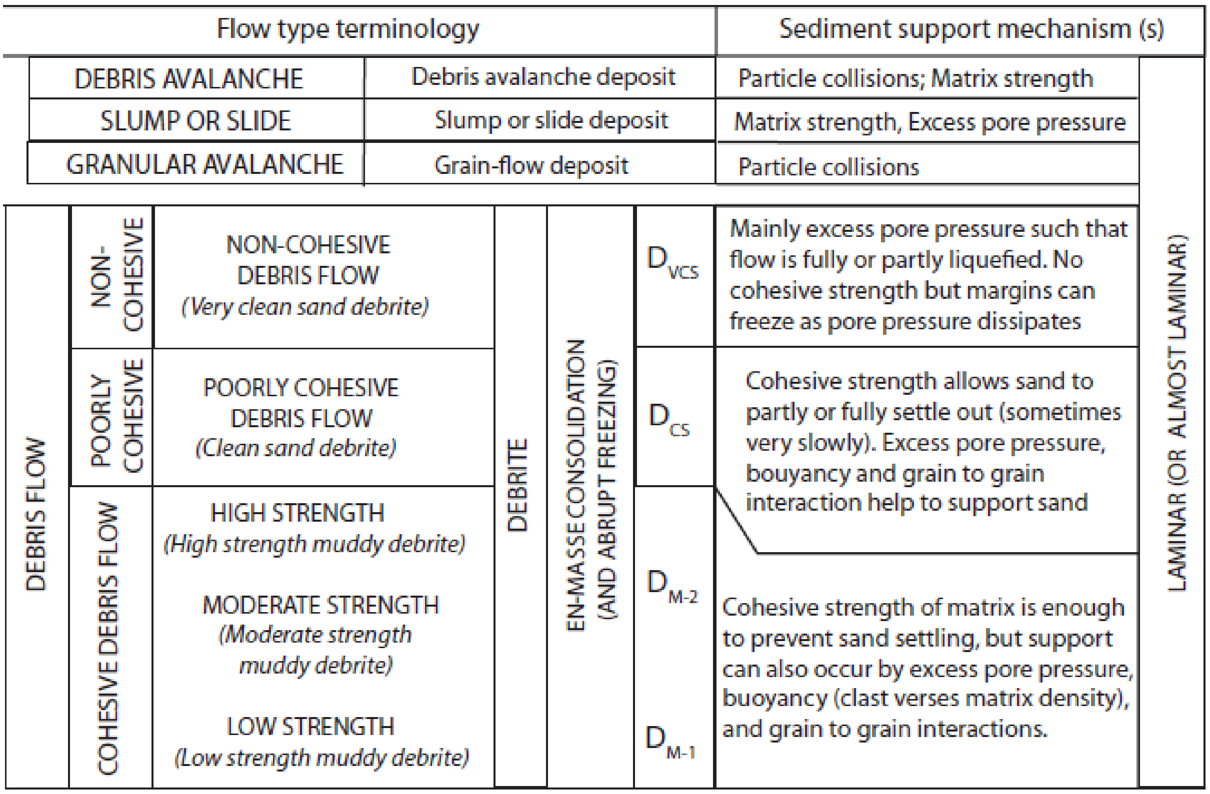

Figure 2-5: Terminology of subaqueous debris flow and their deposits (from Talling et al., 2012a).

Blocks are common components of debrites (Gee et al., 1999), and particularly in subaqueous settings, they can reach lengths of hundreds of metres to several kilometres (e.g., Jackson, 2011; Alves, 2015; Hodgson et al., 2019; Nwoko et al., 2020a; Ortiz-Karpf et al., 2017; Soutter et al., 2018; Li et al., 2022). During transport, blocks embedded within debris flows can act as tools to generate erosional structures (e.g., striations and grooves) on the basal shear surfaces during transport (Figure 2-6). Consequently, these basal grooves are widely used as palaeocurrent indicators (e.g., Nissen et al., 1999; Gee et al., 2005; Ortiz-Karpf et al., 2017; Soutter et al., 2018; Li et al., 2022).

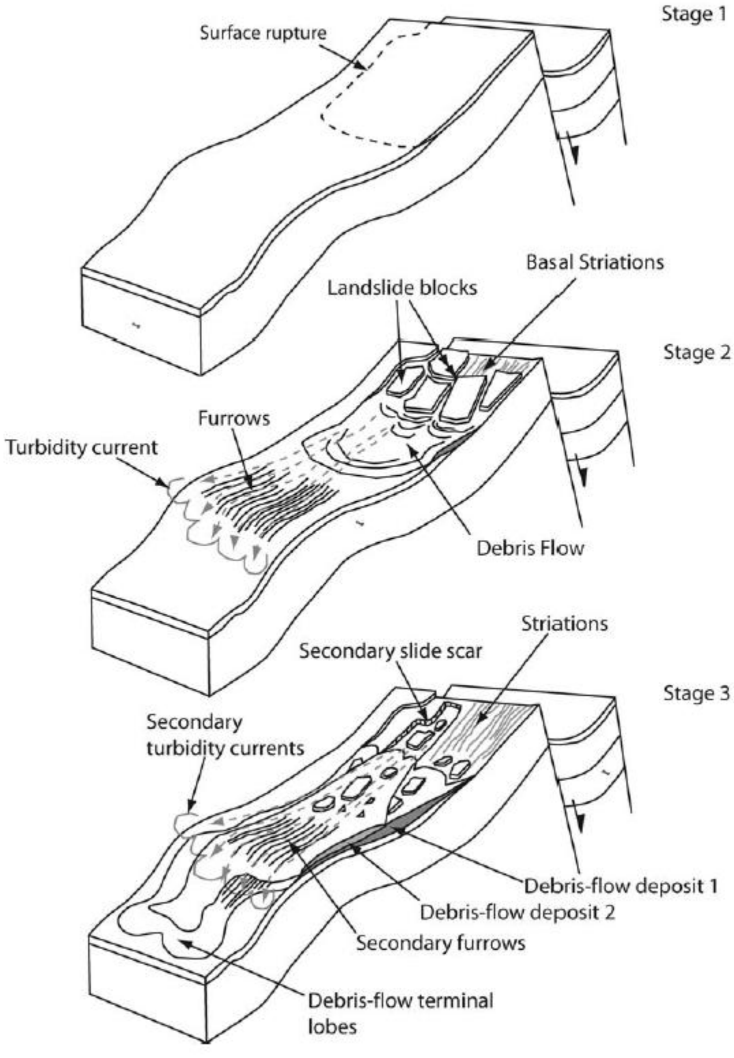

Figure 2-6: Conceptual model of submarine debris flow evolution, demonstrating the formation of substrate erosional structures (e.g., striations and grooves; from Gee et al., 2006). Three stages are involved from the failure initiation to the grooves formation: Stage 1 involves the initiation of submarine slope failure, Stage 2 is the development of blocks and the transition from submarine landslide to submarine debris flow and turbidity current, and Stage 3 shows the formation of striations and successive failures.

Grooves are typically expressed as sub-parallel, linear erosional structures on basal surfaces of failures, and can extend for kilometres while remaining remarkably constant in terms of width, depth and straightness (e.g., Gee et al., 2005; Ortiz-Karpf et al., 2017; Soutter et al., 2018). Such constant geometries impose strict mechanical constraints on both the hosting flow and the substrate, requiring clasts to be dragged in a stable position (without rotation) at a constant height (without bouncing) relative to the flow body, through a substrate strong enough to resist deformation, fluid stresses, or backfilling once the groove has been cut (Peakall et al., 2020). Previous research linked the formation of grooves to turbidity currents (e.g., Kuenen, 1957; Bouma, 1962; Enos, 1969; Pett and Walker, 1971; Crimes, 1973), given that grooves are more frequently observed at the base of T_A beds. However, early studies also recognised that grooves can form beneath slumps and slides (Kuenen, 1957), and later work has further documented their occurrence in association with high-strength cohesive debris flows (Talling et al., 2012a; Dakin et al., 2013) and hybrid event beds (Talling et al., 2004, 2012a,b; Peakall et al., 2020).

More recently, studies such as Peakall et al. (2020) and McGowan et al. (2024), have questioned whether highly turbulent flow conditions are compatible with the observed constancy of groove geometry. Peakall et al. (2020) argued that the constant width, depth and linearity of grooves are indicative of transport by cohesive plug flows (i.e., debris flows, slumps and slides), which have sufficient cohesive strength to hold clasts in position at the base of the flow (Figure 2-7). As the debris flow advances, these clasts can act as erosive tools, in a single position without rotating at a constant height (no bouncing), thus forming the constant geometry of grooves on soft fine-rich substrate (Peakall et al., 2020, 2024). Therefore, the geometry and distribution of grooves provide important insight into the dynamics and the rheology of the hosting flow and the mechanics of the basal layer at the point of formation.

A Low-density turbidity current

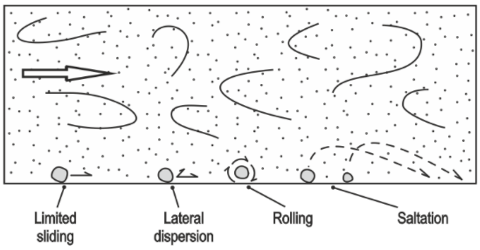

Weaknesses

- Clasts slide for very short distances (<1 grain diameter).
- When overpassing, particles tend to roll.
- Particles rapidly disperse laterally.

B HDTC - traction carpet

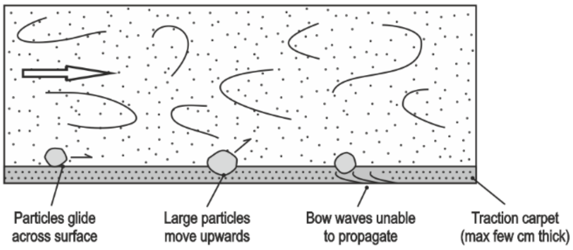

Weaknesses

- Traction carpets thinner than diameter of particles forming many grooves.
- Large particles move away from the bed or glide along the top interface of traction carpet.
- Cannot explain presence of groove marks under T_c beds.
- Bow waves cannot propagate to form chevrons.

C HDTC - high-concentration basal layer

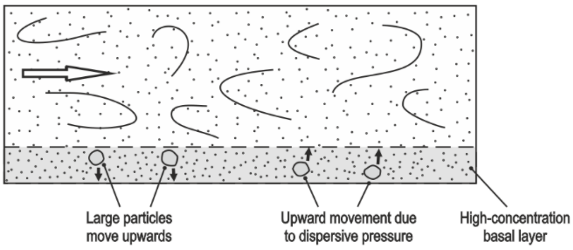

Weaknesses

- Large particles will not remain at a fixed height.
- Large particles may preferentially settle.
- If dispersive pressure is important then large particles may rise.
- If turbulence is extinguished then a very limited tractional signature is produced.

D Granular flow

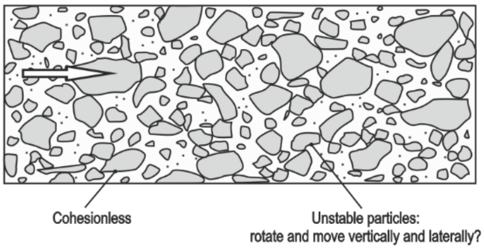

Weaknesses

- Grooves not reported in subaqueous settings.
- Cohesionless flow - clasts likely not fixed in position.
- Restricted to slopes of a few degrees.

E Liquefied/fluidised flow

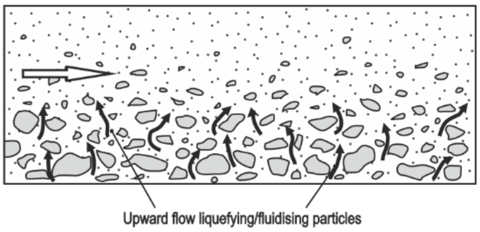

Weaknesses

- Flows have no strength and cannot hold a tool in place.
- Unlikely to liquefy/fluidise large particles.

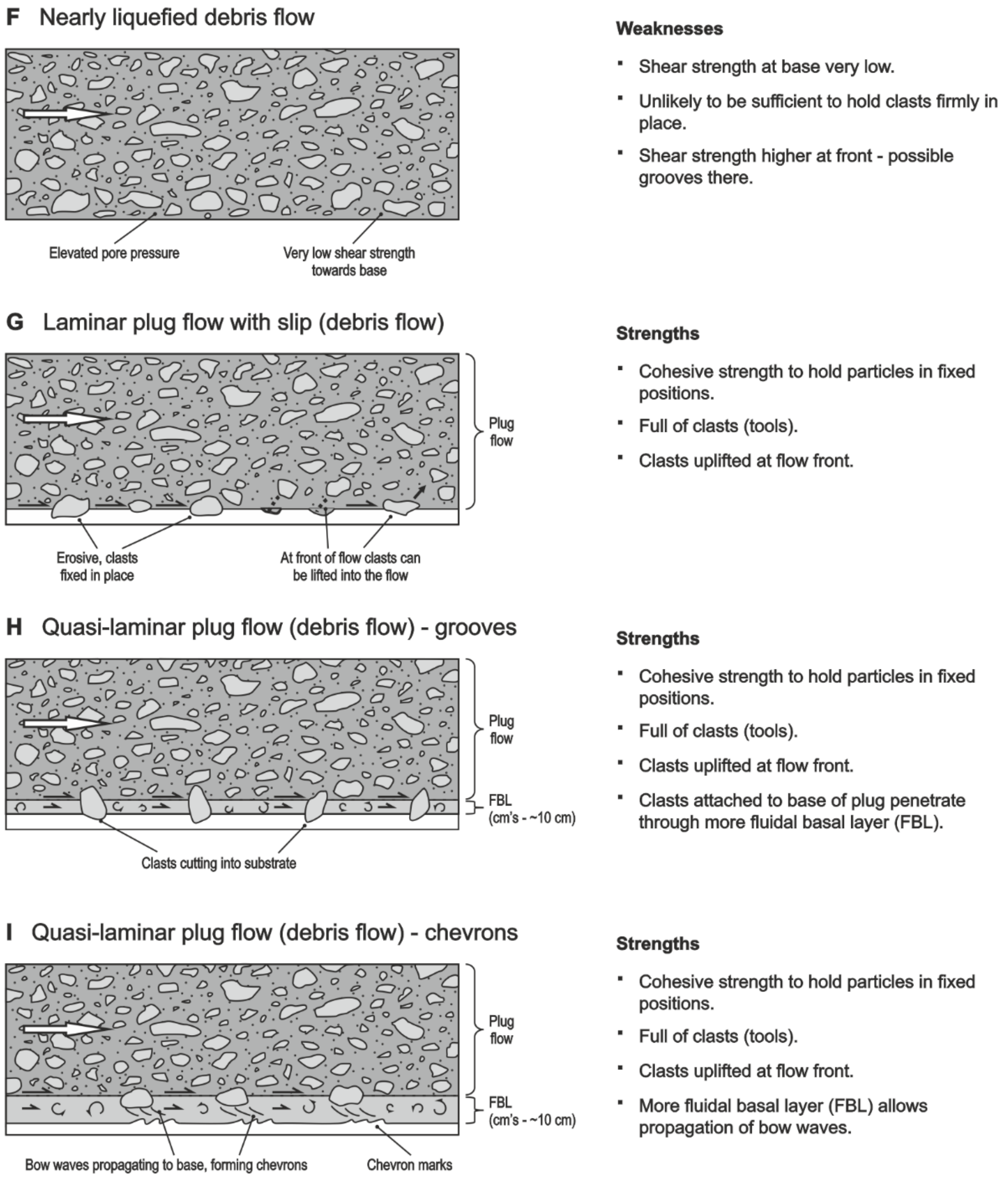

Figure 2-7: Mechanisms within different types of sediment gravity flow. Only those in G-I can explain the formation of grooves and chevrons (from Peakall et al., 2020).

2.2 Fine-grained carbonate sediments

Carbonate sediments (referred to as carbonate soils in engineering geology literature) are classed as calcareous sediments with more than 30% calcite carbonate and/or $CaMg(CO_3)_2$. The carbonate material can be sourced from coral and algal deposits, or foraminifera and mollusc material, or abiotic precipitation (Hamilton, 1976; Palmer-Julson and Rack, 1992; Morse, 2003; Berger and Wefer, 2009).

2.2.1 Physical properties of carbonate sediments (soils)

Carbonate sediments can contain microfossils, such as foraminifera tests, which contain skeletal voids (Bachman, 1984; Palmer-Julson and Rack, 1992; Hairabian et al., 2014; Beemer et al., 2019), including inter-skeletal pore space and intra-skeletal pore space (Figure 2-8). Geotechnical observations demonstrate that as little as 0.47 wt% of foraminifera can result in pronounced increase in porosity of carbonate-rich successions (Sawyer and Hodelka, 2016). Foraminifera are an important component of Cenozoic carbonate sediments (Palmer-Julson and Rack, 1992), and are characterised by hollow calcareous tests in which skeletal pore space can range from approximately 61-73% of the test volume (Bachman, 1984). Measurements indicate that these internal voids can increase total sediment porosity by 35-44% (Bachman, 1984). Bachman (1984) proposed that ‘extra’ water can be stored in these hollow skeletal structures. However, this water is largely isolated from the surrounding pore system unless the skeletal particles can be fractured (Demars, 1982; Rack et al., 1993).

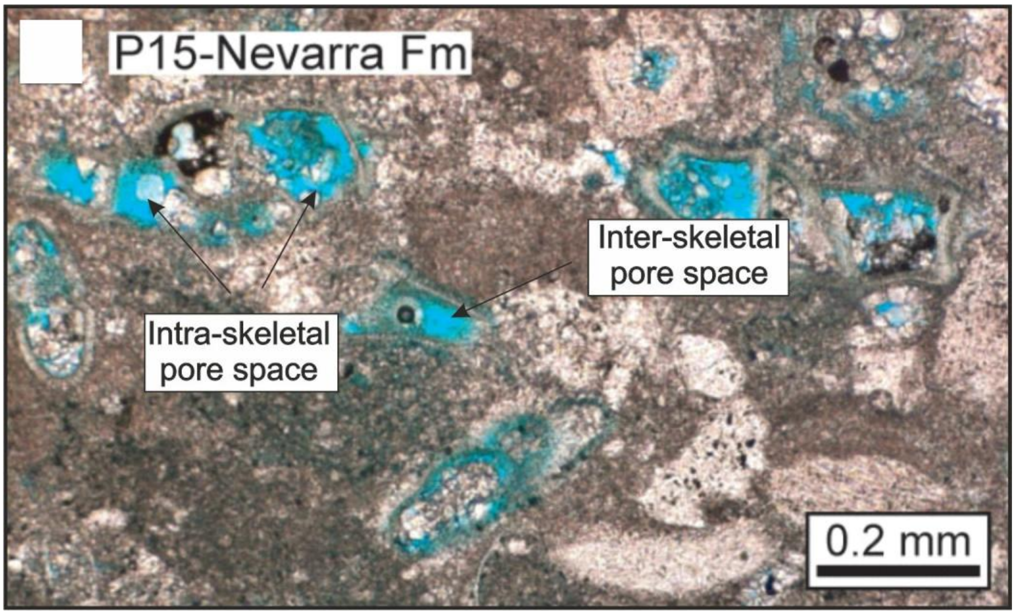

Figure 2-8: Blue-epoxy stained thin-section photomicrograph, illustrating inter-skeletal pores and intra-skeletal pores within foraminifera tests in a carbonate sediment (modified from Hairabian et al., 2014).

Under compacted, carbonate sediments can go through a combination of rearrangement and crushing of the grains (Dijkstra et al., 2013; Beemer et al., 2019; Wang et al., 2020), thus releasing inter- and intra-skeletal pore water preserved within microfossils. The fracture strength of microfossils is strongly controlled by their biomorphology (Beemer et al., 2019). Planktic foraminifera have greater void space but thinner walls, and their strength is one-fifteenth of benthic foraminifera (Beemer et al., 2019). In general, the fabric formed by porous, rigid siliceous skeletons, such as those of diatoms and radiolaria, results in greater resistance to compaction during burial (Rack et al., 1993). This interpretation is supported by consolidation tests of diatomaceous sediments that were subjected to vertical stresses of up to 3200 kPa (Rack et al., 1993). In their consolidation tests, diatoms remained largely intact (i.e., centric diatom) or exhibited severe breakage (i.e., pennate diatom), whereas nannofossil skeletons packed tightly together and often disassociated into crystallites, thereby closing interparticle voids.

When carbonate oozes fail, their residual strength decrease ten-fold relative to their initial strength, whereas the residual strength of siliciclastic sediments show only two-fold reduction in their initial strength (Gaudin and White, 2009). Siliciclastic particles with clay mineralogy have stronger attractive forces (electrostatic bonding) due to the ionic layer present on the surface of clay particles. Whereas carbonate sediments rely primarily on mechanical grain contacts and, in some cases, early-stage cementation (White et al., 2013). This pronounced post-failure strength loss implies that carbonate slopes are particularly susceptible to rapid acceleration and large volume failure once instability is initiated, posing significant threats to submarine economic safety (e.g., seafloor communication pipes and oil and gas platforms; White et al., 2016).

2.2.2 Carbonate sediment types

Carbonate-dominated sediments are commonly classified into four broad types: ‘oozes’, ‘marls’, ‘sarls’, and ‘smarls’, based on relative proportions of non-biogenic material, siliceous biogenic components, and calcareous biogenic components (Barron et al., 1984; Stow and Piper, 1984; Dean et al., 1985; Figure 2-9).

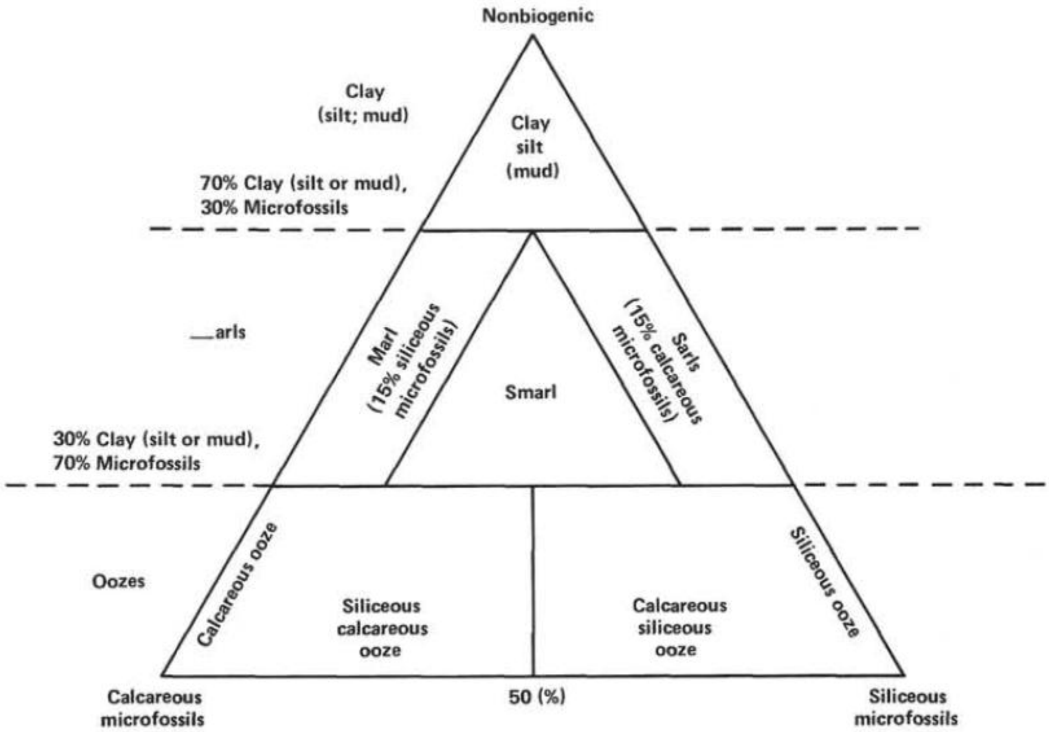

Figure 2-9: Classification of the three-component system, including non-biogenic, siliceous biogenic, and calcareous sediments (from Barron et al., 1984).

Oozes are biogenic sediments in which the total biogenic component exceeds 70%, whereas marls, sarls and smarls, are characterized by 30-70% of biogenic components, with varying proportions of calcareous and siliceous microfossils (Barron et al., 1984; Stow and Piper, 1984). Global compilations of seafloor sediment distribution demonstrate that 'carbonate ooze' is the most widespread deep-sea lithology in the global ocean (Dutkiewicz et al., 2015, 2020). In the Dutkiewicz et al. (2015, 2020) classification, 'calcareous ooze' refers to the unconsolidated sediment containing > 30% calcareous skeletons (e.g., foraminifera, pterapods, coccoliths), which corresponds to calcareous oozes and marls in the classification of Barron et al. (1984).

Oozes are accumulations of skeletons and skeletal fragments of carbonate and biosiliceous phytoplankton and zooplankton (e.g., nannofossils and foraminifera, or diatoms and radiolaria, respectively; Rack et al., 1993; Morse et al., 2003). They usually undergo a series of diagenetic processes with a corresponding progressive change in physical properties during burial. In the shallow burial stage (approximately 160 m), unconsolidated oozes undergo simple mechanical compaction driven by overburden pressure, with high gradients in porosity, bulk density, and sonic velocity but remain soft (Dean et al., 1985; Grützner and Mienert, 1999). In the next stage of burial (~160-250 m), the effect of gravitational mechanical compaction decreases because firm particle contacts between microfossil tests are established (Grützner and Mienert, 1999). During this stage, microfossil test dissolution begins along with partial calcite reprecipitation, characterized by very low gradients in porosity but high in density (Grützner and Mienert, 1999). From approximately ~250 m burial depth, oozes gradually become harder with increased overpressure and form firm chalk, eventually forming hard limestone. At this depth, the particles are affected by cementation and begin to fuse and grow, resulting in the apparent diminution of pore volume (Grützner and Mienert, 1999). At around ~700 m burial depth, the chalk-limestone transition is almost complete (Dean et al., 1985; Grützner and Mienert, 1999).

Marls are mainly dominated by calcareous microfossils with a portion between 30% to 70%, and clay minerals in proportions < 15% (Barron et al., 1984; Lamas et al., 2002). Sarls are characterised as siliceous-argillaceous sediments (for example, diatom clay and clayey diatom ooze), have more biogenic siliceous particles than calcareous microfossils in proportions < 15%, and contain < 75% of particles of extrabasinal origin (Dean et al., 1985; Milliken, 2014). Smarls are composed of > 30% non-biogenic components, characterised as more than 30% total siliceous and calcareous microfossils, with each type > 15% (Barron et al., 1984). No literature has been identified that documents the different physical properties of marls, sarls or smarls. However, Lee (1982) suggested that the shear strength of carbonate sediments (soils) can increase through mechanical interaction of less-plastic, more granular particles, or true cementation, with the increase in carbonate contents. Given the different carbonate content, it can be inferred that the shear strength of marls is the greatest, followed by smarls, then sarls. Thus, it is too simplistic to apply the term “ooze” to cover all carbonate sediments (i.e., sarls, marls, and smarls), considering their different composition and therefore physical properties.

2.2.3 Carbonate sediments on burial

(1) Formation of carbonate weak layers

Carbonate-rich successions undergo significant compaction from overlying stratigraphy during burial, which strongly influences their mechanical behaviour and slope stability. The shear strength of carbonate sediments mainly derives from mechanical factors and sometimes also from chemical factors (cementation) even at much shallow burial depths (e.g. seafloor; Bjørlykke and Høeg, 1997), which are both controlled by the carbonate content (Lee, 1982). Thus, mechanical compaction of carbonate sediments is particularly effective at shallow burial depths (~ 200 m), where high compressibility and limited consolidation combine to produce rapid porosity reduction (Rack et al., 1993; Casas et al., 2006). The enclosed chambers of foraminifera will break under moderate compressive stress at shallow burial depth, leading to abrupt expulsion of non-connected pore water (Demars, 1982; Rack et al., 1993; Beemer et al., 2019). Such rapid release of pore water due to particle rearrangement and breakage (Figure 2-10), particularly where permeability contrasts exist, can generate transient pore pressures that are a key mechanism in the development of laterally extensive weak layers (Gatter et al., 2021).

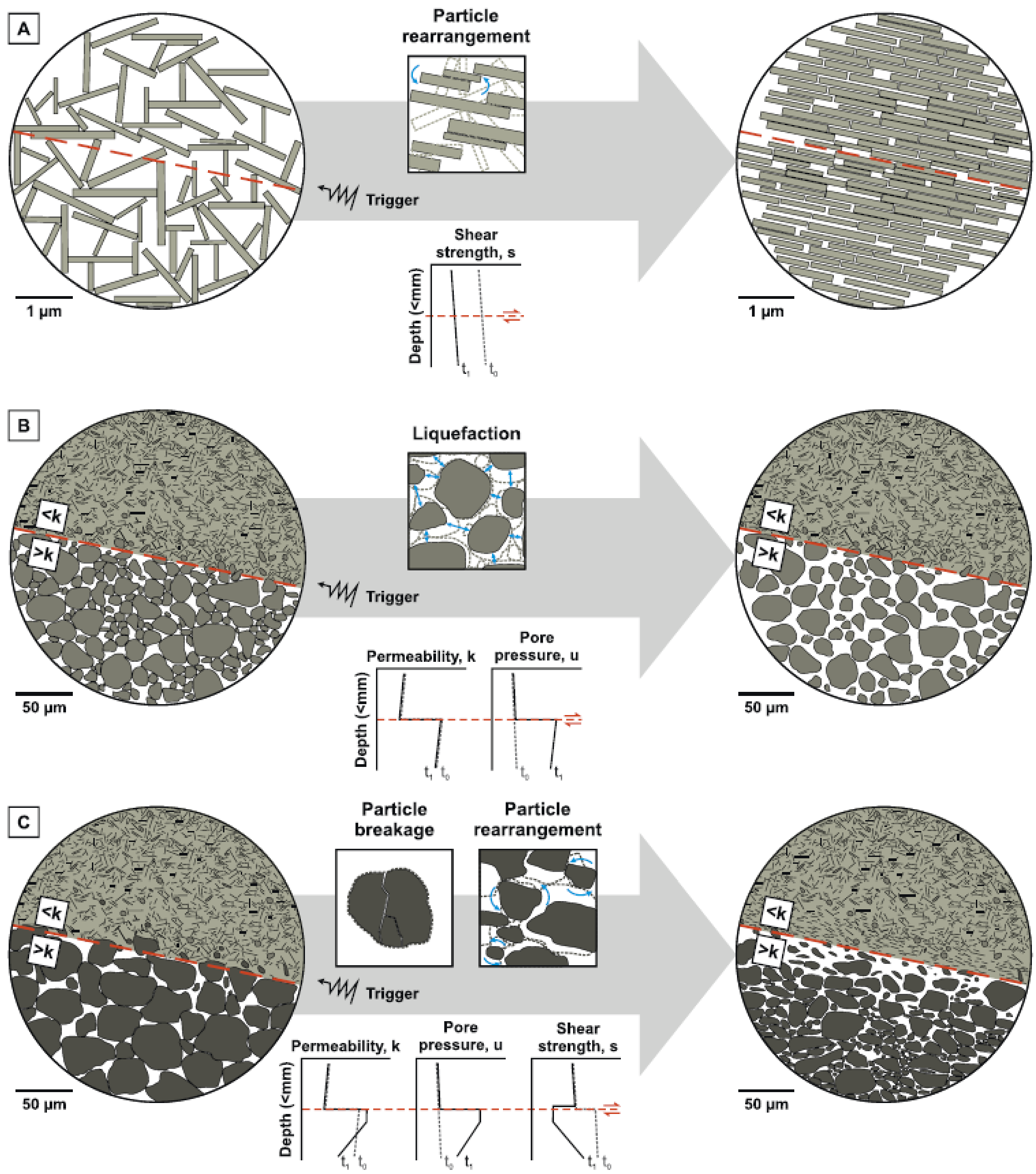

Figure 2-10: Schematic to illustrate three types of weak layers: (A) particle rearrangement, (B) liquefaction, and (C) water film formation. The last two types of weak layers are carbonate-related (from Gatter et al., 2021).

(2) Examples of carbonate failures

Controlled by the laterally extensive weak layers, large-scale carbonate submarine landslides develop even on extremely low slope angles (Figure 2-11), such as the examples on the Exmouth Plateau, offshore NW Australia (<2°; Puga-Bernabéu et al., 2011, 2020; Hengesh et al., 2013; Nugraha et al., 2022; Wu et al., 2023), Inner Sea (Maldives) (<1°; Lüdmann et al., 2022), Ontong Java Plateau (<1°; Berger and

Johnson, 1976; Mosher et al., 1993), and the Great Bahamas Bank (Principaud et al., 2015).

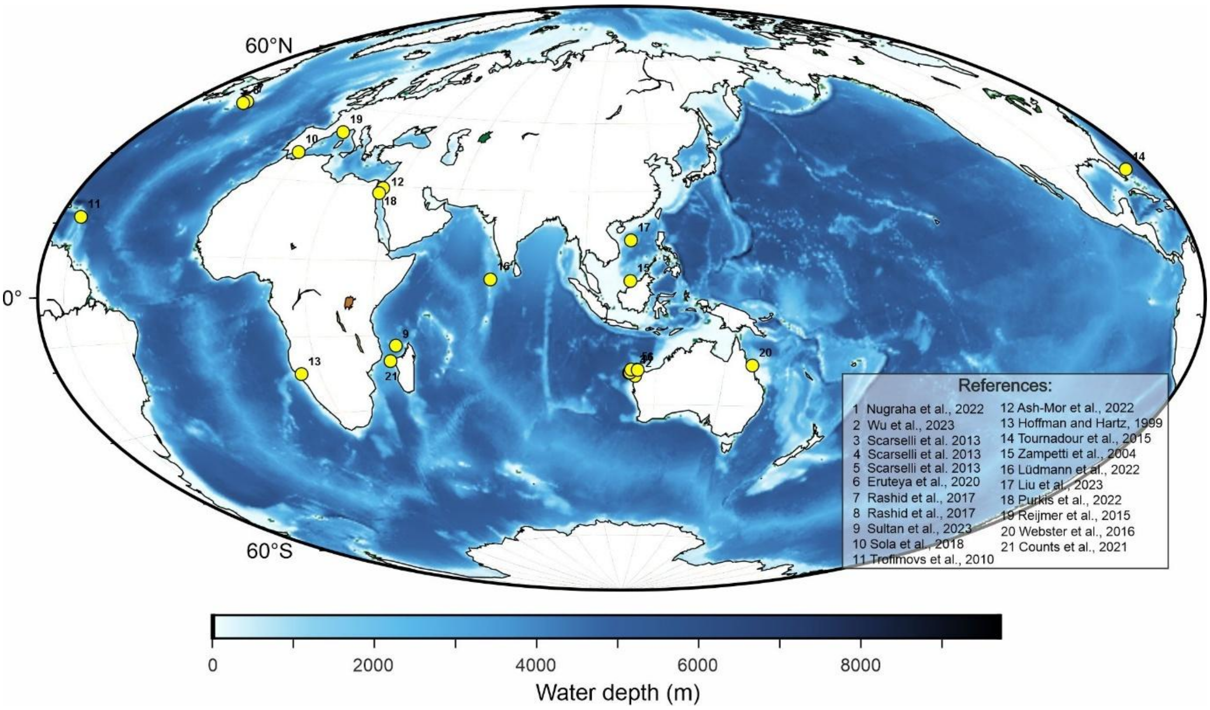

Figure 2-11: Global distribution of carbonate-rich gravity flows, labelled in yellow circles. The basemap comes from SRTM15, acquired by Generic Mapping Tools 6 (Tozer et al., 2019; Wessel et al., 2019).

2.2.4 Flow process mechanism on water-rich substrates

Submarine mass movements can be broadly classified into: (1) free-slip flows, which override substrate with little or no preserved evidence of erosion or deformation beneath the basal shear surface; and (2) no-slip flows, in which the strain front penetrates into the underlying substrate (Sobiesiak et al., 2018). No-slip flows can induce changes in flow volume through bulking-up. Hydroplaning and liquefaction have been proposed as the primary mechanisms enabling free-slip mass movement, and these processes can lead to flow bypass with limited shear stress transmission to the substrate, thereby restricting substrate erosion and deformation. The focus of this section is on the evolution process of free-slip flows over water-rich substrates, which can arise from the physical properties (water-rich and high compressibility) of carbonates.

The process of hydroplaning was first demonstrated in physical experiments by Mohrig et al. (1998), and demonstrated that ambient fluid is dynamically injected beneath the head of subaqueous debris flow, forming a thin lubricating layer that separates the flow from the underlying substrate (Figure 2-12). Hydroplaning is considered to occur when the hydrodynamic pressure at the flow head is sufficient to support the average submerged debris-load (Mohrig et al., 1998). Experimental results demonstrate that hydroplaning preferentially develops in high-clay (>~20 wt%) debris flows, which have a sufficiently high yield stress to establish a low-permeability head that prevents water dissipation upward through the head (Mulder and Alexander, 2001; Ilstad et al., 2004 a, 2004b, 2004c; De Blasio et al., 2006; Elverhøi et al., 2010). The low viscosity water lubricating film beneath the debris flow is easily sheared and associated with a dramatic reduction in the bed-resistance force, thereby providing a possible explanation for long runout of subaqueous flow on very low gradient slopes (De Blasio et al., 2004a, 2004b, 2006; Elverhøi et al., 2005, 2010; Acosta et al., 2017). In most cases, hydroplaning has been directly linked to flow long runout (De Blasio et al., 2006; Elverhøi et al., 2010) and detached outrunner blocks (De Blasio et al., 2004b, 2006; Elverhøi et al., 2005). However, direct evidence of hydroplaning in natural systems remains difficult to obtain, given that the basal water film cannot be preserved in the deposits. All laboratory and numerical studies on hydroplaning involve frontally unconfined coherent flow heads. Such hydroplaning relies on the development of hydrodynamic pressure at the advancing flow head, and therefore will be suppressed under conditions of frontal confinement where flow acceleration is restricted. Additional mechanisms are required to explain the enhanced mobility of submarine debris flows in frontally-confined settings.

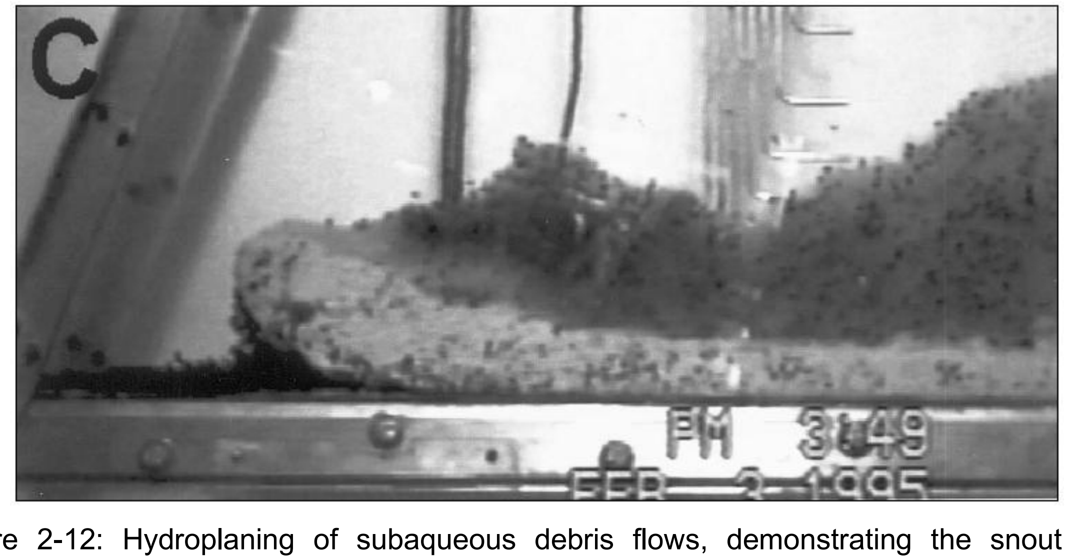

Figure 2-12: Hydroplaning of subaqueous debris flows, demonstrating the snout of a subaqueous flow lifting off of the channel bed (from Mohrig et al., 1998).

Unlike flow-acceleration-controlled hydroplaning, liquefaction is governed by pore-pressure within the substrate. Liquefaction occurs when shear-induced excess pore pressure equals the weight of the grains, so that the effective stress approaches zero, causing the grains to temporarily lose contact and float within the surrounding fluid (Lowe, 1976; Iverson, 1997; Iveson et al., 1997, 2010; Major and Iverson, 1999). Subsequent pore-pressure dissipation permits progressive re-establishment of effective stress, leading to grain settling from the base upward (Lowe, 1976). During the re-sedimentation process, pore water is squeezed out of underlying loaded sediment, and generates excess pressure where water cannot drain rapidly enough (Figure 2-13). Although liquefaction within the substrate is transient as pore pressure dissipates and grain contacts are progressively re-established, the resulting water film tends to outlast liquefaction settlement, thus sustaining interface lubrication and prolonging the period of reduced shear stress beyond the apparent time period of liquefaction (Kokusho, 1999).

Seed et al. (2003) suggested liquefaction susceptibility can be evaluated by comparing the natural water content (Wc) to liquid limit (LL), and sediments with Wc⩾0.80*LL are considered potentially susceptible to liquefaction under cyclic loading while sediments with a Wc%⩾0.85 may be liquefiable. True liquefaction requires shear-induced pore pressure exceeding the weight of the grains (the initial effective normal stress), its occurrence cannot be inferred from Wc/LL ratio alone without considering shear strength and the permeability of any boundary layers that govern pore pressure build up. Elevated pore pressure in such systems primarily arises from contractive shearing, whereby rapid deformation by the overriding flow induces volume contraction through shearing under undrained conditions (Iverson et al., 1997). This elevated pore pressure reflects the competition between the rate of contractive volume change and the rate of pore-pressure dissipation. Under such conditions, grain contacts persist, albeit weakened, and the mechanical shear strength of the substrate is markedly reduced (e.g., Stoecklin et al., 2017). Once the upward drainage is restricted by a relatively lower-permeability overlying layer, a permeability contrast can promote localised fluid accumulation along the basal interface, facilitating the formation of a thin water film at the flow-substrate boundary (e.g., Iverson et al., 1997; Kokusho, 1999; Kokusho and Kojima, 2002; Figure 2-13).

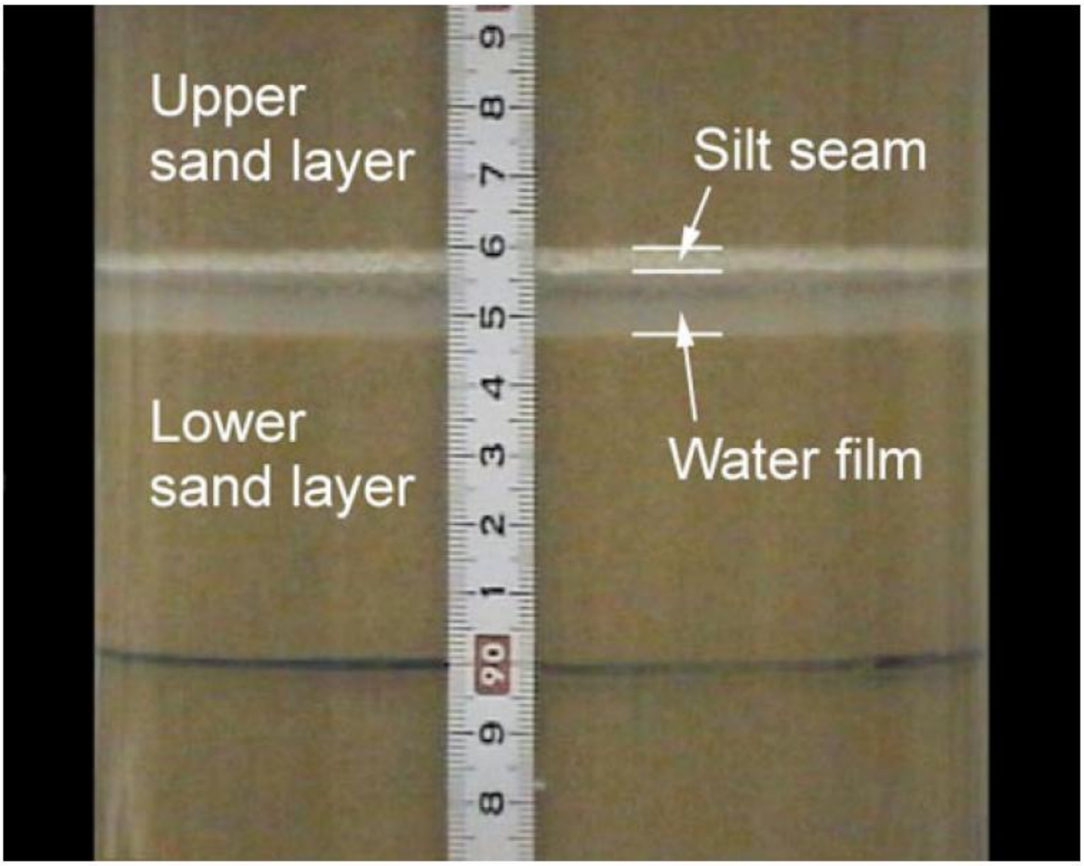

Figure 2-13: Liquefied sands and the resulting water film (from Kokusho, 1999)

2.3 Seismic stratigraphy and facies of deep-water systems

Advances in marine geophysical surveying have markedly improved our ability to analyse submarine landslides in offshore settings, such as two-dimensional (2D) and three dimensional (3D) seismic reflection data, multibeam bathymetry, autonomous underwater vehicles as platforms for some of these techniques, and sidescan sonar imaging (Clare et al., 2017). Among these methods, seismic reflection data, particularly 3D seismic datasets, have proven to be effective and widely used for analysing modern and buried submarine landslide deposits in offshore environments. High-resolution 3D seismic reflection data allow detailed analysis of the geometry, internal architecture, and basal shear surfaces of submarine landslides (e.g., Bull et al., 2009), thereby providing critical insights into the flow-substrate interaction and emplacement processes.

2.3.1 Seismic characteristic of mass-transport deposits

In seismic reflection data, submarine landslide deposits are generally referred to as mass-transport deposits due to their chaotic seismic facies (MTDs; Zampetti et al., 2004; Bull et al., 2009; Sawyer et al., 2009; Omosanya and Alves, 2013; Li et al., 2015, 2017; Nwoko et al., 2020b). In geophysical and subsurface data, it is generally hard to identify individual submarine landslide events, therefore mass-transport complexes (MTCs) are often used to describe the depositional bodies of landslides that are likely emplaced by numerous failure events (Weimer, 1990; Bryn et al, 2005; Ruano et al, 2014; Ortiz-Karpf et al., 2018).

On seismic sections, MTDs are typically characterised by chaotic, transparent to semi-transparent, and discontinuous internal reflections (cf. Posamentier and Kolla, 2003; McGilvery and Cook, 2004; Evans et al., 2005; Gee et al., 2006, 2007; Moscardelli and Wood, 2006; Bull et al., 2009; Gamboa et al., 2011; Brothers et al., 2016; Figure 2-14). This chaotic seismic facies is the primary identification of MTD. Within MTDs, internal thrust faults, or coherent blocks may be identified (Gee et al., 2006; Bull et al., 2009; Gamboa et al., 2011, 2012; Alves, 2015; Hunt et al., 2021). MTDs are bounded by an irregular (hummocky) top surface (Bull et al., 2009), and a distinct, sharp, and usually erosive and stepped basal surface (Kumar et al., 2021; Figure 2-14). MTDs often display a lens-shaped, or sheet-like geometry (Bryn et al., 2005; Berndt et al., 2012; Puga-Bernabéu et al., 2022).

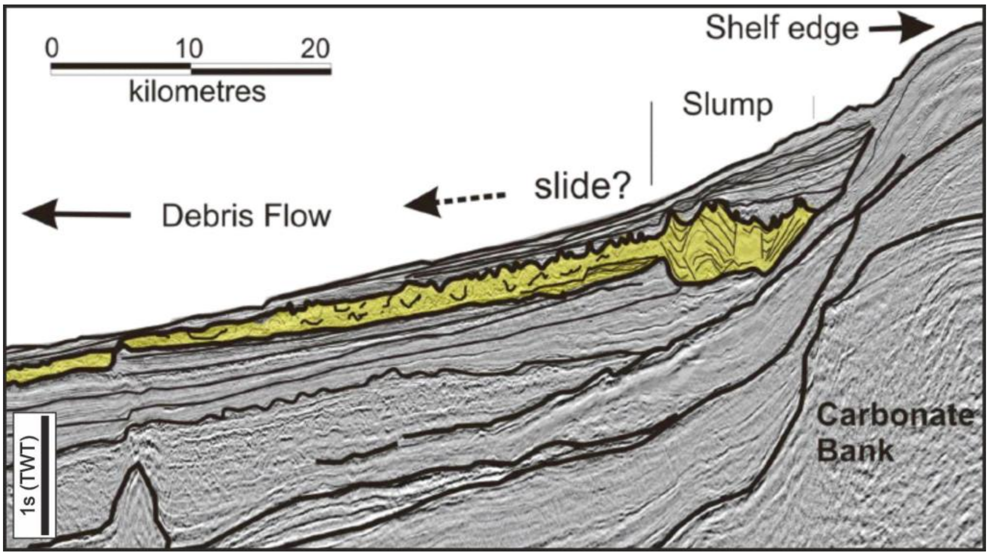

Figure 2-14: A seismic section demonstrating the upslope portion of the Shelburne MTD on the Western Scotian Slope, offshore Nova Scotia (Canada). The MTD is highlighted in yellow, modified from Mosher et al., 2010.

2.3.2 Internal architecture and basal shear surface

The basal shear zone (BSZ) is the interval between the base of the overriding mass flow and the undeformed substrate, and accumulates strain from overriding flows (Winterwerp et al., 2012; Gross et al., 2018; Cardona et al., 2020; Crutchley et al., 2021). Its thickness ranges from a few millimetres to several tens of metres thick (Crutchley et al., 2021). The top boundary of the BSZ forms a discrete and mappable erosional detachment surface, referred to as the basal shear surface (BSS).

A BSS is rarely planar, and instead, it commonly exhibits a stepped geometry and can comprise multiple detachment levels (Bull et al., 2009), reflecting flow incision into, and entrainment of, the substrate. Previous studies suggest that the BSS experiences maximum shear strain during mass movement, and preserves geomorphological and kinematic features, including arcuate headwall scarps (Prior et al., 1984; Frey-Martinez et al., 2005; Li et al., 2017; Figure 2-15), steep lateral margins (Bull et al., 2009), and basal grooves (Gee et al., 2005, 2006; Eruteya et al., 2020; Kumar et al., 2021). However, some studies observed that the basal surface can act as a free-slide interface developed through hydroplaning (Mohrig et al., 1998; De Blasio et al., 2004a; Acosta et al., 2017), liquefaction (Ogata et al., 2014; Sultan et al., 2023), or lubrication mechanism (Sobiesiak et al., 2018). In such conditions, the basal shear surface would experience minimal mechanical shearing, thus no development of erosive structures.

In the headwall region, the basal shear surface commonly ramps upward and intersects the seafloor, forming a headwall scarp that marks the upslope limit of the MTDs (Bull et al., 2009; L'Heureux et al., 2012). Coalesced arcuate headwall scarps are up to 5 km across, and some display a sharp seafloor expression with slope dips in excess of 25° (Scarselli et al., 2020). Headwall scarps typically display arcuate planform geometries and stepped morphologies (Figure 2-15). These stepped headwall scarps are usually used as an indicator for retrogressive failures (e.g., Bryn et al., 2005; Kvalstad et al., 2005; Sawyer et al., 2009; Barrett et al., 2021). The geometry of headwall scarps may record changes in the physical properties of the substrate, although there needs to be definitive links between unfailed strata and the landslide to understand prerequisite controls and conditions.

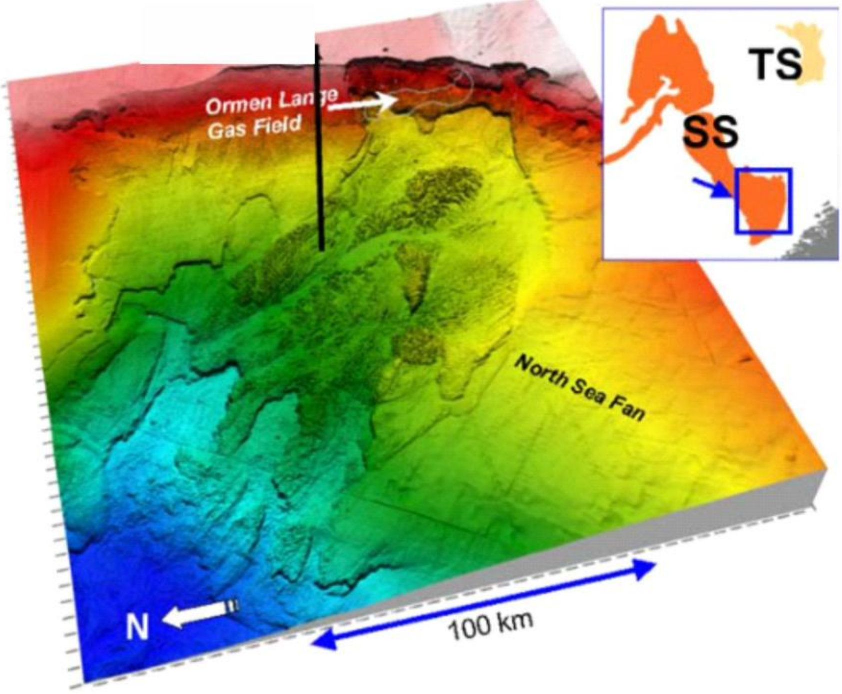

Figure 2-15: Bathymetric image of Storegga Slide, offshore Norway, demonstrating the stepped headwall region (from Bryn et al., 2005).

Some seafloor or shallowly buried submarine landslides can exhibit headwall scarps on the seafloor, such as the Storegga landslide on the Norwegian margin (Haflidason et al., 2004; Kvalstad et al., 2005; Figure 2-15), and the Sahara Slide on the NW African continental margin (Embley, 1982; Krastel et al., 2019; Figure 2-16A and Figure 2-16B). Correlation with cores allows the data resolution to increase from several metres to tens-of-metres scale in seismic reflection data to cm-scale in cores, and allows more details of submarine landslide deposits to be revealed, including lithological analysis (e.g., Gee et al., 1999; Talling et al., 2010, 2012a; L'Heureux et al., 2012), compositional analysis (e.g., Talling et al., 2007; Miramontes et al., 2018), dating (e.g., Haflidason et al., 2005), and physical property analysis (e.g., Sawyer and Hodelka, 2016; Urlaub et al., 2018; Gatter et al., 2021; Wang et al., 2025). For example, the core photographs from the Sahara Slide demonstrate the presence of small blocks that are not detectable due to the resolution limit of seismic reflection data (e.g., Krastel et al., 2019; Figure 2-16C).

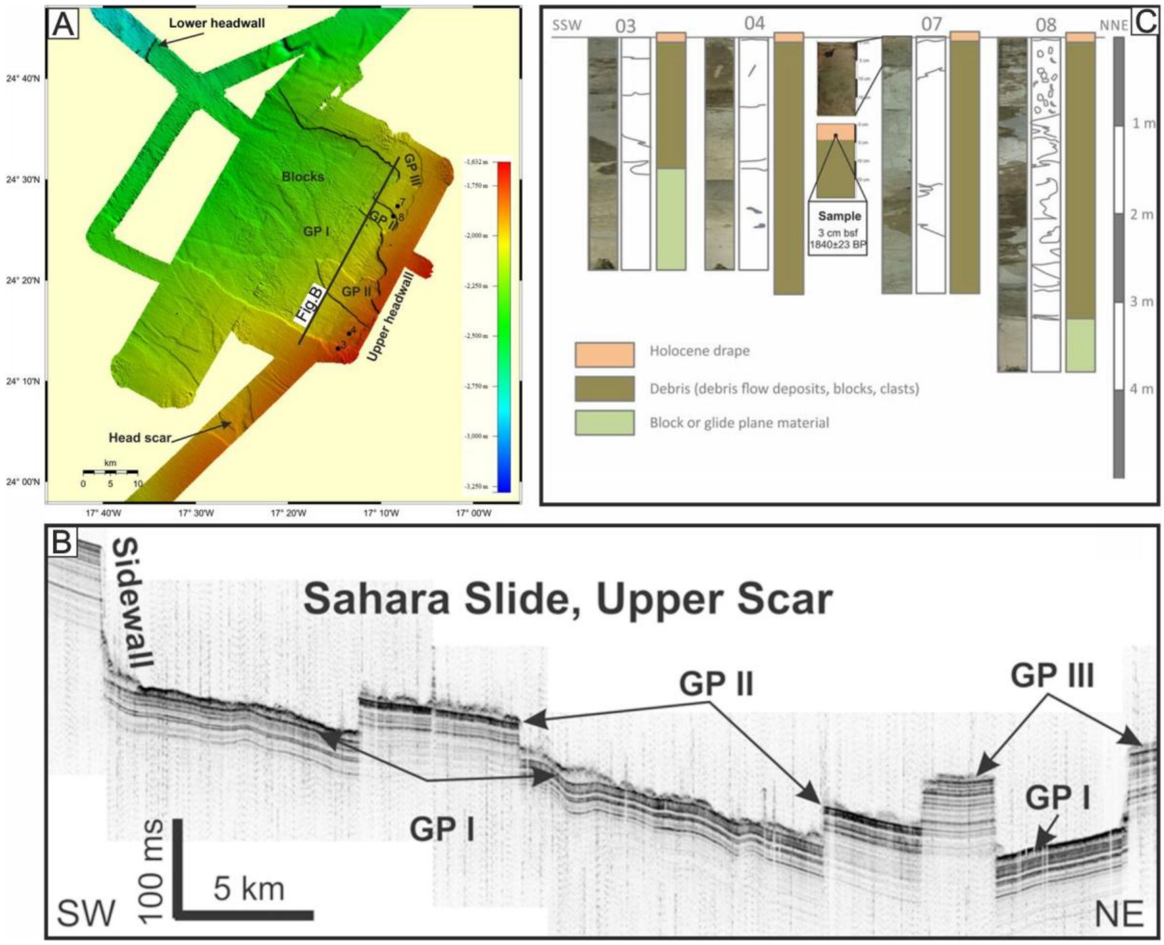

Figure 2-16: (A) Bathymetric map of the Sahara Slide scar on the NW African continental margin. (B) Sediment echosounder profile crossing the upper headwall area, demonstrating three distinct glide planes (GP); the location of the profile is shown in Figure 2-16A. (C) Panel of cores (Cores 3, 4, 7 and 8) collected beneath the upper headwall. The locations of the cores are shown in Figure 2-16A. Dark brown sections mark the debrites. The figures are modified from Krastel et al. (2019).

In some cases, blocks can be identified within the MTDs, that are very large, up to 400 m thick and kilometres in diameter, and referred to as megaclasts (e.g., Jackson, 2011; Hodgson et al., 2019; Nwoko et al., 2020a; Hunt et al., 2021; Li et al., 2022). Normal faults and folds can be observed within megaclasts (Figure 2-17), and folds are typically best developed toward either the frontal or lateral margins of the megaclasts. Therefore, these internal deformed reflections can identify the kinematic indicators (Jackson, 2011). Megaclasts can form uneven topography at the top surface of MTDs, thus influencing subsequent flows and their deposits (Ward et al., 2018; Nwoko et al., 2020a, 2020b). Such megaclasts have been documented in multiple deep-water regions such as offshore Brazil (Alves and Cartwright, 2009), offshore New Zealand (Li et al., 2022), and in the Central North Sea (Soutter et al., 2018).

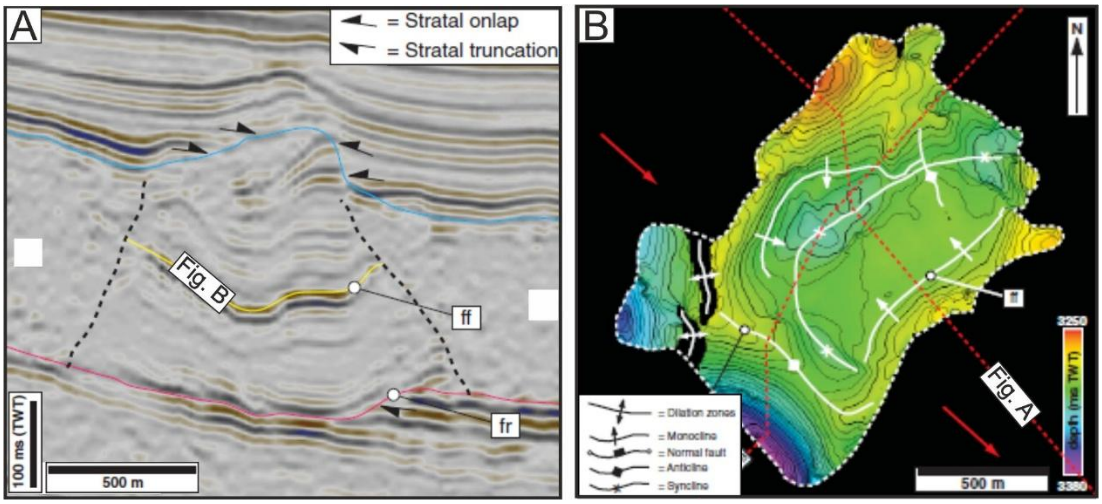

Figure 2-17: Time-structure maps illustrating internal geometry (faults and folds) of megaclasts within a Tertiary mass transport deposit from the Santos Basin, offshore Brazil (modified from Jackson, 2011). 'ms TWT' is millisecond two-way travel time.

2.4 Evolution of carbonate mass flows

Flow-substrate interactions are complicated and highly dynamic processes that involve variations in flow velocity, volume and composition. Numerous studies have interpreted the evolution of subaqueous mass flows though observation of deposits using seismic reflection data and outcrops (e.g., Prior et al., 1984; Masson et al., 1997; Gee et al., 1999, 2007; Talling et al., 2007; Dakin et al., 2013; Krastel et al., 2019; Tang et al., 2022; Harishidayat et al., 2024). However, the existing knowledge on the dynamic processes of subaqueous mass flows remains limited due to the poor predictability of failure events, their destructive power, and the difficulty in elucidating their transport mechanisms and rheology from deposits.

Physical experiments and numerical modelling simulation have been utilized to improve the understanding of submarine mass-flow dynamics. A variety of computational approaches have been used to investigate flow runout, deposit morphology, pore pressure evolution, hydroplaning behaviour, and landslide-generated tsunami (e.g., Imran et al., 2001; De Blasio et al., 2004a, 2004b; Grilli et al., 2009; Li et al., 2015b; Dong et al., 2017; Yang et al., 2020; Grilli et al., 2019; Zhang and Randolph, 2019; Omira et al., 2022). Despite these advances, the numerical modelling of submarine mass flow is limited by scaling constraints and computational efficiency, which needs to simplify geological models relative to the natural systems, including particle size, sediment heterogeneity, failure morphology, and failure volume

(Løvholt et al., 2005; Grilli et al., 2009; Waythomas et al., 2009; Feng and Owen, 2014; Smith et al., 2016; Pudasaini and Mergili, 2019; Choi et al., 2024).

Laboratory experiments allow direct observation of dynamic flow evolution, internal deformation, and flow-substrate interaction under controlled conditions. In low-clay content carbonate settings, where grain-to-grain interactions and kinetic sieving dominate, debris-flow behaviour approaches the behaviour of granular flows, providing a mechanical basis for the comparison with subaerial granular flow experiments (Savage and Lun, 1988; Gray and Kokelaar, 2010; Johnson et al., 2012; Kokelaar et al., 2014; Rocha et al., 2019). These physical experiments have been carried out to advanced our understanding of dynamics process of subaqueous mass flows with long runout on gentle slopes.

2.4.1 Experimental studies of debris flows and granular flows

Several studies have made analogies between low-clay content debris flows and granular flows (e.g., Gray and Thornton, 2005; Deboeuf et al., 2006; Elverhøi et al., 2010; Gray and Kokelaar, 2010; Johnson et al., 2012; Iverson et al., 2010; Iverson, 2012; Kokelaar et al., 2014). Low-clay content debris flows are dominated by grain-to-grain interactions and kinetic sieving, resulting in grain-supported matrix and inverse grading comparable to granular or debris-avalanche processes (Savage and Lun, 1988; Iverson and Vallance, 2001). Field and experimental observations suggest that the subaerial debris flows can segregate into coarse-grained outer levees and fine-grained inner levee and central deposits (Savage and Lun, 1988; Gray and Thornton, 2005; Kokelaar et al., 2014; Gray and Kokelaar, 2010; Gray et al., 2015), which provide a confined environment for subsequent flows.

When a mixed granular mass flow composed of particles with contrasting sizes and densities is subjected to shear under gravity, segregation of the particles over the flow depth usually occurs (Savage and Lun, 1988). Segregation is a shear-driven grading process in which coarse particles migrate towards the top of the sheared layer and fine particles collect on the bottom (Savage and Lun, 1988; Major, 1997; Major and Iverson, 1999). Grain-size segregation in subaerial debris flows can fundamentally affect flow dynamics. During transport, large particles are preferentially advected to the flow front and generate self-confining levees that channelize the subsequent flow (Iverson et al., 2010; Gray and Kokelaar, 2010; Johnson et al., 2012; Kokelaar et al., 2014; Figure 2-18). Such channelisation can restrict lateral spreading of flows and maintain flow thickness, thereby enhancing flow mobility and promote flow runout distances.

Figure 2-18: A self-confining subaerial debrite at Val Prada, Switzerland, demonstrating the coarse-enriched levees and fine-enriched lining (from Gray and Kokelaar, 2010).

Investigations on the mechanics and development of particle segregation are predominantly driven by subaerial experimental studies (Major, 1997; Major and Iverson, 1999; Deboeuf et al., 2006; Iverson et al., 2010; Johnson et al., 2012; Kokelaar et al., 2014; de Haas et al., 2015, 2016; Rocha et al., 2019). Iverson et al. (2010) carried out multiple large-scale (10 m^3) debris flow experiments at the United States Geological Survey debris-flow flume, systematically varying debris composition (sand-gravel versus sand-gravel-mud mixtures) and basal boundary conditions (smooth concrete bed versus artificially roughened beds with 16 mm relief). Across all experimental subsets, debris flow behaviour follows a dilated, high-friction, coarse-grained flow front, pushed from behind by nearly liquefied, finer-grained debris. Their experimental results showed that debris flows on smooth beds travelled ~30% faster but achieved comparable runout distance to the flows on rough beds. Bed roughness results in similar flow runout to smooth beds through promoting development of coarse-grained flow fronts and gravel-rich lateral levees, which channelize flow and reduce loss of downslope momentum (Iverson et al., 2010, 2011).

A series of studies have been conducted to analyse the dynamic pathway of coarse particles within the segregating flow head (Gray and Thornton, 2005; Thornton and Gray, 2008; Gray and Ancey, 2009; Gray and Kokelaar, 2010; Johnson et al., 2012). Through measuring the surface velocity of granular debris flows in subaerial physical experiments, Johnson et al. (2012) found that the surface velocity close to the flow front is almost uniformly 3 m/s, about 1.5 times faster than the propagation speed of the flow front. Coarse particles segregated towards the top surface, where velocities are greater than the average, and can result in coarse particles being preferentially transported to the flow head, eventually leading to a top surface composed entirely of large particles (Gray and Thornton, 2005; Gray and Kokelaar, 2010; Johnson et al., 2012). If particles are sufficiently close to the flow axis they reach the flow front, where they migrate to the base of the flow and are then overpassed and buried by following material. Mathematical models suggest that once buried, large particles can segregate upwards again until they reach the coarse-enriched layer covering the flow surface, allowing them to recirculate within the flow head (Thornton et al., 2006; Thornton and Gray, 2008; Gray and Ancey, 2009; Gray and Kokelaar, 2010). Based on a three-dimensional debris-flow velocity field calculation and centre-plane flux calculations, Johnson et al. (2012) proposed that the debris-flow head being steady in the moving frame requires the fluxes of both coarse or fine particles entering a region to be balanced by a corresponding flux of coarse or fine particles leaving the head region. Their flux analysis suggested that during recirculation, fine particles mostly leave the head at the base of the central channel, whereas coarse particles are advected away from the flow centre-plane by the transverse component of the velocity (~0.75 m/s). In the moving frame, coarse particles therefore follow helical spiral trajectories within the flow head and move progressively farther toward the flow margins (Johnson et al., 2012; Figure 2-19). Near the flow margins, particles throughout the depth of the flow move more slowly than the flow front. When a coarse particle is advected into this region, it ceases recirculation and is left behind by the advancing flow front, thus progressively accreting to the levee. Although there was clear evidence for inverse grading during the flow (Naylor 1980; Thornton and Gray, 2008; Gray and Ancey, 2009), transect sampling by Johnson et al. (2012) revealed that the resulting levee deposit was strongly graded laterally, with only weak vertical grading.

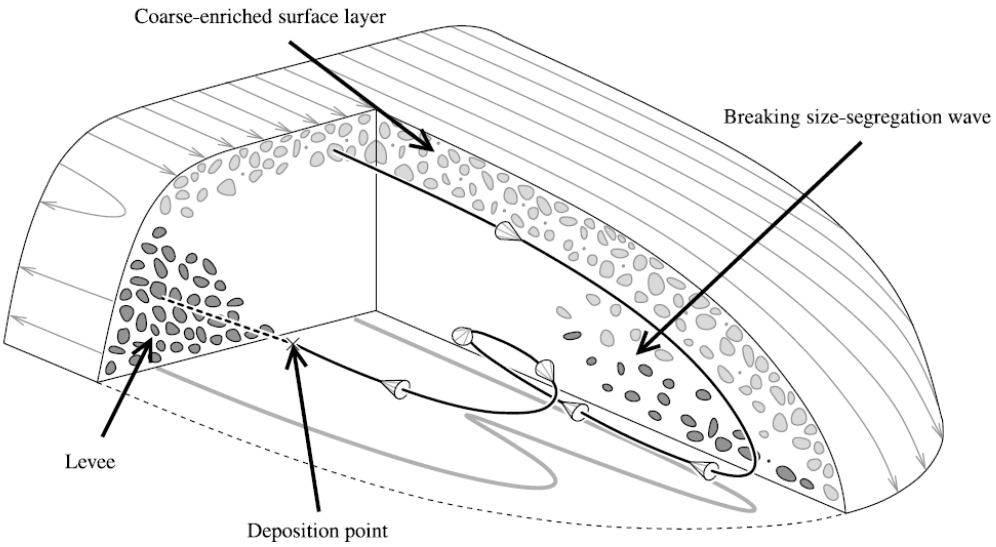

Figure 2-19: Cutaway sketch showing the 3D trajectory of a segregating coarse particle within the debris-flow head. Within the flow head, coarse particles are overridden, then recirculate within the flow head before being advected laterally to form coarse-enriched levees (from Johnson et al., 2012). Note the moving frame of reference, where particle trajectory is shown relative to that of the flow front.

Kokelaar et al. (2014) performed subaerial physical experiments revealing that the dynamic evolution of fine particles plays an important role throughout levee formation and evolution during segregation. As the flow advanced, fine particles within the head segregated downward and were emplaced simultaneously with levee construction. The downward migration of fines contributes to a thin lining formed at the channel base and along the inner levee margins (Kokelaar et al., 2014; Figure 2-20A). Behind the flow head, the channel-flow surface lies slightly below the levees crests, and the inner levee walls are enriched in the fine particles (Kokelaar et al., 2014; Figure 2-20A). During the waning-stage, the inner levee wall progressively collapses as fines shear down into the flow, sharpening the lateral levees (Kokelaar et al., 2014; Figure 2-20B). In the drained channel, further loss of inner levee material produces steeper inner walls, and a fine-grained lining is exposed within the sediments throughout drainage (Kokelaar et al., 2014; Figure 2-20C). The segregation process within the flow head can be classified into a three-layer conceptual model (L1-L3): an upper layer (L1) enriched in coarse particles that advances to the front and constructs the levees, an intermediate layer (L2) that feeds materials into the flow head, and a basal fine-rich layer (L3) that ensures that the less-frictional fine-grained component shears across itself, thus facilitating flow and enhancing runout (Johnson et al., 2012; Kokelaar et al., 2014; Gray et al., 2015; Figure 2-20D).

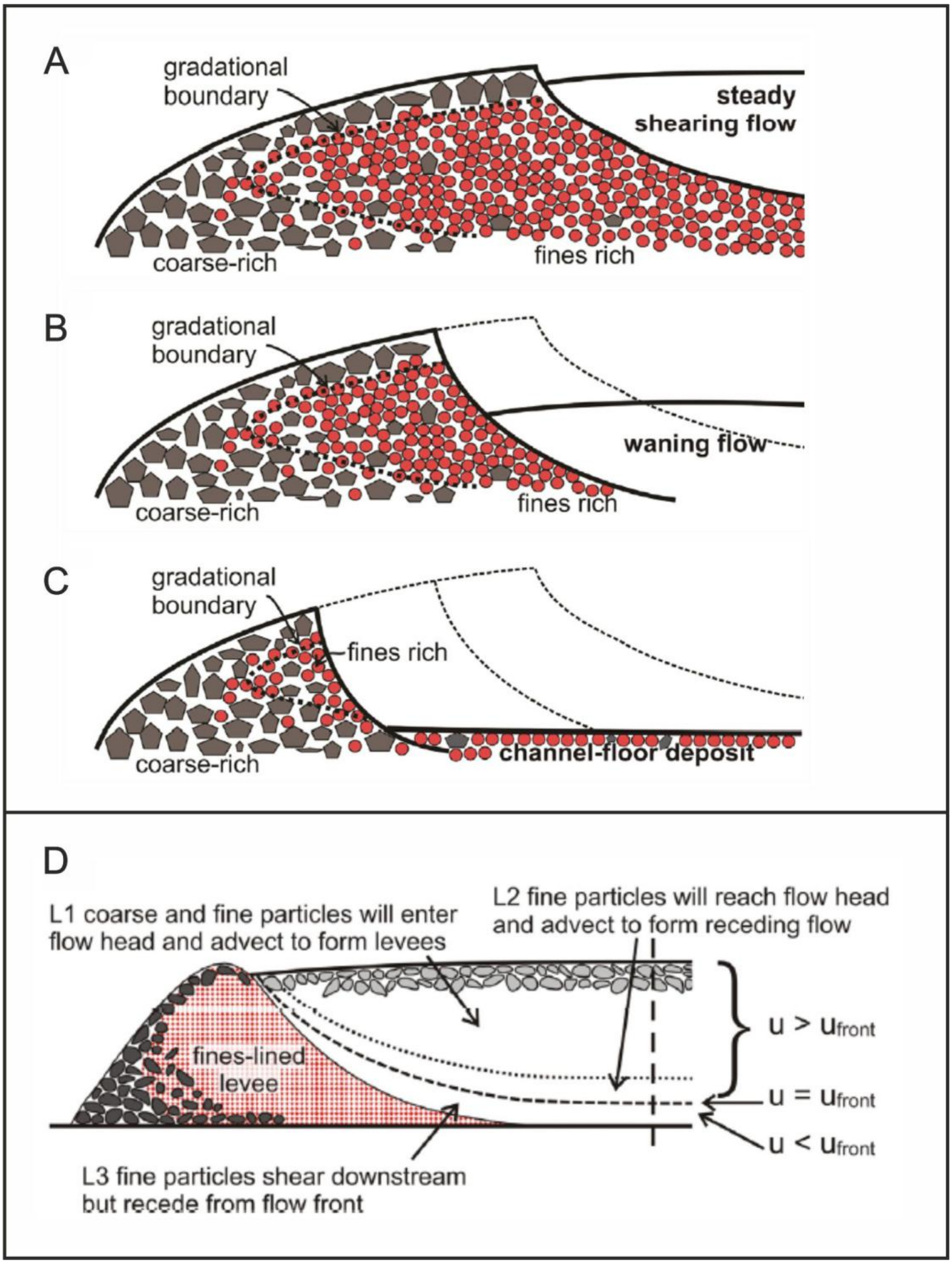

Figure 2-20: Schematic transverse cross-sections illustrating the fine-grained linings during levee sharpening (modified from Kokelaar et al., 2014).

2.4.2 Limitation of the existing models

Most studies conceptualise self-confinement as a segregation-driven process, in which coarse-enriched levees channelise the flow and the fine-enriched lining lubricates the flow, thereby facilitating long runout distances (Iverson et al., 2010; Gray and Kokelaar, 2010; Johnson et al., 2012; Kokelaar et al., 2014). Such a self-confined process has been observed in subaerial single flows, including mass flows (i.e., debris flows and turbidity currents; e.g., Iverson, 1997; Mohrig et al., 2005), snow avalanches (e.g., Jomelli and Bertran, 2001), water-saturated lahars (Procter et al., 2021) and pyroclastic flows (e.g., Jessop et al., 2012), and have been invoked to substantially increase the flow run-out distance (Iverson et al., 2010). Existing segregation models successful capture internal particle reorganisation, levee formation, and segregation-mobility feedback in single, fixed-bed (without mass exchange), subaerial settings (e.g., Deboeuf et al., 2006; Iverson et al., 2010; Gray and Kokelaar, 2010; Johnson et al., 2012; Kokelaar et al., 2014; Rocha et al., 2019).

In natural environments, however, submarine debris flows usually incise the substrate along the path, bulk up, and thus undergo extreme increases in volume (Talling et al., 2007; Böttner et al., 2024). Physical experiments conducted by Johnson et al. (2012) also demonstrate that the segregating subaerial debris flow can entrain coarse particles (pebbles) on the pathway, which are subsequently migrated upward and join the recirculation in the flow head. Through substrate incision, submarine debris flows can build up substantial negative topography on the seafloor and steep lateral margins. The resulting seafloor morphology strongly influences the pathways and depositional patterns of subsequent gravity flows (e.g., Bernhardt et al., 2012; Ortiz-Karpf et al., 2017; Martínez-Doñate et al., 2021), and facilitate the long runout distance of flows into the deep-water basin. Entrainment of substrate by submarine debris flows is a critical process, which governs the flow volume, thickness, and momentum (Gee et al., 1999; Iverson et al., 2010, 2011; Hodgson et al., 2019; Nugraha et al., 2022). How self-confining flows develop in subaqueous settings, how subsequent flow interact with evolving depositional structures, and how such dynamic flow-substrate interactions (substrate incision and flow entrainment) influence self-confinement processes, remain poorly understood.

Submarine gravity flows in natural systems usually comprise multiple events (Gee et al., 1999, 2006; Haflidason et al., 2004, 2005; Bryn et al., 2005; Lamarche and Collot, 2008; Li et al., 2015, 2020). Repeated events incrementally build up topography on the seafloor, which in turn controls the routing of subsequent gravity flows and the patterns of deposition and erosion through time (de Haas et al., 2016; Brooks et al., 2018). Composite submarine debris flows can reach volumes up to thousands of km^3 through successive failures that migrated upslope, such as the Saharan debris flows (Masson et al., 1993; Gee et al., 1999) and the Canary Debris Flow (Masson et al., 1998, 2002; Tang et al., 2022). The subsequent flows are influenced by the pre-existing depositional relief and erosional depression generated by earlier events (e.g., Gee et al., 2001; Lamarche et al., 2008; Brooks et al., 2018).

In summary, a large number of publications have documented the wide range of scales and styles of buried and seabed submarine landslides from siliciclastic successions. However, there remains much to learn about how carbonate sedimentary successions are pre-conditioned to failure, how dynamic flow-substrate interactions influence the evolution of confinement and depositional architecture, and how these factors can control flow runout distance in subaqueous environments.

Chapter 3 Geological framework: Tectonic setting and stratigraphy

This chapter provides a brief geological framework for the Exmouth Plateau, offshore NW Australia, synthesizing regional tectonic evolution, and stratigraphy architecture. Particular emphasis is placed on the middle Miocene to present stratigraphy, as this interval encompasses the deposition of submarine slope failures analysed in Chapters 4 and 5. In particular Chapter 4 focuses the stratigraphy from middle Miocene to later Pliocene, and Chapter 5 focuses on the stratigraphy from late Pliocene to seafloor. Chater 6 utilises subaqueous physical experiments to investigate the evolution process of subaqueous gravity flow independent of regional geological settings. Together, these chapters integrate field-based observations and process-based modelling to provide a comprehensive understanding of subaqueous slope instability and flow dynamic processes.

3.1 Tectonic Setting

Exmouth Plateau is located in the middle of Northern Carnarvon Basin, offshore NW Australia, and is about 600 km long and 300-400 km wide at water depths of 800-4000 m (Exon et al., 1992). The Exmouth Plateau is underlain by continental crust and that was deformed by complex Mesozoic-Cenozoic tectonic events (Audley-Charles et al., 1988). A series of rifting events associated with progressive break-up of Gondwana began probably in the late Permian has resulted in stretched lithosphere, and culminated with the opening of the Ceno-Tethys Ocean when the Argo Block drifted away from Gondwana (Exon et al., 1992; Longley et al., 2002). This period of extension also developed a NE-SW trending rift sub-basin, which collectively formed the Northern Carnarvon Basin, and the Exmouth Plateau in the Late Jurassic to Early Cretaceous (Stagg and Colwell , 1994; Gartrell, 2000; Direen et al., 2008). In the Late Jurassic, the north Northern Carnarvon Basin was further stretched, resulting in seafloor spreading and opening of Argo Abyssal Plain (Direen et al., 2008; Gibbons et al., 2012), followed by Valanginian regional thermal subsidence. The final breakup between Greater India and Australia lead to seafloor spreading and formation of Gascoyne-Cuvier Abyssal Plain (Driscoll and Karner, 1998). The continental crust of the Exmouth Plateau is bounded by Argo, Gascoyne, and Cuvier abyssal plains of oceanic crust (Gibbons et al., 2012).

The plateau subsided to present-day water depths, with clastic sedimentation in the Late Cretaceous, and carbonate sedimentation throughout the Cenozoic (Exon et al., 1992). The present day margins of the Exmouth Plateau have an average dip of < 2° (Scarselli et al., 2013, 2020), forming a low-gradient slope system. Despite the gentle slope, a series of headwall and lateral scarps, which locally coalesce, formed by submarine landslides of late Miocene to Recent deposits are present on the flanks of Exmouth Plateau Arch (Wu et al., 2021; Figure 3-1).

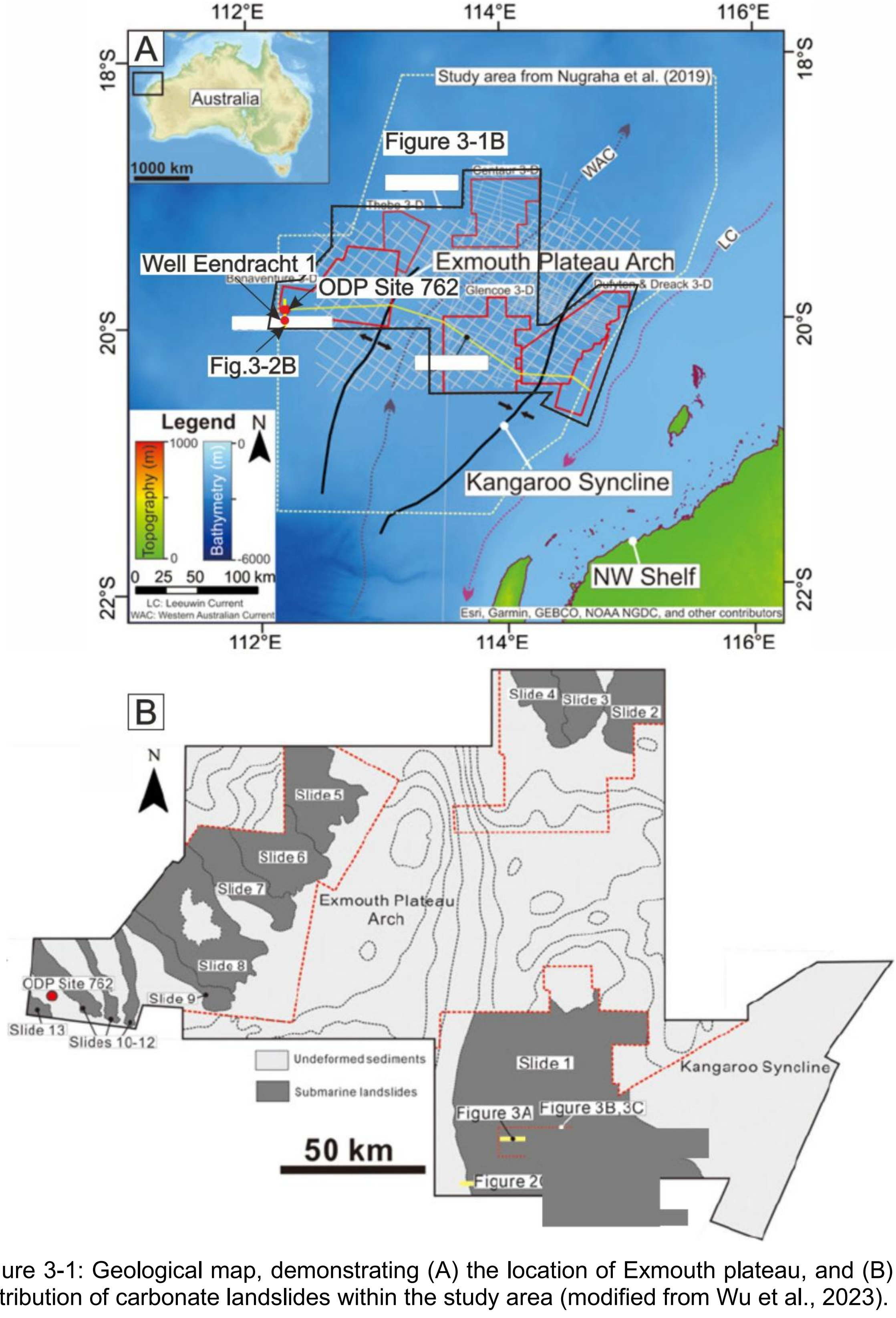

Figure 3-1: Geological map, demonstrating (A) the location of Exmouth plateau, and (B) the distribution of carbonate landslides within the study area (modified from Wu et al., 2023).

3.2 Stratigraphy

The Exmouth plateau is covered by up to ~15-20 km of Paleozoic to Cenozoic sedimentary successions (von Rad et al., 1992). Four megasequences have been identified in the Central Exmouth Plateau: (1) Early-Late Triassic Pre-extension; (2) Latest Triassic-earliest Late Jurassic syn-extension; (3) Late Jurassic-Early Cretaceous post-extension; and (4) Early Cretaceous-recent passive margin strata (Bilal and McClay, 2022). Nugraha et al. (2019) summarise the Early Cretaceous-recent passive margin stratigraphy of the Exmouth Plateau as: (a) from the Late Cretaceous to Late Miocene dominated by bottom current deposits and associated erosional features; and (b) since the late Miocene dominated by the emplacement of MTCs. They ascribe the former as being linked the opening of an ocean gateway along the southern margin of the continent, and the latter to closing of an ocean gateway along the northern margin of the continent.

The interval of interest in this thesis corresponds to the uppermost passive margin succession, particularly the middle Miocene to Recent deposits (Unit I). This interval can be subdivided into 3 subunits: (i) subunit IA (0-61.4 mbsf): Quaternary-late Pliocene foraminifer nannofossil ooze with 79-86% carbonate and <10% terrigenous material, (ii) Subunit IB (61.4-118.4 mbsf): late Pliocene to Middle Miocene foraminifer- and nannofossils-rich ooze containing up to 90% carbonate, (iii) Subunit IC (118.4-181.5 mbsf): late Eocene-early Oligocene to Middle Miocene carbonate-rich interval with a higher proportion of planktonic foraminifer and <10% of non-carbonate minerals (Haq et al., 1990; Figure 3-2A).

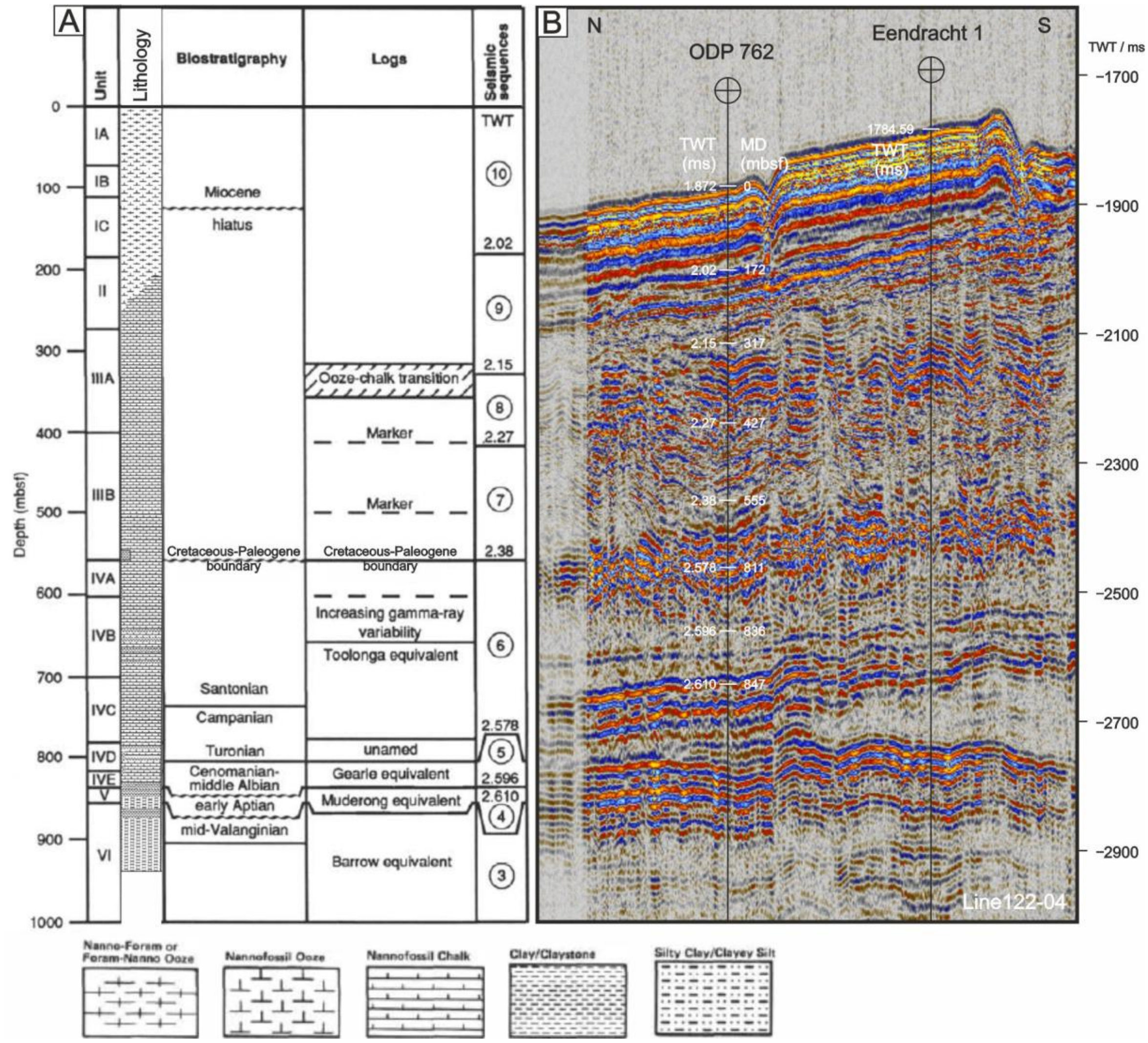

Figure 3-2: (A) A geological framework, showing the correlation of sedimentary units, lithology, biostratigraphy, wireline log picks, and seismic sequences on Exmouth Plateau at Well ODP Site 762 (modified from Haq et al., 1990). (B) A N-S seismic profile crossing well ODP 762 and Well Eendracht 1 that demonstrate regional seismic-stratigraphy units. The seismic section in Figure 3-2B is a single-channel water-gun record acquired from recorded aboard the JOIDES Resolution (from Haq et al., 1990). Location of the section in Figure 3-2B is shown in Figure 3-1.

An unconformity was found in Subunit IC with no deposits of late Early Miocene age (Haq et al., 1990; Figure 3-2A). The late Miocene to Recent sediments in the last passive margin phase are dominated by hemipelagic and pelagic carbonate sedimentation, which are poorly consolidated, weak calcareous ooze with a sedimentation rate as low as only 20 m/Ma (von Rad et al., 1992). A regional climatic transition occurred since the middle Miocene (~15 Ma), and altered sediment supply to the Exmouth Plateau (Bowler, 1976; Johnson, 2009; Martin, 2006). During this time, progressive aridification of Western Australia enhanced continental weathering and promoted increased aeolian transport of fine-grained material into adjacent offshore marine basins (e.g., Northern Carnarvon Basin; Grousset et al., 1992; Rea, 1994; Le Houedec et al., 2012). This climatic transition resulted in strong dust input on the background pelagic carbonate oozes in the Exmouth Plateau from 15 Ma onward (Le Houedec et al., 2012).

At least ten regionally correlated seismic sequences are present across the Exmouth Plateau through the seismic-well calibration (Figure 3-2B; Haq et al., 1990). The uppermost sequence (Sequence 10), spanning the Middle Miocene to Recent, is the focus of this thesis. It is characterised by lateral continuous, high-frequency reflections corresponding to hemipelagic and pelagic carbonate ooze (Unit I; Figure 3-2; Haq et al., 1990), locally disrupted by mass-transport deposits and erosional surface. Its irregular seafloor expression with 100 ms relief indicates the presence of recent submarine landslides (Figure 3-2B; Haq et al., 1990).

Chapter 4 Learning from crushing failures: Changes in physical properties reveal the mechanics of submarine carbonate landslides

4.1 Summary

Calcareous ooze represents the most widespread seafloor sediments in the global ocean, and its elevated water content and high compressibility can lead to the formation of weak layers, thereby increasing slope instability and submarine landslide risk. However, understanding of submarine landslide processes and evolution is hindered by the lack of knowledge of changes in the physical properties of sediments during failure. This issue is considered here by documenting failed and unfailed physical properties of a weak layer by integrating two ODP cores with three-dimensional seismic reflection data from the Exmouth Plateau, offshore northwest Australia. The basal shear zone of two big submarine carbonate landslides was mapped into adjacent undisturbed sediments where it is characterised by elevated water content and porosity, and recognised as a weak layer. The weak layer coincides with a foraminifera-rich succession capped by a clay-enriched zone. Results suggest that the formation of the weak layer is related to enhanced clay fraction transport into the deep-water basin, due to onshore weathering, forming a low-permeability zone above the water-rich foraminifera-abundant succession. This elevated-clay fraction leads to “excess” water being preserved within chambered foraminifera shells, thus causing a weak layer. When the weak layer acts as the basal shear zone it shows, post-landsliding, markedly lower water content, porosity, and foraminifera content. Contractive shearing accounts for these changes in physical properties (dramatic loss in water content, porosity and foraminifera) during failure, through compacting the weak layer, crushing foraminifera, and squeezing water out. Water could not escape to the seafloor, causing elevated pore pressure above the weak layer, and mechanically generating a water-rich layer (or water film) that lubricated the base of the overriding landslide. Thus, the physical properties of calcareous ooze, including the percentage of foraminifera and the presence of weak layers, need to be considered in future studies to improve submarine slope stability assessments.

4.2 Introduction

Globally, submarine landslides have been identified on extremely low angle slopes (<2°) and can cover areas up to several thousands of square kilometres (L'Heureux et al., 2012; Miramontes et al., 2018; Urlaub et al., 2018; Sultan et al., 2023; Wu et al., 2023). The detachment of submarine landslides on one or multiple basal glide planes is thought to be controlled by the presence of weak layers. These weak layers are characterised by low shear strength (L'Heureux et al., 2015; Elger et al., 2018; Lüdmann et al., 2022; Gales et al., 2023; Sultan et al., 2023), which serve as a preconditioning factor for failures even in low gradient environments (Gatter et al., 2021; Wu et al., 2023; Sultan et al., 2023; Wang et al., 2025). Most studies focus on siliciclastic landslides, despite calcareous sediments representing the most widespread deep-sea lithology in the global ocean (Dutkiewicz et al., 2015, 2020). Furthermore, the physical properties of calcareous sediments (i.e., high compressibility and high water content) might lead to the laterally extensive development of weak layers. For example, geotechnical observations suggest that as little as 0.47 wt% of foraminifera can result in pronounced changes to the porosity of carbonate-rich successions (Sawyer and Hodelka, 2016). Consolidation test results show that calcareous oozes at shallow burial depths (~200 metres below seafloor (mbsf)) are usually underconsolidated to normally consolidated, whereas siliceous sediments are overconsolidated (Rack et al., 1993). This indicates calcareous oozes have higher compressibility and are more sensitive to overburden pressure, and more easily form weak layers (e.g., Wu et al., 2023). Compared to clay-rich sediments, calcareous ooze substrates have lower electrochemical forces and often show lower shear strength for a given sediment depth (White et al., 2016; Hussein et al., 2024). These characteristics suggest that calcareous successions could be preferentially susceptible to failure, but the mechanistic processes are poorly constrained. This work investigates how the physical properties of calcareous weak layers — such as porosity, water content, permeability, and fossil abundance — change during failure, utilising ODP wells from the offshore NW Australia, which enable weak layer horizons to be traced from undeformed sediments into carbonate landslides.

Examining how the physical properties of weak layers evolve during landsliding enables the process dynamics and evolution of submarine landslides to be assessed.

The specific aims of this work are thus to: (i) document the physical properties of the unfailed stratigraphy recognised adjacent to the landslides through seismic-well ties; (ii) explore the physical properties of the same key stratigraphic units and surfaces after failure; (iii) discuss the processes accounting for changes in physical properties of key horizons (i.e., weak layers) before and after failure; and (iv) propose a new mechanistic model that captures the process interactions of carbonate landslide evolution.

4.3 Geological Setting

A series of headwall and lateral scarps of submarine landslides, which locally coalesce, are observed on the seafloor or shallowly buried on the flanks of the Exmouth Plateau of the Northern Carnarvon Basin, offshore NW Australia (Figure 4-1; Scarselli et al., 2013, 2019). The Exmouth Plateau is about 600 km long and 300-400 km wide with water depths of 800-4000 m (Exon et al., 1992). It formed from Gondwana breakup occurring in the Late Jurassic to Early Cretaceous (Stagg and Colwell , 1994). During the Late Cretaceous, the plateau subsided to present-day water depths, and accumulated carbonate-dominated hemipelagic sediments throughout the Cenozoic (Haq et al., 1990). From the Early Cenozoic, the Exmouth Plateau area has been tectonically active, driven by Indonesian- Australian Plate Collision, resulting in fault reactivation and broad folding, which elevated the Exmouth Plateau during the Miocene (Boyd et al., 1993).

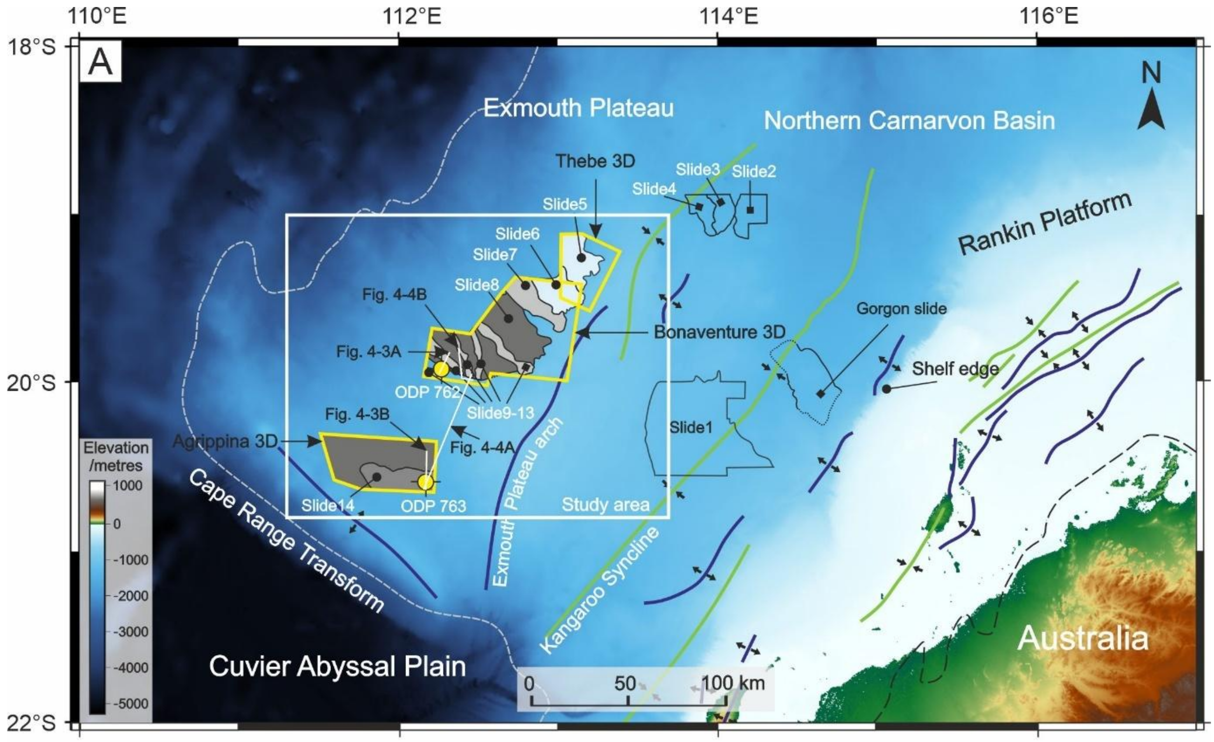
A
110°E
112°E
114°E
116°E
18°S
20°S
22°S
N
Exmouth Plateau
Northern Carnarvon Basin
Rankin Platform
Thebe 3D
Slide3
Slide2
Slide4
Slide5
Slide6
Slide7
Slide8
Fig. 4-4B
Fig. 4-3A
ODP 762
Slide9-13
Bonaventure 3D
Gorgon slide
Shelf edge
Slide1
Fig. 4-3B
Fig. 4-4A
Agrippina 3D
Slide14
ODP 763
Study area
Exmouth Plateau arch
Kangaroo Syncline
Cape Range Transform
Cuvier Abyssal Plain
Australia
Elevation /metres
1000
0
-1000
-2000
-3000
-4000
-5000
0
50
100 km

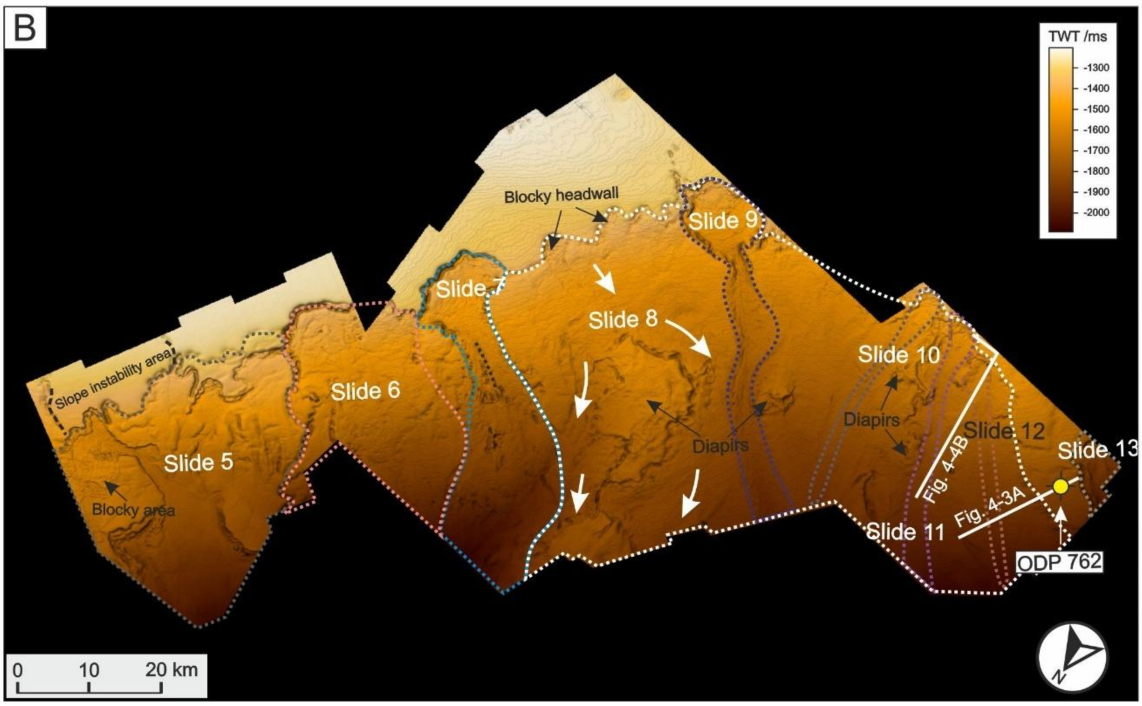
B
TWT /ms
-1300
-1400
-1500
-1600
-1700
-1800
-1900
-2000
Blocky headwall
Slide 9
Slide 7
Slide 8
Slide 10
Slide 6
Slope instability area
Slide 5
Blocky area
Diapirs
Diapirs
Slide 12
Slide 13
Fig. 4-4B
Fig. 4-3A
Slide 11
ODP 762
0
10
20 km

Figure 4-1: (A) The distribution of studied submarine carbonate landslides offshore NW Australia. Landslides are shown by black outlines. The yellow circles with cross lines represent the location of ODP wells (Sites 762 and 763). The study area is shown by a white box; yellow polygons show coverage of three-dimensional seismic reflection datasets. Seafloor landslides are shown with white shading, shallowly buried (~ 30 mbsf) landslides are shown in light grey, and deeper buried (~120 mbsf) landslides are in dark grey. Submarine landslide locations are from Scarselli et al. (2013, 2019) and Wu et al. (2023). The base map is open access from SRTM15, acquired by Generic Mapping Tools 6 (Tozer et al., 2019; Wessel et al., 2019). (B) The seafloor of the Bonaventure 3D and Thebe 3D areas showing the distribution of landslides. The dashed lines with different colours indicate the boundaries of Slide 5 to Slide 13. The white thick arrows indicate the movement direction of Slide 8. The yellow circle shows the location of ODP Site 762. The white solid lines indicate the positions of 2D seismic sections in Figure 4-3 and Figure 4-4.

The stratigraphic interval of interest mainly comprises pelagic calcareous oozes having accumulated at a sedimentation rate as low as 20 m/Myr (Exon et al., 1992; von Rad et al., 1992). ODP Site 762 core sample analysis suggests that this stratigraphy comprises light green-grey foraminifer nannofossil ooze from late Pliocene to Quaternary (0-61.4 mbsf), light grey nannofossil ooze with foraminifer from late Middle Miocene to late Pliocene (61.4-118.4 mbsf), and white, pale yellow and light grey foraminifer nannofossil ooze from late Eocene-early Oligocene to Middle Miocene (118.4-181.5 mbsf; Haq et al., 1990). An unconformity at 132-135 mbsf, was identified with no late Early Miocene age deposits (Haq et al., 1990). The ODP Site 762 analysed in the study is the same well used in Wu et al. (2023), which focuses on a slide, located 200 km from the well (Slide 1 of Wu et al., 2023; Figure 4-1). I focus on landslides more closely adjacent to the well (<2 km), allowing more confident utilisation of material in the well for detailed analysis of the physical properties of the sediments before and after failure.

4.4 Data and Methodology

Three-dimensional (3D) and two-dimensional (2D) seismic reflection data acquired by Geoscience Australia (https://www.nopims.gov.au), and two wells from the Ocean Drilling Program (ODP) are integrated. The 3D seismic reflection data, including Bonaventure 3D, Thebe 3D and Agrippina 3D, are acquired in water depths from 850 m to 1600 m, and image 10 submarine landslides within the late Miocene to recent stratigraphy of the Exmouth Plateau (Figure 4-1A). Bonaventure 3D dataset is 4132 km^2, has a dominant seismic frequency of 30-60 Hz, and a vertical seismic resolution of around 6~13 m, with a near seafloor (~180 mbsf) velocity of 1520-1600 m/s. Thebe

3D dataset covers 1198 km^2, and its dominant seismic frequency is 40-80 Hz with a vertical seismic resolution of 5~10 m for shallow intervals. Agrippina 3D is 1867 km^2, has a dominant seismic frequency of 27-56 Hz, and a vertical resolution of 7-15 m for shallow intervals. The Leopard 2D seismic reflection dataset connects the Bonaventure 3D and Agrippina 3D seismic reflection data, with a near seafloor velocity of 1520-1600 m/s, dominant seismic frequency of 30-60 Hz, and vertical resolution of 6-13 m.

Two ODP wells (i.e., ODP Sites 762 and 763) from Leg 122 provide calibration of the physical properties of the stratigraphy that hosts the landslides. ODP Site 762 intersects an undisturbed succession within the Bonaventure 3D adjacent to several submarine landslides (Figure 4-1), preserving the pre-slide physical properties of the stratigraphy. ODP Site 763 is in a landslide-disturbed area within Agrippina 3D (Figure 4-1A), recording the post-slide physical properties from remobilised sediments. Thus, the physical properties of sediments before and after failure can be revealed from ODP Sites 762 and 763 core and well logs. The physical property data used in the study include velocity (Vph), water content, porosity, bulk density, and shear strength, provided by the ODP Leg 122 initial report (Haq et al., 1990). Vph is horizontal velocity (perpendicular to the core axis) and is calculated from the determination of the travel time for a 500-kHz compressional wave through a measured thickness of sediment sample by Hamilton Frame measurements and Tektronix DC 5010 counter/timer system (Haq et al., 1990). The sediment properties (water content, porosity, and bulk density) were measured using the same material and location as the samples for velocity measurements (Haq et al., 1990). Weight and volume of the samples were measured wet, and remeasured after the samples were freeze-fried for 12 hours. The measured physical properties of sediments are defined as follows: (1) water content (%) = 100 × weight of seawater/weight of wet sediment; (2) porosity (%) = 100 × volume of seawater/volume of wet sediment; (3) bulk density (g/cm^3) = weight of wet sediment/volume of wet sediment (Haq et al., 1990). Shear strength is determined from the interval adjacent to the velocity measurement sample using a motorised vane apparatus with four 1.28×1.28-cm blades (Haq et al., 1990). The sediment composition was constrained from the smear slides, and sedimentation rates were estimated from biostratigraphic ages using ODP Site 762 core samples (Haq et al., 1990). Neodymium isotopic ratios of detrital sediments from ODP Site 762, were measured on a Neptune MC-ICP-MS (Le Houedec et al., 2012), and are expressed in ε_{Nd}detrital as: ε_{Nd}detrital=[($^{143}Nd/^{144}Nd_{sample}$)/($^{143}Nd/^{144}Nd_{CHUR}$)-1]·10000 with $^{143}Nd/^{144}Nd_{CHUR}$ = 0.512638. CHUR is the chondritic uniform reservoir, a theoretical reference composition representing the average, undifferentiated material of the solar system, and usually used in isotope geochemistry as a baseline for comparing radiogenic isotope ratios in planetary materials.

The geomorphology and distribution of carbonate landslides in the seismic reflection data are mapped and interpreted by using Petrel® software from Schlumberger. Seismic-well tie allows the well logs from ODP Sites 762 and 763 to be utilised to identify the core expression in the seismic reflection data, to build a regional seismic stratigraphic framework, and to provide relative age constraints for carbonate landslides. To correlate the core and seismic reflection data, depths were converted to seismic two-way travel times using time-depth conversion based on the P-wave velocities from ODP Sites 762 and 763 (Figure 4-2). The resulting time-depth relationship was calibrated using two marker horizons (seabed and middle Miocene unconformity). The depths of these marker horizons were reported in the ODP Site 762 and 763 reports (Haq et al., 1990), and their TWTs were picked from the seismic section based on their geological features (Figure 4-2 and Figure 4-3). Given the difference in resolution between seismic reflection data and well logs, each reflector in the seismic reflection data corresponds to a stratigraphic interval of approximately 7 metres thickness in the ODP well logs. The ε_{Nd}detrital-depth curve at ODP Site 762 shows the variation of Nd isotopes in different intervals, and the abundance of ε_{Nd}detrital can be used to infer stratigraphic trends in the nature and delivery of detrital sediments (Le Houedec et al., 2012).

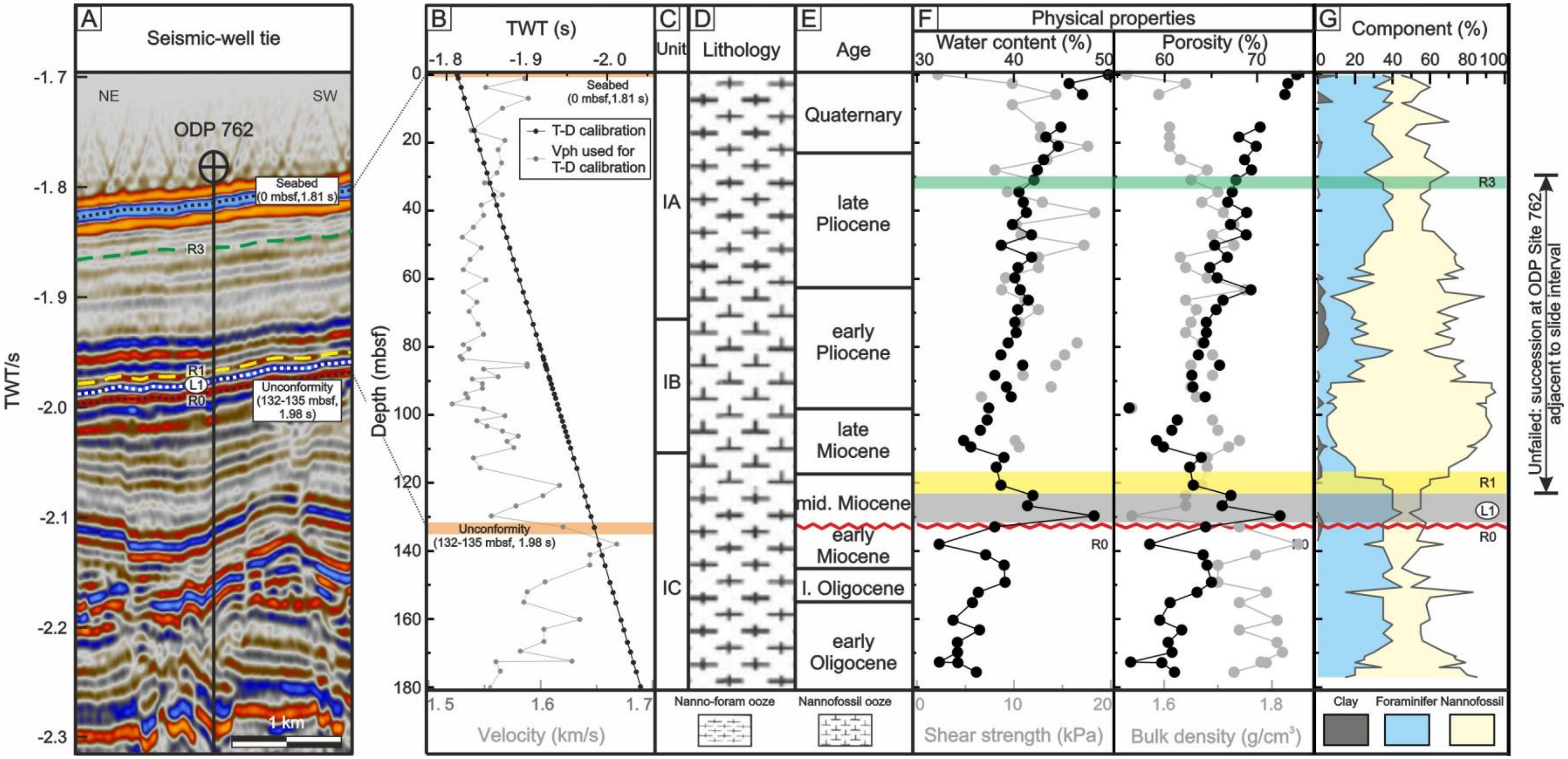
A
Seismic-well tie
NE
SW
ODP 762
Seabed (0 mbsf,1.81 s)
R3
R1
L1
R0
Unconformity (132-135 mbsf, 1.98 s)
1 km
TWT/s
B
TWT (s)
T-D calibration
Vph used for T-D calibration
Unconformity (132-135 mbsf, 1.98 s)
Depth (mbsf)
Velocity (km/s)
C
Unit
IA
IB
IC
D
Lithology
Nanno-foram ooze
Nannofossil ooze
E
Age
Quaternary
late Pliocene
early Pliocene
late Miocene
mid. Miocene
early Miocene
l. Oligocene
early Oligocene
F
Physical properties
Water content (%)
Porosity (%)
Shear strength (kPa)
Bulk density (g/cm³)
G
Component (%)
Clay
Foraminifer
Nannofossil
Unfailed: succession at ODP Site 762 adjacent to slide interval

Figure 4-2: Seismic-well tie and stratigraphic calibration at ODP Site 762. (A) Seismic section crossing ODP Site 762, showing the interpreted key horizons, including R0, L1, R1 and R3. R0 is the unconformity, L1 corresponds to the basal water-rich layer, R1 is the horizon corresponding to the lowest basal shear surface of Slide 8), R3 is the horizon corresponding to the top surface of Slide 8. (B) Depth-TWT calibration together with the core-measured depth-velocity profile. The Vph is velocity profile data used for depth-time calibration. (C) Lithostratigraphic units, (D) lithology, (E) age, (F) physical properties (water content, shear strength, water content and bulk density) and (G) sediment components are shown alongside the time-depth conversion. Note, depth-TWT calibration was established using a checkshot constructed from core-measure-velocity and the corresponding depth. Resulting TWT was constrained by two marker horizons: the seabed and the unconformity. The depths of the marker horizons are from Haq et al. (1990). The TWTs of these marker horizons are picked from the seismic profile, with the R0 unconformity identified primarily by reflector truncation beneath the surface (see Figure 4-3A for more details). The seismic section in the first panel is from Figure 4-3A. The depth-velocity data, lithostratigraphic units, lithology, age, physical properties and sediment components are from Haq et al. (1990). TWT = Two-way travel time. T-D calibration = Time-depth calibration.

4.5 Results

4.5.1 Seismic geomorphology of the study area

Ten submarine landslides are identified in the study area (Figure 4-1A), on a very gentle (<2°) NW-facing slope (Scarselli et al., 2013). Nine submarine landslides are present in the Bonaventure 3D and Thebe 3D seismic reflection datasets (Figure 4-1B), referred to as Slides 5 to 13 by Wu et al. (2023). An additional submarine landslide in the Agrippina 3D seismic reflection data I refer to as Slide 14 (Figure 4-1A). These ten submarine landslides can be classified into two groups based on their depth of burial. The more deeply buried group (~120 mbsf), comprising Slide 8 and Slide 14, is >40 km long and the focus of this study (Figure 4-3 and Figure 4-4). The other shallow group comprises submarine landslides that are either more shallowly buried (~30 mbsf; Slides 9-13; Figure 4-3), or that show seafloor expression (Slides 5 and 6).

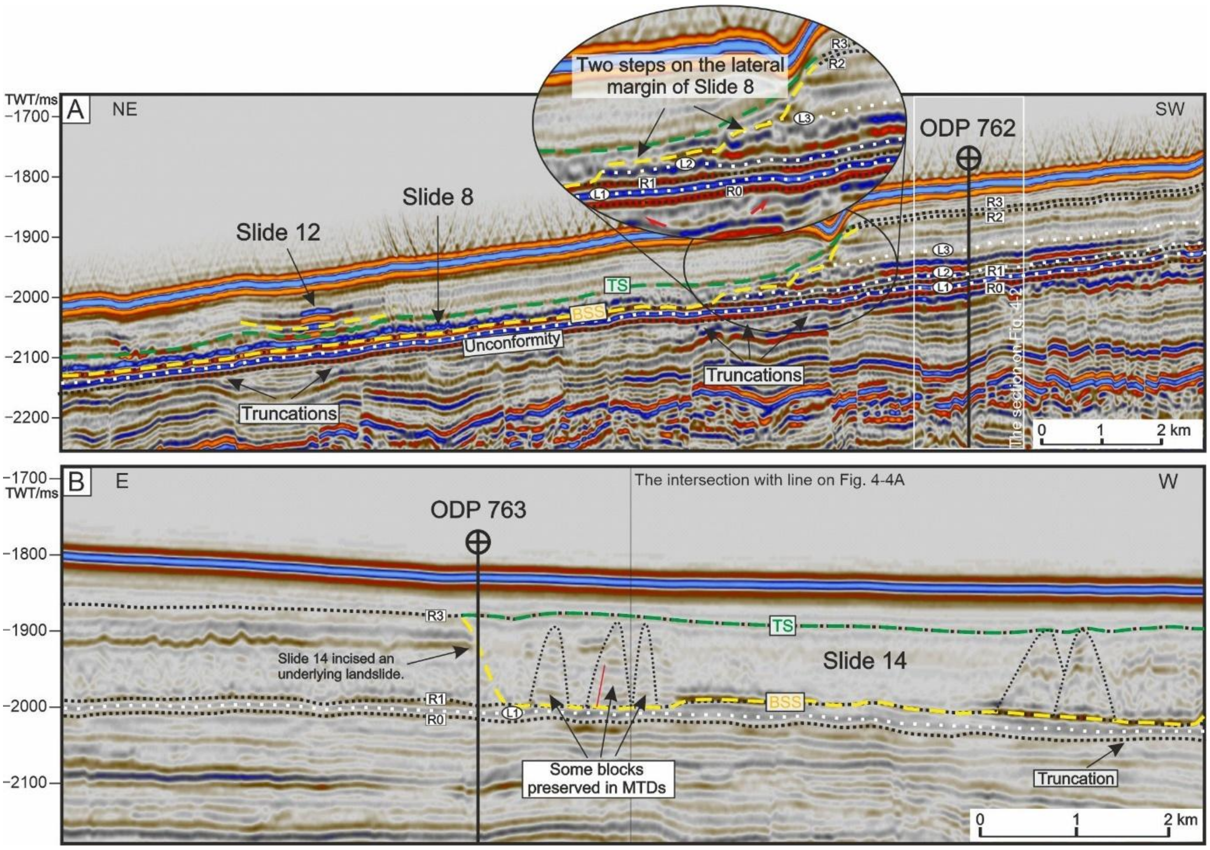

Figure 4-3: (A) A NE-SW trending seismic section from Bonaventure 3D, showing the distribution of Slides 8 and 12, and seismic-well tie between ODP site 762 and Bonaventure 3D seismic reflection data. The top surface (TS) and basal shear surface (BSS) of Slide 8 are labelled by green and yellow dashed lines, respectively. Seven key horizons (R0-R3, and L1-L3) are recognised at ODP Site 762. R0-R3 are directly related to the unconformity or geomorphology of Slide 8 and are marked as black dashed lines. L1-L3 are recognised by intervals with high water content (Figure 4-5A) and marked as white dashed lines. Red half-side arrows in the zoom-in figure indicate the location of truncations. (B) An E-W trending seismic section from Agrippina 3D, showing the distribution of Slide 14 and a landslide cut by Slide 14 in the east, and the seismic-well tie between ODP Site 763 and Agrippina 3D seismic reflection data. The vertical thin line in the middle of the figure shows the intersection with the line in Figure 4-4A. The top surface and basal shear surface of Slide 14 are labelled by green and yellow dashed lines, respectively. Four key horizons are recognised at ODP Site 763, R0, R1 and R3 correspond to the unconformity surface, basal shear surface and the top surface of Slide 14, and are labelled by black dashed lines. L1 is labelled by a white dashed line. The locations of the seismic sections in Figure 4-3A and Figure 4-3B are shown in Figure 4-1.

Slide 8 is >50 km wide, >40 km long and ~85 m thick, buried at 35-120 mbsf, with its headwall in the SE. It extends beyond the seismic reflection data to the NW. In terms of seismic facies and boundaries, Slide 8 is characterised by high to medium amplitude, discontinuous reflectors, and is bounded by high amplitude reflectors (top surface and basal shear surface; Figure 4-3A). Slide 8 becomes increasingly inset within the stratigraphy through downcutting, with two steps in the SW, forming a staircase-like basal surface at the lateral margins (Figure 4-3A). The steps form at the same stratigraphic level on the lateral margins and are 10s km wide (parallel to the local margin) and kilometres long (Figure 4-1B, Figure 4-3A and Figure 4-4B).

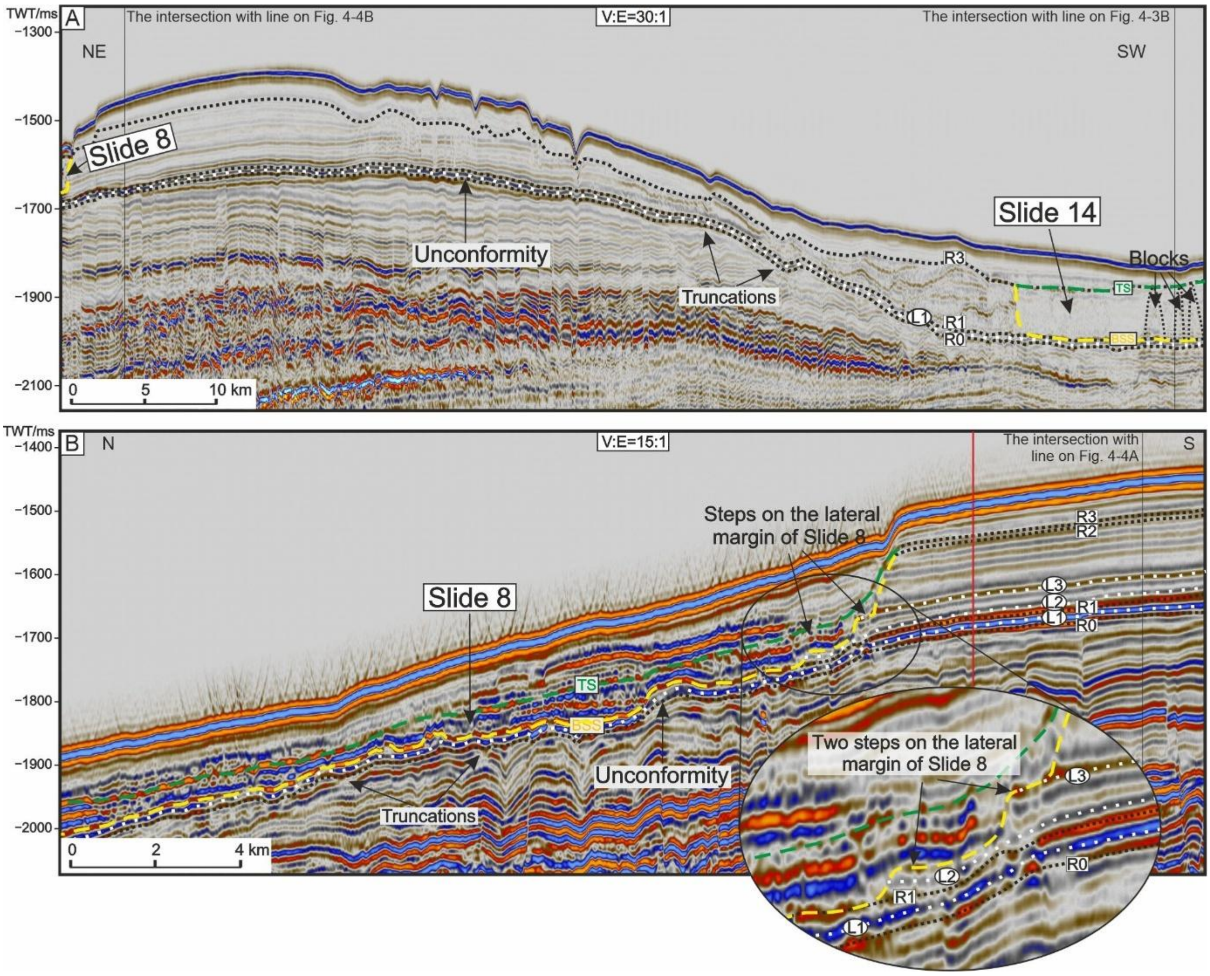

Figure 4-4: (A) The Leopard 2D seismic reflection line connecting the Bonaventure 3D and the Agrippina 3D seismic reflection datasets, showing part of Slide 14 and Slide 8. (B) A N-S trending seismic section from Bonaventure 3D, showing the lateral margin and part of the axis of Slide 8. The vertical black lines with labels in Figure 4-4A and Figure 4-4B indicate the intersection with other lines. The vertical red line on the right side of Figure 4-4B without a label indicates an ~90° change in the orientation of the section. The top surface (TS) and basal shear surface (BSS) of Slides 8 and 14 are labelled by green and yellow dashed lines, respectively. The locations of the sections in Figure 4-4 are shown in Figure 4-1.

Slide 14 is located 50 km to the SSW of Slide 8 and is ~15 km wide in its toe region and >40 km long, with its headwall region beyond the seismic reflection data in the SE and buried at 40-130 mbsf (Figure 4-1A and Figure 4-3B). Slide 14 is characterised by transparent, low frequency, low amplitude, and discontinuous reflectors, comprising some local blocky-shapes, parallel to sub-parallel, medium amplitude, and continuous reflectors (Figure 4-3B). The basal shear surface and top surface of Slide 14 are characterised by high-medium amplitude, continuous surfaces (Figure 4-3B). Slide 14 incises an underlying submarine landslide, where it forms a steep eastern lateral margin (Figure 4-3B).

4.5.2 Key stratigraphic surfaces

Seven key stratigraphic horizons were mapped (Figure 4-3 and Figure 4-4). Four horizons (R0-R3) are distinctive seismic reflectors, which are related to the tectonic structure or geomorphology of Slide 8 and Slide 14 (Figure 4-3 and Figure 4-4). Three horizons (L1 to L3) are recognised from seismic-well calibration and characterised by elevated water content at the ODP Site 762, compared to their bounding strata (Figure 4-5). The Leopard 2D seismic line permits the seven seismic stratigraphic horizons to be mapped from the Bonaventure 3D to the Agrippina 3D dataset (Figure 4-1A and Figure 4-4).

4.5.2.1 Submarine landslide seismic stratigraphy

ODP Site 762 was drilled ~2 km southwest of the headwall scarp of Slide 8 (Figure 4-3A). Four sub-parallel seismic reflectors related to the tectonic structure or geomorphology of Slide 8 have been mapped from Slide 8 to ODP Site 762 where the stratigraphic horizons do not show evidence of remobilization. These are labelled R0 to R3 from oldest to youngest (Figure 4-3A). An unconformity (R0) is identified beneath Slide 8 by a regional high frequency, high amplitude, and continuous reflector with underlying truncation of reflectors (Figure 4-3A), and can be tracked to the interval from 132-135 mbsf in ODP Site 762 instead of a surface, given the resolution of the seismic-well tie (Haq et al., 1990). The deepest seismic horizon cut by Slide 8 corresponds to a regional high amplitude and continuous reflector (R1), and is buried at 117-123 mbsf in ODP Site 762 (Figure 4-3A). The shallowest horizon cut by Slide 8 corresponds to a low amplitude and continuous reflector (R2), buried at 35-39 mbsf in ODP Site 762 (Figure 4-3A). The top surface of Slide 8 corresponds to a medium amplitude and continuous reflector (R3), and is buried at 31-35 mbsf in ODP Site 762 (Figure 4-3A).

ODP Site 763 drilled through Slide 14 and intersected the top surface and basal shear surface of Slide 14 (Figure 4-3B). At ODP Site 763, three sub-parallel seismic reflectors have been mapped corresponding to the unconformity, and the basal shear surface and the top surface of Slide 14 (Figure 4-3B). The unconformity is buried at

141-143 mbsf in ODP Site 763 and is characterised by a high amplitude and continuous reflector, underlain by truncated reflectors (Figure 4-3B). The basal shear surface of Slide 14 is characterised by a high amplitude and continuous reflector, buried at 129-136 mbsf in ODP Site 763 (Figure 4-3B). Thirdly, the top surface of Slide 14, is characterised by a medium amplitude and continuous reflector at a burial depth of 36-41 mbsf in ODP Site 763 (Figure 4-3B). With the connection of the Leopard 2D seismic line, reflectors corresponding to the unconformity, the basal shear surface, and the top surface of Slide 14 in the Agrippina 3D dataset can be shown to correlate to the same stratigraphic layers in the Bonaventure 3D dataset, and therefore are also labelled R0, R1, and R3 (Figure 4-4).

Slides 8 and 14 share their top surface (R3), and determining the age of this surface provides the maximum age limit of slide emplacement (Figure 4-4). The youngest incisional reflector (R2) of Slide 8 can be traced, and knowing R2's age gives a minimum age limit of Slide 8 (Figure 4-3A). The youngest incisional reflector of Slide 14 was eroded by younger slides and cannot be tracked (Figure 4-5A). From ODP Site 762, both R2 and R3 are Late Pliocene, supporting a Late Pliocene age for the emplacement of Slide 8 and the maximum age of Slide 14 (Figure 4-7).

4.5.2.2 Seismic-well calibration to ODP Sites 762 and 763

Three stratigraphic layers are recognised in well logs at ODP Site 762, characterised by elevated water content compared to the overlying and underlying strata, and labelled L1, L2 and L3 from oldest to youngest (Figure 4-5A). L1 is buried at 123-132 mbsf and is characterised by very high water content (41.43-48.3%), very high porosity (66.24-72.51%), low velocity (1.556-1.602 km/s), and very low bulk density (1.54-1.64 g/cm^3) in ODP Site 762 (Figure 4-5A). Through seismic-well calibration, L1 corresponds to the seismic reflector beneath the basal shear surface (R1) of Slide 8 on the seismic section (Figure 4-3A and Figure 4-4B). L2 is buried at 111-117 mbsf, and characterised by high water (38.20-38.99%), high porosity (62.72-63.97%), low velocity (1.540-1.546 km/s), and low bulk density (1.68 g/cm^3) in ODP Site 762 (Figure 4-5A). On the seismic reflection section, L2 corresponds to the seismic reflector beneath the deeper step on the basal shear surface of Slide 8 (Figure 4-3A and Figure 4-4B). L3 is buried at 79-93 mbsf and characterised by relatively elevated water content (40.93%), high porosity (64.44%), and low bulk density (1.65 g/cm^3) in its middle part (~86 mbsf) (Figure 4-5A). The shear strength of L3 varies from 11.0 kPa to 16.6 kPa (Figure 4-5A). In seismic reflection data, L3 is characterised by the low amplitude and continuous reflector, related to a shallower step of the basal shear surface of Slide 8 (Figure 4-3A and Figure 4-4B).

Mapping the Leopard 2D seismic line (Figure 4-4), the layer beneath the basal shear surface of Slide 14 in ODP Site 763 is the same layer beneath the basal shear surface of Slide 8, corresponding to L1 in ODP Site 762. At ODP Site 763, L1 is buried at 136-141 mbsf, and characterised by relatively high water content and porosity, and low bulk density (Figure 4-5B). The shear strength of L1 is very high at its top (136.8 mbsf), and can be up to 47.1 kPa compared to <6 kPa in surrounding strata (Figure 4-5B). L2 and L3 are eroded by Slide 14 and cannot be correlated to ODP Site 763 (Figure 4-4A). The elevated water content, high porosity and high compressibility of L1-3 means they fit the criteria for weak layers (Gatter et al., 2021; Wu et al., 2023), which are prone to failure and being used as shear surfaces.

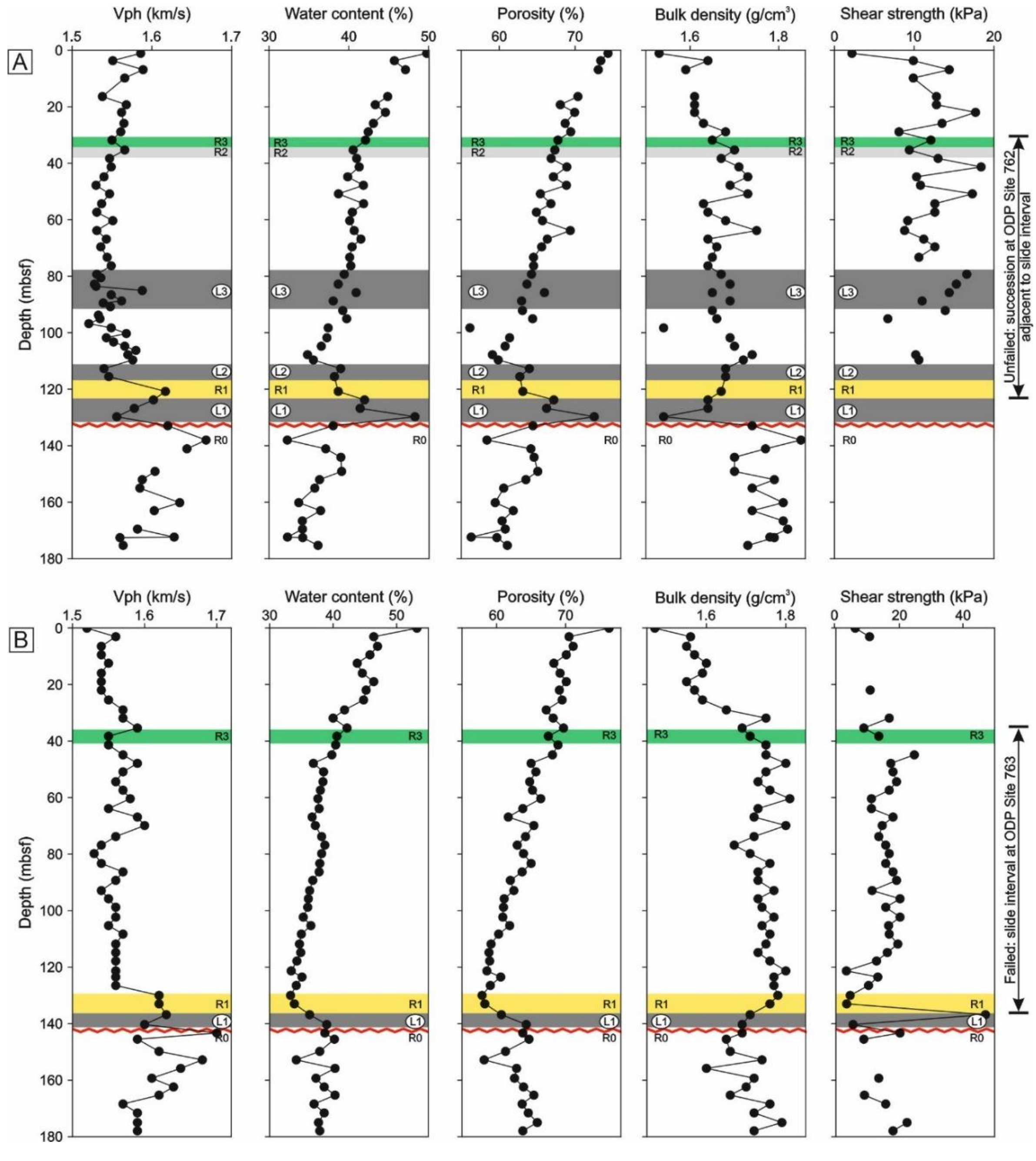

Figure 4-5: (A) Physical properties of stratigraphic layers at ODP Site 762 in unfailed sediment adjacent to Slide 8, corresponding to those layers that occur in the slide, and (B) physical properties of these stratigraphic layers at ODP Site 763 within the failed area affected by sliding (modified from Haq et al., 1990). R0 is the reflector corresponding to the unconformity. L1 corresponds to the layer beneath the basal shear surface (BSS), and R1 represents the BSS of Slide 8, and adjacent undeformed strata at ODP Site 762. R1 and L1 also correspond to the BSS and the layer beneath BSS of Slide 14 at ODP Site 763. L2 and L3 correspond to the weaker stratigraphic layers of Slide 8 at ODP Site 762, R3 is the reflector at ODP Site 762 that corresponds to the top surface of Slide 8, and the top surface of Slide 8 at ODP Site 763.

4.5.3 Comparison of horizons at ODP Sites 762 and 763

4.5.3.1 Comparison of physical properties at ODP Sites 762 and 763

At ODP Site 762, in undeformed strata, R0 and R1 are characterised by high velocity, low water content, low porosity, and high bulk density compared to the overlying and underlying strata (Figure 4-5A). R2 and R3 are characterised by similar water content and porosity compared to their bounding strata (Figure 4-5A). Conversely, L1, L2 and L3 are characterised by high water content, high porosity, and low bulk density at ODP Site 762 (Figure 4-5A). At ODP Site 763, the stratigraphy from L2 to R2 is remobilized, and only R3 and the R0 to R1 stratigraphy are preserved (Figure 4-3 and Figure 4-4).

From ODP Sites 762 to 763, the stratigraphic interval corresponding to the seismic reflector representing the unconformity (R0) shows only slight increases in velocity (from 1.62 km/s to 1.70 km/s) and water content (from 38.04% to 38.70%), and decreases in porosity (from 64.44% to 63.8%) and bulk density (from 1.74 g/cm^3 to 1.69 g/cm^3; Table 4-1). Conversely, the physical properties of the lowermost weak layer (L1) at ODP Site 763, are marked by a sharp decrease in water content and porosity, and an increase in bulk density, compared to ODP Site 762 (Figure 4-5; Table 4-1). The average water content of L1 at ODP Site 763 shows a 14.24% percentage change decrease (from 43.90% to 37.65%; Table 4-1), although this remains more water-rich than overlying and underlying layers (Figure 4-5B). The average porosity of L1 at ODP Site 763 records an 8.96% percentage change decrease (68.65% to 62.50%), and its bulk density shows ~5.6% percentage change increase from 1.61 g/cm^3 to 1.70 g/cm^3 (Table 4-1). R1, the base of which constitutes the basal shear surface, shows a similar trend with lower water content and porosity, and higher bulk density at ODP Site 763 than at Site 762 (Figure 4-5; Table 4-1). The average water content of R1 is only 33.60% at ODP Site 763, compared to 38.68% at Site 762 (13.13% percentage change decrease; Table 4-1). The average porosity of R1 decreases from 63.11% at ODP Site 762 to 58.10% at Site 763 (~8% percentage change decrease; Table 4-1). The bulk density of R1 increases by ~6% from 1.67 g/cm^3 to 1.77 g/cm^3 (Table 4-1). Compared to L1 and R1, R3 only slightly decreases in water content and porosity, and increases in bulk density and shear strength at ODP Site 763 compared to Site 762 (Table 4-1).

Table 4-1: Comparison of average physical properties of selected stratigraphic layers at ODP Sites 762 (outside slide area) and 763 (within slide area), showing the changes of physical properties.

Name	Vph (km/s)	Water content (%)	Porosity (%)	Bulk density (g/cm^3)	Shear strength (kPa)	Data source	Interpretation	
R3	1.55	42.10	67.73	1.65	12.1	ODP Site 762	Top surface	
	1.55	40.60	67.50	1.71	13.5	ODP Site 763		
	0	**-3.56%**	**-0.34%**	**3.64%**	**+11.57%**	**Percentage change***		
R1	1.62	38.68	63.11	1.67	-	ODP Site 762	Basal shear “surface” (6 m thick)	Basal shear zone
	1.62	33.60	58.10	1.77	3.95	ODP Site 763		
	0.00	**-13.13%**	**-7.94%**	**+5.99%**	**-**	**Percentage change**		
L1	1.58	43.90	68.65	1.61	-	ODP Site 762	Lowermost weak layer	
	1.62	37.65	62.50	1.70	26.25	ODP Site 763		
	+2.53%	**-14.24%**	**-8.96%**	**+5.59%**		**Percentage change**		
R0	1.62	38.04	64.44	1.74	-	ODP Site 762	Unconformity	
	1.70	38.70	63.80	1.69	20.2	ODP Site 763		
	+4.94%	**+1.74%**	**-0.99%**	**-2.87%**		**Percentage change**		

Percentage change*= ((Value at ODP 763-Value at ODP 762)/Value at ODP 762)*100%

4.5.3.2 Comparison of sediment composition at ODP Sites 762 and 763

The Pliocene to Quaternary sedimentary succession mainly comprises nannofossils (45-95%) and planktonic foraminifera (5-45%) with minor clay, quartz, bioclast, spicules and mica (< 30%) (Figure 4-7; Haq et al., 1990). Thus, the successions are classed as calcareous oozes.

At ODP Site 762, the compositions of stratigraphic units change with burial depth, with a decrease in foraminifera and an increase in nannofossils in the first 80 mbsf (Figure 4-7A). The exceptions to this trend occur in L3, and the L2 to L1 succession (Figure 4-7A). Foraminifera content within L3 is up to 40% at its top (81 mbsf) and decreases to 7% at its base (92 mbsf), while the nannofossils content at the top is 57% and increases to 93% at the base (Figure 4-7A; Haq et al., 1990). The foraminifera content within the L2 to L1 succession increases steadily, from 17.5% within L2 to 32.5% within R1, and 40% within L1 (Table 4-2). Nannofossils content decreases with depth, from 75% within L2 to 61.3% within R1 and 54% within L1 (Table 4-2).

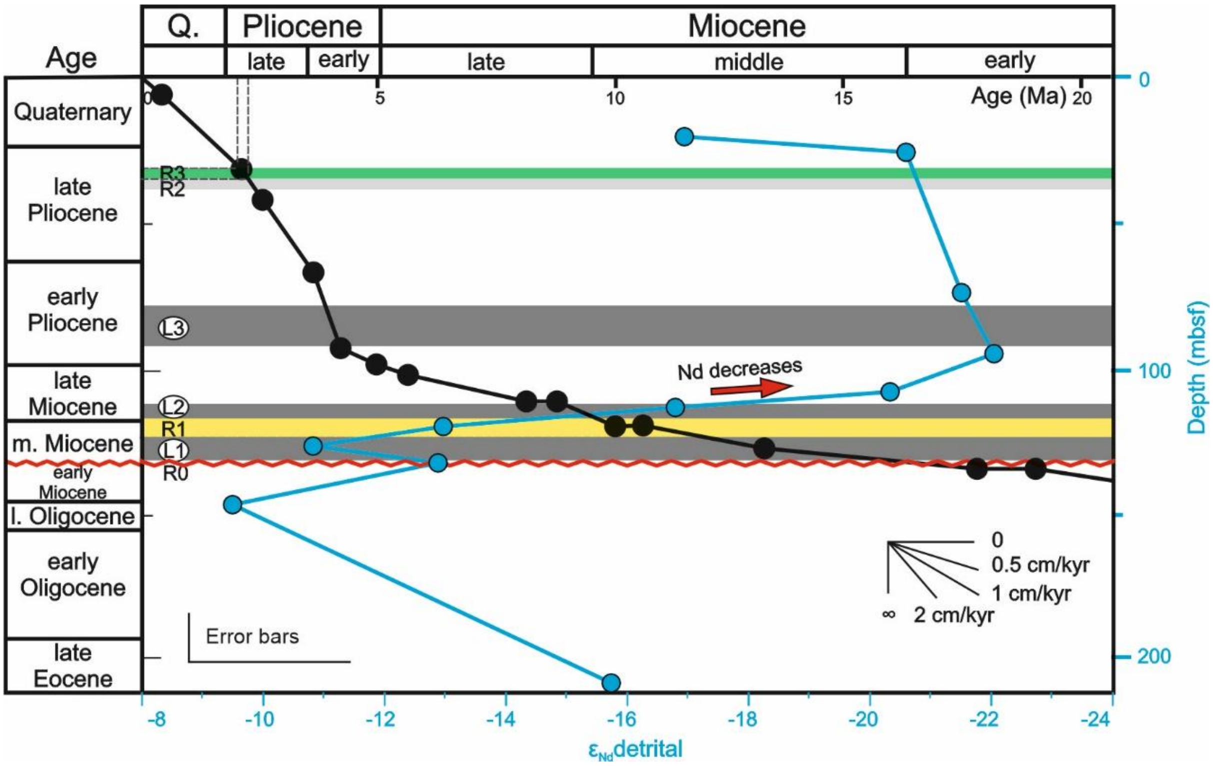

Figure 4-6: Age model, sedimentation rate, and detrital neodymium isotopic ratios for ODP Site 762. The black line indicates the sedimentation rate with depth (scale shown at bottom right, as angular relationships); depth and age error bars are added in the lower left (modified from Haq et al., 1990). The blue line indicates the change in depth of the Nd isotopic ratio of detrital sediments (ε_{Nd}detrital) at ODP Site 762; from Le Houedec et al. (2012). R0 to R3, and L1 are described in Figure 4-5. mbsf - metres below sea floor; Q - Quaternary.

Clay content increases near L1, L2 and L3 at ODP Site 762 (Figure 4-7A). Above L3, clay content varies from 2% to 4% at 60-78 mbsf and gradually increases to 6% above the top of L3 (76 mbsf), higher than the 0.5% level within L3 (Figure 4-7A; Table 4-2). Beneath L3, clay content increases to 3% at 97 mbsf (Figure 4-7A). Clay content is up to 10% at 109 mbsf above L2, decreases to 0% at 113 mbsf within L2, then increases to 2% at the interface of L2 and R1 (Figure 4-7A). Clay content is 0% within R1 and L1, and increases to 3% at the base of L1 (Figure 4-7A).

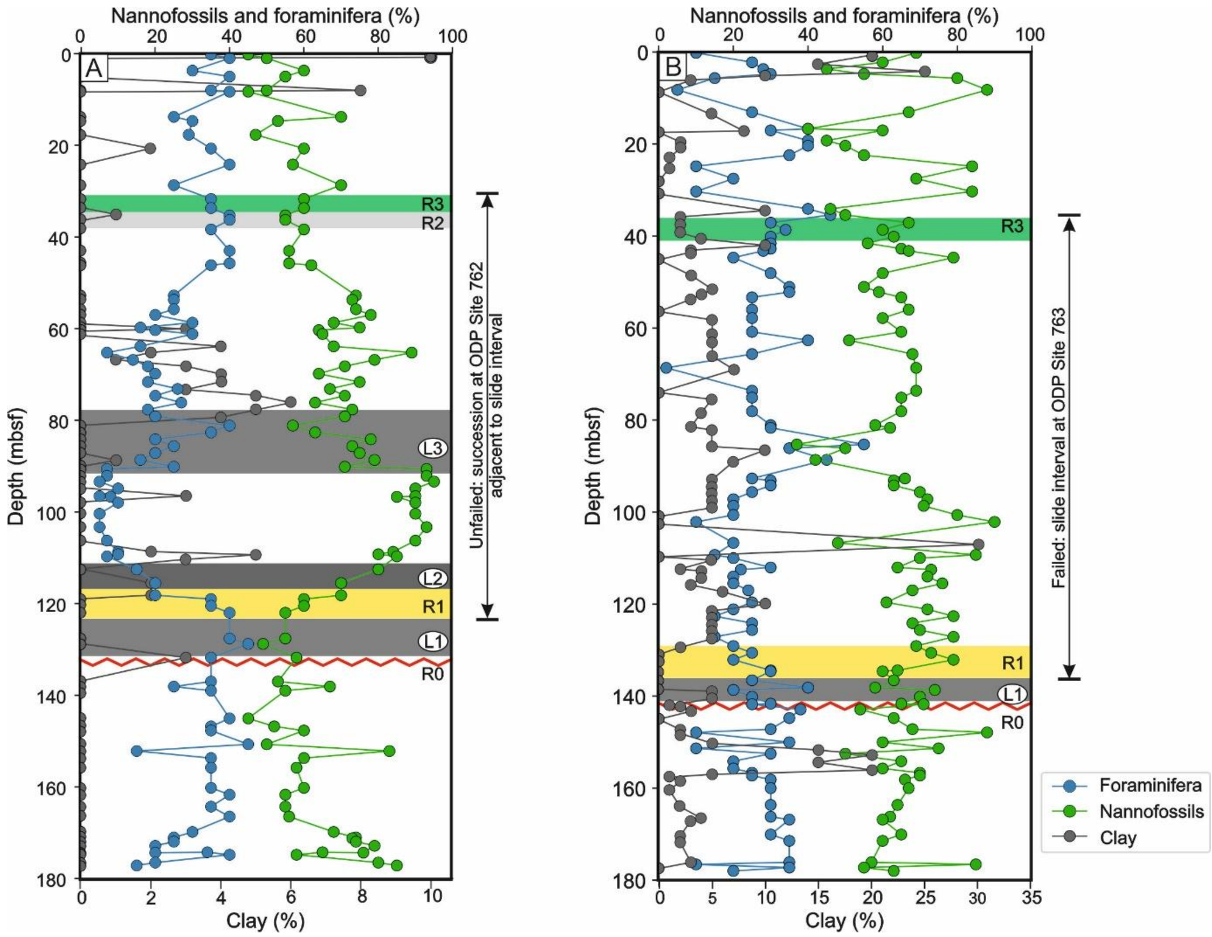

Figure 4-7: The relative foraminifera (blue), nannofossil (green) and clay (grey) components of sediments at ODP Site 762 in unfailed sediment beyond the edge of slide (A), and corresponding stratigraphy at ODP Site 763 within the failed area affected by slide (B). The component data come from Haq et al. (1990). mbsf - metres below seafloor. R0-R3 and L1-L3 are described in Figure 4-5.

At ODP Site 763, the stratal compositions show no clear trends with burial depth. Overall, foraminifera vary from 2% to 60%, nannofossils vary from 37% to 90%, and clay varies in the range of 0-30% (Figure 4-7B; Haq et al., 1990). Compared to ODP Site 762, foraminifera content decreases, and nannofossils content increases at Site 763, especially for the lowermost weak layer L1, and R1, the layer whose base constitutes the basal shear surface (Table 4-2). L1 consists of 66.3% nannofossils and 27.5% foraminifera at ODP Site 763, showing a 12.5% decrease (from 40.0% to 27.5%) in foraminifera and 12.3% increase (from 54.0% to 66.3%) in nannofossils compared to Site 762 (Table 4-2). R1 consists of 69% nannofossils and 25% foraminifera at ODP Site 763, with a 7.5% loss (from 32.5% to 25.0%) in foraminifera and 7.7% increase (from 61.3% to 69.0%) in nannofossils compared to Site 762 (Table 4-2). R3 shows a slight change (<4%) in foraminifera and nannofossils at Site 763 compared to Site 762 (Table 4-2).

Clay content within the slide interval varies over a wide range at ODP Site 763 (0% to 30%) compared to 0% to 10% at Site 762 (Figure 4-7). Clay content within R1 is very low at ODP Site 763, only 0.4% on average (Table 4-2). However, the clay content in L1 increases from 1% at ODP Site 762 to 2.5% at Site 763 (Table 4-2).

Table 4-2: Comparison of relative average components of stratigraphic layers at ODP Sites 762 and 763. Note, that the relative component data were acquired from smear slices in Haq et al. (1990).

Layers	Nannofossils (%)	Foraminifera (%)	Clay (%)	Others* (%)	Data source	Interpretation	
R3	60.0	35.0	0	5.0	ODP Site 762	Top surface	
	63.4	31.3	2.7	2.6	ODP Site 763		
	+3.4	**-3.7**	**+2.7**	**-2.4**	**Change****		
R2	56.7	38.3	0.3	4.7	ODP Site 762	Youngest truncation by Slide 8	
L3	75.3	21.5	0.5	2.7		Weak layers	
L2	75.0	17.5	1.0	6.5			
R1	61.3	32.5	0.5	5.7	ODP Site 762	Basal shear "surface" (6 m thick)	Basal shear zone
	69.0	25.0	0.4	5.6	ODP Site 763		
	+7.7	**-7.5**	**-0.1**	**-0.1**	**Change**		
L1	54.0	40.0	1.0	5.0	ODP Site 762	Lowermost weak layer	
	66.3	27.5	2.5	3.7	ODP Site 763		
	+12.3	**-12.5**	**+1.5**	**-1.3**	**Change**		

Others* include quartz, spicules, bioclast, mica, etc. (Haq et al., 1990).
Change*= Value at ODP 763-Value at ODP 762

ε_{Nd}detrital values show variations in the interval that corresponds stratigraphically to the failed sediments (L1 to R3; Figure 4-6 and Figure 4-8). The detrital Nd isotopic composition remains uniform from R0 to R1, around ε_{Nd}=-11 to -13 (Figure 4-6; Le Houedec et al., 2012). Above L1, ε_{Nd}detrital is -10.81 in L1, drops to -16.78 in L2 and to the minimum of -22.00 beneath L3, then gradually increases to -17.00 at 21 mbsf above L3 (Figure 4-6; Le Houedec et al., 2012). The decrease at ODP Site 762 from L1 to L3 (Figure 4-6) reflects the enhanced delivery of detrital sediments, including clays (Le Houedec et al., 2012).

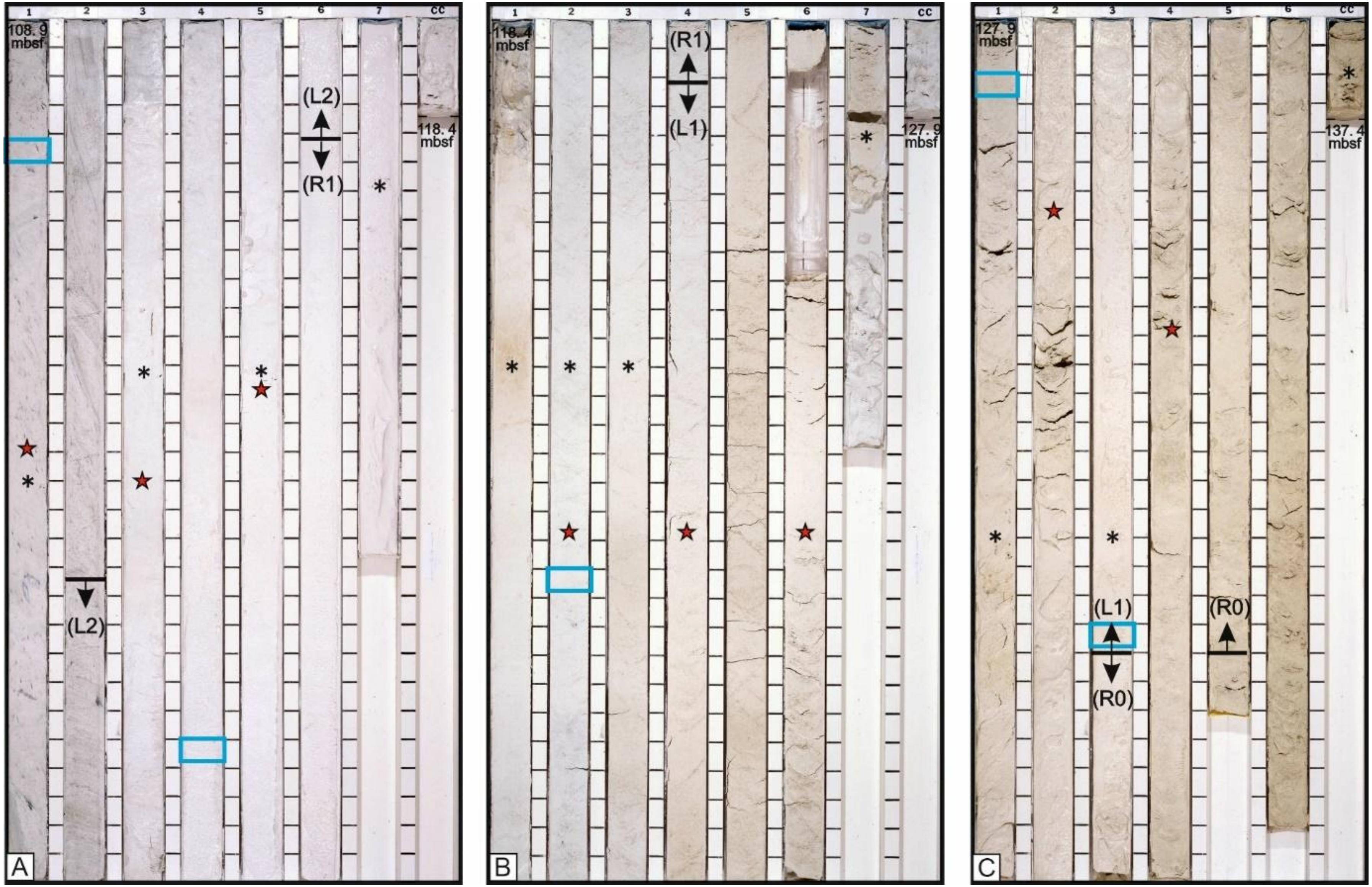
A
B
C
108.9 mbsf
118.4 mbsf
127.9 mbsf
137.4 mbsf
(L2)
(R1)
(L1)
(R0)
cc

Figure 4-8: Photographs of ODP Site 762 Hole B Core 13H (A), 14H (B), and 15H (C) (modified from Haq et al., 1990), showing the sample locations (physical properties, sedimentary components, and Nd isotopic ratios), and the intervals of some key horizons. Note: * indicates the location for smear slide samples for analysis of the sedimentary components. Red stars indicate the locations of the physical property samples. Blue frames indicate the locations of samples for Nd isotopes. R0 is identified from the reflected interval, corresponding to the unconformity. L1 is a water-rich layer underneath the basal shear "surface" of Slide 8. The R1 layer is ~6 m thick and is correlated with the lowermost part of the basal shear "surfaces". L2 is a water-rich layer. The interval labelled R0 indicates where the unconformity is, but the resolution of the seismic-well tie makes knowing the exact position of the unconformity surface challenging.

4.6 Discussion

4.6.1 Process Interactions between the Submarine Landslides and the Substrate

The unfailed and failed physical properties of the same horizons can be revealed from ODP Sites 762 and 763, respectively (Figure 4-5). The changes in physical properties can be used to investigate the controls and processes that form weak layers and ultimately enabling elucidation of the process mechanics of the submarine landslides.

4.6.1.1 The role of the water-rich layers

Calcareous ooze at shallow burial depths (~200 mbsf) is sensitive to overburden pressure, and undergoes mechanical compaction, which results in decreased porosity and water content with increased burial depth (Locat, 1995; Casas et al., 2006). However, the water content of L1-3 in undisturbed strata at ODP Site 762 is higher than the bounding strata (up to 48.30% in L1, 38.99% in L2, and 40.93% in L3; Figure 4-5A). Furthermore, L1-3 exhibit increased foraminifera content compared to the bounding strata (Figure 4-7A). These foraminifera are well preserved, without dissolution or abrasion (Haq et al., 1990). Therefore, foraminifera have a large amount of intraskeletal void space in their tests, where "excess" water volumes can be stored. For example, in the Gulf of Mexico, a 0.47wt% increase in foraminifera content was shown to increase porosity by 5 times, and therefore increase water content, compared to the background value (Sawyer and Hodelka, 2016).

The higher water content layers, L1-3, are also affected by the presence of clays. L1-3 at ODP Site 762 are capped by intervals with higher clay content (up to 6%; Figure 4-7A). At ODP Site 762, ε_{Nd}detrital shows a dramatic decrease during the late Miocene, from -16.78 in L2 to -22 beneath L3 (Figure 4-6). The decrease of >5 ε_{Nd}detrital is attributed to increased input of wind-driven dust (low ε_{Nd}) from continental erosion, enhanced by increased Western Australia aridity during the middle Miocene (Le Houedec et al., 2012). This explains why clays are preferentially deposited in middle Miocene sedimentary successions above L1. As shown in physical experiments, a minor increase in the clay fraction can decrease porosity, and reduce permeability exponentially (McCoy et al., 2012; Roelofs et al., 2023), thereby decreasing the ease at which fluids drain upwards through a calcareous ooze. The decrease in porosity and permeability induced by the clay component prevents the underlying fluids from escaping, which is a key factor in the formation of weak layers.

Bounded by the low permeability clay-rich deposits, the “excess” water is trapped within the foraminifera-rich layers (L1-3) resulting in anomalously high water content and enhanced pore pressures (cf. Major, 2000; Iverson, 2012; Roelofs et al., 2023). Their abnormally low velocity, low density, and high porosity also point to these intervals being overpressured and undercompacted relative to surrounding layers (Tingay et al., 2009; Liu et al., 2019) and are therefore identified as weak layers. L1 contains more well-preserved foraminifera than L2 and L3 (Figure 4-7A; Haq et al., 1990), which explains its higher water content compared to the shallower L2 and L3.

4.6.1.2 Why do the weak layers decrease in water content after failure?

The physical properties of the seismically mapped basal shear surface (R1) and the underlying weak layer (L1) identified in ODP 762 share dramatic changes after failure, with marked decreases in water content and porosity and increases in bulk density (Table 4-1). The most pronounced change in physical properties is water content, with the underlying weak layer decreasing by ~14.24% and the basal shear surface by ~13.13% (Table 4-1). Conversely, the unconformity (R0) slightly increases in water content (1.74%; Table 4-1). Simple mechanical compaction post-failure is not considered to be the main reason for the changes in physical properties before and after failure, given the contrasting changes in water content of the basal shear surface and the underlying weak layer compared to the unconformity (R0). Instead, the dramatic change in physical properties is attributed to the evolution processes during failure experienced by the basal shear surface and the underlying weak layer.

The basal shear surface and underlying weak layer were dominated by fragile planktonic foraminifera and nannofossils before failure (Figure 4-7A; Haq et al., 1990). After failure, these two layers show a marked decrease in planktonic foraminifera, with up to 7.5% loss in the basal shear surface and 12.5% loss in the underlying weak layer (Table 4-2). Planktonic foraminifera have a lot of void space and thin walls (Beemer et al., 2019), and their non-connecting chambers under certain compressive stresses will crush, which results in an abrupt expulsion of the intraskeletal water (Palmer-Julson and Rack, 1992; Rack et al., 1993). The crushing of the fragile foraminifera also contributes to the relative increase in the proportion of nannofossils.

Gas release may cause a local increase in pore pressure within weak layers. Indicators of gas release, including gas-bearing seismic stratigraphy, pockmarks, and gas chimneys, are documented updip of the headwall regions of Slides 8 and 9 (see Section 7.1.2 for further details). In the Bonaventure study area, a hydrocarbon plumbing system has been active since the late Triassic-late Jurassic, with migration of deep thermogenic gas towards the shallow subsurface through faults and stratigraphic pathways, contributing to the formation of a gas-hydrate stable zone within the upper ~150-200 mbsf (Paganoni et al., 2019). High-amplitude reflections associated with the L1 to L2 interval indicate the presence of free gas (Figure 4-2A; Paganoni et al., 2019). Deep-fluid migration and gas released from shallow gas-hydrate dissociation could locally increase pore pressures within the high porosity interval, thereby increasing slope instability (cf. Micallef et al., 2016; Elger et al., 2018). However, there is no direct evidence that the L1 to L2 interval was gas-charged prior to the initiation of Slide 8. Given the regional distribution of submarine failures on Exmouth Plateau, the foraminifera present in laterally extensive weak layers are interpreted as the primary stratigraphic control on the slope instability. The breakage of fragile foraminifera tests could cause the rapid release of water, elevated pore pressure, and reduction in effective stress, even though the exact trigger remains unclear. Gas migration and gas-hydrate dissociation are considered possible additional mechanisms that locally elevate pore pressure, thereby facilitate the slope instability.

In summary, the basal shear surface (R1) and the underlying weak layer (L1) change in their physical properties in similar ways before and after the landslide. Given this, and that each of them represents a 6-9 m thick interval, I treat them together as a basal shear zone (Figure 4-9A).

4.6.1.3 How do the submarine landslides interact with their underlying weak layers?

Substrate entrainment and the bulking-up of submarine landslides are widely documented phenomena (e.g., Hodgson et al., 2019; Nugraha et al., 2022; Böttner et al., 2024). Slides 8 and 14 entrained the calcareous ooze substrate during emplacement and formed strata parallel steps at L2 and L3 (Figure 4-3A, Figure 4-4B and Figure 4-9A). A mechanistic model is proposed to explain the interactions between the evolution of the submarine landslide and the carbonate substrate (Figure 4-9B).

(1) Contractive Shearing

The clay-bounded foraminifera-rich intervals trap “excess” water, become water-rich and undercompacted, and thus overpressured, thereby acting as weak layers (Figure 4-9B-i). As the substrate sediments are overridden by the landslide, the basal shear zone undergoes contractive shearing, during which the sediment is very rapidly compacted, foraminifera are crushed, inter- and intra-skeletal water is squeezed out, and pore pressure rises rapidly (Figure 4-9B-ii; Iverson et al., 2000; Peakall et al., 2020; Roelofs et al., 2023). Contractive shearing occurs across both L1 and R1 demonstrating that they act as a basal shear zone. The abnormal high shear strength at the interface between L1 and R1 post-failure (Figure 4-5B) is in keeping with R1 being the primary basal shear surface, above a broader deformation layer (L1).

(2) Confined lubrication of the basal shear surface

The underlying weak layer is confined by the overlying high-density submarine landslide mass, and the low permeability unconformity below (Figure 4-9B). Consequently, the water squeezed from the underlying weak layer, through the process of contractive shearing, is trapped below the landslide and cannot migrate across the unconformity as indicated by the minor increase of water content in R0 (Table 4-1). Because the landslide is essentially impermeable, at least on the timescales at which water is being squeezed out of the weak layer, then elevated pore pressure is generated as water is trapped beneath the landslide, as also postulated in other examples (e.g., Urlaub et al., 2018; Gales et al., 2023). Such trapped water will mechanically generate a water-rich layer (e.g., Iverson et al., 2010, 2011), or potentially a water film (Kokusho, 1999; Kokusho and Kojima, 2002; Kawakita et al., 2020), at the top of the underlying weak layer and/or below the basal shear surface (Figure 4-9B-ii). In either case, the water-rich layer or water film acts as a natural lubricating layer, resulting in reduced friction, thus enhancing the mobility of the landslide (Figure 4-9B-ii). The temporal stability of this lubricating layer is enhanced in the present example, as the basal surface of the landslide is strongly incised into surrounding fine-grained sediments characterised by low-permeabilities, thus hindering the loss of overpressure laterally. The overpressured water is confined in all directions and cannot readily escape. I term this process of contractive-shearing induced fluid expulsion in a confined setting ‘confined lubrication’.

The enhanced mobility of the landslide resulting from reduced friction will lead to increased basal shear stresses. If a water-rich layer is present, rather than a discrete water film, then the shear strength of the substrate will also be reduced. Either process, or both if present, will lead to enhanced erosion and flow bulking. Confined lubrication likely also contributes to distributive shearing along weak layers ahead of the bulldozing slide (e.g. Hodgson et al., 2019). This process weakens the substrate ahead of the landslide, which enables more entrainment and bulking up, and thus enables the landslide to propagate farther into the basin (Figure 4-9B-iii).

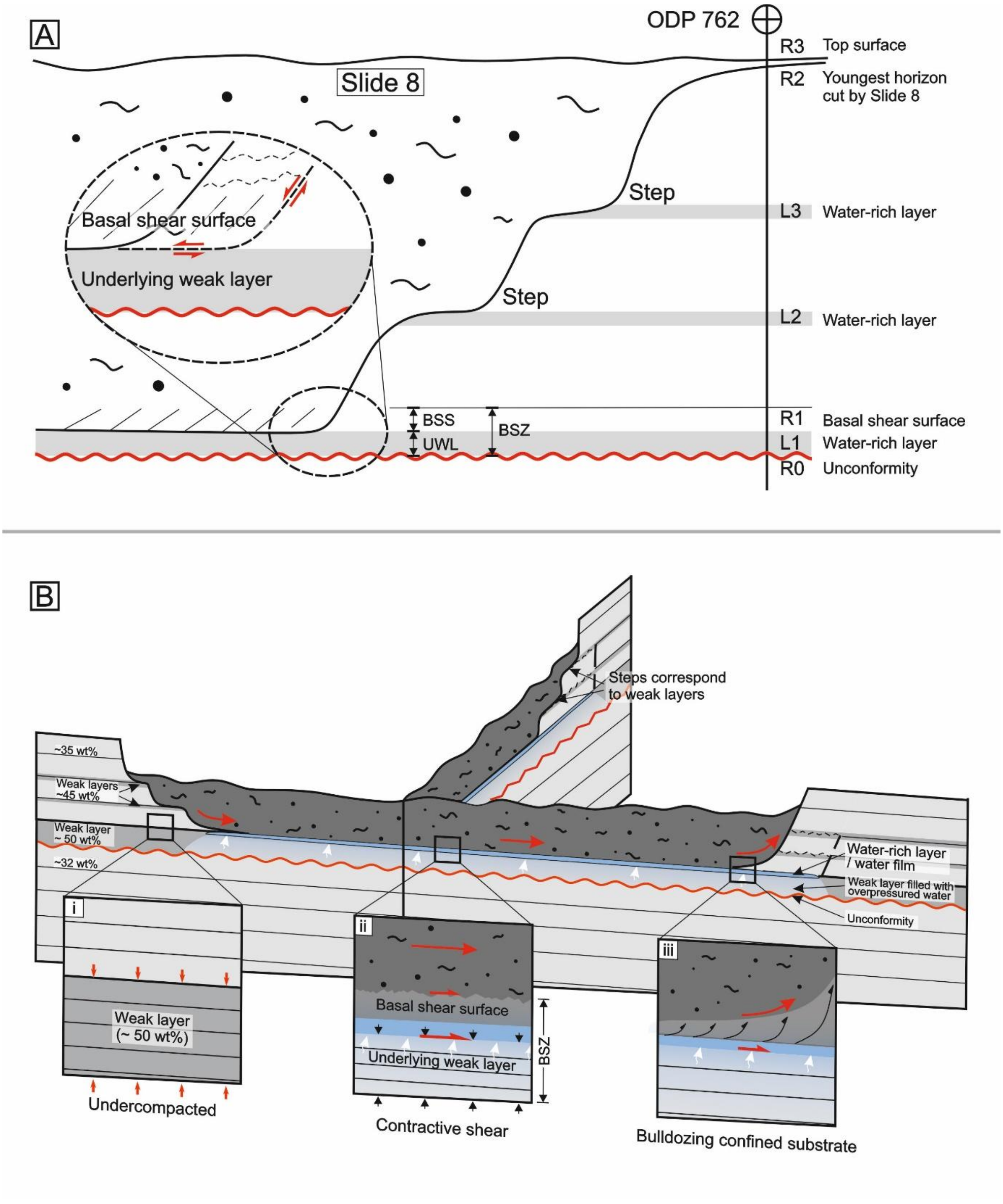
A
ODP 762
Slide 8
R3
Top surface
R2
Youngest horizon cut by Slide 8
Step
L3
Water-rich layer
Step
L2
Water-rich layer
Basal shear surface
Underlying weak layer
BSS
UWL
BSZ
R1
Basal shear surface
L1
Water-rich layer
R0
Unconformity
B
Steps correspond to weak layers
~35 wt%
Weak layers ~45 wt%
Weak layer ~ 50 wt%
~32 wt%
Water-rich layer / water film
Weak layer filled with overpressured water
Unconformity
i
Weak layer (~ 50 wt%)
Undercompacted
ii
Basal shear surface
Underlying weak layer
BSZ
Contractive shear
iii
Bulldozing confined substrate

Figure 4-9: (A) Schematic of Slide 8 and ODP Site 762, showing the relationship of key horizons from the landslide to ODP Site 762, and the deformation of the basal shear zone. In adjacent undeformed strata at ODP Site 762, R0 is the reflector corresponding to the unconformity, L1 corresponds to the water-rich layer beneath the basal shear surface (BSS), R1 is the reflector corresponding to the BSS of Slide 8, L2 and L3 are the water-rich layers corresponding to the steps of Slide 8, R2 is the youngest reflector cutting by Slide 8, and R3 corresponds to the top surface of Slide 8. UWL = underlying weak layer. (B) Carbonate submarine landslide evolution model, in longitudinal section (with partial strike-section) showing the emplacement of the slide, the changes in physical properties of calcareous ooze sediments, and the interaction between the flow and the substrate. (B-i) The weak layer in the undisturbed area has a high water content and is undercompacted. (B-ii) As the submarine landslide moves, the weak layer deforms through contractive shearing, resulting in the crushing of foraminifera, the release of water, and a reduction in porosity. Expulsion of water from the underlying weak layer leads to a water-rich layer, or water film, forming that lubricates the base of the landslide. (B-iii) The landslide bulks up through bulldozing and weakening the substrate through distributive shearing ahead of the landslide (modified from Hodgson et al., 2019). These processes lead to contractive shearing at, and ahead of, the flow front, continuously forming the water-rich layer. wt% in Figure 4-9B is the water content percentage. BSZ in Figure 4-9A and Figure 4-9B-ii is the basal shear zone, consisting of the underlying weak layer and the basal shear surface. Red half-side arrows in Figure 4-9B-ii and -iii indicate the shear strength.

4.6.2 Are calcareous ooze successions more prone to large-scale failure?

Compared to siliciclastic successions, calcareous ooze successions are more prone to form weak layers due to their higher compressibility, and higher non-connected pore water content (Palmer-Julson and Rack, 1992; Rack et al., 1993; Dutkiewicz et al., 2020). This propensity of failure in calcareous oozes is recognised in this part of the Exmouth Plateau, where a total of 13 submarine landslides are recognised in the interval above the L1 layer, and cumulatively cover ~6330 km^2 (Figure 4-1A; Wu et al., 2023). Two weak-layer related steps are recognised from the lateral margins of Slide 8, the deeper one is underlain by L2, and the shallower one can be traced to L3 (Figure 4-3A and Figure 4-4B). Therefore, once the overlying strata start to move downslope the basal detachment steps down, initially to L3, then to L2, and eventually to L1 (Figure 4-3A, Figure 4-4B and Figure 4-9A). L2 and L3 are characterised by elevated water content, high porosity, low velocity and bulk density, and are more foraminifera-enriched compared to the bounding strata (Figure 4-5A and Figure 4-7A). L2 and L3, like L1, will also generate “excess” pore water and pore pressures along an interface with low permeability on crushing of the foraminifera, resulting in a decrease in friction and shear strength (Kvalstad et al., 2005; Stoecklin et al., 2017; Gatter et al., 2021).

Once a failure initiates, regardless of the trigger mechanism, a submarine landslide originating in a calcareous ooze succession can exploit weak layers, such as L2 and L3, by cutting down in steps (Figure 4-9B). This might be achieved through distributive shearing of the substrate ahead of the inset and bulldozing landslide (Frey-Martínez et al., 2006; Hodgson et al., 2019; Sobiesiak et al., 2018). The basal shear surface would progressively develop on weak layers where the friction is low and form ramps and steps as more substrate is entrained (e.g., Sawyer et al. 2009; Hodgson et al., 2019; Barrett et al., 2021). Therefore, the volume of submarine landslides would increase during evolution by exploiting the presence of the weak layers and be nourished by expulsion of water from contractive shearing that cannot escape to the seafloor, resulting in a high-pressure water-rich layer or water film. My component results suggest as little as an 8.5% (from 32.5% in R1 to 40% in L1) increase in foraminifera can result in a pronounced increase in water content and porosity (Figure 4-5A), which provides a good conditioning to form the laterally extensive weak layers. The process interaction between the over-riding landslide and the substrate, especially those layers containing higher amounts of foraminifera, could help explain the large increases in the volume of carbonate landslides with similar properties during emplacement (e.g., Nugraha et al., 2022; Wu et al., 2023). The confined lubrication mechanism will likely be self-reinforcing, with contractive shearing leading to high basal water pressures, thus reducing basal friction and increasing flow velocity. It is postulated that this increases basal erosion, and enhances the bulldozing and sediment entrainment at the front of the landslide, and in turn the efficacy of subsequent contractive shearing. As the flow cuts down through successive weak layers, I postulate that the additional weight of the progressively thickening landslide enhances contractive shearing in each successive weak layer encountered. The implication is that submarine landslides on margins with calcareous oozes exhibiting multiple weak layers may be susceptible to enhanced mobility and flow bulking, with implications for hazard assessment for seafloor infrastructure and the triggering of tsunamis. Therefore, I recommend careful analysis of the physical properties and composition of calcareous oozes in unfailed strata during hazard assessments, given that calcareous ooze is the most widespread deep-sea sediment type on the seafloor.

4.7 Conclusions

Two buried giant submarine landslides are documented on the gentle submarine slopes of the Exmouth Plateau, offshore northwest Australia, using 3D seismic reflection data. Three geotechnically-distinct layers are identified in well data from the undisturbed stratigraphy adjacent to the slides, which are characterised by anomalously high water content and porosity, and low velocity and bulk density. In the undisturbed sedimentary succession, these layers are enriched in foraminifera, are bounded by increases in clay content, and represent undercompacted water-rich weak layers.

The lowermost weak layer can be mapped with the basal shear surface of slides, and acts as part of a basal shear zone. Its physical properties in the disturbed sedimentary sequence show marked decreases in water content and porosity, increases in bulk density and shear strength, and decrease in foraminifera compared to the undisturbed sedimentary sequence. Driven by the overriding landslide, the basal shear surface, and this underlying weak layer, would have undergone contractive shearing. This contractive shearing resulted in compaction, crushing of foraminifera, and water release, leading to pore pressure increasing rapidly. As the substrate sediments were overridden by the landslide, the water released from the underlying weak layer could not readily escape being confined in all directions. This trapped water resulted in the maintenance of elevated pore pressure in the layers. A water-rich layer, or a water film was generated, which acted as a confined lubricating layer at the top of the underlying weak layer and/or below the basal shear surface, resulting in a decrease in friction and shear strength.

The process interaction between the overriding flow and the underlying weak layer is likely a self-reinforcing mechanism. Once failure is initiated, the submarine landslides will incise until reaching a weak layer, forming steps in the headwall and lateral margins with contractive shearing leading to high basal water pressures, thus reducing basal friction and increasing flow velocity. The decreased basal friction and increasing flow velocity enhance basal shear stresses, and the bulldozing at the flow front, and result in extensive substrate entrainment and bulking up of the landslide, and in turn the efficacy of subsequent contractive shearing to increase the runout distance. My work shows that the process dynamics and evolution of submarine landslides are closely related to the changes in physical properties of sediments during failure, and understanding physical properties and compositions of stratigraphic horizons, especially the foraminifera-clay succession, is crucial in improving hazard assessments.

Chapter 5 Self-confining submarine debris flows: A mechanism for long run-out on gentle slopes

5.1 Summary

Cohesive submarine debris flows can travel remarkable distances (>400 km) even on gentle slopes (<1°). However, the processes responsible for their long run-out distances remain poorly constrained. Using three-dimensional seismic reflection data from the Exmouth Plateau, offshore northwest Australia, this research documents the architecture of a submarine debris flow deposit to reveal its process evolution on a gentle slope (~0.89°). The debrite is elongate (length-to-width ratio of 7~8) and exhibits a deeply incised, stepped, channel-like basal shear surface. The debrite volume is approximately three times that of the evacuated material in the headwall, suggesting substantial substrate entrainment during emplacement. The basal shear surface is ornamented with km-long grooves, with megaclasts (up to 250 m wide and 70 m thick) at their termination. Mapping of groove orientations and cross-cutting relationships of sets of radiating grooves reveals a series of partially preserved, basinward-stacking debrite lobes formed during flow evolution. The debris flow became self-confined through lateral depositional relief that drove substrate incision and the development of the stepped basal shear surface, which in turn enhanced flow confinement. Locally, the confinement is amplified by diapiric topography on the pathway that narrowed the flow pathway, contributing to deeper incision along the conduit. Late-stage remobilization of instable debrite lobes into the high relief of the underfilled conduit is revealed from the location and geometry of cross-cutting grooves and knickpoints. The self-confining mechanism enabled debris flows to bulk-up and undergo long run-out distances even on low slope angles. Recognition of this enhanced mobility of debris flows has implications for submarine geohazard assessment.

5.2 Introduction

Subaqueous debris flows are known to be highly mobile and can reach runout distances of several hundred kilometres even on low gradient slopes, such as examples on the Mississippi Fan (Locat and Lee, 2002), the NW African continental slope (Masson et al., 1997; Gee et al., 1999), and the Norwegian-Greenland Sea continental margins (Vorren et al., 1998). This high flow mobility is remarkable, considering that the characteristic slope angles are typically less than 5° and often less than 1°. Several hypotheses have been proposed to explain the extreme mobility of subaqueous debris flows, including hydroplaning (Mohrig et al., 1998; De Blasio et al., 2004a, 2004b; Acosta et al., 2017), high internal pore pressure within the debris flow (Gee et al., 1999; Talling, 2013; Peakall et al., 2020), and flow transformation (Talling et al., 2007). These mechanisms primarily focus on the basal lubrication processes at the basal interface of the flow through flow-substrate interaction, or the rheological properties of the flow (e.g., high internal pore pressures), with little consideration of the role of flow-driven modification of the seafloor. In particular, the extent to which depositional relief and substrate entrainment influences flow evolution and mobility remain poorly constrained. This chapter describes, explains and discusses an elongate submarine debrite that reveals a novel self-confinement mechanism for enhancing the mobility of subaqueous debris flows.

Self-confinement of subaerial debris flows has been invoked as a mechanism to increase run-out distances (e.g., Iverson et al., 1997; Johnson et al., 2012). Subaerial physical experiments demonstrate that debris flows can develop self-confinement through the construction of lateral depositional relief (e.g., Iverson et al., 2010; Johnson et al., 2012; de Haas et al., 2015, 2016), and/or substrate incision (e.g., de Haas et al., 2016). Such self-confinement can establish a positive feedback between confinement and mobility. Increased confinement can limit lateral flow spreading, increase flow thickness, and thus result in faster and more efficient transport (Iverson et al., 2010; Johnson et al., 2012; Kokelaar et al., 2014; de Haas et al., 2015, 2016). Submarine debris flows have many characteristics similar to terrestrial debris flows (Prior et al., 1984; Masson et al., 1997) but occur on a larger scale. They can generate deposits with volumes of hundreds of km^3 (e.g., Masson et al., 1997; Gee et al., 1999; Georgiopoulou et al., 2010), which are orders of magnitude larger than their subaerial counterparts. Submarine debris flows are capable of entraining substantial substrate (Dakin et al., 2013; Krastel et al., 2019), and field observations demonstrate that substrate incision by submarine debris flows can form steep lateral margins that confine subsequent flows (e.g., Brooks et al., 2018; Martínez-Doñate et al., 2021). Depositional relief has been observed at lateral margins of subaqueous debris flows, such as up to 20 m high lateral levees on the Bear Island debris flows (Laberg and Vorren, 1995), the 15 m high relief on the Saharan debrite (Masson et al., 1993), and the ~5 m high lateral levees in the Kitimat fjord debrite (Prior et al., 1984). Previous studies on confining submarine debris flows have predominantly focused on those confined by pre-existing seafloor topography, including submarine canyons, submarine channels and structural confinement (e.g., Prior et al., 1984; Alves and Cartwright, 2009; Ortiz-Karpf et al., 2015, 2017). However, the development of self-confinement by subaqueous debris flows on initially unconfined, very low gradient slopes, and its role in promoting long runout distances, has not been reported.

This study aims to document a self-confined submarine debrite using three-dimensional seismic reflection data from the Exmouth Plateau, offshore northwest Australia, where the slope gradient is less than 1°. The main objectives of this study are: (1) to examine how depositional relief is generated; (2) to understand the nature of substrate incision at the base of the debrite; (3) to reconstruct the spatio-temporal patterns of submarine debrite formation through integration of depositional lateral relief and erosional substrate incision; and (4) to develop a model of self-confinement in submarine debris flows.

5.3 Geological Setting

Multiple submarine landslides have been documented on the Exmouth Plateau, offshore northwest Australia (Figure 5-1). The Exmouth Plateau is about 600 km long and 350 km wide, and is located around 225 km offshore northwest Australia, with water depths of 800 to 4000 m (Figure 5-1A; Exon et al., 1992). The plateau formed during the breakup of Gondwana from the Late Triassic to the Early Cretaceous (Stagg and Colwell , 1994), before subsiding during the Late Cretaceous and accumulating bathyal carbonate sediments throughout the Cenozoic (Haq et al., 1990). The collision of the Australian and Eurasian plates from the Late Oligocene reactivated rift structures, leading to the formation of inversion anticlines, such as the Exmouth Plateau Arch (Figure 5-1A; Boyd et al., 1993). The slope near the Exmouth Plateau Arch is <1° and is covered by poorly consolidated calcareous ooze (Exon et al., 1992; von Rad et al., 1992). The stratigraphic interval of interest is the middle Miocene, which in the study area corresponds to strata buried < ~140 mbsf, comprising pelagic calcareous oozes with sedimentation rates as low as 20 m/Myr (Exon et al., 1992; von Rad et al., 1992).

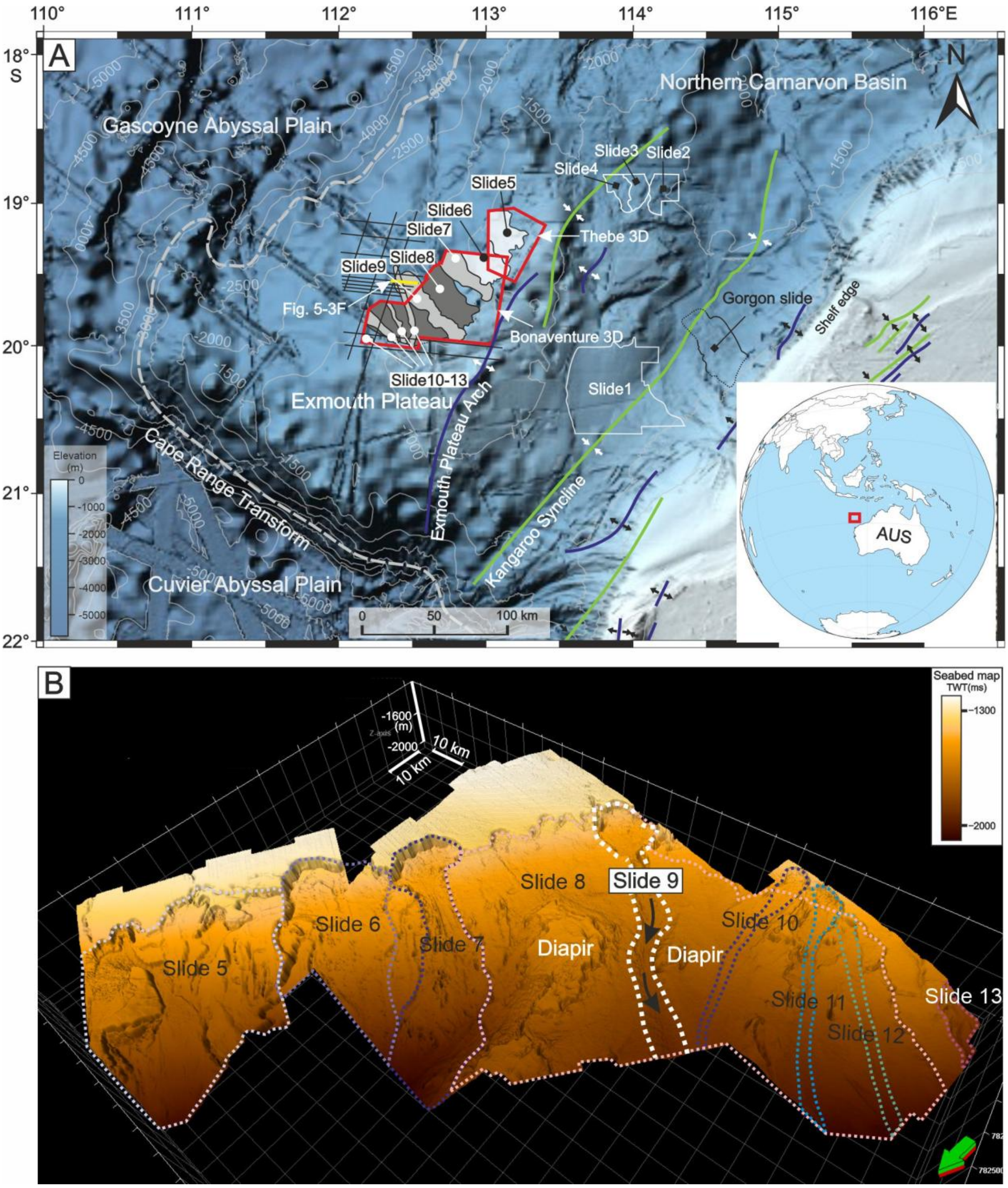
A
Gascoyne Abyssal Plain
Northern Carnarvon Basin
Slide5
Slide6
Slide7
Slide8
Slide9
Fig. 5-3F
Slide10-13
Slide4
Slide3
Slide2
Thebe 3D
Bonaventure 3D
Gorgon slide
Shelf edge
Slide1
Exmouth Plateau
Exmouth Plateau Arch
Kangaroo Syncline
Cape Range Transform
Cuvier Abyssal Plain
AUS
Elevation (m)
100 km
B
Seabed map TWT(ms)
10 km
Slide 5
Slide 6
Slide 7
Slide 8
Slide 9
Diapir
Diapir
Slide 10
Slide 11
Slide 12
Slide 13

Figure 5-1: (A) Location map of the study area offshore NW Australia, incorporating key geomorphological features. The study area is outlined by red polygons. Black polygons mark the location of submarine landslides, and their fill colour corresponds to the burial depth of these slides; white = seafloor exposed, light grey = shallow burial (<100 mbsf), and dark grey = deep burial (~120 mbsf). Submarine landslide locations come from Scarselli et al. (2013, 2020) and Wu et al. (2023). The basemap is seafloor bathymetry data from the General Bathymetric Chart of the Oceans (GEBCO, https://www.gebco.net/data-products/gridded-bathymetry-data). Inset shows the location of the study area within Australia (AUS). (B) Perspective view of the seafloor, showing the distribution of submarine landslides within the Bonaventure 3D and Thebe 3D seismic reflection data. Vertical exaggeration (VE) is 8:1. The dashed lines with different colours indicate the boundaries of submarine landslides (Slide 5 to Slide 13). Black arrows on Slide 9 indicate the direction of Slide 9. The location of the seafloor shown in Figure 5-1B corresponds to the red polygons on Figure 5-1A. Green arrow points North.

5.4 Data and Methodology

This study utilises two three-dimensional (3D) seismic reflection datasets (Bonaventure 3D and Thebe 3D) and two-dimensional (2D) seismic sections (Leopard 2D) from Geoscience Australia (https://www.nopims.gov.au). Bonaventure 3D and Thebe 3D partially overlap, collectively covering an area of 5556 km^2 in water depths from 890 m to 1570 m, and image nine submarine landslides within the late Miocene to recent stratigraphic interval (Figure 5-1 and Figure 5-2). The Bonaventure 3D dataset is 4132 km^2, has a dominant seismic frequency of 30-60 Hz, and a vertical seismic resolution of around 6~13 m, with a near seafloor (~180 mbsf) velocity of 1520-1600 ms^{-1}. The Thebe 3D dataset covers 1198 km^2, and its dominant seismic frequency is 40-80 Hz with a vertical seismic resolution of 5~10 m for shallow intervals. The Leopard 2D seismic reflection dataset (Line 0007) is used to image the distal end of the system (Slide 9; Figure 5-1), dominant seismic frequency of 20-40 Hz with vertical resolution of 10~20 m.

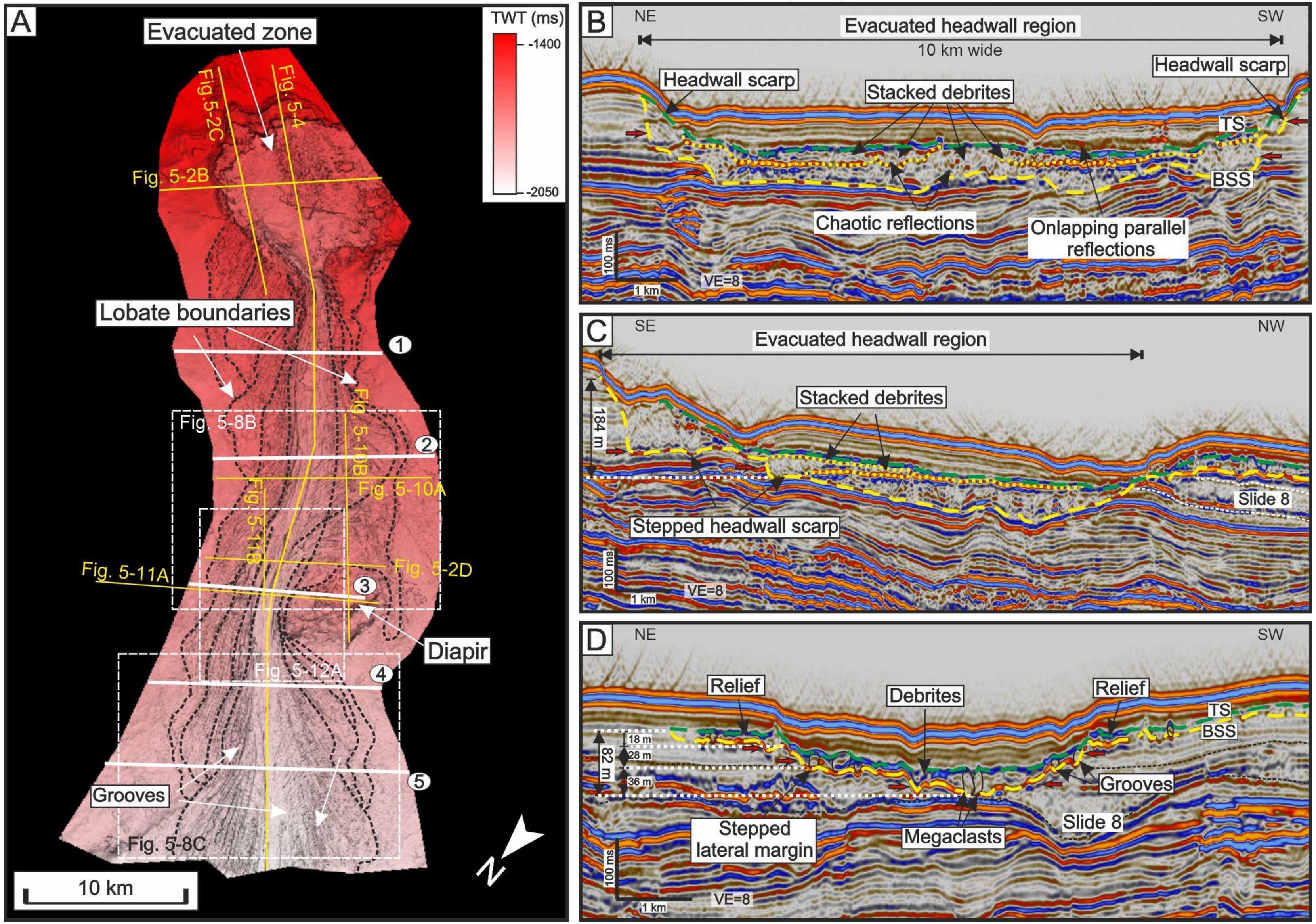

A
Evacuated zone
TWT (ms)
-1400
-2050
Fig.5-2C
Fig. 5-4
Fig. 5-2B
Lobate boundaries
1
2
3
4
5
Fig. 5-8B
Fig. 5-10B
Fig. 5-10A
Fig. 5-11B
Fig. 5-11A
Fig. 5-2D
Diapir
Fig. 5-12A
Grooves
Fig. 5-8C
10 km
N
B
NE
SW
Evacuated headwall region
10 km wide
Headwall scarp
Stacked debrites
Headwall scarp
TS
BSS
Chaotic reflections
Onlapping parallel reflections
100 ms
1 km
VE=8
C
SE
NW
Evacuated headwall region
Stacked debrites
184 m
Slide 8
Stepped headwall scarp
100 ms
1 km
VE=8
D
NE
SW
Relief
Debrites
Relief
TS
BSS
18 m
28 m
36 m
82 m
Grooves
Stepped lateral margin
Megaclasts
Slide 8
100 ms
1 km
VE=8

Figure 5-2: (A) Plan-view of the basal shear surface of Slide 9, showing the circular geomorphology of the headwall region, the lobate boundaries, and the presence of a diapir on the pathway. The thick, white, lines with numbers (1 to 5) on Figure 5-2A indicate the locations of the topographic profiles shown in Figure 5-7. (B) NE-SW trending seismic section, and (C) SE-NW trending seismic section in the headwall region, showing the stepped headwall scarps and stacked debrites. (D) NE-SW trending seismic section in the downstream area, showing the relief on the lateral margins, the axial-ward deepening of the basal shear surface, the megaclasts (~130 m wide and 40 m thick), and the grooves (~130 wide and 15 m deep) developed on the basal shear surface. Note, the green dashed lines mark the top surface (TS) of Slide 9, the yellow lines represent the basal shear surface (BSS) of Slide 9. The red horizontal arrows with black outlines on these seismic sections highlight substrate truncations. Locations of sections 2B, 2C and 2D are shown in Figure 5-2A. Vertical exaggeration (VE) is 8:1.

Seismic interpretation and geomorphological mapping of the seismic reflection data are carried out using Petrel® software from Schlumberger to document the basal surface and internal structures of a submarine landslide in the study area (i.e., Slide 9; Figure 5-3 and Figure 5-4). A gradient map is generated based on the basal surface of Slide 9, to illustrate variations in the lateral margin steepness (Figure 5-5A). An isopach (thickness) map is calculated between the top surface and the basal surface of Slide 9, to quantify spatial variance in deposit thickness (Figure 5-5B). To evaluate basal structures and internal architecture, the basal surface, the top surface and the iso-proportional variance map are extracted, highlighting basal lineations and local coherent blocky structures (Figure 5-3). The deposit volume of Slide 9 (Vd) is calculated using the mapped top and basal surfaces following the approach of Nugraha et al. (2022; Figure 5-4). To estimate the initially evacuated volume, a pre-failure surface is reconstructed by interpolating the youngest incised reflector to follow the form of the adjacent intact slope (~0.89°; Figure 5-4A).

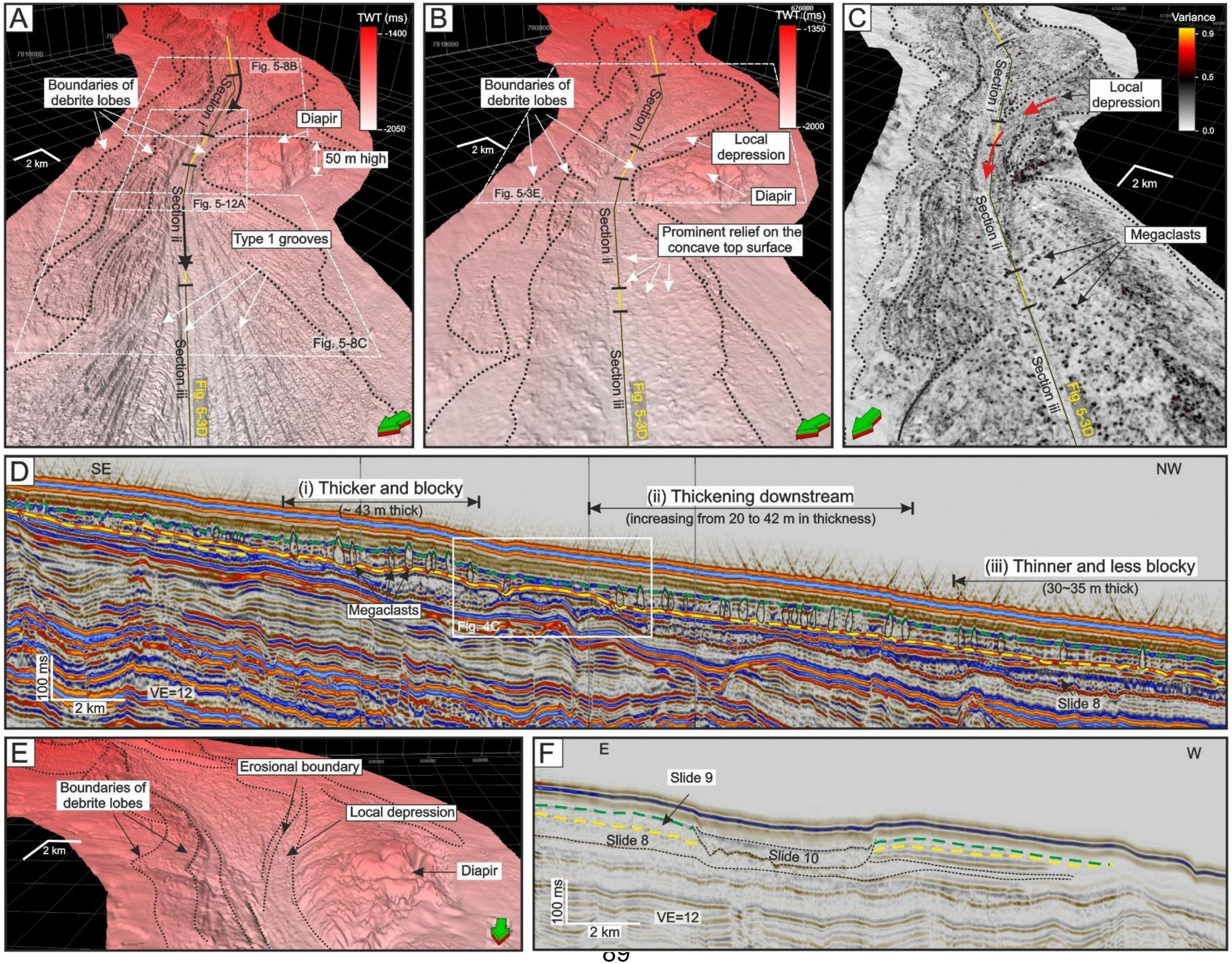
A
TWT (ms)
-1400
-2050
Boundaries of debrite lobes
Fig. 5-8B
Section i
Diapir
50 m high
2 km
Section ii
Fig. 5-12A
Type 1 grooves
Fig. 5-8C
Section iii
Fig. 5-3D
B
TWT (ms)
-1350
-2000
Boundaries of debrite lobes
Section i
Local depression
Diapir
Fig. 5-3E
Section ii
Prominent relief on the concave top surface
Section iii
Fig. 5-3D
C
Variance
0.9
0.5
0.0
Section i
Local depression
2 km
Section ii
Megaclasts
Section iii
Fig. 5-3D
D
SE
NW
(i) Thicker and blocky
(~ 43 m thick)
(ii) Thickening downstream
(increasing from 20 to 42 m in thickness)
(iii) Thinner and less blocky
(30~35 m thick)
Megaclasts
Fig. 4C
100 ms
2 km
VE=12
Slide 8
E
Boundaries of debrite lobes
Erosional boundary
Local depression
2 km
Diapir
F
E
W
Slide 9
Slide 8
Slide 10
100 ms
2 km
VE=12

Figure 5-3: (A) Perspective view of the basal shear surface of Slide 9, showing the distribution of grooves. (B) Perspective view of the top surface of Slide 9, showing areas of prominent local relief (*ca.* 10-25 m). (C) Perspective view of the variance map (~10 ms below the top surface), highlighting the distribution of megaclasts. (D) A SE-NW trending seismic section along the central axis of Slide 9. Light grey vertical lines in section indicate a change in the orientation of the section. Location of section 3D is shown in Figure 5-3A, Figure 5-3B and Figure 5-3C, and corresponds to the downstream part of the seismic section in Figure 5-4A. (E) Enlarged view of the upstream part of the top surface, emphasising the depositional boundary, the local depression and the boundaries of debrite lobes. (F) A E-W trending two-dimensional seismic section, displaying the distal extent of debrite beyond the 3D dataset region. Location of section 3F is shown in Figure 5-1A. Note that, the lobate margins in Figure 5-3A to Figure 5-3C and Figure 5-3E are outlined by black dashed lines. Green arrow in Figure 5-3A to Figure 5-3C and Figure 5-3E points North. The green dashed lines on sections 3D and 3F mark the top surface (TS) of the debrite, the yellow lines on sections 3D and 3F represent the basal shear surface (BSS) of the debrite. sections 3D and 3F are at the same scale, with vertical exaggeration (VE) of 8:1.

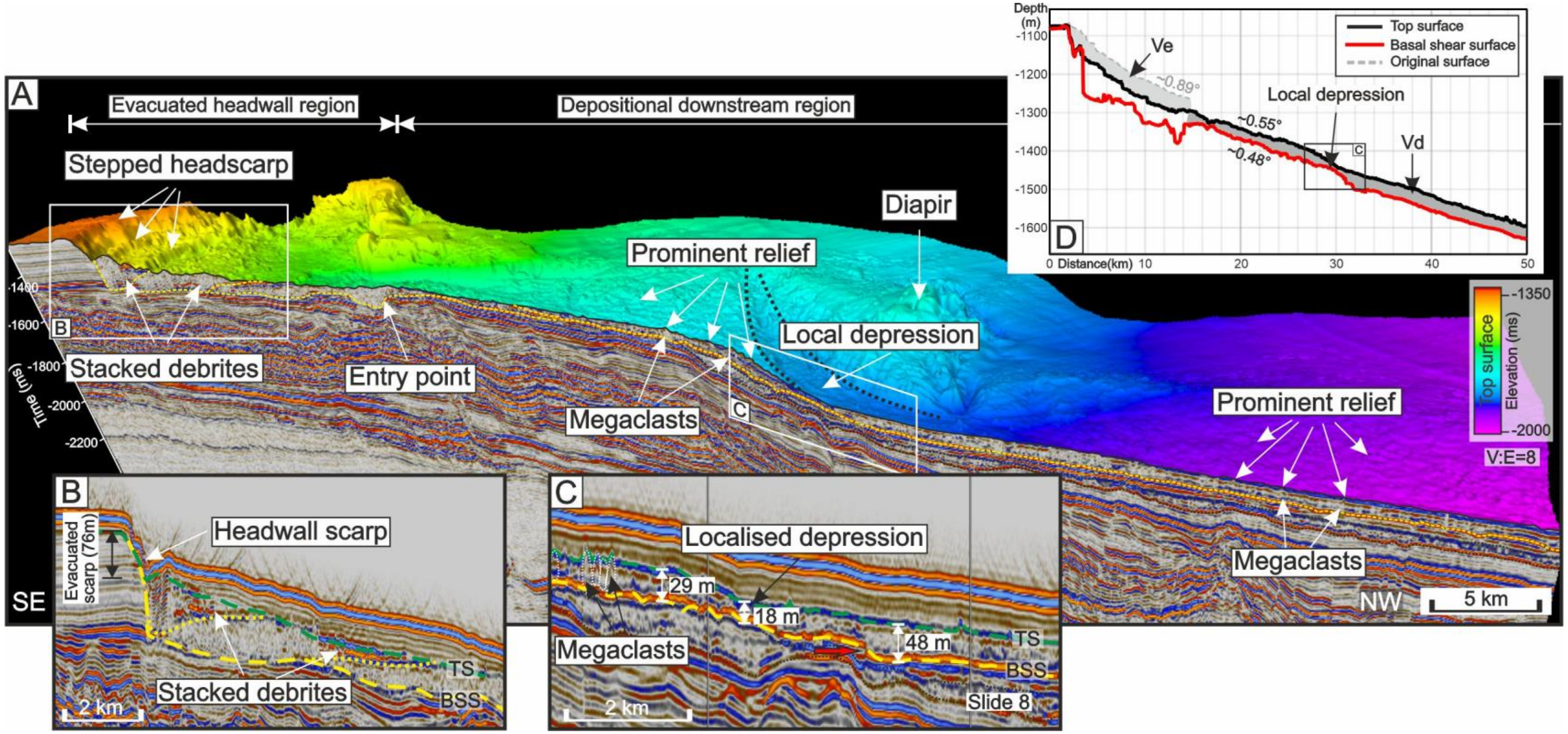
A
Evacuated headwall region
Depositional downstream region
Stepped headscarp
Prominent relief
Diapir
Local depression
Stacked debrites
Entry point
Megaclasts
Prominent relief
Megaclasts
SE
NW
5 km
Time (ms)
-1400
-1600
-1800
-2000
-2200
Top surface
Elevation (ms)
-1350
-2000
V:E=8
B
Headwall scarp
Evacuated scarp (76m)
Stacked debrites
TS
BSS
2 km
C
Localised depression
29 m
18 m
48 m
Megaclasts
TS
BSS
Slide 8
2 km
D
Depth (m)
Top surface
Basal shear surface
Original surface
Ve
~0.89°
Local depression
~0.55°
~0.48°
Vd
Distance(km)
-1100
-1200
-1300
-1400
-1500
-1600
0
10
20
30
40
50

Figure 5-4: (A) Three-dimensional model, showing the topography of the top surface of the debrite and a SE-NW trending seismic section along the central axis. The top surface (TS) in Figure 5-4A represents a stratigraphic horizon that includes the top of the debrite but also extends across areas without debrite. It corresponds to the green dashed line on the seismic profiles in Figure 5-4B and Figure 5-4C. (B) Enlarged view of the seismic section in the headwall region, showing stacked debrites and the headwall scarp. (C) Enlarged view of the seismic section across the localised depression, illustrating the variations in debrite thickness. (D) Topographic profile of the seismic section, illustrating headwall sediment evacuation and downstream deposition. The red line and black line in Figure 5-4D represents the topography of the basal shear surface (BSS) and the TS, respectively. the light grey dashed line in Figure 5-4D indicates the reconstructed pre-failure surface, obtained by interpolating the youngest incised reflector. The light- and dark- grey shading in Figure 5-4D indicates the sediment loss in the headwall region and the sediment accumulation in the deposition zone, respectively. The yellow lines on sections 4A-4C represent the BSS. Light grey vertical lines in section 4C indicate an ~120° and ~160° change in the orientation of the section, respectively. Locations of sections 4A are shown in Figure 5-2A. Location of sections 4B is shown in Figure 5-4A. Location of section 4C is shown in Figure 5-3D and Figure 5-4A. Vertical exaggeration (VE) of sections 4A, 4B and 4C is 8:1.

5.5 Results

Nine submarine landslides are identified from the Bonaventure 3D and Thebe 3D datasets (Figure 5-1), and labelled Slide 5-13 from north to south following the nomenclature of Wu et al. (2023). These landslides are either directly exposed on the seafloor (i.e., Slide 5), shallowly buried (< 100 m), such as Slides 6-7 and 9-13, or relatively deeply buried (~120 m; i.e., Slide 8). Slide 9 is the focus of this study and was referred to as the Bonaventure complex I by Scarselli et al. (2013). Slide 9 overlies and locally incises into the much larger Slide 8 (Figure 5-2D). Between the base of Slide 9 and the top of Slide 8, there is an undisturbed seismic stratigraphic succession up to 46 m thick (Figure 5-2D). The intact slope adjacent to Slide 9 has a gradient of ~0.89° (Figure 5-4A).

5.5.1 Characteristics and interpretation of Slide 9

Description: Slide 9 covers an area of 560 km^2 and is characterised by its elongated shape (Figure 5-2A). The distal termination of Slide 9 lies beyond the limits of the Bonaventure 3D survey area (Figure 5-1B and Figure 5-3). Using the 2D seismic lines (Figure 5-3F), Slide 9 is up to 61 km long and ~8-9 km wide (Figure 5-1), with a length-to-width ratio of 7~8. The Slide 9 deposits are buried at ca. 55-95 mbsf, although the headwall region retains a clear seafloor expression (Figure 5-1B and Figure 5-2).

The updip region of Slide 9 exhibits a circular planform morphology, about 10 km in diameter, opening northwestward (Figure 5-2A and Figure 5-2B). Within the updip region, several high-amplitude reflectors truncate underlying reflectors and merge downslope into a stepped composite basal surface, which erodes up to 184 m of the substrate (Figure 5-2B and Figure 5-2C). The gradient of this basal surface is relatively gentle (~1°) in the northeast and steeper (3-4°) in the southwest (Figure 5-5A). The overlying chaotic seismic facies are Slide 9 deposits, which reach a thickness of 63 m in the northeast and are 39 m thick in the southwest (Figure 5-2B and Figure 5-5B).

Basinward, the basal surface evolves into a concave-up geometry, bounded by stepped lateral margins, which incise to depths of ~82 m (Figure 5-2D and Figure 5-3A). These lateral steps incise through underlying undisturbed strata down to the disturbed strata associated with the underlying Slide 8 (Figure 5-2D). The lateral steps have gradients of ~5°, in contrast to the regional slope outside the incision, which is gentler with the gradient only ca. 0.89° (Figure 5-4 and Figure 5-5A). The basal surface is ornamented by sub-parallel, elongate linear scours (on average ~2 km long and 130 m wide; Figure 5-3A), which are V-shaped in cross-section (Figure 5-2D). The seismic facies within Slide 9 are dominated by chaotic, low-amplitude seismic reflections (Figure 5-2D and Figure 5-3D). Locally, structurally coherent reflections form block-like bodies embedded within the chaotic seismic facies, which in some places are coincident with the end of the lineations (Figure 5-2D, Figure 5-3A and Figure 5-3C). The top surface of Slide 9 is rugose, with prominent areas of local relief (ca. 10-25 m; Figure 5-3B and Figure 5-3E), which are associated with the presence of block-like bodies (Figure 5-2D, Figure 5-3D and Figure 5-4A). The top surface is around 0.55°, slightly steeper than the basal surface (~0.48°; Figure 5-4A).

Interpretation: The composite erosional basal surface is interpreted as the basal shear surface to Slide 9. The basal shear surface passes basinward from a headwall with a circular planform to a surface with stepped lateral margins, forming an incisional channel-form feature. The linear structures that ornament the basal shear surface are interpreted as grooves, formed by substrate erosion (Gee et al., 2005; Bull et al., 2009). The consistent orientation of grooves reflects the downslope flow direction (e.g., Dakin et al., 2013; Peakall et al., 2020, 2024). The stepped incisional channel-form feature formed an axial conduit. The large, internally coherent blocks are interpreted as megaclasts entrained and transported with the flow (e.g., Moore et al., 1995; Jackson, 2011; Alves, 2015; Hodgson et al., 2019; Nwoko et al., 2020). Megaclasts exist at the end of grooves, and act as erosional tools to gouge the substrate in a laminar flow (Peakall et al., 2020). The combination of the grooves on the erosional basal shear surface and megaclasts in a downslope chaotic seismic facies supports the interpretation of Slide 9 as a submarine debrite, emplaced by a cohesive debris flow. The absence of through-going reflectors between top surface and basal shear surfaces further indicates that Slide 9 represents a single emplacement event, rather than a stacked composite of multiple flows. The stepped composite basal surface and the stacked debrites in the headwall region support retrogression during the evolution of the debris flow (Scarselli et al., 2013; Tang et al., 2022). The basal shear surface, grooves, and overlying deposits, are described and interpreted in more detail below.

5.5.2 Morphology of debrite lobes

Mapping the basal shear surface reveals sets of radiating grooves, which are partially preserved along the lateral margins adjacent to the deep incision by the basal shear surface (Figure 5-2A, Figure 5-3A and Figure 5-5A). Cross-cutting relationships between sets of grooves show an overall basinward stepping pattern (Figure 5-5A). Each radiating groove set is overlain by chaotic seismic facies. Thickness mapping reveals truncated lobate bodies, with thickness progressively increasing basinward within each lobate geometry (Figure 5-2D and Figure 5-5). Eight such groove sets and associated overlying chaotic facies are identified from their partial preservation at the lateral margins of Slide 9 (Figure 5-5B and Figure 5-6). The groove sets, seismic facies, and lobate bodies support their interpretation as submarine debrite lobes. These submarine debrite lobes are commonly connected upslope to the headwall region by the stepped conduit, which locally truncates the underlying reflectors (Figure 5-2D, Figure 5-5B and Figure 5-6). The stepped conduit differs from submarine channels that are long-lived and form through bypass by many sediment gravity flows (e.g., Peakall et al., 2000). The stepped lateral margin of the conduit, together with the underlying truncations supports progressive substrate incision by the debris flow.

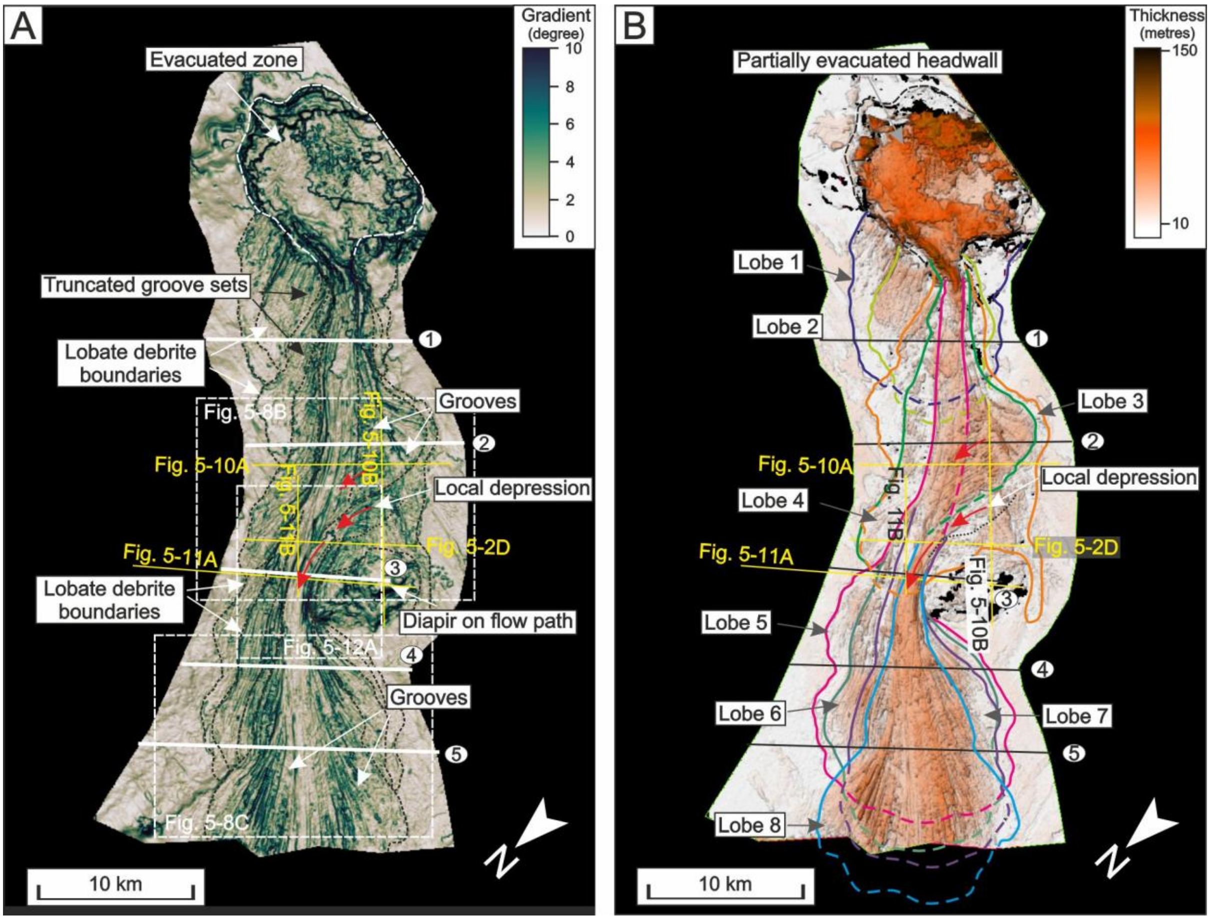

Figure 5-5: (A) Dip angle map of the basal shear surface, showing the variation in gradient of the basal shear surface, the distribution of grooves, and the boundaries of individual debrite lobes. (B) Thickness map of Slide 9, showing the spatial distribution of debrite thickness. Note, coloured dashed lines outline and distinguish individual debrite lobes. Red arrows indicate local collapse. The white, thick lines numbered 1-5 on Figure 5-5A and the black lines numbered 1-5 on Figure 5-5B indicate the locations of the topographic sections shown in Figure 5-7.

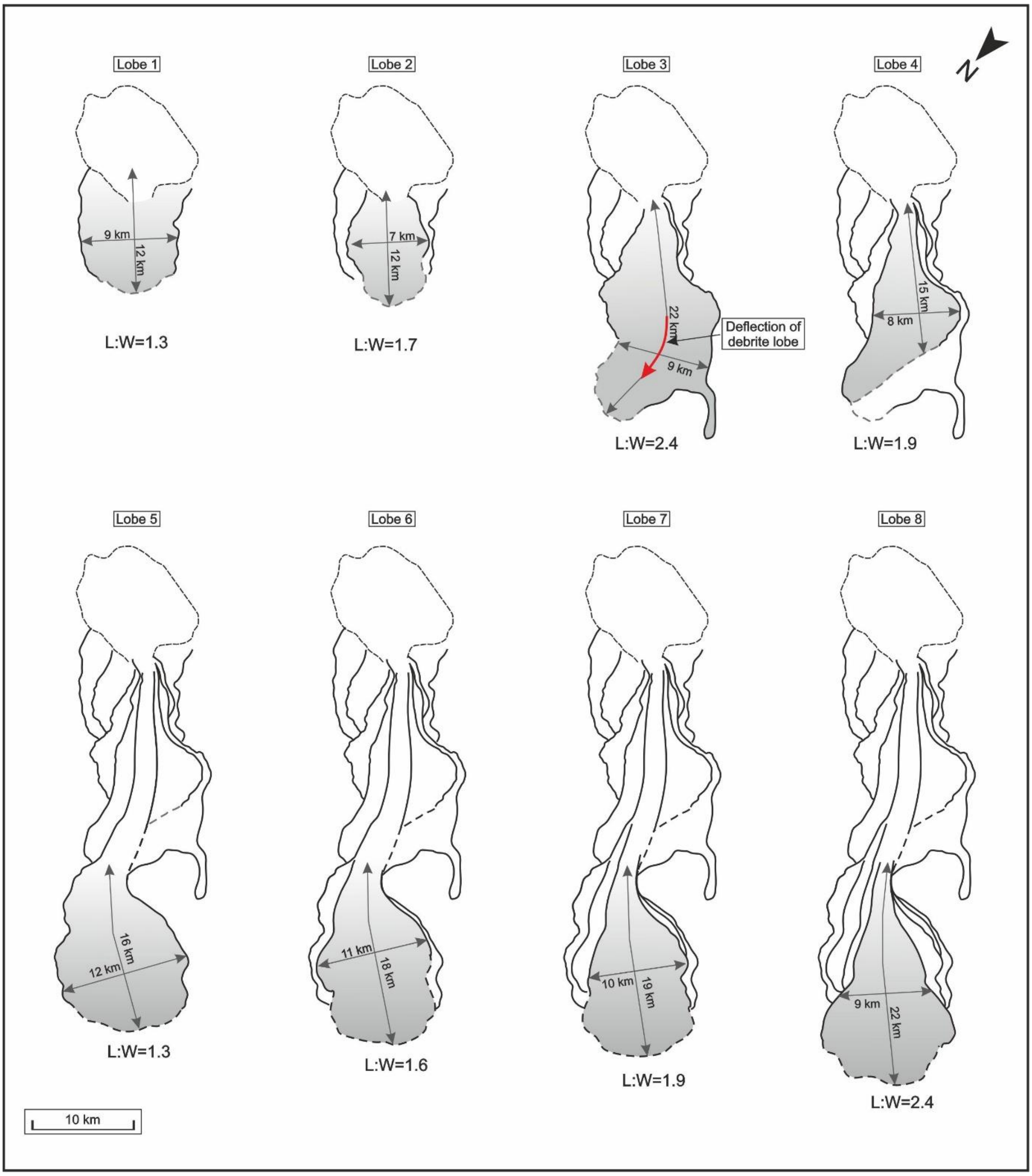

Figure 5-6: Mapping of debrite lobes, showing the geomorphology of individual debrite lobe (Lobes 1-8) and their progressive evolution. The grey lines along the central axis indicate the length (L) of the lobes, and the grey lines perpendicular to the central axis show lobe width (W). L:W is the length-to-width ratio of each lobe, though note that these are minimum values as lengths may be longer; dashed lines at the ends of the mapped lobes indicate that the lobes may extend further. Red arrows mark the deflection of Lobe 3.

The relative chronology of the debrite lobes can be reconstructed from their preserved geometry and cross-cutting relationships of groove sets (Figure 5-5 and Figure 5-6). Note that there is uncertainty in the reported values of length and width of the debrite lobes; the inferred distal end of the reconstructed lobes may have extended further, and the updip extent of individual debrite lobes is poorly constrained (see Figure 5-6 for details). The oldest debrite lobe (Lobe 1) occurs in the most upstream area, and measures approximately 12 km long (L) and 9 km wide (W) (length to width ratio (L:W) = 1.3; Figure 5-6). Lobe 1 is partially overlain by the thicker Lobe 2, which is 12 km long and 7 km wide (L:W = 1.7; Figure 5-5 and Figure 5-6). Lobe 3 is 22 km long and 9 km wide (L:W = 2.4), confined by the relief of a 50 m-high diapir in the southwest, and extends further downstream (Figure 5-3A, Figure 5-5 and Figure 5-6). Lobe 3 truncates pre-existing Lobe 1 and Lobe 2 groove sets and incises into the undisturbed substrate, forming a stepped morphology on the lateral margin (Figure 5-5A and Figure 5-7-1). Lobe 4 truncates the updip portion of the Lobe 3 groove set (Figure 5-5A), exhibits a stepped basal shear surface at its upstream end (Figure 5-7-1), but does not extend as far basinward as Lobe 3. Lobe 4 is around 15 km long and 8 km wide (L:W = 1.9; Figure 5-6), with ~8 m high relief on its northeastern lateral side (Figure 5-5B and Figure 5-7-2). Lobe 4 displays an asymmetric thickness distribution, with thicker deposits on the southwest lateral margin (43 m), than within the conduit (31 m; Figure 5-7-2). Upstream ~6 m of relief exists at the NE margin of Lobe 3 (Figure 5-7-1), and ~8 m of relief occurs downstream at the NE margin of Lobe 4 (Figure 5-7-2), recognised from the laterally preserved deposits.

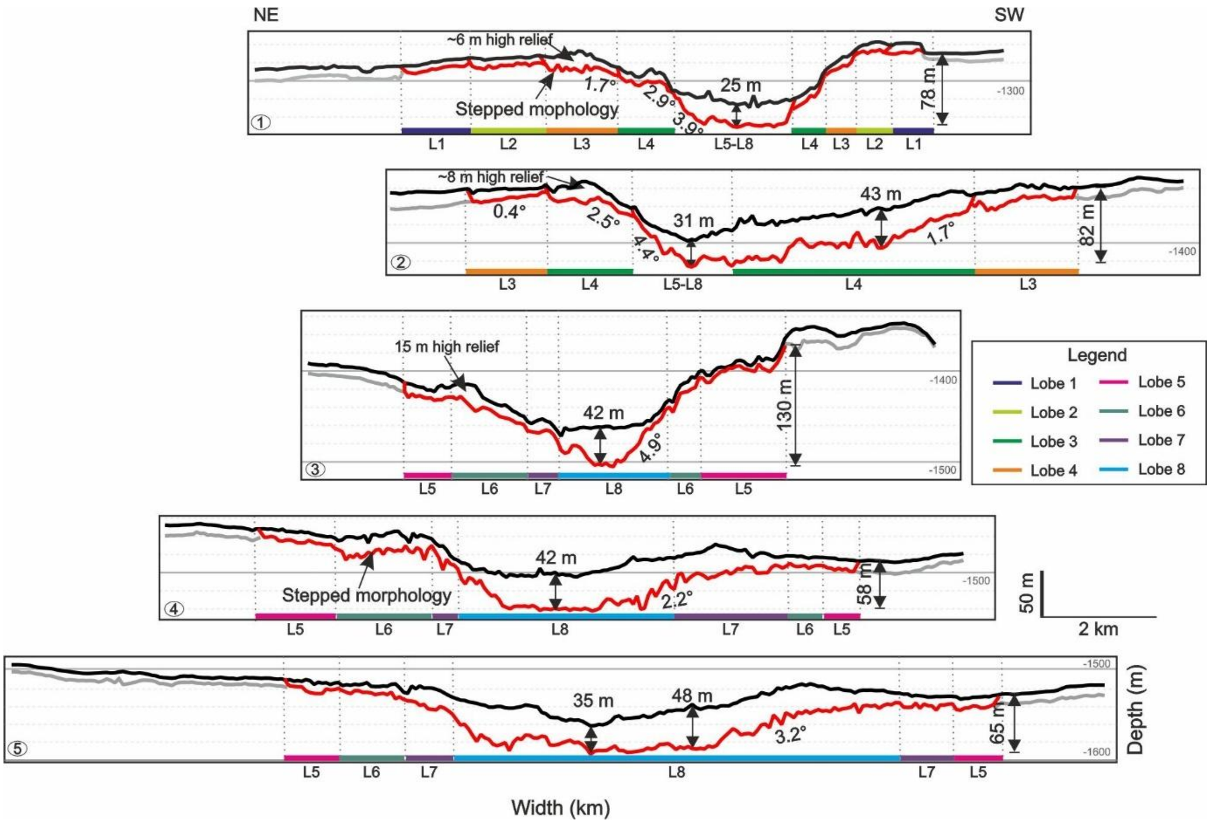

Figure 5-7: A series of cross-sections (profiles 1-5), showing the topography of the basal shear surface and the top surface, and illustrating downstream variations in the depth of substrate incision and the gradient of the basal shear surface. The profiles reveal the channel-like morphology of the basal shear surface. Red lines represent the topography of the basal shear surface, black lines correspond to the topography of the top surface, and grey lines represent the topography of the original strata. Outer vertical black arrows show the maximum depth of substrate incision, and the inner vertical black arrows show the thickness of debrites. Coloured bars at the base of each section identify the locations of the basal shear surface and the top surface for the corresponding lobe. L1-L8 signify Lobe 1 to Lobe 8. The locations of profiles 1-5 are shown in Figure 5-2A and Figure 5-5.

In the upstream area, the substrate incision increases axial-ward, from ~30 m at the base of Lobe 3 to ~40 m at the base of Lobe 4 (Figure 5-7-1). The gradients of the lateral margins increase axis-ward, from relatively gentle slopes (1.7°) under Lobe 3 to steeper margins of up to 2.9° under Lobe 4 (Figure 5-7-1). Whilst lobe length broadly increases from Lobes 1 to 4, deposit width systematically decreases, narrowing toward the central conduit-axis at the same location, such as from ~9 km in Lobe 1, to ~7 km in Lobe 2, ~5 km in Lobe 3 and ~4 km in Lobe 4 at upstream section 1 (Figure 5-7-1). These trends record the deepening of substrate incision, the narrowing of flow width, and the steepening of lateral margins, which indicate the axial-ward increase in confinement from Lobes 1 to 4. Within individual lobes, confinement decreases downslope, with the shallowing of the gradient of the lateral margin. For example, the lateral margin gradient in Lobe 3 decreases from ~1.7° in the uppermost part of the lobe (Figure 5-7-1) to near-horizontal (~0.4°) in downstream section 2 (Figure 5-7-2). A similar downslope reduction is observed in substrate incision. Substrate incision of Lobe 3 decreases from ~30 m in the uppermost part to ~15 m downstream, and in Lobe 4, incision decreases from ~40 m in the upstream section 1 to 30 m in the downstream section 2 (Figure 5-7-1 and Figure 5-7-2). The downstream reduction in substrate incision depth and lateral margin gradient, and the downstream increase in lateral depositional relief in individual lobes, indicate that substrate incision decreased downstream as each debrite lobe formed.

Downslope of the diapir, Lobes 5-8 form a basinward-stacked succession of elongate, debrite lobes linked to the axial conduit. Lobes 5-8 maintain comparable widths to upstream debrite lobes of ~9-12 km (Figure 5-5 and Figure 5-6), but their lengths are poorly constrained because of subsequent erosion and minimum lengths are provided. Lobe 5 is 16 km long and 12 km wide (L:W = 1.3; Figure 5-6). It truncates the substrate, with incision depths exceeding 50 m in the upstream part of the lobe (Figure 5-7-2) decreasing to ~10-20 m thick further downslope (Figure 5-7-5). The gradient of the lateral margin in Lobe 5 reaches up to 4.4° in the upstream area (Figure 5-7-2), and progressively flattens downstream (Figure 5-7-3 to -5). Lobe 6 is 18 km long and 11 km wide (L:W = 1.6; Figure 5-6). It incises through Lobe 5 into the underlying strata, exhibiting a stepped basal shear surface with substrate incision reaching ~60 m (Figure 5-7-3). Depositional relief of Lobe 6 is up to 15 m high on the northeastern margin in the middle part near the diapir (Figure 5-7-3 and Figure 5-7-4). Lobe 7 truncates Lobe 6 and extends 19 km in length and ~10 km in width (L:W = 1.9; Figure 5-5 and Figure 5-6). The most distal unit imaged in the 3D seismic cube, Lobe 8, is 22 km long and 9 km wide (L:W = 2.4; Figure 5-6). Its lateral slope gradients reach up to ~4.9° adjacent to the diapir (Figure 5-7-3), decreasing to 2-3° downstream (Figure 5-7-4 and Figure 5-7-5). The thickness of Lobe 8 slightly increases downslope, with maximum deposits from ~42 m near the diapir to ~48 m in the downslope area (Figure 5-7-4 and Figure 5-7-5). Lobe 8 is thicker on the lateral flanks (40-48 m thick) than in the central conduit (~35 m thick; Figure 5-7-5). The Slide 9 deposit extends another 16 km beyond the 3D seismic survey, where a debrite lobe (or lobes) younger than Lobe 8 further incised through undisturbed stratigraphy and into Slide 8 deposits (Figure 5-3F).

5.5.3 Types of Grooves and their Distribution

Two types of grooves are recognised on the basal shear surface (Figure 5-8). Type 1 grooves are km-scale in length, orient downstream, and present across the entire downstream basal shear surface (Figure 5-8 and Figure 5-9). Type 2 grooves are hundreds of metres long on average, preferentially developed on the lateral margins, and cross-cut Type 1 grooves (Figure 5-8 and Figure 5-9).

Type 1 grooves (downstream grooves) are distributed from the headwall region across the entire basal shear surface (Figure 5-8A). Individual grooves range from 0.4 to 7.2 km in length (average ~2 km long; Figure 5-9A) and are around 130 m wide and 15 m deep (Figure 5-2D). Their dominant NW-SE orientation indicates a northwestward transport direction of the debris flow (Figure 5-9B). Megaclasts identified at the end of Type 1 grooves (Type 1 megaclasts) are typically ~100-130 m wide and ~30-40 m thick (Figure 5-2D). Some can be up to 150 m wide and 50 m thick (Figure 5-10A). Type 1 megaclasts have deformed internal reflections (Figure 5-2D, Figure 5-10A and Figure 5-10B), indicating they were subjected to compression and/or shear stress during transport by the flow (Jackson, 2011; Gamboa and Alves, 2015; Li et al., 2023).

Type 2 grooves (lateral grooves) are preferentially identified on the lateral margins of the basal shear surface. These grooves are 100 m long on average and crosscut the Type 1 grooves at angles ranging from 45° to near 90° (Figure 5-8). Type 2 grooves are best developed in three sets: Set 1, located on the southwest margin of the mid-downstream area adjacent to the diapir (Figure 5-8B); Set 2, distributed along the northeast margin of the lower downstream area; and Set 3, situated on the southwest margin of the lower downstream area (Figure 5-8C).

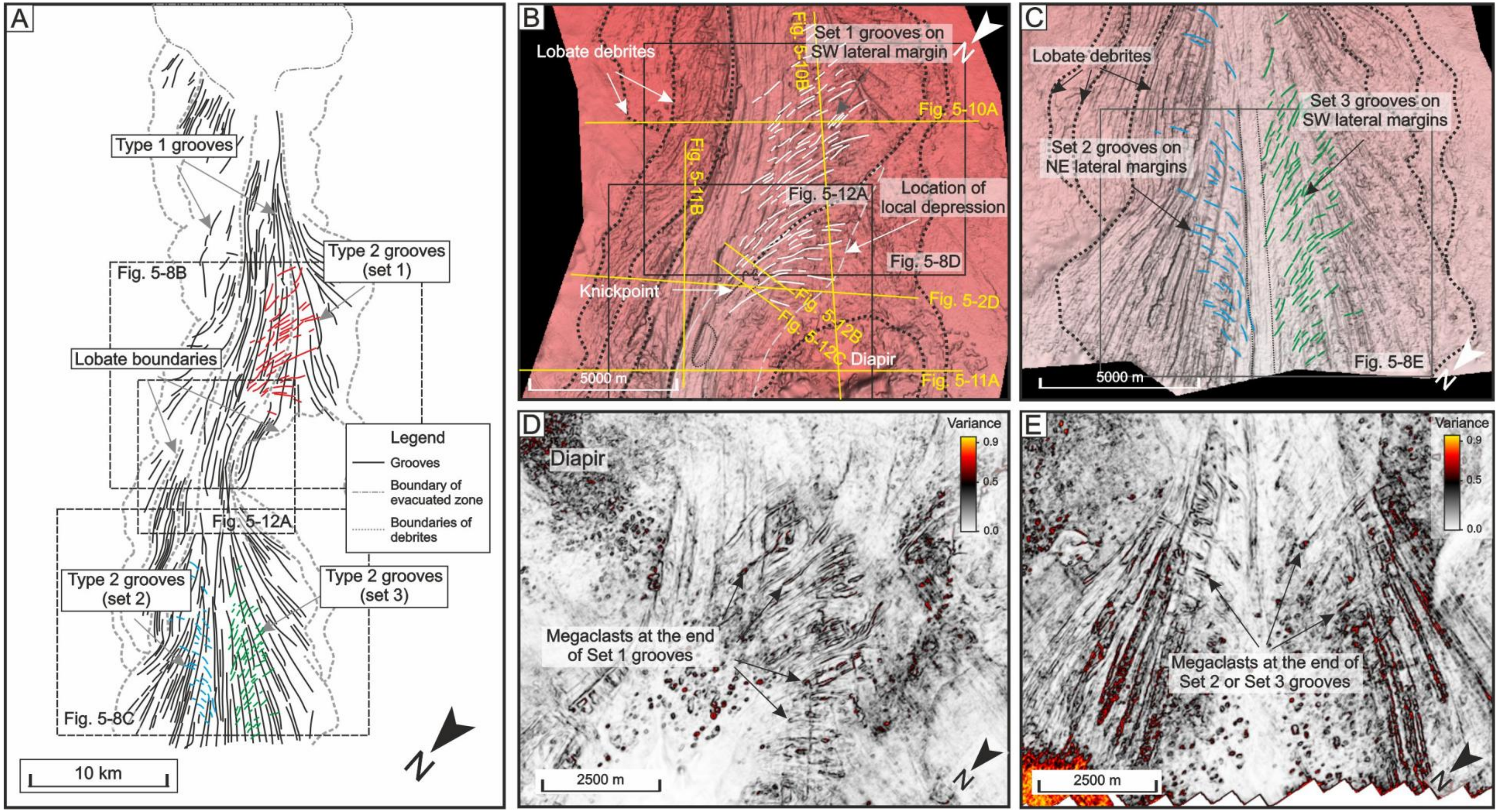
A
Type 1 grooves
Type 2 grooves (set 1)
Fig. 5-8B
Lobate boundaries
Legend
Grooves
Boundary of evacuated zone
Boundaries of debrites
Fig. 5-12A
Type 2 grooves (set 2)
Type 2 grooves (set 3)
Fig. 5-8C
10 km
N
B
Lobate debrites
Set 1 grooves on SW lateral margin
Fig. 5-10B
Fig. 5-10A
Fig. 5-11B
Fig. 5-12A
Location of local depression
Fig. 5-8D
Knickpoint
Fig. 5-2D
Fig. 5-12B
Fig. 5-12C
Diapir
Fig. 5-11A
5000 m
C
Lobate debrites
Set 3 grooves on SW lateral margins
Set 2 grooves on NE lateral margins
Fig. 5-8E
5000 m
D
Diapir
Variance
0.9
0.5
0.0
Megaclasts at the end of Set 1 grooves
2500 m
E
Variance
0.9
0.5
0.0
Megaclasts at the end of Set 2 or Set 3 grooves
2500 m

Figure 5-8: (A) Sketch map showing the distribution and orientation of two types of grooves (i.e., Type I and Type 2) on the basal shear surface, reflecting the lobate distribution of the debrite (Slide 9). Plan view of the basal shear surface in the middle (B) and downstream (C) areas, showing the distribution of three sets of Type 2 grooves and the lobate distribution of debrites. The variance maps at 1780 ms (D) and 1980 ms (E), show the spatio-temporal correlation between Type 2 grooves and megaclasts. Note that four sets of grooves are shown in Figure 5-8, including Type 1 grooves (downstream type) labelled by black lines in Figure 5-8A, and three sets of Type 2 grooves on the lateral margins. Type 2 groove sets consist of those on the southeast side in the updip part of the debrite (Set 1, labelled by red lines in Figure 5-8A, and labelled by white lines in Figure 5-8B), the grooves on the northwest side downdip (Set 2, labelled by blue lines in Figure 5-8A and Figure 5-8C) and the one on the northwest side downdip (Set 3, labelled by green lines in Figure 5-8A and Figure 5-8C). The location of Figure 5-8B and Figure 5-8C are shown in Figure 5-2A, Figure 5-3A and Figure 5-8A. The line for Figure 5-11A and the location for Figure 5-12A are partly visible in Figure 5-8B due to figure extent; the full line for Figure 5-11A is shown in Figure 5-2A, and the full location for Figure 5-12A is shown in Figure 5-2A, Figure 5-3A and Figure 5-8A.

Set 1 grooves developed upstream of the diapir (Figure 5-8B and Figure 5-8D), and reach up to 2.4 km in length (average 800 m; Figure 5-9A). They orient towards the deepest part of the basal shear surface and crosscut the pre-existing Type 1 grooves with an angle of ~45° on the lateral margin (Figure 5-8D and Figure 5-9B). Adjacent to the diapir, the orientation of Set 1 grooves gradually changes from ~S-N to SE-NW towards the conduit (Figure 5-8B and Figure 5-9B). Downstream on the northeast margin, Set 2 grooves typically range from 170 m to 880 m in length (average ~460 m), and curve from a high angle (~40°) to Type 1 grooves to sub-parallel with the Type 1 grooves towards the deepest part of the basal shear surface (Figure 5-8C, Figure 5-8E and Figure 5-9). Set 3 groove lengths on the southwest margin range from 210 m to 1.5 km long (average 490 m; Figure 5-9A), and also curve from a high angle (45°) to Type 1 grooves, from S-N to SE-NW towards the deepest part of the basal shear surface (Figure 5-8C, Figure 5-8E and Figure 5-9B). Megaclasts at the end of Type 2 grooves are typically 150-170 m wide (up to 250 m) and 40-55 m high (Figure 5-10B), and exhibit deformed to transparent internal reflections (Figure 5-10A).

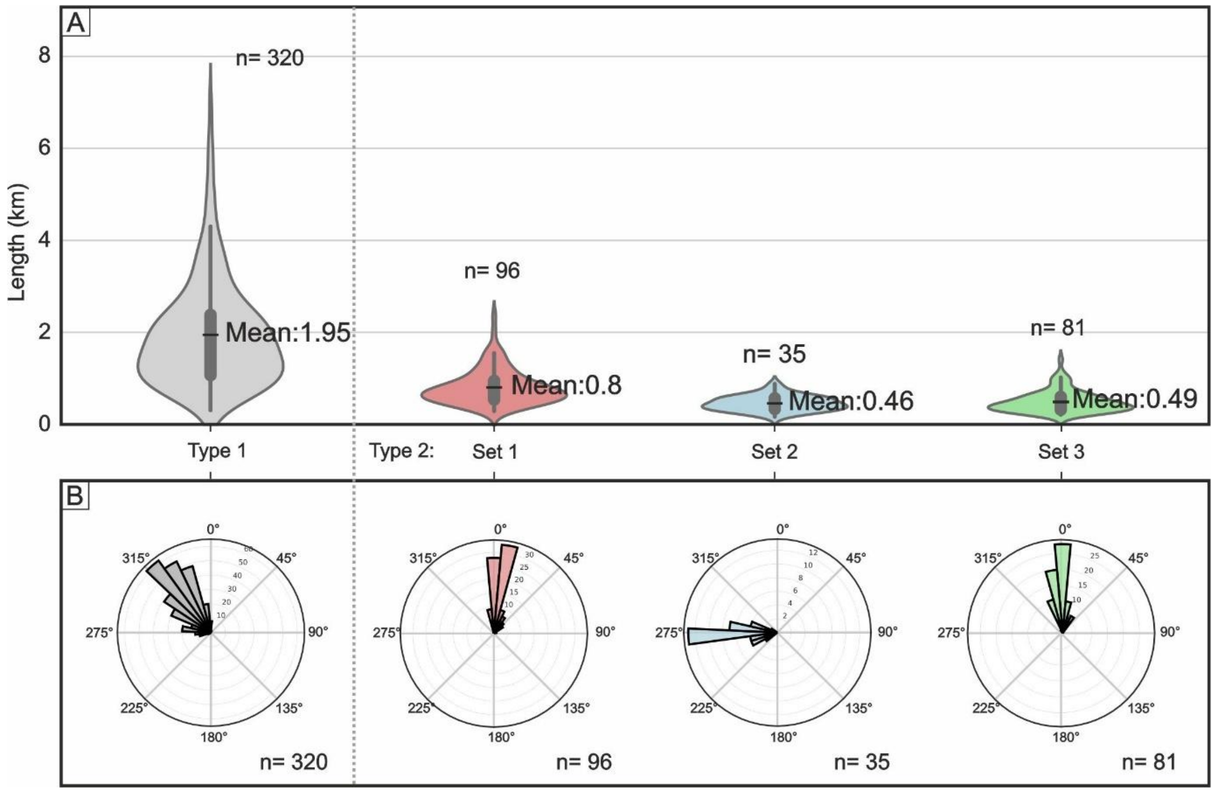

Figure 5-9: (A) Violin plots showing the length distribution in respect to each groove type and set. The width of each individual plot represents the density of length, while the central vertical grey box and whiskers display the interquartile range and overall spread of the length. Black short horizon lines in violin plots show the mean value of groove length. Lower capital *n* means the number of grooves. (B) Rose diagrams showing the orientation of grooves. Note that four sets of grooves are shown in Figure 5-9, including Type 1 grooves (downstream type) labelled in grey, and three sets of Type 2 grooves on the lateral margins, including those on the southeast side in the updip part of the debrite (Set 1, labelled by red lines in Figure 5-9), the grooves on the northwest side downdip (Set 2, labelled by blue lines in Figure 5-9) and the one on the northwest side downdip (Set 3, labelled by green lines in Figure 5-9).

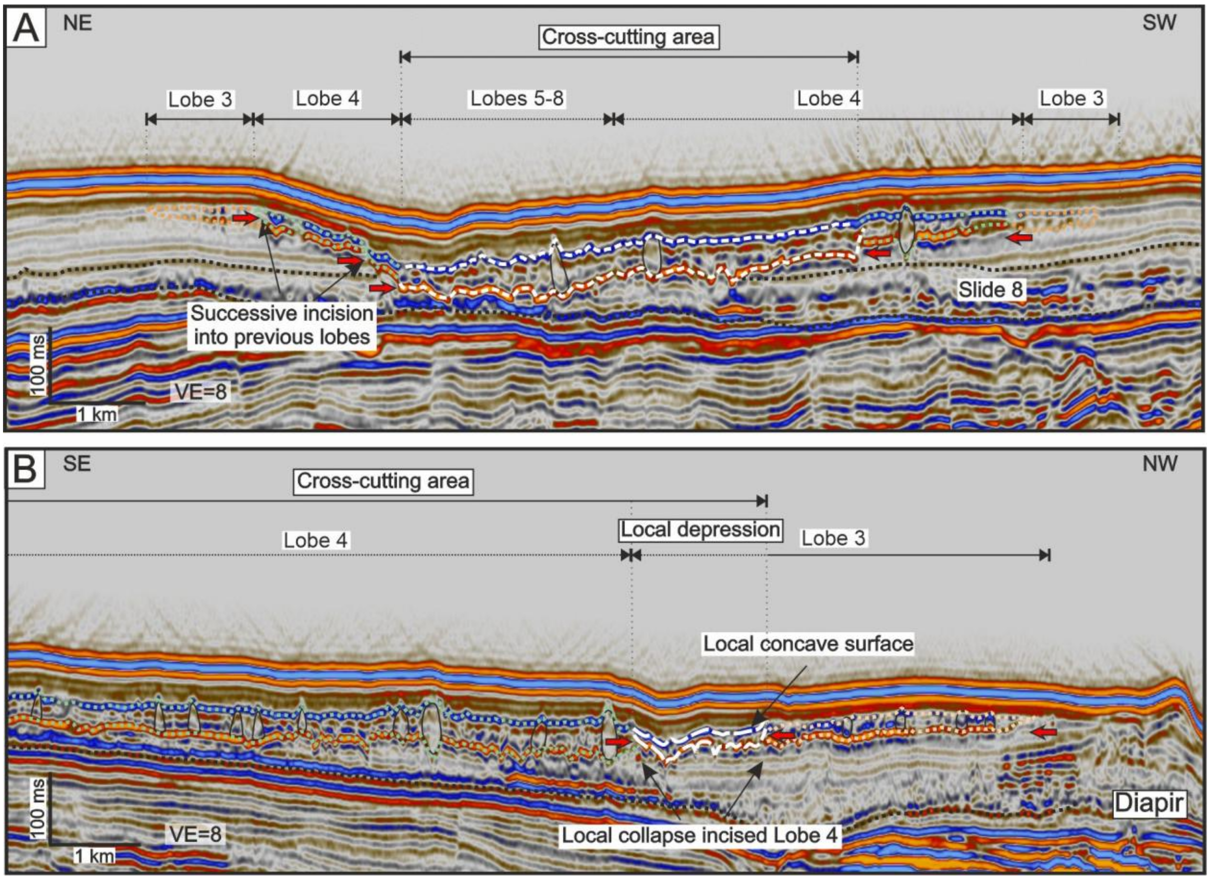

Figure 5-10: (A) SE-NE seismic section in the upstream area, showing the cross-cutting (Type 2) area, the progressive axial-ward narrowing of debrite lobes (Lobes 3-8), the stepped basal shear and substrate incisions. (B) SE-NW seismic section adjacent to the diapir, showing the cross-cutting (Type 2) area, the truncation of pre-existing lobes (Lobes 3 and 4) by the localised collapse. Note that the dotted lines with different colours indicate the boundaries of debrite lobes (Lobes 3-4), the white short dashed lines on section 5-10A reflect the location of the cross-cutting area, the white long dashed lines on section 5-10B reflect the location of the local depression, and the black dotted lines outline the boundaries of Slide 8. The red horizontal arrows with black outlines show substrate incisions. Vertical exaggeration (VE) is 8:1. The location of the sections in Figure 5-10A and Figure 5-11B are shown in Figure 5-2A, Figure 5-5 and Figure 5-8B.

5.5.4 Debris flow incision

The debrite can be divided into the partially evacuated headwall region and the depositional downstream region (Figure 5-4). The headwall scarp is 184 m deep (Figure 5-2C), indicating the substantial entrainment of substrate during initial failure. Its stepped morphology suggests a component of retrogressive collapse (e.g., Deptuck et al., 2007; Sawyer et al., 2009; Elverhoi et al., 2010; Barrett et al., 2021). Although a ~60 m thick deposit of remobilised sediment is preserved in the headwall region (Figure 5-5B), a much larger volume was evacuated and transported basinward, forming an evacuated scarp in the headwall region up to 76 m high (Figure 5-4). In the depositional zone, the debrite in the central conduit thickens downslope from ~25 m thick near the transition zone to ~30-35 m thick in the distal area, with two thicker areas reaching >40 m (Figure 5-3D). Reflector truncations beneath the basal shear surface indicate the flow incised into Slide 8 (Figure 5-2D). The depth of incision overall decreases downstream, from ~80 m in the upstream region (Figure 5-7-1 and Figure 5-7-2) to 58-65 m in the downstream area (Figure 5-7-4 and Figure 5-7-5), with a local increase adjacent to the diapir to a maximum of 130 m (Figure 5-7-3).

To quantify substrate entrainment, the volume of evacuated sediments (Ve) in the headwall region and the volume of deposited sediments (Vd) in the deposition zone are calculated, following the method of Nugraha et al. (2022). To estimate Ve, the pre-failure surface is reconstructed through extrapolating the youngest incised reflector using the form of the adjacent intact slope (0.89°; Figure 5-4). Vd can be calculated from the volume between the top surface and basal shear surface in the depositional zone. The volume of evacuated sediments within the 3D seismic volume is 4.67 km^3, and the volume of deposited sediments is 12.89 km^3. Therefore, the deposit volume of the debrite is at least three times greater than its evacuated mass in the headwall region (i.e., $Vd/Ve \approx 3$), implying that most of the material comprising Slide 9 is derived from substrate entrainment during emplacement of the debris flow.

5.5.5 Changes near the diapirs

Two diapirs are present along the northeast and southwest margins of the debrite (Figure 5-1), and formed seafloor relief at the time of Slide 9 emplacement of up to 120 m in the northeast (Figure 5-11A) and 50 m in the southwest (Figure 5-3A). The northeast diapir is located ~5 km away from the debrite, whereas the southwest diapir lies on the transport pathway of the debris flow, and formed a local upstream facing slope on the seafloor, up to 5.1°, at the time of Slide 9 (Figure 5-11A).

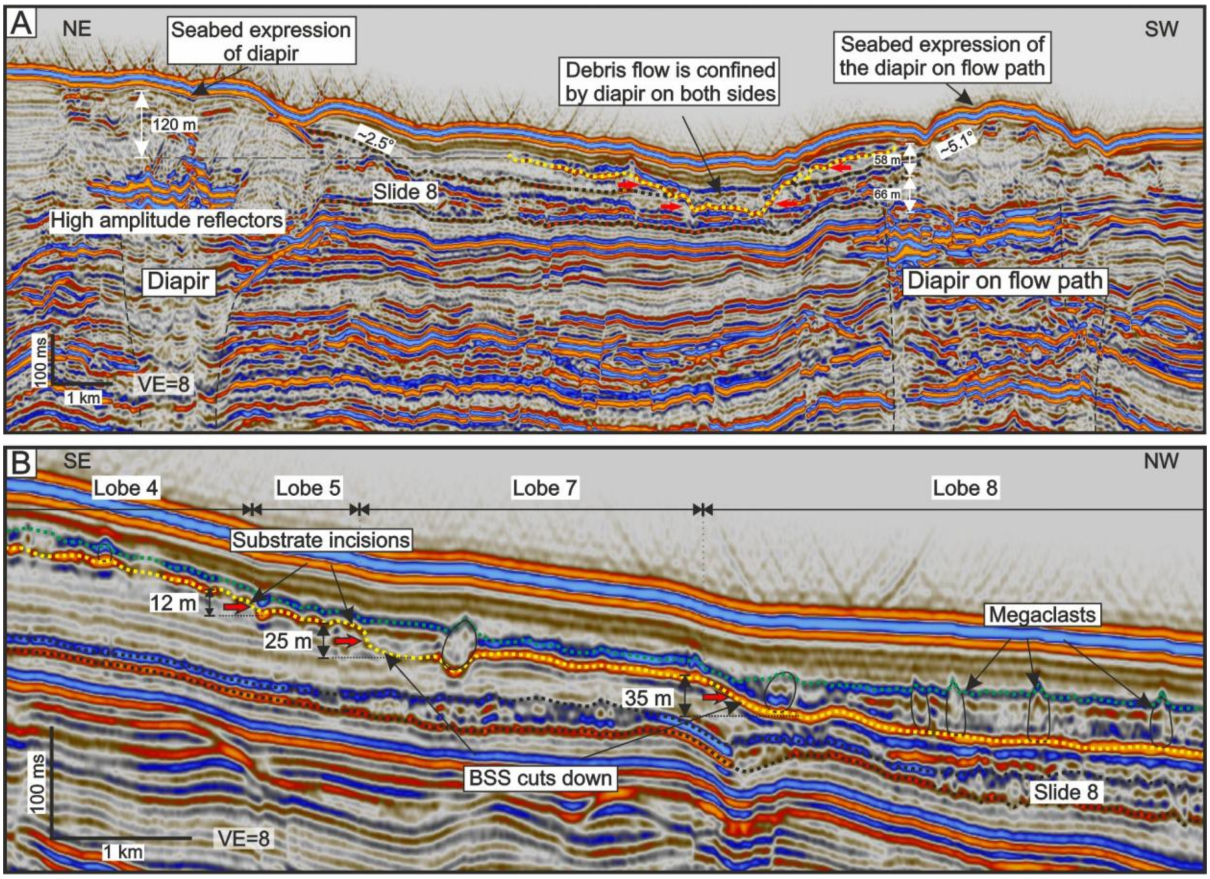

Figure 5-11: (A) NE-SW seismic section, showing diapirs in the northeast and southwest, the stepped basal shear surface that narrows toward central axis, and the confinement of the debris flow by the diapirs. (B) SE-NW seismic section adjacent to the SW diapir, showing increasing substrate incision and progressive deepening of basal shear surface on an obliquely cutting line from the flank towards the central axis near the diapir. Note, yellow dotted lines represent the basal shear surface of the debrites (Slide 9), the green dotted line marks the top surface of the debrites, and black dotted lines outline the boundaries of Slide 8. The red horizontal arrows show substrate truncations. In Figure 5-11A, the vertical white arrows show the depth of substrate incision, and the vertical black line indicates the depth of seabed expression of the diapir in the SW. The vertical black lines in Figure 5-11B show the depth of substrate incision. The location of sections is shown in Figure 5-2A, Figure 5-5 and Figure 5-8B. Vertical exaggeration (VE) is 8:1.

Lobe 3 exhibits a more complex geometry than other lobes, with a finger-like extension on the southwestern side of the diapir (Figure 5-5B and Figure 5-6). This extension records a small part of the flow that maintained its original trajectory, surmounted the ramp created by the diapir, and deposited material on the southwestern side of the diapir (Figure 5-5B). The top surface of the debrite displays an elongate depression adjacent to the upstream margin of the diapir (Figure 5-3E and Figure 5-4A). Here, the basal shear surface truncates Lobe 3 (Figure 5-10B), and is confined by Lobe 4 (Figure 5-12A and Figure 5-12B). The basal erosive surface features a prominent multiheaded scour that steps down basinward and is ~400 m wide and ~ 16 m deep, which has migrated at least 1 km updip (Figure 5-8B, Figure 5-12A and Figure 5-12C). This feature is identified as a knickpoint. The eroded area lacks the large Type 1 grooves identified elsewhere on the basal shear surface of the conduit (Figure 5-8B and Figure 5-12A). The upper surface of Lobe 3 is characterised by an elongate depression that extends down the lateral slope and some distance along the main conduit (Figure 5-3E and Figure 5-4C). The depression reflects that the thickness of the debrite is only ~18 m, thinner than in the adjacent upstream and downstream areas (Figure 5-3D and Figure 5-4A).

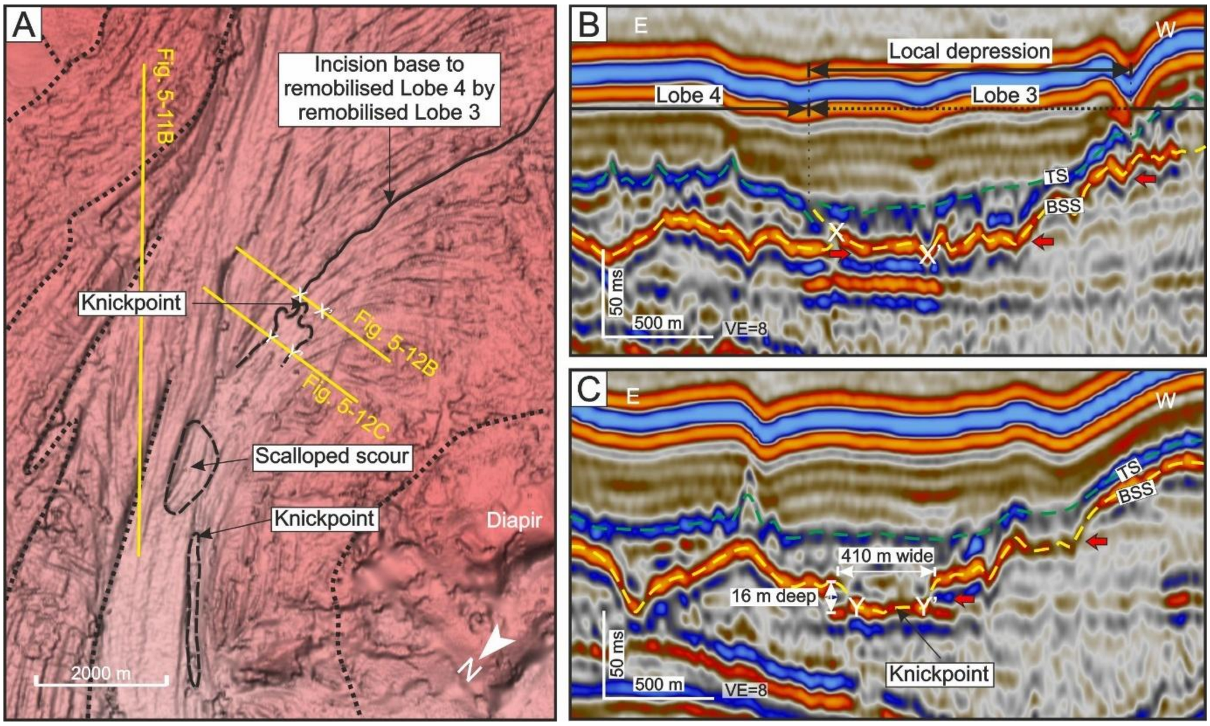

Figure 5-12: (A) Plan view of the basal shear surface adjacent to the diapir, demonstrating the location of knickpoints and the spatial extent (black line) of where remobilised Lobe 4 is eroded by remobilised Lobe 3. (B) A E-W crosscutting section, showing the remobilised Lobe 3 incising into remobilised Lobe 4. (C) A E-W section crosscutting the knickpoint. Note, yellow dotted lines in Figure 5-12B and Figure 5-12C represent the basal shear surface of the debrites (Slide 9), the green dotted line in Figure 5-12B and Figure 5-12C marks the top surface of the debrites, and black dotted lines outline in Figure 5-12A the boundaries of Slide 8. The red horizontal arrows show substrate truncations. The location for Figure 5-12A is shown in Figure 5-2A, Figure 5-3A and Figure 5-8A. The locations of sections 5-12B and 5-12C are shown in Figure 5-8B and Figure 5-12A. Vertical exaggeration (VE) is 8:1.

Within the central area between two diapirs (Figure 5-1B and Figure 5-11A), substrate incision reaches its maximum depth of ~130 m (Figure 5-7-3), more than twice the downstream incision depth (58 m; Figure 5-7-4). The lateral margin gradient steepens near the diapir, reaching approximately 4.9° (Figure 5-7-3), compared to 1.7° and 2.2°

in adjacent upstream and downstream areas, respectively (Figure 5-7-2 to Figure 5-7-4). The incisional conduit is ~1 km wide in the diapiric zone, narrower than both upstream and downstream where it is >2 km (Figure 5-5, Figure 5-7 and Figure 5-11A). Lobes 5-8 develop downstream of this diapiric area, and progressively truncate the substrate along the conduit axis, with incision depths increasing downstream from 12 m in Lobe 5, to 25 m in Lobe 7, and to 35 m in Lobe 8 (Figure 5-11B). The seismic facies within the downstream lobes are characterised by chaotic, low-amplitude seismic reflections, and are like those observed in the upstream debrite lobes (Figure 5-4A and Figure 5-11B).

The similarity in seismic facies, systematic spatial variations in lobe orientation, incision depth, lateral slope gradients, and complex basal shear geometry, suggest that the downstream debrite lobes were sourced from the headwall region and were strongly influenced by diapir-related topography. This interpretation implies that the downstream lobes, in particular Lobes 6-8, whose lateral margins can be traced to the diapir area, utilised the updip conduit that developed during the formation of Lobe 5. The deposits of Lobes 6-8 are at progressively lower elevations, with marked steps in their basal surfaces (Figure 5-11B), and they narrow towards the conduit, suggesting that the conduit continued to deepen and remained open during the emplacement of Lobes 6-8 (Figure 5-7-3 to -5, and Figure 5-11B).

5.6 Discussion

5.6.1 Self-confinement of submarine debris flows

The orientation and cross-cutting relationship of groove sets, the stepped geometry of the basal shear surface, the downstream stacking pattern of debrite lobes, and the three-fold increase in flow volume can be used to reconstruct the evolution of the debris flow. The overall basinward stacking of the debrite lobes, as evidenced by an increase in run-out distance and length-to-width ratio (Figure 5-6), indicates progressive elongation of the debris flow through time. The debrite lobes are truncated by the stepped basal shear surface (Figure 5-2D and Figure 5-10A), which suggests that the debris flow deepened and narrowed through time forming the axial conduit that remained largely empty. What factors drove this systematic lengthening and deepening of the debris flow on such a gentle slope (<1°)?

During the initial failure, the unstable sedimentary succession in the headwall region generated unconfined debrite lobes (Lobes 1 and 2). The occurrence of well-developed grooves and associated megaclasts within the earliest depositional lobes (Lobes 1 and 2; Figure 5-5A) indicates early-stage basal shearing and internal deformation characteristic of debris flow motion. The presence of grooves and megaclasts in the debrite lobes immediately downstream of the headwall region (only ~500 m away) suggests a rapid downstream flow transformation from headwall collapse to debris flow (e.g., Gee et al., 2006; Gamberi et al., 2011). These early debrite lobes built up depositional relief on the gentle underlying slope (Figure 5-5B, Figure 5-7-1 and Figure 5-7-2; e.g., Laberg and Vorren, 1995; Johnson et al., 2012; Martínez-Doñate et al., 2021). As the flow continued, fed by retrogressive headwall failures, successive debrite lobes stacked in an overall basinward pattern with the flow being steered by its own initial depositional topography (Bernhardt et al., 2012; Ortiz-Karpf et al., 2017; Martínez-Doñate et al., 2021). These subsequent depositional events incrementally built-up seafloor topography, which in turn controlled the routing of the flow. Once laterally confined by its initial depositional relief, the flow became narrower and thicker, as evidenced by the stepped conduit during the formation of Lobes 1-5 (Figure 5-7-1, Figure 5-7-2 and Figure 5-10A), and the deposition of lobes at progressively lower elevations, also characterized by steps, in Lobes 6-8 (Figure 5-11B). Narrowing and deepening would cause increased momentum, enhanced velocity, and greater basal shear stresses, leading to substrate incision even on a gentle slope (cf. Whipple and Dunne, 1992; de Haas et al., 2016, for subaerial debris flows, albeit on orders of magnitude smaller scales).

Once incision is initiated, the deepened and narrowed conduit further restricts lateral spreading of the flow. Limited lateral dispersion, and a relatively thick flow (cf. Whipple and Dunne, 1992), amplify erosional efficiency resulting in positive feedback of confinement and erosion. Substrate entrainment by the submarine debris flow likely further increased flow momentum and velocity (Gee et al., 1999, 2001; Iverson et al., 2010; Hodgson et al., 2019; Nugraha et al., 2022). The progressive axial-ward deepening of lateral truncations on the stepped basal shear surface, from flat in initial unconfined lobes (Lobes 1 and 2) to 30-40 m deeper in subsequent confined lobes (Lobes 3 and 4; Figure 5-7-1), further reveals the progressive increase in confinement and erosive capacity of the debris flow through time. Unlike long-lived submarine channels, this stepped feature was not a long-lived conduit, but rather represented a transient erosional feature formed by a highly erosive submarine debris-flow event (e.g., Dakin et al., 2013). Enhanced erosion may have driven retrogressive failure in the headwall, enlarging the flow volume and magnitude by incorporating more debris from the surrounding area.

The debris flow became increasingly confined through a combination of initial lateral depositional relief and progressive axial incision, leading to the stepped conduit developing (Figure 5-13A to Figure 5-13C). This autogenic behaviour of positive feedback during debris flow-deposit interactions is called self-confinement. I postulate that it is self-confinement that explains how the flow travelled such a long way even on low gradient (<1°) slopes, despite the initial failure volume being small relative to the other mass transport deposits in the area (such as Slide 8 in Figure 5-1B).

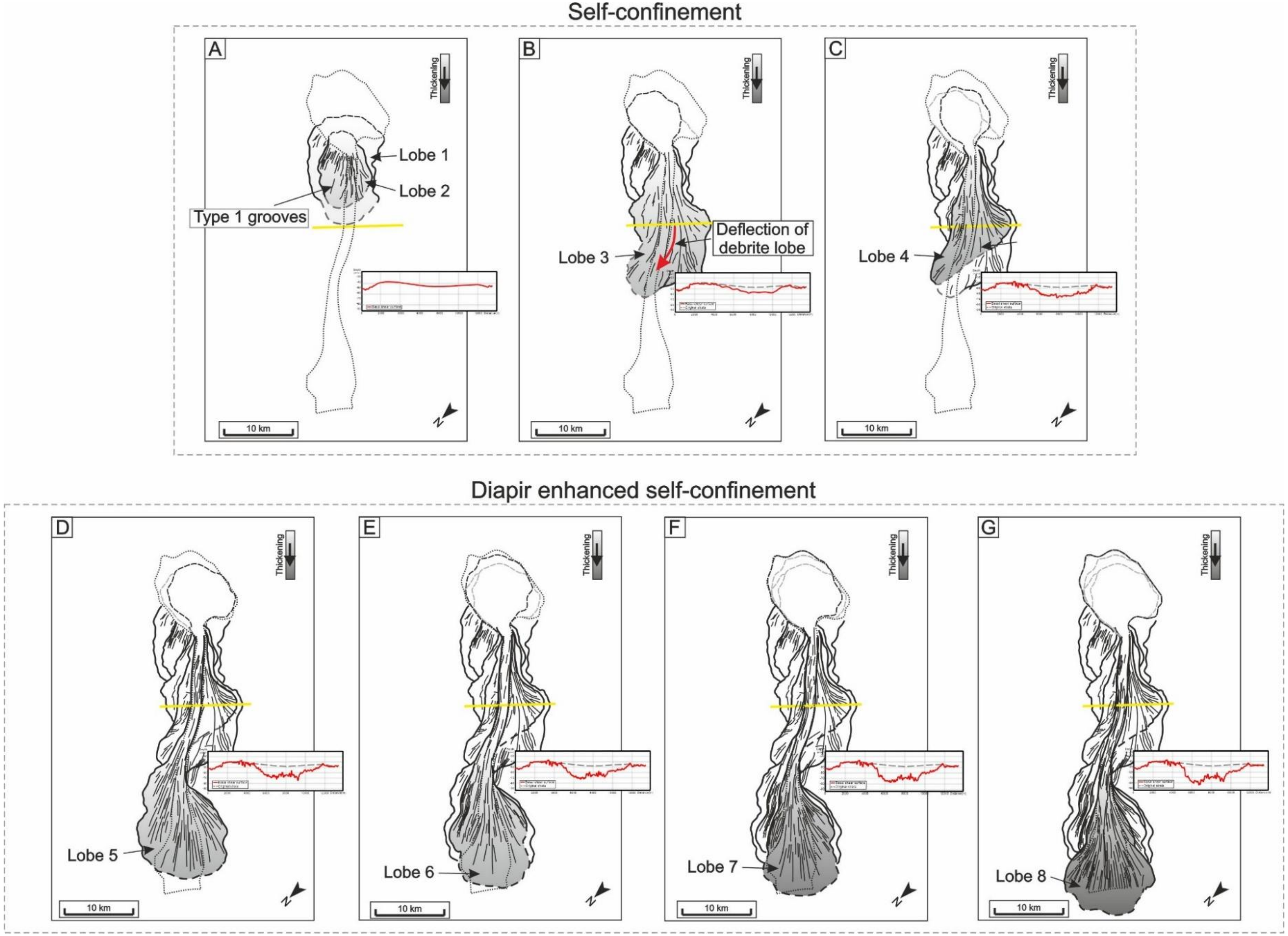
Self-confinement
A
Thickening
Lobe 1
Lobe 2
Type 1 grooves
10 km
B
Thickening
Deflection of
debrite lobe
Lobe 3
10 km
C
Thickening
Lobe 4
10 km
Diapir enhanced self-confinement
D
Thickening
Lobe 5
10 km
E
Thickening
Lobe 6
10 km
F
Thickening
Lobe 7
10 km
G
Thickening
Lobe 8
10 km

Figure 5-13: Conceptual model illustrating the progradational evolution of debrite lobes, the stepped axial-ward narrowing of the basal shear surface, the retrogressive headwall development, and the formation of Type 1 (downstream) and Type 2 (cross-cutting) grooves. The progradational evolution of debrite lobes is divided into two stages: (A-C) a self-confining stage on a gentle slope, and (D-G) a diapir enhanced self-confinement stage. Inset profiles reflect the progressive axial-ward deepening and narrowing of the basal shear surface during the evolution of the system. In the inset profiles, red curves represent the topography of the basal shear surface, and grey dashed lines indicate the topography of the original strata before failure. Thin black lines mark the Type 1 grooves. The grey dashed lines in the headwall region indicate the headwall steps formed during retrogressive headwall evolution. The black dashed lines at the ends of the mapped lobes indicate that the lobes may extend further.

5.6.2 Enhanced substrate incision: the influence of a diapir on flow evolution

The overall decreases in substrate incision downstream, from ~80 m to ~60 m (Figure 5-7), and associated thickening of the debrite (Figure 5-5B), reflects that deposition became dominant due to friction loss. An exception to this trend is in the central area between two diapirs, where substrate incision reached 130 m deep, more than twice that observed further downstream (58 m; Figure 5-7-3 and Figure 5-7-4).

The presence of the two diapirs with 50-120 m seafloor relief, particularly the one to the southwest located on the flow pathway, is interpreted to have perturbed the flow (Figure 5-2A and Figure 5-5). The southwestern diapiric relief acted as a topographic barrier, and precluded flow deflection to the southwest (Figure 5-13B; cf. Gee et al., 2001), although some of Lobe 3 did deposit on the southwestern side of the diapir. The asymmetric thickness of debrite lobes, with thicker ones on the upstream slope of the diapir, reflects the topographic steering as the debrite accumulated preferentially against the diapiric slope. Such localised topography likely induced transient aggradation upstream of the diapir before eventually overspilling downslope (Martínez-Doñate et al., 2021; Allen et al., 2022), as evidenced by the aggradation of Lobe 4 upstream of Lobe 3 (Figure 5-13C).

The downstream lobes (Lobes 5-8) exhibit uniform seismic facies with the upstream conduit (Figure 5-2D and Figure 5-11), and the lateral margin of Lobes 6-8 can be traced back to the diapir region (Figure 5-5). Together, these observations indicate that these downstream lobes are sourced from the headwall region and subsequently became further confined by the diapir. Within the central area between the two diapirs, the topographic constriction and the locally steepened lateral slope, which increases from 1.7° upstream to ~5° along the diapir flank, acted to form a steeper and more laterally confined pathway. This along-axis narrowing would have focused flow energy and momentum, thereby increasing axial velocity (Allen et al., 2022). The concentration of flow energy would elevate basal shear stress (Iverson et al., 1997) and allow a single flow to incise progressively deeper downstream along the central axis of the developing conduit. Enhanced incision adjacent to the diapir would increase the sediment load of the flow through substrate entrainment, reinforcing a positive feedback whereby basal shear stress and vertical loading increase that might drive movement on deeper shear surfaces (Iverson et al., 1997), especially in weakly consolidated substrates. Thus, a series of basinward stacking lobes (Lobes 6-8) develop at progressively lower elevations updip and downdip of the diapir, successively narrowing towards the conduit (Figure 5-5, Figure 5-7-3 to Figure 5-7-5, and Figure 5-11B).

Overall, the diapiric topography strongly enhanced the degree of debris flow confinement and magnitude of the substrate incision, reinforcing self-confinement. The interaction between diapiric topography and debris-flow incision exemplifies how autogenic and allogenic controls combine, where structural relief (diapirs) acted to enhance the amount of substrate incision by pinning the debris flow to this area, resulting in the deepening of incision and lengthening of the flow.

5.6.3 Origin of megaclasts and debrite lobe remobilisation

Megaclasts are widely distributed across the basal shear surface (Figure 5-3C), and their close spatial association with grooves (Figure 5-8D and Figure 5-8E) supports the interpretation that the megaclasts acted as erosional tools, dragged along at the base of the cohesive, laminar debris flow (Peakall et al., 2020). Megaclasts associated with the long downstream grooves (Type 1) are interpreted to originate from the headwall and upstream parts of the flow (e.g., Jackson, 2011; Alves, 2015; Gamboa and Alves, 2015; Li et al., 2023), where they were detached and subsequently transported downslope within the main debris flow. The pristine preservation of the Type 1 grooves (Figure 5-8A) suggests that most of the substrate entrainment occurred at the front of the flow, and that the megaclasts that cut the grooves were located some distance behind. This interpretation is consistent with previous models of groove formation (Peakall et al., 2020, 2024; Baas et al., 2021).

Megaclasts associated with the Type 2 grooves are restricted to the lateral margins that cross-cut Type 1 grooves. The cross-cutting relationships of the Type 2 grooves relative to the Type 1 grooves demonstrate that the debris flow transited through the conduit forming Type 1 grooves without leaving a substantive deposit in the axial parts, essentially forming an underfilled conduit. Bypass by debris flows have been observed on the modern seafloor (Kastens, 1984), in experiments (Hampton, 1970) and inferred from sedimentary deposits (Peakall et al., 2020; Baas et al., 2021).

Therefore Type 2 grooves on the lateral margins of Lobes 3, 4, and 8, formed at some later stage when the conduit was largely empty, but prior to the development of substantial pelagic and hemipelagic sedimentation. Their location on the lateral margins, their orientation at a high angle to the Type 1 grooves, and the curved form to parallel the axis, support interpretation that they formed from instability and remobilisation of debrite lobe deposits, including megaclasts, into the adjacent underfilled conduit.

The relative timing of formation of the cross-cutting grooves and debrite lobe remobilisation can be constrained. The locally thicker debrite in the conduit (Figure 5-3D) that tapers updip and downdip adjacent to Lobe 4 supports remobilisation a limited distance towards, and local plugging of, the conduit (Figure 5-14). Subsequently, Lobe 3 underwent remobilisation. This is evidenced by the presence of the local depression on the top surface upstream of the diapir (Figure 5-4A), and the truncation of Lobe 4 deposits at the basal shear surface (Figure 5-10B), including the formation of knickpoints that cut the Type 1 grooves (Figure 5-8B and Figure 5-12). Furthermore, the deposits are thicker in the central conduit than the flanks (Figure 5-7-3 and Figure 5-7-4) and these taper downstream (Figure 5-3D) suggesting that the remobilisation of Lobe 3 deposits occurred when the downstream flow was no longer active, and did not bypass through the conduit.

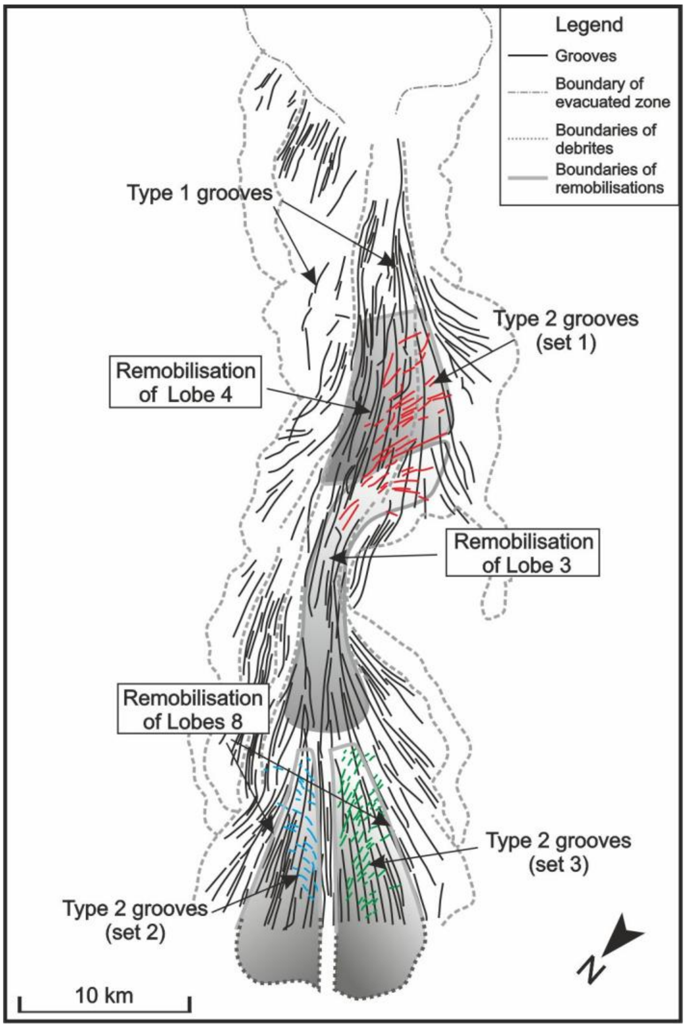

Figure 5-14: Conceptual model illustrating the remobilisation of lobes. Remobilisation of Lobe 8 is followed by the remobilisation of Lobes 4 then Lobe 3. Thin black lines mark the Type 1 grooves, and coloured thin lines mark the Type 2 grooves, including Set 1 grooves (shown as red thin line), Set 2 grooves (shown as blue thin line), and Set 3 grooves (shown as green lines). The grey areas indicated the location of remobilisation.

The remobilisation of both lateral margins of Lobe 8 (Sets 2 and 3, Figure 5-8A, C, E) into the underfilled conduit is supported by the continuation of Slide 9 deposits 16 km farther to the northwest beyond the 3D seismic data (Figure 5-5B and Figure 5-14). The timing of Lobe 8 remobilisation is interpreted to have taken place before the remobilisation of Lobes 4 and 3 because the deposits from these events partially fill and block the conduit upstream.

Remobilisation of Lobe 3 deposits resulted in hundreds-of-metres wide knickpoints that cross-cut pre-existing basal grooves (Figure 5-12A and Figure 5-12C). Knickpoints that migrate rapidly upstream have been identified in modern submarine canyons (e.g., Guiastrennec-Faugas et al., 2020, 2021; Ribó et al., 2025) and channels (e.g., Gales et al., 2019; Heijnen et al., 2020; Zulkifli et al., 2024) under overriding turbidity currents, and are occasionally preserved at the base of ancient submarine channel-fills (Casagrande et al., 2024). However, they have not been identified to develop under debris-flows, although Allen et al. (2022) speculated that there was potential for their development based on outcrop observations. The entrainment of substrate and the development of erosional bedforms under mobile debris flows can be readily preserved by their en masse deposition.

To explain the cross-cutting grooves on the basal shear surface of Slide 9 (their Bonaventure Complex I), Scarselli et al. (2013) and Scarselli (2020) proposed that Slide 9 represents either two consecutive events, in which an initial downslope collapse of a slump was followed by a series of flank collapses; or a single slump that developed through two stages, during which failure switched transport direction and caused inward collapse of the entire system during a waning phase of the main failure. Thus, these crosscutting grooves were attributed to either late-stage flank collapse, or inward flank collapse during the waning phase of the slump (Scarselli et al., 2013; Scarselli, 2020).

My observations of the: i) downstream stacking pattern of debrite lobes, ii) the stepped geometry of the basal shear surface, iii) the presence of knickpoints, iv) the volume analysis, v) the deposits in the conduit linked to flank remobilisation, and vi) the relationship of the debrites to the diapir, allow refinement of both the origin of these grooves and the evolution of the flow. In contrast to the slump interpretation proposed by Scarselli et al. (2013) and Scarselli (2020), the Type 1 grooves and the megaclasts embedded within downstream chaotic and acoustically transparent seismic facies, support interpretation of a self-confining submarine debris flow. Within the debris-flow framework, three cross-cutting groove sets record three discrete remobilisation events, interpreted to be remobilisations of Lobe 8, Lobe 4 and Lobe 3. The axial conduit was bypassed by the debris flow after formation of Lobe 8, without leaving a substantive deposit in the conduit, thus generating sufficient local negative topography to trigger the remobilisation of earlier debrite lobes, during which the distinctive cross-cutting grooves formed.

5.7 Conclusions

Using three-dimensional seismic reflection data from the Exmouth Plateau, offshore northwest Australia, I document an elongate submarine debrite (length-to-width ratio of ~7-8) on a gentle slope (~0.89°). The basal shear surface of the debris flow is deeply incised, stepped, exhibits channel-like morphology, and is ornamented by km-scale grooves that are frequently terminated by megaclasts (up to 250 m wide and 70 m thick). Mapping of radiating groove sets and associated lobate geometries shows that the deposits comprise at least eight debrite lobes arranged in an overall basinward stacking pattern.

On the gentle slope, early debrite lobes (Lobes 1 and 2) generated lateral depositional relief, which imposed initial confinement on the subsequent flow pulses. This early confinement focused flow energy, and drove substrate incision and entrainment, even on such a gentle slope, resulting in the formation of stepped lateral margins. Flanked by the steep lateral margins, the submarine debris flow self-confined, incised, and deposited more debrite lobes (Lobes 3-8). Volume calculation demonstrates that the downstream deposited volume (12.89 km^3) is a minimum of approximately three times the headwall evacuated volume (4.67 km^3), suggesting substantial substrate entrainment during emplacement, which further increased confinement and flow erosive capacity. The self-confining process establishes a positive feedback where flow confinement increases, drives substrate incision and further enhances the confinement of flow, thereby increasing the run-out distance even on a gentle slope.

The presence of a diapir on the pathway acted as a topographic barrier for the subsequent flow, which induced flow deflection (Lobe 3) and aggradation upstream (Lobe 4). Flow was focused within a steeper and laterally confined pathway adjacent to the diapir, driving additional substrate incision reaching a maximum (~130 m). The increased confinement enhanced the focusing of flow energy and momentum, allowing the flow to incise progressively deeper downstream along the conduit axis, and developing a series of lobes (Lobes 5-8).

The grooved conduit was left unfilled and characterized by steep lateral margins. Such conditions led to instability and remobilisation of several lobe deposits, that then partially filled the conduit. The remobilization of these flank deposits formed grooves

(Type 2) that crosscut the main axial grooves (Type 1) at high angles, along with a series of upstream migrating knickpoints that developed beneath the debris flows. Together, the distribution of lobes and the crosscutting relationship of grooves record the dynamic interaction between depositional and diapiric relief, flow confinement, and substrate incision, during the evolution of a self-confining submarine debris flow. This was followed by subsequent remobilisation of the unstable seascape. The self-confining evolution provides a new mechanism to explain the long runout distances documented for submarine debris-flows, despite their occurrence on low gradient slopes, with important implications for predicting debris-flow mobility and seafloor erosion.

Chapter 6 Segregation and evolving substrate interaction: Process insights from observation of single and successive subaqueous granular flows

6.1 Summary

Dense granular flows, analogous in many respects to debris flows, can segregate particles and form coarser-grained levees, which restrict lateral spreading and promote long runout distances. Previously, observations of physical experiments of single subaerial debris flows have been used to inform the processes of levee formation during segregation. However, equivalent work on single or multiple experimental subaqueous flows has not been documented. A series of subaqueous single-flow experiments were conducted using the same set-up as previous subaerial experiments, with mixtures of carborundum (300-425 μm) and spherical fine ballotini (150-250 μm) on a roughened slope of 29°. In addition, multiple-flow experiments were conducted and their composite deposit composition were analysed. This allowed investigation into the process interactions of successive subaqueous granular flows and their deposits, and the segregation of particles, enabling comparison with subaerial flow equivalents. Results show that both single and multiple flows form coarser-grained levees and finer-grained conduit deposits in subaqueous settings. Single subaqueous flows exhibit higher mobility and narrower flow widths than equivalent subaerial experiments. In multiple flows, particle segregation is a dynamic process. The first flow forms a leveed channel, acting as an erodible substrate that increases mobility for subsequent flows. Subsequent multiple flows exhibit upslope particle remobilisation and downslope redeposition that together act to reduce particle segregation. These sedimentation processes occur in conjunction with channel widening. The experiments reveal that particle segregation occurs in subaqueous environments and can re-shape seafloor morphology though substrate interaction, and segregation-driven modification of the seafloor can influence the mobility and runout of subsequent flows.

6.2 Introduction

Submarine debris-flow deposits are analogous to subaerial debris-flow deposits (Prior et al., 1984; Masson et al., 1997) and can develop lateral levees and blocky flow fronts.

Examples include the up to 15 m high relief on the lateral ridges of the Saharan debris flow deposit (Masson et al., 1993), and the lateral depositional relief of debris flow deposits on the Bear Island Trough Mouth Fan (Laberg and Vorren, 1995). The depositional relief can influence subsequent flow pathways and enhance confinement (Gee et al., 2001; Iverson et al., 2010; Johnson et al., 2012; Kokelaar et al., 2014; de Haas et al., 2015, 2016), which limits lateral spreading and increases flow runout distances even on gentle slopes.

However, gaining an improved understanding of debris flow processes, the links to deposit morphology, and the segregation of grains in subaqueous settings, is hindered by the impracticalities of attempting to take direct measurements in almost all cases due to destructive and unpredictable nature of flow events. Yet, useful insights can be gained from physical experiments of subaerial flows conducted to investigate grain-size segregation (Savage and Lun, 1988; Major, 1997; Major and Iverson, 1999; Gray and Thornton, 2005; Iverson et al., 2010; Gray et al., 2015; Kaitna et al., 2016), levee formation (Iverson et al., 2010; Johnson et al., 2012; Kokelaar et al., 2014; Rocha et al., 2019), and flow self-confinement/self-channelisation (Deboeuf et al., 2006; de Haas et al., 2015, 2016). Subaerial debris-flow experiments show that debris flows travelling over smooth and rough beds can achieve comparable runout distances through segregation, despite flows over smooth beds moving ~30% faster (Iverson et al., 2010). Sediment composition plays an important role in runout distance and evolution during particle segregation (e.g., Elverhøi et al., 2010; Kokelaar et al., 2014). Through systemic variation of composition, the maximum runout distance in subaerial granular-flow experiments is attained with mixtures containing 30-40% sand, which is just sufficient to segregate and form levees that are robust enough to restrict spreading (Kokelaar et al., 2014). Subaerial experiments demonstrate that debris flows can entrain coarse particles (pebbles) from the substrate, which subsequently migrate upward and join the recirculation within the flow head (Johnson et al., 2012). Substrate entrainment can therefore modify particle size distribution in the advancing flow head, which has direct implications for the formation of levees and the local mobility of subsequent flows. Experimental and conceptual models of debris flows and dense granular flows have captured particle segregation processes from single flow systems in subaerial settings (e.g., Savage and Lun, 1988; Major, 1997; Major and Iverson, 1999; Gray and Thornton, 2005; Iverson et al., 2010; Gray and Kokelaar, 2010;

Johnson et al., 2012; Kokelaar et al., 2014; de Haas et al., 2015, 2016). However, there remains a notable lack of equivalent work on subaqueous flows, and particularly on the dynamic interactions between flows, the composition of the flow and the substrate, and their resulting depositional architecture, in both single- and multiple-flow systems.

The aim of this study is to understand the process interactions between subaqueous granular flows and their deposits through physical experiments. The specific objectives of the study are to: (1) investigate grain-size segregation in single subaqueous granular flows with systematically varying mixture compositions, and to highlight the distinctive characteristics of subaqueous segregation through the comparison with subaerial counterparts; (2) quantify the downstream variations in levee thickness using digital elevation models (DEMs), and analyse the grain-size distribution and sphericity of deposits in single and multiple events to investigate how particle size and shape control segregation; and (3) evaluate the role of flow-deposit interactions during multiple events in controlling runout distances, and propose a new model capturing the flow-substrate interaction during segregation.

6.3 Methodology

This study comprises subaqueous single-and multi-flow experiments. The single-flow experiments follow the experimental configuration of the subaerial granular-flow experiments of Kokelaar et al. (2014) but in a subaqueous setting. Using a comparable experimental configuration allows the subaqueous single-flow deposits produced in this study to be compared with previously published subaerial experiments, and therefore provides a basis for assessing how the presence of interparticle fluid influences particle segregation and deposit morphology. Comparison between subaqueous single- and multi-flow deposits allows the analysis of how the successive segregating flows interact with the pre-confined substrates, through the comparison of subaqueous multiple-flow deposits with single-flow deposits. The present approach, based on comparison with Kokelaar et al. (2014), also avoids issues around the modelling of finer-grained cohesive fractions. The charged particles within clays do not scale, and thus cohesive forces end up orders of magnitude too large in small-scale models relative to natural examples, and thus cohesive forces are excessively large relative to shear within the experiments (Peakall et al., 1996, 2007). Alternative approaches to modelling cohesion, such as fine-grained cohesionless materials (e.g., silica flour), that exhibit appreciable van der Waals forces have been utilised elsewhere (Peakall et al., 1996, 2007; van Dijk et al., 2012; Kleinhans et al., 2014; Baker et al., 2017). However, these are at larger experimental scales than those undertaken herein.

6.3.1 Experimental setup and materials

Flows were run in a water-filled tank with an inset experimental rig, comprising a planar slope (29°, 140 cm long, 50 cm wide; Figure 6-1A and Figure 6-1B) in the Sorby Environmental Fluid Dynamics Laboratory, University of Leeds, UK. The slope was roughened using blue close-packed, fixed, coarse spherical ballotini (0.75-1 mm diameter). A plastic funnel with an outlet valve was positioned 4 mm above the slope (Figure 6-1B) to regulate a steady discharge of a granular mixture of fine-grained spherical ballotini (150-250 μm; white) and medium-grained angular carborundum (300-425 μm; black; Figure 6-1C). The angle of the experimental slope exceeds the subaerial angle of repose of the finer ballotini (~24.5°) and is lower than the subaerial angle of repose of the coarser carborundum (~36.7°; Kokelaar et al., 2014).

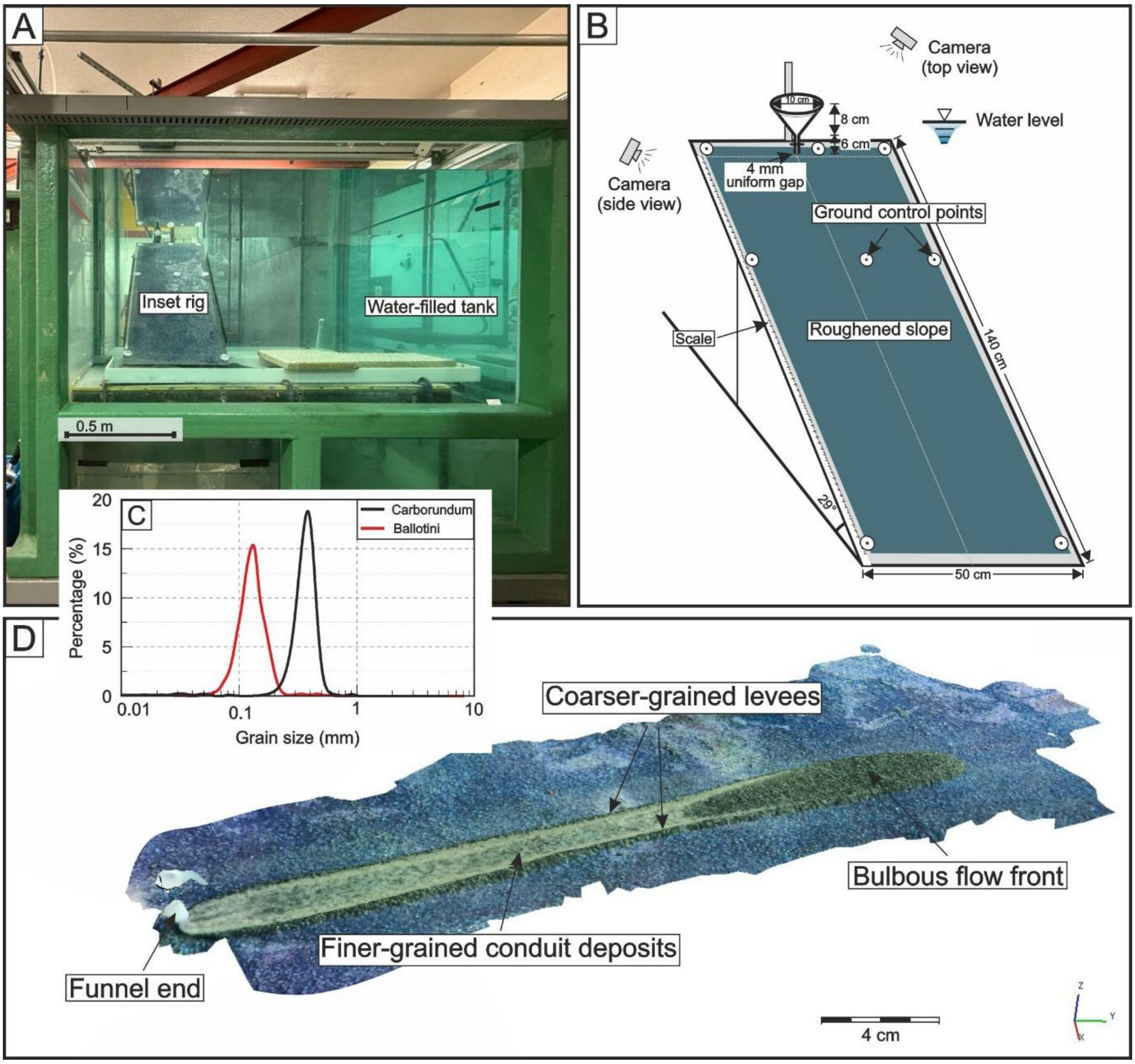

Figure 6-1 (A) Experimental setup, showing a water-filled tank and an inset ramp. (B) Outline of the roughened ramp with scale and locations of 8 ground control points. The ramp was roughened using blue, close-packed, fixed, coarse spherical ballotini (0.75-1 mm diameter). (C) Grain-size distributions of the ballotini and carborundum, used in the experimental mixtures. (D) Perspective view of a digital elevation model, illustrating a subaqueous self-confining granular-flow deposits from a mixture containing 20 vol.% fines. The 20 vol.% fines mixture underwent particle segregation, forming coarse-grained levees, fine-grained conduit deposits, and a bulbous flow front. White particles are fine-grained spherical ballotini (150-250 µm) and black particles are the medium-grained angular carborundum (300-425 µm). Note that this 20 vol.% fines mixture experienced issues with jamming at the outlet valve, resulting in partial release of the mixture. Therefore, the main experimental results focus on mixtures containing 30-100 vol.% fines.

The volume of the granular mixture used in each experimental run was 15 cm^3, with systematic changes in the ratio of ballotini to carborundum. The granular mixture was well mixed dry and transferred into the water-filled funnel. The water level within the funnel was maintained above the surface of the mixture to ensure complete saturation of the granular material, while being kept at the same height as the water level in the tank to avoid pressure differences that could cause flushing of the sediment. The saturated granular mixture was gently stirred within the funnel to ensure mixing before release. Flow initiation was controlled by opening the outlet valve, from which point timing of the experimental run commenced.

Mixtures containing ⩽20 vol.% fines either jammed at the outlet valve or failed to completely initiate flow (Figure 6-1D); therefore, this study focuses on mixtures containing 30-100 vol.% fines at 10 vol.% intervals (Figure 6-2 and Figure 6-3). Single flow experiments are conducted across this range, and the multiple flow experiments on mixtures containing 30, 50 and 70 vol.% fines. Each multiple flow experiment consists of six successive runs, each 15 cm^3, with a fixed interval of one hour between runs to ensure complete cessation of motion before the next release. The single-flow experiments with 30-90 vol.% fines were each run twice, which produced similar deposit morphology (Figure 6-3 and Figure 6-4), widths (Figure 6-5A and Figure 6-6A), velocities (Figure 6-6B and Figure 6-6C; Table 6-1 and Table 6-2). The first run of the multiple-flow experiments exhibits similar deposit morphology, runout distance and average velocity to the equivalent single-flow experiment, supporting the reproducibility of the experiments.

6.3.2 Width, runout distance and flow velocity measurements

Flow runout was recorded using overhead photographic image sequences acquired at 25 frames per second. This allowed quantification of the flow kinematics (width, runout distance and velocity of the flow head). Instantaneous runout distances of each flow were measured using Fiji ImageJ by tracking the distance to the front of the flow head from images extracted at one second intervals. The runout data are available from ~10 to ~110 cm downslope from the outlet valve (Figure 6-3, Figure 6-4, Figure 6-5 and Figure 6-6). Average flow velocities are calculated from the gradient of the runout distance-time plot, over the first 120 s or up to 110 cm of runout. Instantaneous velocities are given by the gradient between two successive measurement points. During steady discharge, switching between black coarser and white finer grains enables the visual identification of levee initiation and growth (Figure 6-2). Left and right levees refer to the position looking downslope. Width of subaqueous flow deposits is measured based on the top view images after flow cessation. The unreported width of the equivalent subaerial experiments carried out by Kokelaar et al. (2014) was measured from their images using ImageJ (Figure 6-5A).

6.3.3 DEM, sampling and estimated components

After cessation of flows with 30, 50 and 70 vol.% fines, underwater photographs of single-flow deposits and multiple-flow deposits after the six events were systematically acquired along a zigzag pattern, using a waterproof GoPro camera. Digital elevation models (DEMs) of the deposits are constructed in Agisoft Metashape, using 8 ground control points on the slope to quantify the deposit topography (Figure 6-1A and Figure 6-1B), with a vertical and horizontal resolution of 0.2 mm for single- and multiple-flow deposits.

To analyse the grain size and sphericity of deposits, samples were collected from the single-flow deposits and the sixth run of multiple-flow deposits (with 30, 50 and 70 vol.% fines). Samples were collected using a syringe from three locations across the deposit: the left levee crest, the right levee crest, and the central conduit deposits. At each location, samples were taken from two downslope intervals (45-50 cm and 20-25 cm) over an area approximately 1.5 cm wide, to analyse the downslope variance of composition and sphericity. Sampling proceeded from downslope to upslope, with the 45-50 cm location sampled first, to avoid disturbing sediment from the upslope sampling location and mobilising this sediment downslope thus affecting downslope sampling. Grain size and sphericity of particles were measured using a Camsizer XT dynamic image analysis system. The sphericity of particles was calculated by the system as $4\pi A/P^2$, where A is particle area and P is particle perimeter derived from the particle outline (Miller and Henderson, 2010). Sphericity of samples was calculated as the volume-weighted mean of individual particle sphericities (e.g., Hu and Xiao, 2025). The reference grain size and the sphericity of 100% fine ballotini and 100% carborundum were measured to compare against the mixed deposits (Figure 6-1C).

Compositions were derived from the grain-size distributions (GSDs) to quantify the particle segregation in the single- and multiple-flow experiments. Specifically, compositions were estimated from the GSD of samples using a two-end-member least-square unmixing approach (e.g., Weltje and Prins, 2007), given that the samples comprise only ballotini and carborundum. For each sample, the finer ballotini fraction is estimated by minimizing the sum of squared differences between the observed GSD and a linear combination of the ballotini and carborundum. Residuals were calculated as the difference between the measured and modelled GSDs, and the goodness-of-fit is quantified using the L2 norm of the residuals (rnorm). Lower rnorm value indicates a better fit between the modelled and measured grain-size distributions, and thus a more reliable unmixing results.

Net area change was calculated from differences in profile area between the single-flow deposits and the multiple-flow deposits after six runs. Net erosion area (E) corresponds to the area of single-flow deposits that was net eroded by successive flows, and net deposition area (D) of profiles corresponds to the additional depositional area of multiple-flow deposits relative to the single-flow. Thus, the net area change is calculated as: net area change = net deposition area (D) - net erosion area (E). A positive value indicates net deposition by the successive flows relative to the single-flow deposits, while a negative value indicates net erosion.

6.4 Subaqueous single flow results

After discharge from the funnel, the subaqueous granular flows rapidly undergo particle segregation, and a bulbous head forms at the flow front (Figure 6-2A and Figure 6-2B). Upstream of the advancing bulbous head, levees form and are visually dominated by black carborundum (Figure 6-2B and Figure 6-2C). The flow becomes fully confined, and the flow level remains below both the flow front and the levee crest height (Figure 6-2B). As the flow head advances, the levees lengthen downslope, establishing a stable conduit for particle transport (Figure 6-2B and Figure 6-2C). As the discharge decreases, the flow level lowers, and the levees inwardly narrow (sharpen) along the active flow margin (Figure 6-2C to Figure 6-2E). A white fine-ballotini conduit is gradually exposed, while sediments from the flow tail continue to be transported downslope (Figure 6-2C to Figure 6-2E). The axial conduit deposits between the levees are referred to as the fines-lining by Kokelaar et al. (2014).

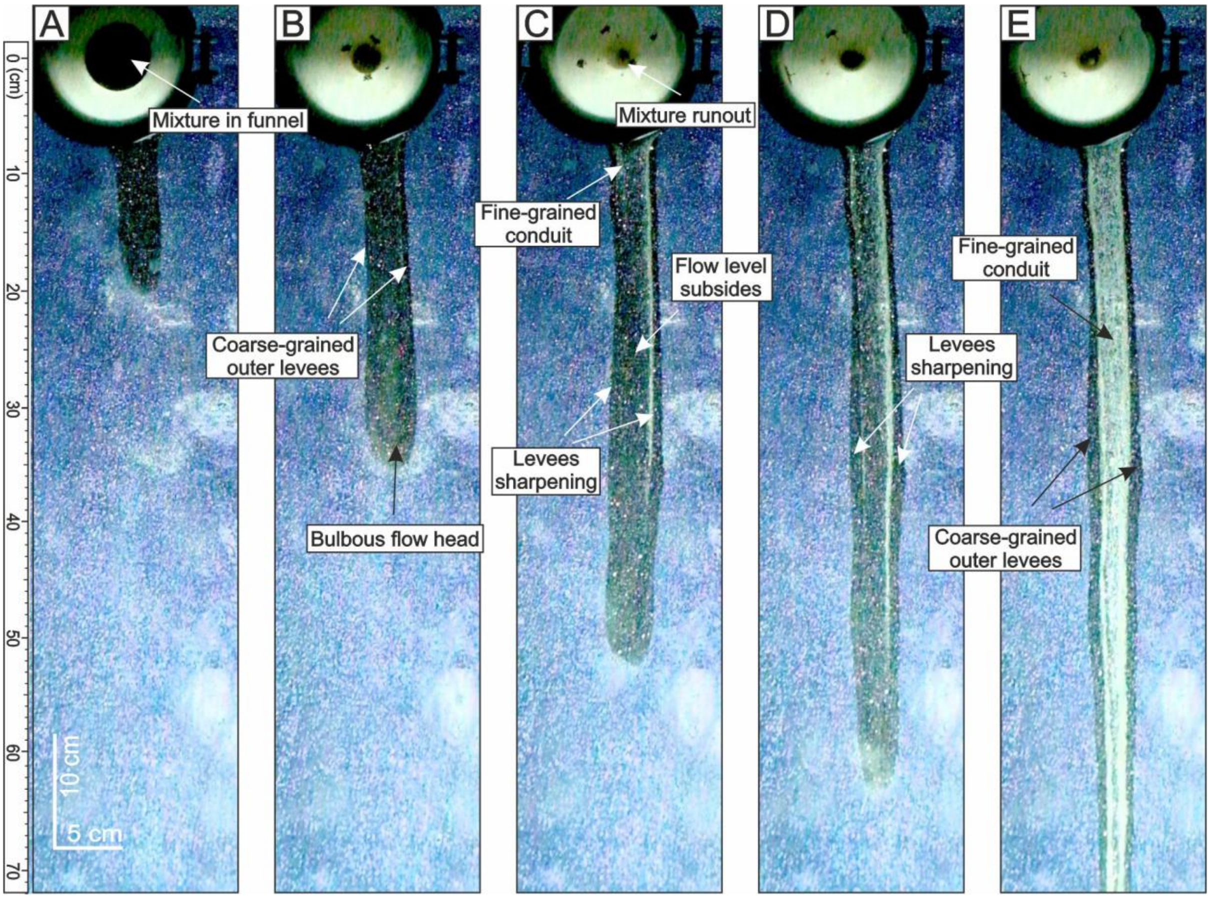

Figure 6-2: Top view of a single subaqueous flow containing 30 vol.% fines, illustrating the evolution of self-channelisation through five phases: (A) flow initiation phase (0-35 s), (B) levee formation phase (36-69 s), (C) source mixture cessation phase (70 s), (D) levee sharpening phase (70-299 s), and (E) upslope throughput material phase (300 s). White particles are fine-grained spherical ballotini (150-250 μm), and black particles are the medium-grained angular carborundum (300-425 μm). During steady discharge, switching between coarser black grains and finer white grains enabled the visual identification of levee initiation and growth.

6.4.1 Runout, width, and velocity under different sediment mixtures

The 30 vol.% fines flow had the shortest runout distance (~115 cm) and terminated near the distal end of the experimental slope, whereas the flows with higher fine fractions (40-100 vol.% fines) travelled beyond the slope (>120 cm; Figure 6-3). The maximum deposit width overall increases systematically with higher fines fraction, from 3.63 cm in the 30 vol.% fines experiment to 5.30 cm in the 100 vol.% fines experiment (Figure 6-5A). Average flow velocity initially increases with fines fraction, from 0.63 cm/s in the 30 vol.% fines experiment to 1.13 cm/s in the 70 vol.% fines experiments, and then progressively decreases to 0.66 cm/s in 100 vol.% fines experiments (Table 6-1).

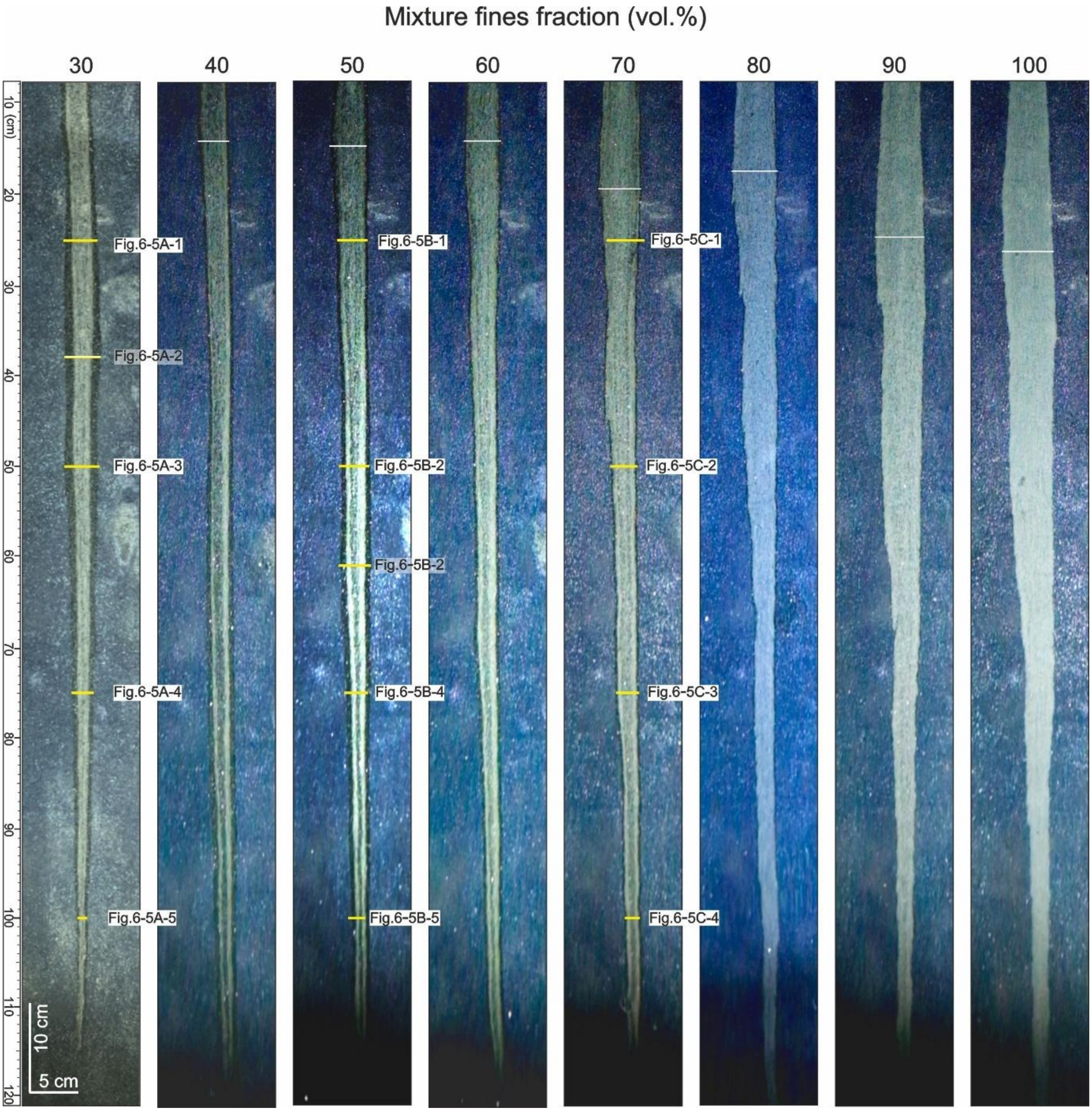

Figure 6-3: Deposits of subaqueous self-confining granular flows with initial fines proportions ranging from 30 to 100 vol.% at 10 vol.% intervals. With the exception of the 100 vol.% fines case, the deposits of all other flows exhibit black, coarse-grained levees and white, fine-grained conduit deposits. The thin white lines mark the locations of the maximum deposit widths shown in Figure 6-5A.

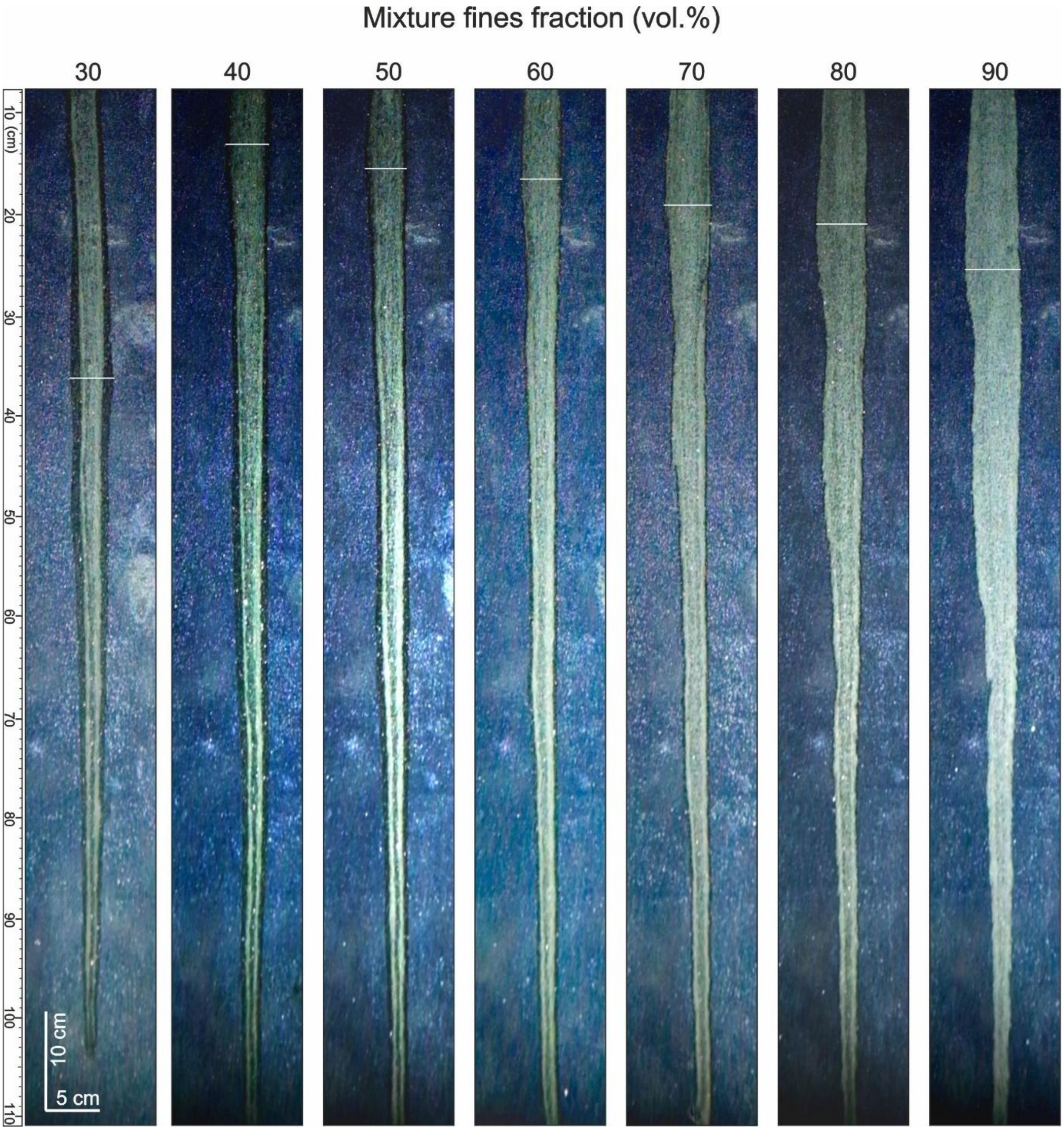

Figure 6-4: Deposits from repeat runs of the subaqueous single-flow experiments, with initial fines proportions ranging from 30 to 90 vol.% at 10 vol.% intervals. These deposits are comparable to the deposits shown in Figure 6-3, characterised by black coarser-grained levees and white finer-grained conduit deposits.

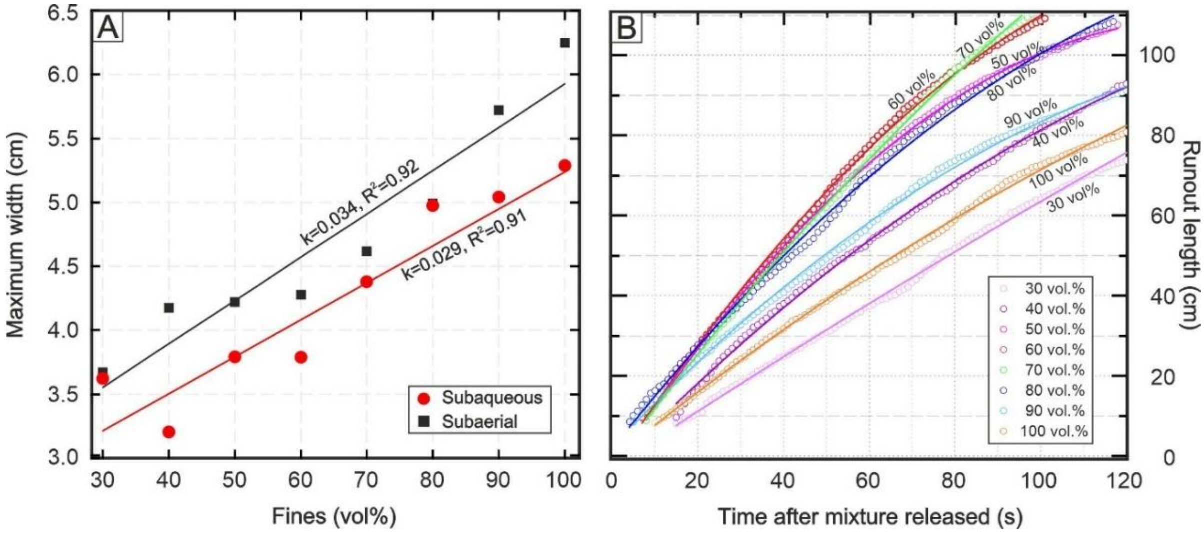

Figure 6-5: Variations in flow characteristics with the fines fraction of mixtures ranging from 30 to 100 vol.% at 10 vol.% intervals. (A) Maximum flow width plotted as a function of fines fraction. Red dots represent measured data from the subaqueous single-flow deposits shown in Figure 6-3, and squares correspond to referenced widths of equivalent subaerial single-flow deposits from Kokelaar et al. (2014). The red straight line represents the trend line for the subaqueous experiment runs, and the black straight line represents the trend line for the maximum width of the equivalent subaerial single-flow deposits. (B) Flow runout distances as a function of time for mixtures with differing fines fractions. Empty circles represent measured runout distances of subaqueous single flows shown in Figure 6-3, and the gradient of each measured data curve reflects flow velocity. Coloured lines represent the corresponding trend lines fitted to the measured data. The deviations between the measured data and the trend lines reflecting local fluctuations in flow head velocity.

In all single-flow experiments, flow velocity generally decreases downslope (Figure 6-5B). Compared with the trendline, the measured velocity data show localised fluctuations in several experiments, reflecting slight increases or decreases in flow-head velocity (Figure 6-5B). These fluctuations are most pronounced in the 30 and 100 vol.% fines experiments, where average flow velocities are lowest (Figure 6-5B). In the 30 vol.% fines experiment, flow-head velocity shows an initial deceleration over the initial 40 cm (from 0.62 cm/s at 10 cm to 0.19 cm/s at 40 cm), followed by a marked acceleration to a local peak (1.31 cm/s at 50 cm), before gradually decreasing downslope (Figure 6-5B; Table 6-1). A similar trend is observed in the single 40 vol.% fines flow, where velocity generally decreases downslope to a minimum (0.47 cm/s at ~84 cm) coinciding with the development of the thickest levees, followed by a short-lived local acceleration and the subsequent deceleration downslope. By contrast, flows with intermediate fines fractions (50-70 vol.%) show overall smooth decreases in velocity, without dramatic fluctuations (Figure 6-5B). For example, in the 50 vol.% fines experiment, velocity decreases downslope from 1.40 cm/s at 10 cm to 0.50 cm/s at

~110 cm (Table 6-1). At higher fines fractions (80-100 vol.%), localised deviations become overall more noticeable, but remain weaker than in the 30 vol.% fines experiments. In the 80 vol.% fines experiment, flow-head velocity decreases from 1.60 cm/s at 10 cm to a minimum of 0.77 cm/s at 53 cm, then increases steadily to a maximum of 1.56 cm/s at 67 cm, prior to decreasing downslope to 0.58 cm/s at ~110 cm (Figure 6-5B; Table 6-1). Similar fluctuations can be seen in the 90 and 100 vol.% fines experiments, where head velocity initially decreases and then abruptly at ~50-70 cm downslope (Figure 6-5B; Table 6-1).

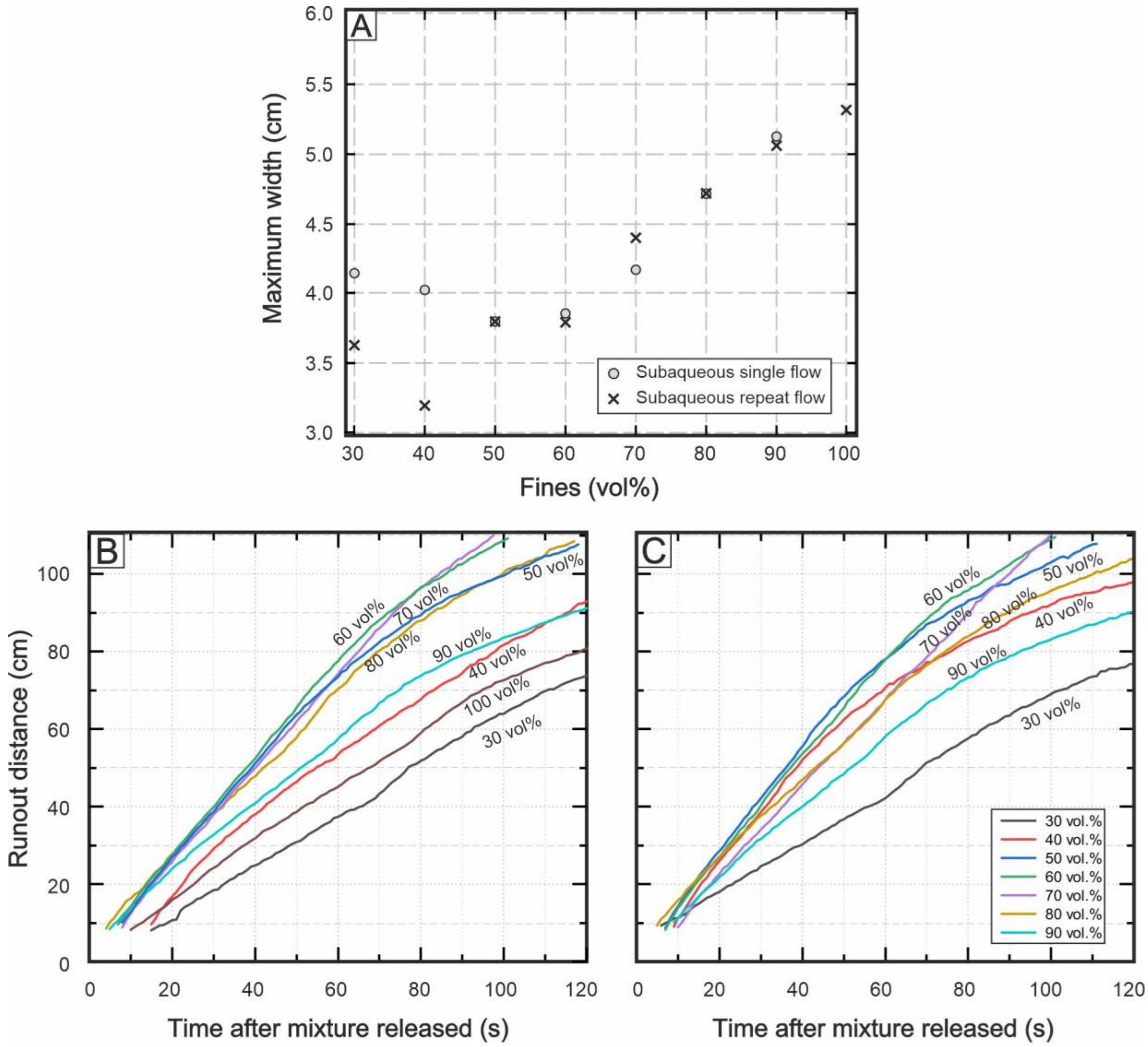

Figure 6-6: (A) Maximum deposit width of subaqueous single granular flows, plotted as a function of initial fines fraction. Grey dots show the maximum deposit width data from Figure 6-5A, and the crosses represent the maximum deposit width from repeat runs of the single-flow experiments. (B) Runout distance of the single flows shown in Figure 6-3. (C) Runout distance of the repeat runs of the single-flow experiments shown in Figure 6-4.

Table 6-1: Velocity of subaqueous single flows, demonstrating the average flow velocity and the local fluctuations in flow head velocity. Note, the average flow velocity is calculated within the limit of running time of 120 s and runout distance of 110 cm.

Fines (vol.%)	**Average velocity (cm/s)**	**Initial velocity (cm/s) at ~10 cm**	**Velocity (cm/s) at ~110 cm**	**Maximum & adjacent levee thickness (mm)**	**Location of local enhanced velocity**
30	0.63	0.62	0.44 (at 74 cm)	3.5 mm (at 38 cm) & 2.0-2.5 mm (at 25 cm)	40-50 cm
40	0.79	1.44	0.47 (at 93 cm)	(at ~70-80 cm)	~80-90
50	0.89	1.40	0.50	1.8 mm (at ~58 cm) & ~1.5 mm (at 50 cm)	Steady decrease
60	1.08	1.34	0.62		Steady decrease
70	1.13	1.54	0.80	> 1 and <1.5 mm (at ~55-60 cm) & 1.0 mm (at 50 cm)	Steady decrease
80	0.89	1.60	0.58		53-67 cm
90	0.72	1.21	0.42 (at 90 cm)		52-71 cm
100	0.66	0.58	0.37 (at 80 cm)		55-70 cm

Table 6-2: Average flow head velocity in subaqueous single flow experiments with different fine mixtures. Note, the first runs correspond to the single flows in Figure 6-3, Figure 6-5 and Figure 6-6. Repeat runs represent the repeat runs of subaqueous single-flow experiments presented in Figure 6-4 and Figure 6-6C.

Initial fines percentage in mixtures (%)	**Average flow velocity in first runs (cm/s)**	**Average flow velocity in repeat runs (cm/s)**
30	0.63	0.59
40	0.79	0.80
50	0.89	0.95
60	1.08	1.08
70	1.13	1.13
80	0.89	0.82
90	0.72	0.72
100	0.66	

6.4.2 Levees and conduit thickness under different sediment mixtures

The thickness of the levees and the conduit deposits vary downslope and with fines fraction. Levees thicken from the upper slope to a maximum at mid-slope and then thin downslope (Figure 6-7). In the single 30 vol.% fines experiment, levee thickness increases from ~1.5 mm at 25 cm to a maximum of 2.5 mm at ~38 cm (Figure 6-7A-1 and Figure 6-7A-2), and then progressively decreases downslope to ~0.5 mm at 100 cm (Figure 6-7A-3 to Figure 6-7A-5). In the single 50 vol.% fines experiment, levee thickness is ~1.5 mm in the upslope region, reaches a maximum of 1.8 mm at 61 cm, before slightly decreasing downslope (Figure 6-7B-1 to Figure 6-7B-5). In the single 70 vol.% fines event, levee thickness is lower overall (~1.0 mm), with a similar mid-slope maximum followed by downslope thinning (Figure 6-7C). The maximum levee thickness in 70 vol.% fines experiment cannot be precisely determined as the DEM is poorly resolved between 55-60 cm, but is estimated to be <1.5 mm based on the comparison with levees thickness in 50 vol.% fines experiment (Figure 6-3 and Figure 6-7B-2).

Maximum levee thickness decreases with increasing fine fraction, reaching up to 2.5 mm in the 30 vol.% fines experiment, compared with 2.0 mm in the 50 vol.% fines experiment and <1.5 mm in the 70 vol.% fines experiment (Figure 6-7). The thickness of conduit deposits increases with fines fraction. The conduit deposits are thinner than 0.2 mm in the 30 vol.% fines experiment (below the DEM resolution; Figure 6-7A), and increase up to 0.5 mm in the 50 and 70 vol.% fines experiments (Figure 6-7B-2 and Figure 6-7C-1).

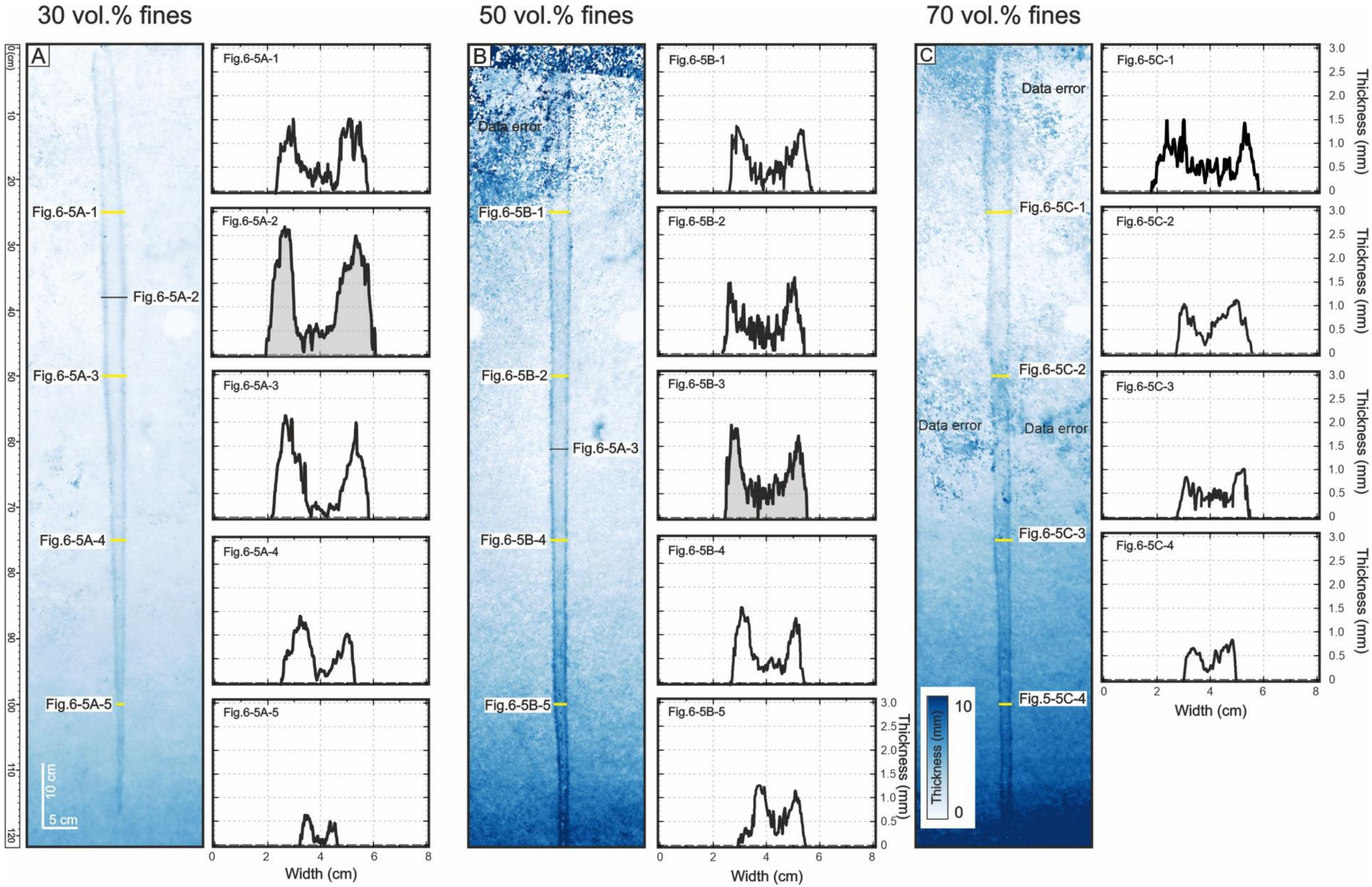

30 vol.% fines
50 vol.% fines
70 vol.% fines
A
B
C
Fig.6-5A-1
Fig.6-5A-2
Fig.6-5A-3
Fig.6-5A-4
Fig.6-5A-5
Fig.6-5B-1
Fig.6-5B-2
Fig.6-5B-3
Fig.6-5B-4
Fig.6-5B-5
Fig.6-5C-1
Fig.6-5C-2
Fig.6-5C-3
Fig.6-5C-4
Fig.5-5C-4
Data error
10 cm
5 cm
0(cm)
Thickness (mm)
Width (cm)
10
0

Figure 6-7: Digital elevation models (DEMs) of subaqueous single-flow experiments with (A) 30, (B) 50 and (C) 70 vol.% fines. Corresponding cross-section profiles (profile 1-5) include four fixed downstream positions at 25, 50, 75 and 100 cm, and an additional profile at the location of maximum levee thickness. All DEMs in Figure 6-7 are displayed using the same thickness scales, and all profiles in Figure 6-7 are plotted using the same horizonal and vertical scales. These profiles illustrate downstream variations in deposit thickness. The prominent asymmetric relief on the profiles corresponds to lateral levees, and the central areas between the lateral relief represent conduit deposits. The locations of the DEMs correspond to the single-flow deposits (30, 50 and 70 vol.%) in Figure 6-3. These profiles are derived from DEMs with a resolution of 0.2 mm. The DEMs in Figure 6-7A to C are presented using the same units and scales. Note, several localised photogrammetric reconstruction errors are present in the DEMs of the single 50 and 70 vol.% fines experiments (Figure 6-7B and Figure 6-7C). These errors occur in area where local image coverage and overlap were insufficient during image acquisition, resulting a lower density of matched points and poor constraints on the reconstructed surface elevation. Comparison with the original photographs and inspection of the reconstructed point cloud confirmed that these irregular patches are reconstruction artefacts. The artefact-affected areas were excluded from profile extraction and quantitative interpretation.

6.4.3 Grain-size distribution, composition and sphericity under different sediment mixtures

Grain-size distributions (GSDs) of the levees and the conduit deposits vary from 25 cm to 50 cm across all single-flow experiments (Figure 6-8). Left- and right- levees show similar GSDs in all single-flow experiments, are enriched in coarser particles, and approach the carborundum reference curve from 25 cm to 50 cm downslope (Figure 6-1C and Figure 6-8). In contrast, conduit deposits are enriched in finer particles and approach the fine ballotini reference curve from 25 cm to 50 cm (Figure 6-1C and Figure 6-8).

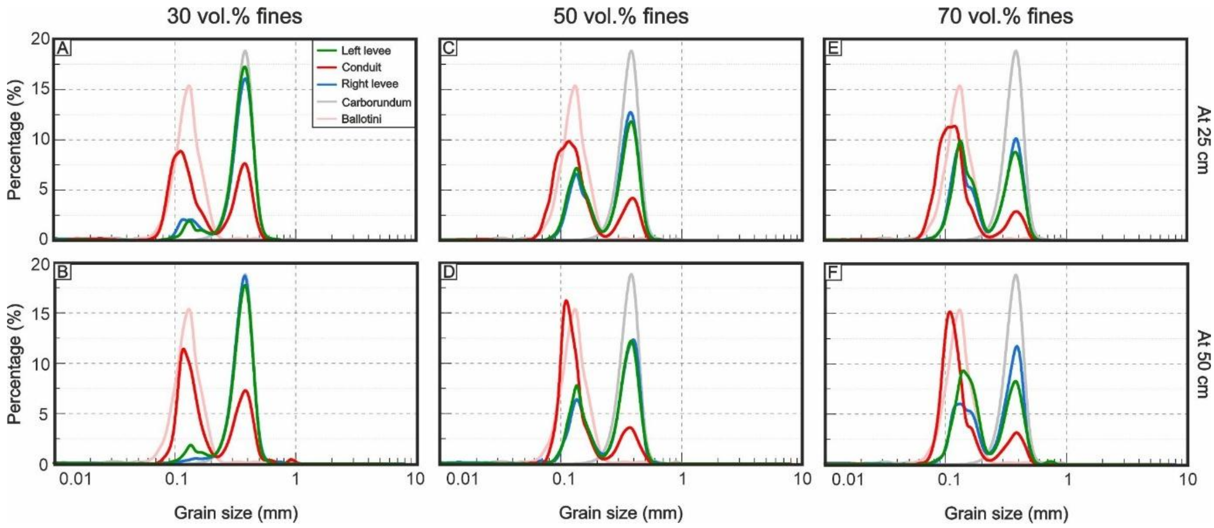

Figure 6-8: Grain-size distributions (GSDs) of subaqueous single-flow experiments with 30, 50 and 70 vol.% fines, showing the enrichment of coarse particles in lateral levees and the enrichment of fine particles in conduit deposits at downstream distances of 25 cm and 50 cm. The light curves (i.e., light red and light black) represent the referenced GSDs of ballotini and carborundum, respectively. The coloured curves show the GSDs of the left levee (marked in green), the central conduit deposits (marked in red), and the right levee (marked in blue).

Similar to GSDs, quantitative composition analysis also shows that levees are enriched in coarser particles, whereas conduit deposits are enriched in finer particles, with this composition contrast becoming more pronounced downslope (Table 6-3). For example, in the 30 vol.% fines cases, levee deposits consist of 86.5% carborundum and <13.5% fine ballotini at 25 cm, whereas the conduit deposits contain 58.6% fine ballotini, approximately twice that of the source mixture (Table 6-3). Downslope at 50 cm, levees further increase in coarse particles (>92.5% carborundum and <7.5% fine ballotini), while the conduit deposits increase in fines to 64.1% (Table 6-3). Similar downslope increases in fines are observed in the conduit deposits of the 50 and 70 vol.% fines experiments, from 75.2% to 83.8% and from 81.3% to 83.3%, respectively (Table 6-3). Levees become coarse downslope cm in the 70 vol.% experiment, increasing from 45.2-48.7% to 44.2-59.5% carborundum, whereas in the 50 vol.% experiment the coarse percentage remains broadly consistent downslope (from 60.1-65.1% to 61.8-65.5%; Table 6-3).

Table 6-3: Calculated fines of subaqueous single-flow experiments with 30, 50 and 70 vol.% fines, showing the fines percentage of the left levee, the conduit deposits and the right levee at 25 cm and 50 cm.

Fine ballotini (%) *(rnorm)*	**Left levee**	**Conduit deposits**	**Right levee**	***Sample location***

Single 30 fines	8.2 (0.017)	58.6 (0.082)	13.4 (0.017)	*25 cm*
	7.3 (0.018)	64.1 (0.055)	2.3 (0.012)	*50 cm*
Single 50 fines	39.9 (0.037)	75.2 (0.086)	34.9 (0.039)	*25 cm*
	38.2 (0.044)	83.8 (0.126)	34.5 (0.046)	*50 cm*
Single 70 fines	54.8 (0.054)	81.3 (0.129)	51.3 (0.041)	*25 cm*
	55.8 (0.087)	83.3 (0.137)	40.5 (0.049)	*50 cm*

Higher sphericity values characterise the conduit deposits, approaching the referenced value of 100% ballotini, whereas levees display lower sphericity close to that of 100% carborundum (Table 6-4). This sphericity contrast is overall consistent downslope (Table 6-4). Sphericity increases in both levees and conduit deposits with increasing fines fraction. From 30 to 50 and 70 vol.% fines experiments, the levee deposit sphericity increases from ~0.80 to 0.85-0.86 and 0.86-0.88, and conduit deposits sphericity increases from 0.9 to ~0.93 and 0.93-0.94 (Table 6-4). From 25 cm to 50 cm, sphericity of deposits remains consistent overall, with differences of <0.01 (Table 6-4).

Table 6-4: Sphericity of subaqueous single-flow deposits with 30, 50 and 70 vol.% fines mixtures, showing the sphericity of the left levee, the conduit deposits and the right levee at 25 cm and 50 cm.

Sphericity	Left levee	Conduit deposits	Right levee	*Sample location*
Single 30 fines	0.79	0.89	0.81	*25 cm*
	0.79	0.89	0.80	*50 cm*
Single 50 fines	0.86	0.93	0.85	*25 cm*
	0.85	0.93	0.85	*50 cm*
Single 70 fines	0.87	0.94	0.87	*25 cm*
	0.88	0.93	0.86	*50 cm*
		Reference value		
Fine ballotini		*0.96*		
Carborundum		*0.79*		

6.5 Subaqueous multiple flow results

6.5.1 Evolution of multiple flows

In all multiple-flow experiments (30, 50 and 70 vol.% fines), the initial flow (Run 1), similar to the single-flow experiment, underwent particle segregation and formed black coarse-enriched levees and white fine-enriched conduit deposits. The initial deposits provide a confined and erodible bed for subsequent flows. Successive flows (Runs 2-6) follow the pre-exiting flow pathway and interact with pre-existing deposits (Figure 6-9 and Figure 6-10), exhibiting higher velocities than the initial flow (Figure 6-11), undergoing lateral expansion (Figure 6-12), and re-establishing and lengthening levees (Figure 6-9, Figure 6-10, and Figure 6-13).

For example, in the multiple 30 vol.% fines experiments, Run 2 is confined within the pre-existing conduit formed during Run 1 (Figure 6-9A), shows a higher velocity than Run 1 (Figure 6-11A), and undergoes lateral expansion (Figure 6-9A and Figure 6-9B). This expansion becomes more pronounced downslope (Figure 6-9C), increasing from 1.1 and 1.3 times at 25 and 50 cm, respectively, to ~2 times at 75 cm and >3 times at 100 cm (Figure 6-12A). During expansion, flow entrains coarse particles from pre-existing levees leading to a higher proportion of coarse particles compared to the single flow (e.g., Figure 6-2C and Figure 6-9C). Once discharge decreases, the flow level lowers, and the levees sharpen along the active flow margin (Figure 6-7C to Figure 6-7E). As the flow head advances, levees lengthen downslope, establishing a wider conduit for particle transport (Figure 6-7C to Figure 6-7E and Figure 6-10A). Compared to the initial flow, the subsequent flow exhibits higher mobility and advances beyond the deposit of Run 1 (Figure 6-7D and Figure 6-7E). Subsequently, the flow head transforms from a confined shape to a bulbous form (Figure 6-9C, Figure 6-9D and Figure 6-9E), flow velocity decreases dramatically (Figure 6-11A), and thicker levees form behind the head (Figure 6-7E). With continued sediments throughput from upslope, the flow advances further downslope, forms thinner levees, and gradually exposes the fine-grained conduit (Figure 6-7F and Figure 6-7G). Modification of the levee geometry is observed, with upslope levees becoming narrower at the same locations compared to Run 1 (Figure 6-9G). The location of the thickest levees shifts downward, from the mid-slope (~40 cm) in Run 1 to further downslope (~70 cm) in Run 2.

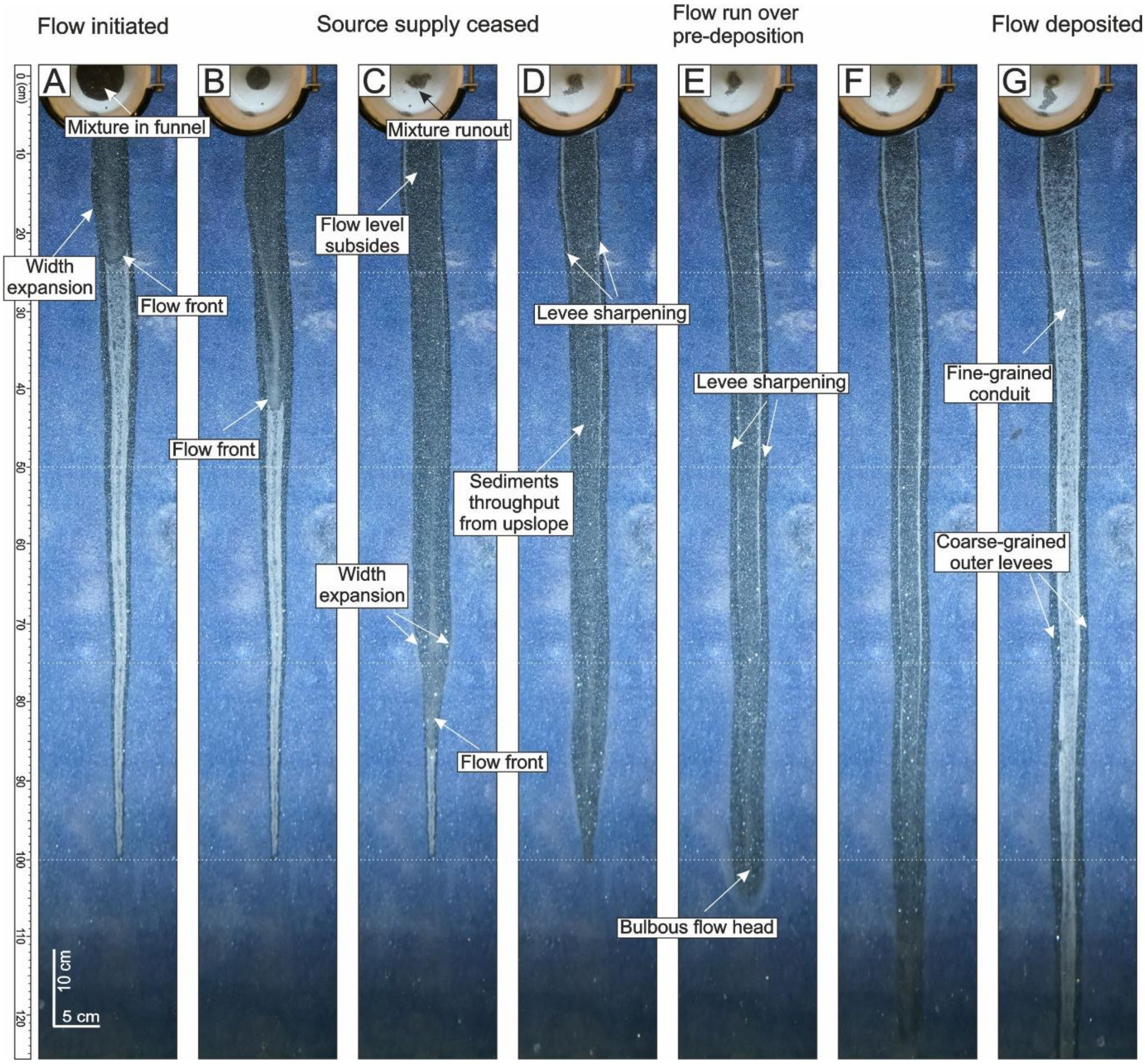

Figure 6-9: Evolution of Run 2 in subaqueous multiple-flow experiments with 30 vol.% fines, showing the process of flow expansion, particle remobilization and levee re-formation. (A) Flow initiation statge, with Run 2 following the pre-formed conduit from Run 1. (B) Flow transporte stage. (C) Mixture cessation stage, with the flow tranporting downslope to a narrower pre-formed conduit and undergoing pronounced lateral expansion. (D) Sediment throughput stage, with levee sharpening. (E) Run 2 extends beyond the pre-formed conduit, and the flow head develops a bulbous morphology. (F) Further levee sharpening, and (E) fine-enriched conduit deposited exposed.

With continued stacking (Runs 3-6), similar geometrical changes are observed, including the progressive increase of deposit width, the thinning of upslope levees, and the downslope migration of the thickest levee location (Figure 6-10).

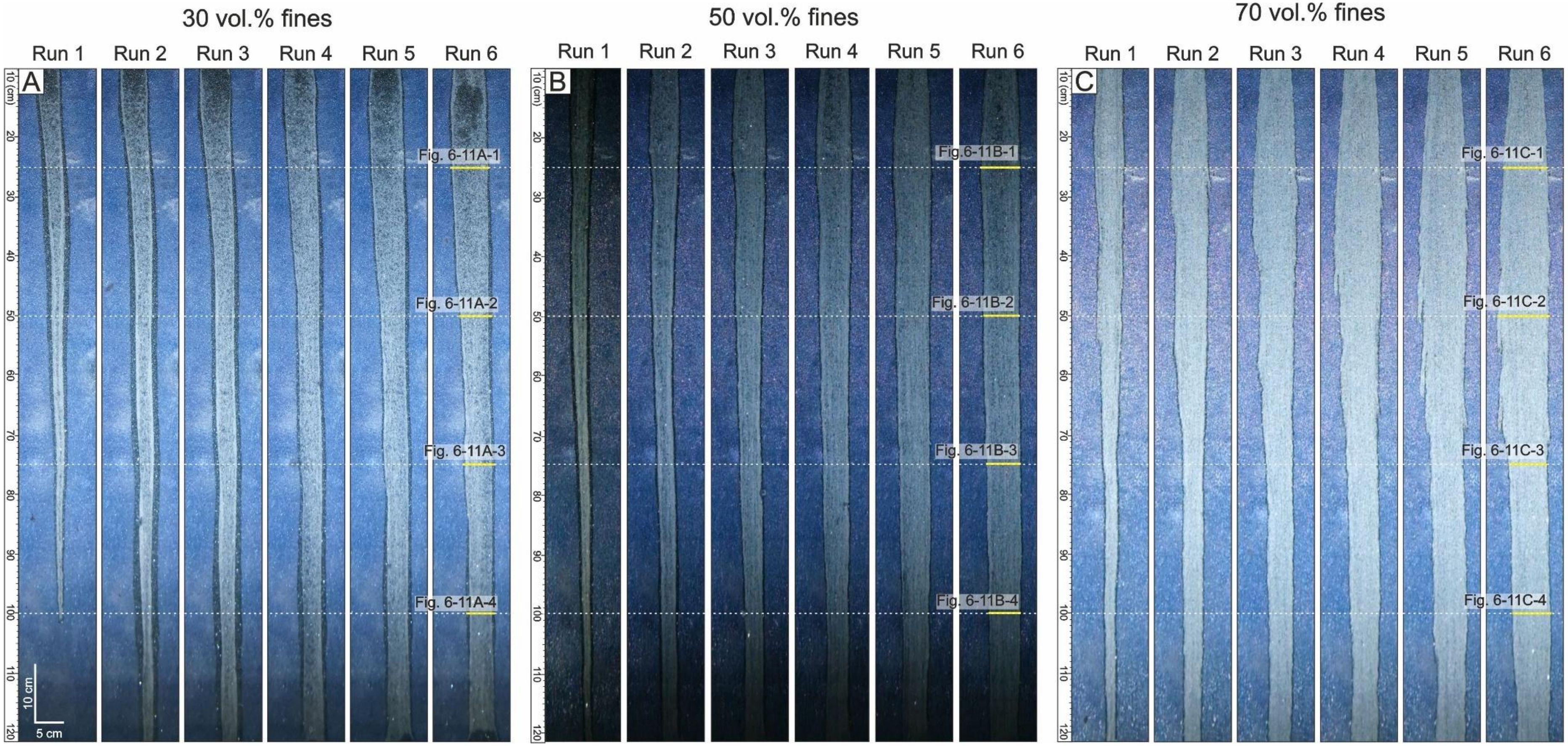

Figure 6-10: Top views of subaqueous multiple-flow deposits with (A) 30, (B) 50 and (C) 70 vol.% fines, showing the evolution of the deposits from Run 1 to Run 6. Run 2 of the subaqueous 30 fines multiple-flow deposits corresponds to the deposits shown in Figure 6-9G. The DEMs of subaqueous multiple-flow deposits after six runs are shown in Figure 6-13.

6.5.2 Flow velocity and deposit geometry changes

Comparison of the multiple flow experiments highlights commonalities in flow velocity, deposit width, levee thickness, and grain composition and sphericity trends.

6.5.2.1 Velocity

Flow velocity increases after the first run in all multiple experiments (30, 50 and 70 vol.% fines), with Run 2 or Run 3 showing the fastest velocity (Figure 6-11). Velocities of later runs (Runs 4 to 6) decrease slightly relative to Runs 2 and 3 but remain faster than Run 1 (Figure 6-11).

In the multiple 30 vol.% fines experiments, Run 1 has a runout distance of 101 cm and an average velocity of 0.56 cm/s, similar to the single 30 vol.% fines flow (0.63 cm/s; Figure 6-11A; Table 6-1). Runs 2 to 6 travel beyond the slope (Figure 6-10). In Run 2, the average velocity is 1.17 cm/s, a marked increase compared to Run 1 (Figure 6-11A). The flow slightly accelerates over the upper 73 cm, with velocity increasing from 1.53-1.55 cm/s at ~20 cm to 1.92 cm/s at 73 cm (Figure 6-11A). Between 73-101 cm, Run 2 initially passes through a narrower pathway, and then exhibits pronounced lateral expansion, decreases in velocity, and forms thicker levees (Figure 6-10A). Velocity decreases to 1.42 cm/s at 101 cm, lower than at 73 cm (1.92 cm/s; Figure 6-11A). Further downslope, beyond Run 1 deposits (>101 cm), flow velocity decreases sharply to 0.05 cm/s at 107 cm, where thick coarse-rich levees form, before increasing again to 1.31 cm/s at 120 cm (Figure 6-11A). Runs 3-6 show overall acceleration over the full downslope distance (Figure 6-10A and Figure 6-11A). Run 3 is fastest with an average velocity of 1.87 cm/s, comparable to the initial acceleration phase of Run 2 (Figure 6-11A). Runs 4-6 are progressively slower but remain faster than Run 1, with average velocity of 1.45 cm/s, 1.39 cm/s and 1.38 cm/s, respectively (Figure 6-11A).

The multiple 50 and 70 vol.% fines experiments show similar velocity evolution during successive events. In both cases, Run 1 decelerates downslope, whereas Runs 2-6 accelerate downslope, with the highest average velocity in the second run, followed by overall progressively lower average velocities in Runs 3-6 (Figure 6-11B and Figure 6-11C). In the multiple 50 vol.% fines experiments, the velocity of Run 1 decreases from 2.00 cm/s at ~13 cm to 0.37 cm/s at 110 cm, with an average velocity of 0.90 cm/s, similar to the corresponding single-flow experiment (0.89 cm/s; Figure 6-11B;

Table 6-1). In contrast, the second run accelerates over the entire slope, from 1.61 cm/s at 12 cm to 2.74 cm/s at 117 cm, with an average velocity of 2.14 cm/s (Figure 6-11B). The average velocity decreases in subsequent runs, with 1.82, 1.66, 1.53, and 1.46 cm/s in the third to sixth flows, respectively (Figure 6-11B).

In the multiple 70 vol.% fines experiments, the first run decelerates downslope, similar to the corresponding single-flow experiment (Figure 6-5C and Figure 6-11C). However, its average velocity is 0.83 cm/s, lower than the corresponding single-flow experiments (1.13 cm/s). Unlike the single-flow experiment, a local fluctuation is observed at the mid-slope of Run 1. Its velocity decreases from 1.48 cm/s at ~13 cm to the minimum of 0.38 cm/s at ~56 cm, followed by local increases downslope to 1.34 cm/s at 73 cm, before decreasing further downslope (Figure 6-11C). During this mid-slope fluctuation, the flow narrows downslope, decreasing from 3.52 cm wide at 56 cm to 2.65 cm wide at 73 cm (Figure 6-10C). Run 2 is fastest, with an average velocity of 1.63 cm/s (Figure 6-11C). Average velocities decrease in Runs 3 to 6 (1.56 cm/s, 1.44 cm/s, 1.19 cm/s and 1.3 cm/s, respectively).

In summary, the multiple 50 vol.% fines flows show the highest average velocities, followed by the multiple 70 and 30 vol.% flows (Figure 6-11). The multiple 30 vol.% fines experiments exhibit the largest increase in flow velocity from Run 1 (0.56 cm/s) to Run 3 (1.87 cm/s). In contrast, the multiple 70 vol.% fines experiments show the smallest velocity increase, from 0.83 cm/s (Run 1) to 1.63 cm/s (Run 2).

6.5.2.2 Deposit width and levee thickness

Deposit width: Deposit width increases progressively with successive runs in all multiple-flow experiments (30, 50 and 70 vol.% fines), with the most pronounced widening (up to 3 times increase) occurring during the second run. Subsequent runs (Runs 3-6) show only minor additional widening, typically on the order of ~1.0-1.3 times per run.

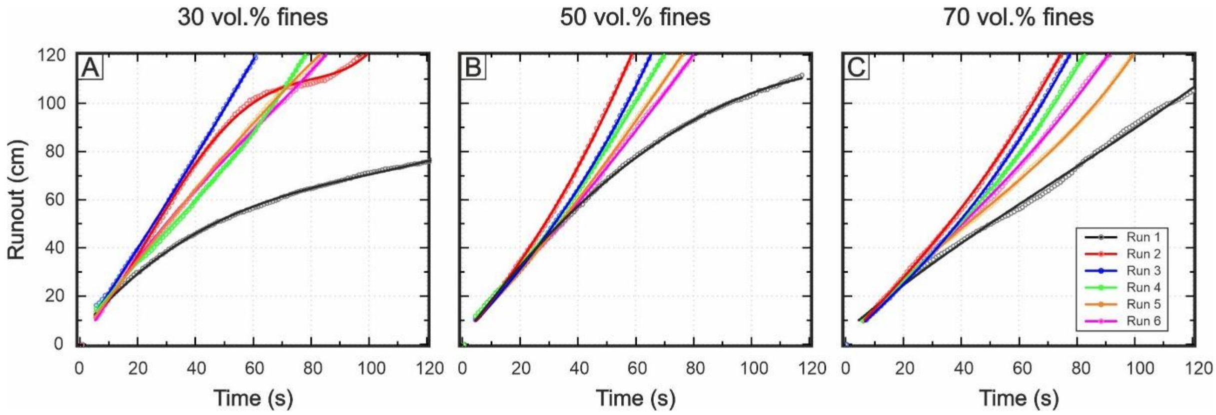

Figure 6-11: Runout distance versus time curves for successive subaqueous granular flows, with (A) 30, (B) 50 and (C) 70 vol.% fines. Empty circles represent measured runout data from Run 1 to Run 6, with the slope of each measured data sequence corresponding to the flow velocity. The gradient of each measured data curve reflects flow velocity. Coloured lines represent the trend lines simulated from the corresponding measured data. The deviations between the measured data and the trend lines reflecting local fluctuations in flow head velocity.

In the multiple 30 vol.% fines experiments, widening of the second flow (i.e., Run 2) is strongly enhanced, particularly in the downslope region (75-100 cm; Figure 6-12). Flow width of Run 2 increases modestly in the upslope region (1.1-1.3 times at 25 cm and 50 cm, respectively; Figure 6-12A). Further downslope, widening of flow width becomes more pronounced, nearly doubling at 75 cm (from 2.4 cm to 4.6 cm), and exceeding a threefold increase at 100 cm (from 0.9 cm to 4.0 cm; Figure 6-10A and Figure 6-12A). Subsequent runs (Runs 3-6) show minor widening, typically on the order of ~1.0-1.1 times per run (Figure 6-12A). In the multiple 50 vol.% experiments, the widening of Run 2 deposits is relatively uniform along the slope, increasing by 1.4 times at 25 cm, 1.1 times at 50 cm, 1.3 time at 75 cm, and 1.5 times at 100 cm (Figure 6-12B). In the multiple 70 vol.% fines experiments, widening of Run 2 deposits shows a slight downslope increase, increasing by 1.3 times at 25 and 50 cm, 1.4 times at 75 cm and 1.6 times at 100 cm relative to Run 1 (Figure 6-12C). Subsequent runs (Runs 3-6) in both cases show minor widening, with ~1.0-1.3 times increase per run (Figure 6-12B).

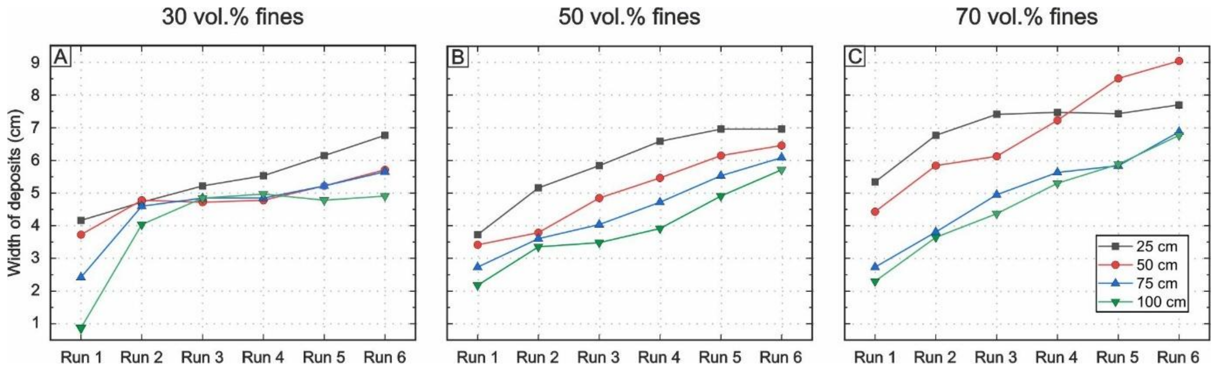

Figure 6-12: Deposit width versus successive experimental runs (i.e., Run 1 to Run 6) with (A) 30, (B) 50 and (C) 70 vol.% fines, measured at downstream locations of 25, 50, 75 and 100 cm.

Levee thickness: The levees after six runs are consistently thinner than those formed during the single-flow experiments (Figure 6-7 and Figure 6-13), which are equivalent to Run 1 of the multiple-flow experiments. In the multiple 30 vol.% fines experiments, levee thickness after the sixth run decreases dramatically, with a thickness of ~0.5-1.6 mm at 25, 50, 75 and 100 cm (Figure 6-13A-1 to Figure 6-13A-4), much thinner than the single-flow levees (up to 2 mm; Figure 6-7). This trend is also observed in the multiple 50 and 70 vol.% fines experiments. Levees in the multiple 50 vol.% fines experiment thin downslope, being 1-1.3 mm thick at 25 cm, ~0.6-0.8 mm thick at 50 and 75 cm, and 0.6-0.7 mm thick at 100 cm (Figure 6-13B-1 to -4), and are thinner than the single-flow levees (~1.0-2.0 mm; Figure 6-7). In the multiple 70 vol.% fines experiments, levees are relatively uniform, being ~0.5-0.8 mm thick across the entire slope (Figure 6-13C-1 to Figure 6-13C-4), thinner than the single 70 vol.% fines experiment (Figure 6-7).

During multiple flows, the depositional topography becomes progressively wider and thinner (Figure 6-10). Widening and levee thinning decreases with increasing fines fraction, with the biggest changes in multiple 30 vol.% fines experiments, followed by the 50 and 70 vol.% fines experiments.

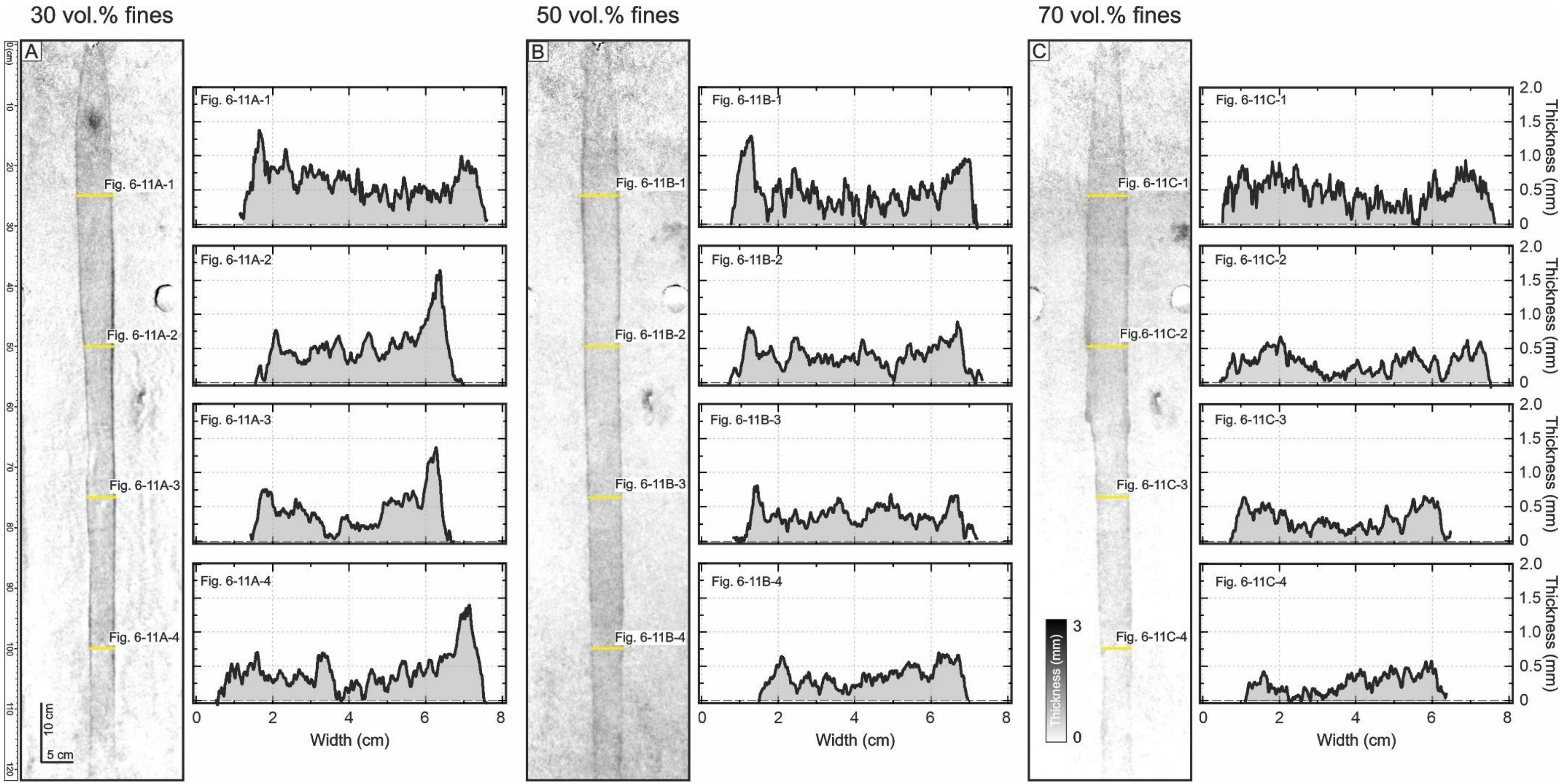

Figure 6-13: Digital elevation models (DEMs) of multiple-flow deposits (after six runs), with (A) 30, (B) 50 and (C) 70 vol.% fines. Their corresponding cross-section profiles (profile 1-4) are measured at 25, 50, 75 and 100 cm, respectively, illustrating the downstream variation in deposit thickness. The prominent asymmetric relief on the profiles corresponds to levees, and the middle regions between the lateral relief represent conduit deposits. The DEMs correspond to the Run 6 deposits in Figure 6-10. These profiles (profile 1-4) are derived from DEMs, with a resolution of 0.2 mm for subaqueous multiple-flow deposits.

6.5.2.3 Grain-size distribution, composition and sphericity

Grain-size distributions (GSDs) of the levees and conduit deposits vary from 25 cm to 50 cm across all multiple-flow experiments (Figure 6-8). Left and right levees show similar GSDs in all multiple-flow experiments, are enriched in coarser particles, and approach the carborundum reference curve from 25 cm to 50 cm downslope (Figure 6-1C and Figure 6-8). In contrast, conduit deposits are enriched in finer particles and approach the fine ballotini reference curve from 25 cm to 50 cm (Figure 6-1C and Figure 6-8). In contrast to the bimodal distribution of the single-flow conduit deposits, the GSDs of multiple-flow conduit deposits show a bimodal distribution with a subsidiary peak in the fine-grained range (Figure 6-8 and Figure 6-14).

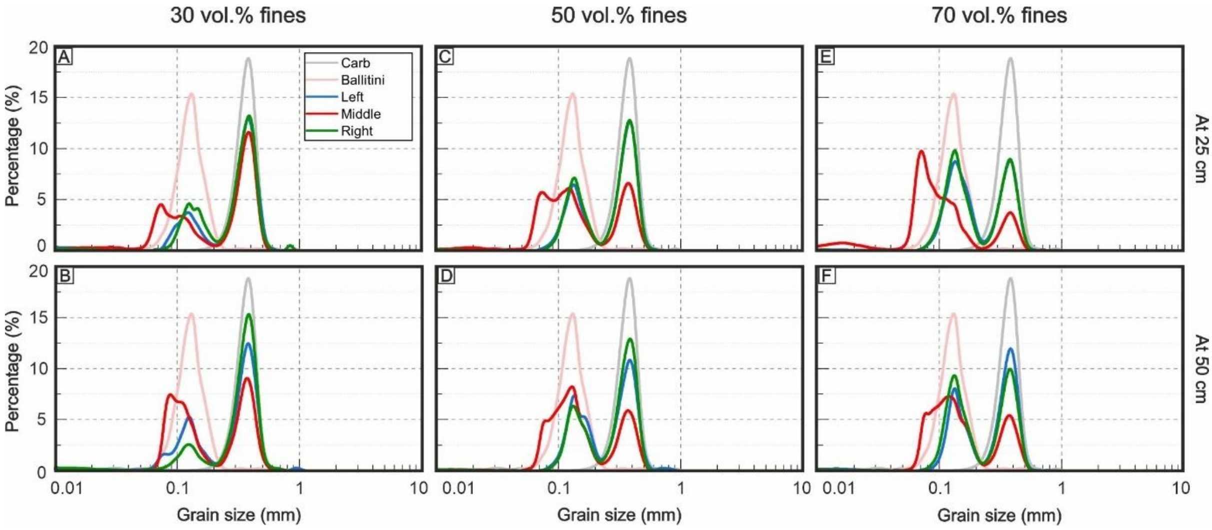

Figure 6-14: Grain-size distribution of subaqueous multiple flow deposits (after six experimental runs) with varying initial fines fraction (30, 50 and 70 vol.%), showing the enrichment of coarse particles in lateral levees and the enrichment of fine particles in conduit deposits at downstream distances of 25 cm and 50 cm. The light curves (i.e., light red and light black) represent the referenced GSDs of ballotini and carborundum, respectively. The coloured curves show the GSDs of the left levee (marked in green), the central conduit deposits (marked in red), and the right levee (marked in blue).

Compared with single-flow deposits, the composition of multiple-flow deposits after six runs approaches the initial mixtures at both 25 and 50 cm (Figure 6-15). From 25 cm to 50 cm, conduit deposits after multiple flows are enriched in fines but remain lower than the corresponding single flow, whereas multiple-flow levees overall slightly increase in fines (Figure 6-15).

In the multiple 30 vol.% fines experiments, the composition of both levees (27.5-29.6% fines) and conduit deposits (32% fines) at 25 cm is similar to the initial mixture (30%;

Figure 6-15B; Table 6-5). Downslope to 50 cm, the left levees decrease in fines (17%), whereas the right levee slightly increase in fines (32.8%), locally exceeding the fines percentage in initial mixture (Table 6-5). The conduit deposits enrich in fines to 48.4%, but remain lower than in the single flow (Figure 6-15; Table 6-5). In the multiple 50 vol.% fines experiments, levee composition varies downslope, with the left levee decreasing in fines (from 37.3% to 34.2%), whereas the right levee increases in fines (from 36.1% to 42.5%; Figure 6-15; Table 6-5). The conduit deposits increase in fines downslope (from 57% to 64.6%), remaining lower than the single-flow conduit deposit (Figure 6-15; Table 6-5). In the multiple 70 vol.% fines, both side levees decrease in fines from 25 cm to 50 cm, from 56.6% to 51.6% in left levee and from 54.9% to 40.5% in right levee (Figure 6-15; Table 6-5). The right levee composition is same as the single flow (Table 6-5). Conduit deposits increase in fines, from 63.3% at 25 cm to 65.5% at 50 cm, lower than the single flow and even lower than in the initial mixture (70%; Figure 6-15; Table 6-5).

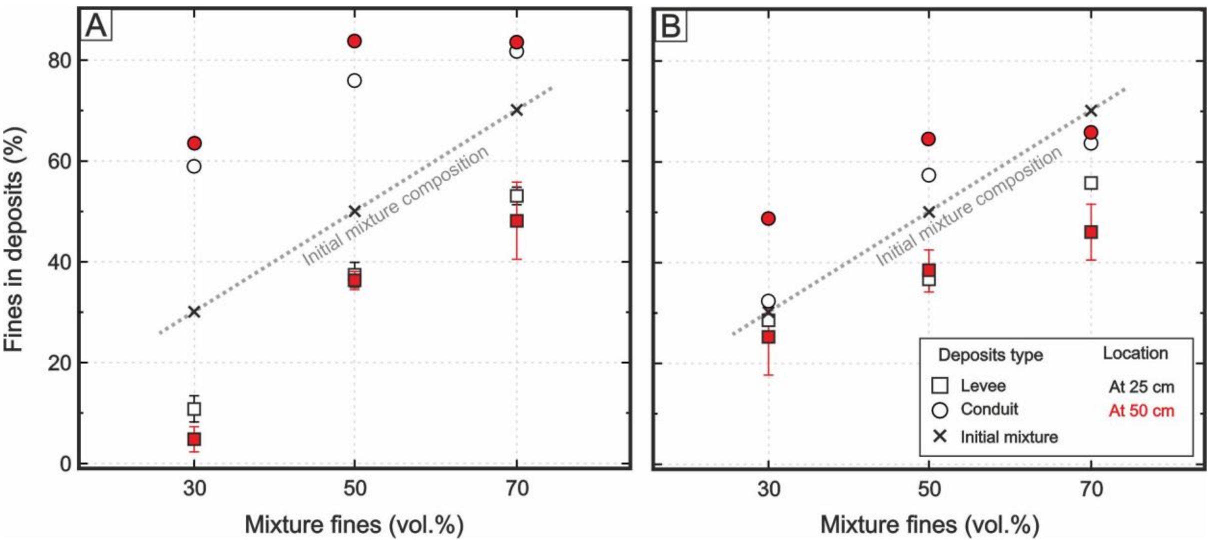

Figure 6-15: Composition analysis of subaqueous (A) single-flow deposits and (B) multiple-flow deposits (after six runs) with varying initial fines fraction (30, 50 and 70 vol.%), measured at downstream locations of 25 and 50 cm. The figure illustrates the downstream variation in composition of levee (circles) and conduit (squares) deposits. The two ends of each error bar represent the fines percentage in the left and the right levee deposits. The red square corresponds to the average fines percentage of the left and right levees.

Table 6-5: Calculated compositions of subaqueous multiple-flow deposits at 25 cm and 50 cm, with initial fines fraction of 30, 50 and 70 vol.%, showing the fine percentages of lateral levees and conduit deposits.

Fine ballotini (%) *(rnorm)*	**Left levee**	**Conduit deposits**	**Right levee**	**Sample location**
Successive 30 fines	29.6 (0.028)	32.0 (0.091)	27.5 (0.029)	*25 cm*

	17.7 (0.019)	48.4 (0.111)	32.8 (0.027)	*50 cm*
Successive 50 fines	37.3 (0.038)	57.0 (0.112)	36.1 (0.026)	*25 cm*
	34.2 (0.042)	64.6 (0.073)	42.5 (0.050)	*50 cm*
Successive 70 fines	56.6 (0.038)	63.3 (0.198)	54.9 (0.047)	*25 cm*
	51.6 (0.044)	65.5 (0.094)	40.5 (0.049)	*50 cm*

In all multiple flow cases, levee deposits have lower sphericity than the conduit deposits, and both increase in sphericity with increases in the fines fraction (Figure 6-16). The highest sphericity is observed in the 70 vol.% fines deposits, followed by the 50 vol.% fines and the 30 vol.% fines deposits (Figure 6-16). Sphericity of deposits is overall comparable at 25 cm and 50 cm, with very minor variation (<0.02). For example, in the multiple 30 vol.% fines experiments, sphericity in levees is consistently 0.82-0.83 at both 25 cm and 50 cm (Table 6-6). Compared with single-flow deposits, the sphericity contrast between levees and conduits in multiple-flow experiments is overall less pronounced (Figure 6-16).

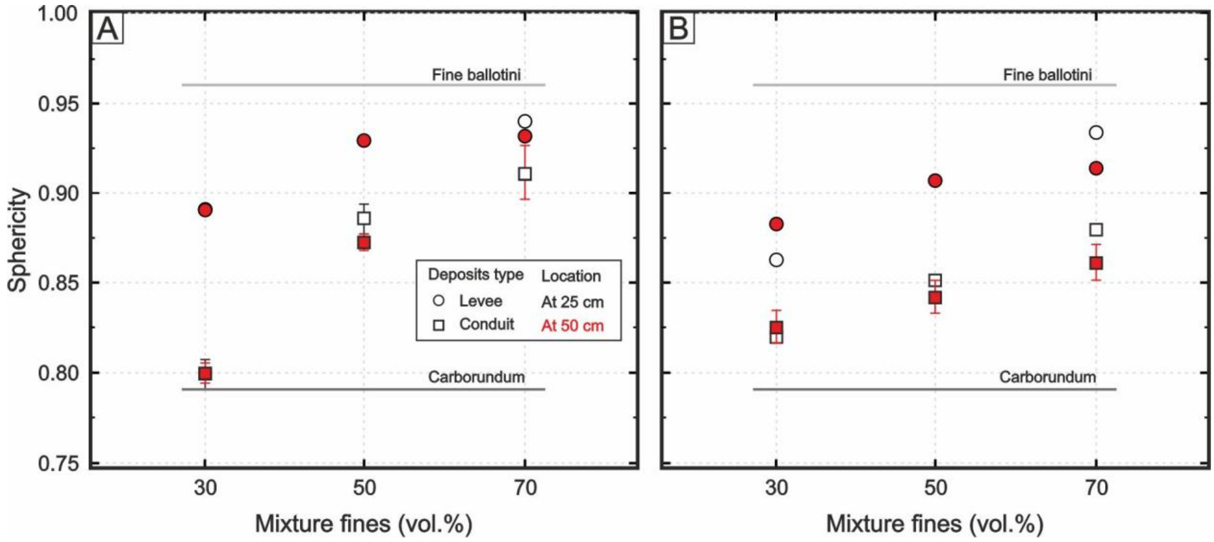

Figure 6-16: Sphericity analysis of subaqueous (A) single-flow deposits and (B) multiple-flow deposits (after six runs) with varying initial fines fraction (30, 50 and 70 vol.%), measured at downstream locations of 25 and 50 cm. The figure illustrates the downstream variations in sphericity of levee and conduit deposits, as well as the sphericity comparison between multiple- and single-flow deposits.

Table 6-6: Sphericity of samples from subaqueous 30, 50 and 70 vol.% fines multiple-flow deposits measured at 25 cm and 50 cm.

Sphericity	Left levee	Conduit deposits	Right levee	*Sample location*
Successive 30 fines	0.83	0.86	0.82	*25 cm*
	0.82	0.88	0.83	*50 cm*
Successive 50 fines	0.85	0.91	0.85	*25 cm*

	0.83	0.91	0.85	*50 cm*
Successive 70 fines	0.88	0.93	0.88	*25 cm*
	0.87	0.91	0.85	*50 cm*
		Reference value		
Fine ballotini			*0.96*	
Carborundum			*0.79*	

6.5.3 Net change between the single- and multiple-flow deposits

Changes in depositional patterns are quantified by comparing the areas of the cross-sectional profiles after Run 6 to the single-flow experiments (equivalent to Run 1). In the 30 vol.% fines experiments, net profile changes show a transition from net deposition (+0.14 cm^2) at 25 cm, through net erosion (-0.02 cm^2) at 50 cm, to net deposition (+0.06 and 0.26 cm^2) at 75 cm and 100 cm (Figure 6-17 and Figure 6-18; Table 6-7). In the 50 and 70 vol.% fines experiments, net deposition occurs at all measured locations, with lower values at 50 and 75 cm and higher values at 25 and 100 cm. In the 50 vol.% fines experiments, net deposition decreases from +0.11 cm^2 at 25 cm to 0.07 cm^2 at 50 cm and 0.03 cm^2 at 75 cm, before slightly increasing to 0.04 cm^2 at 100 cm (Table 6-7). In the 70 vol.% fines experiments, net deposition decreases from 0.09 cm^2 at 25 cm, to 0.01 cm^2 at 50 cm, and then increases to 0.04 cm^2 at 75 cm and 100 cm (Table 6-7).

In summary, after six 15 cm^3 flows, all experiments result in net deposition at 25 and 100 cm, and the amount of net deposition overall decreases with increasing fines fraction (Figure 6-18; Table 6-7). In contrast, at 50 and 75 cm, there is either net erosion (30 vol.% fines) or minor net deposition (50 and 70 vol.% fines; Figure 6-18; Table 6-7). The variance in net profile changes reflects a downslope transition that decreases in net deposition upslope and increases in net deposition downslope.

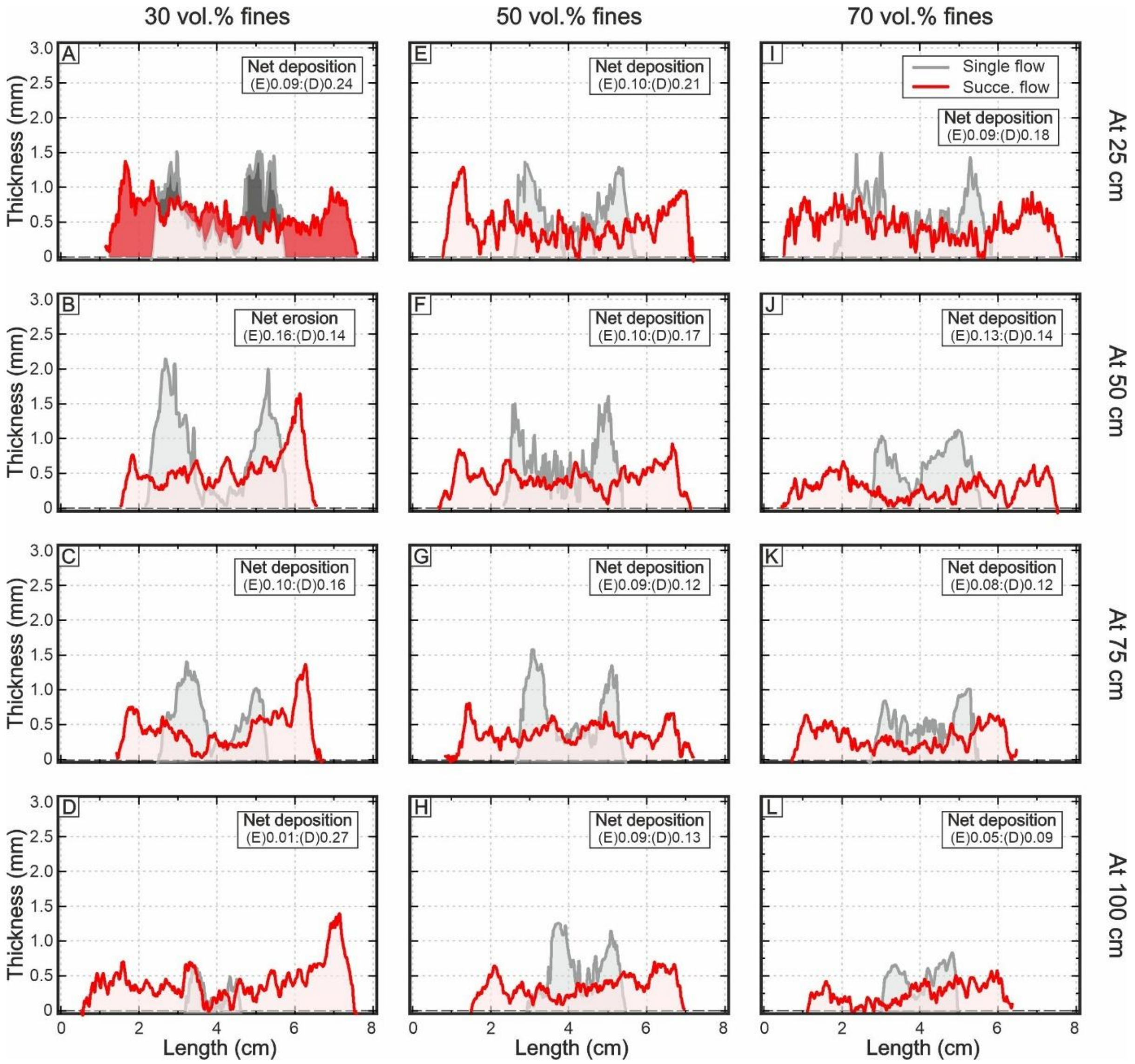

Figure 6-17: Cross-section profiles of subaqueous single- and multiple-flow deposits (after six experimental runs) with varying fines fraction, measured at downstream location of 25, 50, 75 and 100 cm, illustrating the downstream variation in deposit thickness. The prominent asymmetric relief on the profiles corresponds to levees, and the middle regions between the lateral relief represent conduit deposits. Net erosion area (E) of the profiles correspond to the area of single-flow deposits that was net eroded by successive flows, marked by dark grey shadow area in Figure 6-13A. Net deposition area (D) of profiles correspond to the additional net depositional area of successive-flow deposits relative to the single-flow deposits, marked by the dark red shadow area in Figure 6-13A. Thus, the net variance of successive profile relative to single profile = net deposition area (D) - net erosion area (E). A positive value indicates net deposition by the successive flows relative to the single-flow deposits, while a negative value indicates net erosion. The locations of single-flow deposit profiles are outlined in Figure 6-7, and the successive-flow deposits are shown in Figure 6-13. These profiles are derived from DEMs with a resolution of 0.2 mm.

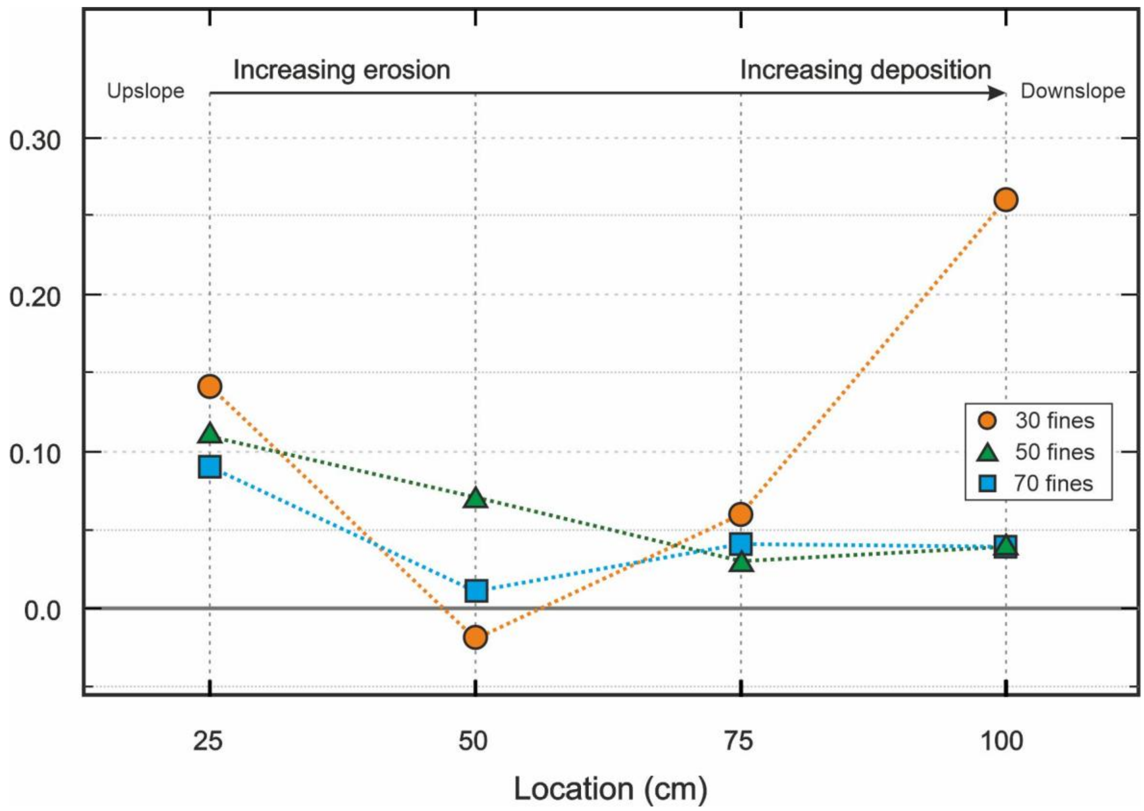

Figure 6-18 Net profile change of subaqueous multiple-flow deposits (after six runs) relative to equivalent single-flow deposits with varying fines fraction (30, 50 and 70 vol.%), measured at downslope locations of 25, 50, 75 and 100 cm. The figure illustrates the erosion and deposition changes downslope. Net profile change is calculated as the variance of profile of multiple-flow deposits relative to single-flow profile = net deposition area (D) - net erosion area (E), as shown in Figure 6-17. A positive value of net profile change indicates net deposition after successive flows, while a negative value indicates net erosion relative to the single-flow deposits.

Table 6-7: Net erosion and net deposition area of multiple flows compared with single flow as a function of fines content and downslope position (25, 50, 75 and 100 cm). D = net deposition area, and E = net erosion area, as shown in Figure 6-17.

	Net change* (erosion area & deposition area) /cm^2	**30 vol.% fines**	**50 vol.% fines**	**70 vol.% fines**
Location	25 cm	+0.14 (E0.09 & D0.24)	+0.11 (E0.10 & D0.21)	+0.09 (E0.09 & D0.18)
	50 cm	-0.02 (E0.16 & D0.14)	+0.07 (E0.10 & D0.16)	+0.01 (E0.13 & D0.14)
	75 cm	+0.06 (E0.10 & D0.16)	+0.03 (E0.09 & D0.12)	+0.04 (E0.08 & D0.12)
	100 cm	+0.26 (E0.01 & D0.27)	+0.04 (E0.09 & D0.13)	+0.04 (E0.05 & D0.09)

Net profile change* = net deposition area (D) - net erosion area (E); comparing the multiple-flow deposits after sixth run relative to single flow deposits. Positive values represent net deposition, and negative values mean net erosion.

6.6 Discussion

6.6.1 Particle segregation processes in subaqueous setting

Particle segregation occurs within subaqueous flows across all single-flow experiments. The formation of coarser and less spherical carborundum-rich levee deposits and finer and more spherical ballotini-rich conduit deposits (Figure 6-8; Table 6-3 and Table 6-4) suggests segregation in subaqueous flows is controlled by particle mobility.

Observations of flow evolution show that coarser, low-sphericity particles (carborundum) are concentrated at the flow surface and transported toward the advancing flow front (Figure 6-2A to Figure 6-2D), whereas fine ballotini-rich conduit deposits are gradually exposed at lower levels within the flow (Figure 6-2C to Figure 6-2E). This behaviour is consistent with grain size-driven segregation observed in subaerial granular and debris flows (e.g., Savage and Lun, 1988; Johnson et al., 2012; Kokelaar et al., 2014; Gray, 2018). The upward migration of coarse particles is controlled by kinetic sieving and squeeze expulsion. Smaller particles preferentially percolate into voids that open beneath them, and in turn lever the larger particles upward toward the flow surface by instantaneous force imbalances (Savage and Lun, 1988; Gray and Thornton, 2005). As the flow propagates downslope, the coarse-enriched surface layer is advanced toward the flow front by velocity shear through the depth (e.g., Johnson et al., 2012; Gray, 2018), leading to progressive accumulation of coarse particles in the advancing head, as evidenced by the increasingly bulbous morphology of the head (Figure 6-2A and Figure 6-2B). Within the head, particles would undergo recirculation (e.g., Gray and Ancey, 2009; Gray and Kokelaar, 2010), during which coarse particles follow helical spiral trajectories within the flow head and are progressively transported toward the flow margins (Johnson et al., 2012). Near the flow margins, where velocities are lower than the advancing front, coarse particles cease recirculation and are left behind by the advancing flow front (Johnson et al., 2012). Following passage of the bulbous flow front, these laterally displaced coarse particles are deposited along the margins, forming carborundum-enriched levees behind the flow head, as directly observed in Figure 6-1D and Figure 6-2B to -2D. The experimental results of lower sphericity levees and higher sphericity conduit deposits (Table 6-4) suggests that particle shape may exert an additional control on segregation, albeit particle size and shape are tightly coupled in these experiments making it difficult to separate out their relative influences. Considering process dynamics, low-sphericity (more blocky) particles, due to their sharper corners, exhibit larger and faster energy dissipation and poor mobility, for a given size, compared to high-sphericity (more rounded) particles (Pereira and Cleary, 2017). This poor mobility may restrict rotational dynamics and lead to the deposition of the slowest moving particles out of the shear zone (Pereira and Cleary, 2017), thereby contributing to the formation of levees.

All subaqueous runs achieve runout distances exceeding 100 cm (Figure 6-3 and Figure 6-4), whereas the runout of equivalent subaerial flows is < 80 cm (Kokelaar et al., 2014). The experimental subaqueous single flows exhibit longer runout distances and narrower flow widths, compared with the equivalent subaerial single flow experiments presented by Kokelaar et al. (2014) (Figure 6-5), indicating that segregating granular flows are more mobile in subaqueous settings. The enhanced mobility is attributed to the presence of interparticle fluid, which reduces basal friction (Iverson et al., 2010), thereby promoting higher flow velocities. Higher velocities can increase downslope momentum relative to lateral momentum, thereby contributing to longer runout and narrower deposit width in the subaqueous flows.

6.6.2 Why does fluctuation occur in flow head velocity?

DEMs reveal that the thickest levees occur at mid-slope in the single-flow deposits (Figure 6-7). This relationship is interpreted to record the downstream evolution of particle segregation and flow mobility. The levee thickness is controlled by the geometry and composition of the flow head. Levees are thickest where the flow head is steepest. Levees become enriched in carborundum downslope (Figure 6-15), which suggests the progressive enrichment of coarse particles in the flow front during downslope segregation. Thus, the flow front thickens downstream, resulting in the formation of progressively thicker levees, until coarse particle accumulation at the flow front reaches a maximum. The coarse particles tend to be more resistant to motion, thus the accumulation of coarse particles within the flow head increases frontal resistance and thereby reduces flow mobility, as shown in the observed decrease in velocity associated with levee thickening (Figure 6-3 and Figure 6-5). This increased frontal resistance can be alleviated by lateral transport of coarse particles out of the downstream-vertical plane, toward the sides of the flow, to form lateral levees (Johnson et al., 2012; Edwards et al., 2023).

When the source supply decreases or ceases, the flow level in the channel subsides (Figure 6-2C), which causes the transfer of particles to the flow front to decrease due to decreased velocity shear through the lower flow depth (Gray, 2018). The flow front decreases in height, and associated lower carborundum supply, therefore leading to levees decreasing in height downslope. The flow head with reducing proportion of coarse particles shows higher mobility and consequently flow velocity increases (e.g., Edwards et al., 2023). This explains the slight increase in flow velocity observed downslope of the thickest levees. The velocity increase after thickest levee formation is mostly clearly observed in the single 30 vol.% fines experiments, with the thickest levees increasing dramatically, up to 67%, compared to adjacent upslope levees (2.5 mm at 38 cm relative to 1.5 mm at 25 mm; Figure 6-5B and Figure 6-7; Table 6-1). The magnitude of levee thickening decreases in other flows with higher fines fractions, with a ~20% increase in single 50 vol.% levees and <50% increase in the single 70 vol.% levees (Table 6-1). This decrease in the magnitude of levee thickening explains why the fluctuation is not noticeable in intermediate fines fraction flows. In the higher fines mixtures (i.e., 80-100 vol.%), velocity fluctuation becomes overall more pronounced (Figure 6-5B). These flows with high fines-to-coarse ratio show less segregation, forming thinner levees and thus are more weakly self-confinement in turn promoting lateral expansion. As the flow expands, reduced flow thickness and increased basal interaction enhance fictional dissipation, leading to a downstream decrease in velocity. Further downslope, flow narrowing occurs, for instance in the single 100 vol.% fines experiments, flow width decreases by 29 % (from 4.4 cm to 3.4 cm wide) from 53 cm to 64 cm (Figure 6-3), during which flow velocity shows a minor increase (Figure 6-5B).

Maximum levee thickness decreases with increasing fine fractions of mixtures, decreasing from 2.5 mm in 30 vol.% fines, to 1.8 mm in 50 vol.% fines and <1.5 mm thick in 70 vol.% fines (Figure 6-7). Reduced contrast in particle size and shape in the mixtures limits segregation at the flow front and reduces the supply of coarse particles to the flow margins, resulting in thinner levees. Increasing the spherical fines fraction could also reduce friction between particles thereby enhancing flow mobility. The observed mobility of subaqueous flows therefore reflects a balance between segregation-driven levee development that promotes flow confinement, and fines-related internal friction that enhances flow mobility. This provides a plausible explanation for the higher mobility observed in flows containing 60-70 vol.% fines compared with flows containing either higher or lower fines fractions (Figure 6-5B).

6.6.3 The evolution of particle segregation in multiple experiments

Observations of photographs show the evolution of multiple granular flows, characterised by progressive widening of deposits, thinning of upslope levees and thickening of downslope levees with successive runs (Figure 6-10). Net profile changes show a transition, from decreased net deposition upslope to increased net deposition downslope, in the multiple-flow deposits relative to single-flow deposits (Figure 6-18). Together, these morphological changes suggest a dynamic interaction between successive granular flows and pre-existing deposits, through upslope particle entrainment and remobilisation and downslope redeposition. Particle segregation remains active throughout this process, as evidenced by the presence of coarse-enriched levees and fine-enriched conduits (Figure 6-13 and Figure 6-14), although the levee thickness is less pronounced than in single-flow experiments.

(1) Upslope erosion and particle remobilisation

Downstream acceleration and enhanced erosion: During multiple-flow evolution, the initial flow (Run 1), equivalent to the single-flow experiments, establishes coarse-enriched levees and fines-enriched conduit deposits through effective particle segregation. This configuration acts as an erodible and laterally confined substrate for subsequent flows (Figure 6-19A). Subsequent flows show enhanced mobility relative to the initial flow, as evidenced by increased velocities and runout distances in Runs 2-6 (Figure 6-11). The enhanced mobility of subsequent flows is attributed to the presence of the lateral levees that limit lateral spreading, and the fines-enriched conduit deposits that provides a sheared low friction channel base lining (Edwards et al., 2023). The correlation between flow mobility and the pre-existing low-friction conduit can be further supported by the observations of the second run of the multiple 30 vol.% fines experiments, where flow velocity decreases rapidly beyond the extent of pre-existing conduit deposits (Figure 6-10A and Figure 6-11A).

The decrease in basal friction, due to pre-existing low-friction conduit deposits, explains the overall acceleration in successive flows. The increasing velocity during flow acceleration can increase substrate erosion downstream, and successive events further enhance the phenomenon, as shown in the increased net erosion from 25 cm to 50 cm across all multiple-flow experiments (Table 6-7). The substrate erosion is particularly pronounced in the conduit deposits of the multiple 70 vol.% fines experiment, where fines percentage in the conduit deposits is lower than the initial mixture composition while the levees remain coarse-enriched (Figure 6-15B). This also shows a preferential export of fines beyond the slope during multiple flows. Subaerial debris-flow experiment measurements suggest that the velocity of the advancing flow centre is higher than the flow margin (Johnson et al., 2012). The higher velocity in the flow centre, together with higher mobility of fine particles in the conduit, contributes to preferential entrainment of fine particles during upslope remobilisation. The preferential loss of mobile fines beyond the conduit may further modify the grain-size distributions, as shown by the subsidiary peak developed on the fine-grained range of the bimodal GSDs of multiple-flow conduit deposits (Figure 6-14).

Reduced segregation during flow bulking: The composition of the multiple-flow deposits in the upslope region is closer to the initial mixtures than the single-flow deposits (Figure 6-15). This suggests that the strong particle segregation developed during a single flow is substantially reduced after successive flows. The pre-deposited levees are eroded and entrained by subsequent flows during flow widening. Observations from photographs suggest that successive flows gain additional coarse particles through levee erosion (Figure 6-2C and Figure 6-9C). This levee entrainment, enhanced by flow acceleration, increases downstream particularly when passing through the mid-slope where the thickest levee deposits are present, resulting in substantial coarse particles accumulation in the subsequent flows. For example, at the source supply cessation stage, the fine-enriched conduit is exposed in the single flow with carborundum transported downstream (Figure 6-2C), whereas the carborundum remains abundant in Run 2 in the multiple 30 experiments without exposing the conduit. The increased coarse content in the flow would promote particle segregation and re-establishment of levees downslope.

Compared with single-flow experiments, the levees after successive flows increase in fines percentage, but remain enriched in coarse material relative to the initial mixtures (Figure 6-15). These less coarse-enriched levees reflect the reduced segregation during multiple-flow evolution and the remobilisation of pre-existing deposits. In summary, a dynamic process of upslope erosion and remobilization over multiple flows is identified that acts against particle segregation. Therefore, the resulting deposits are not as well segregated as single flow deposits. This is likely exacerbated by the preferential export of fines beyond the ramp.

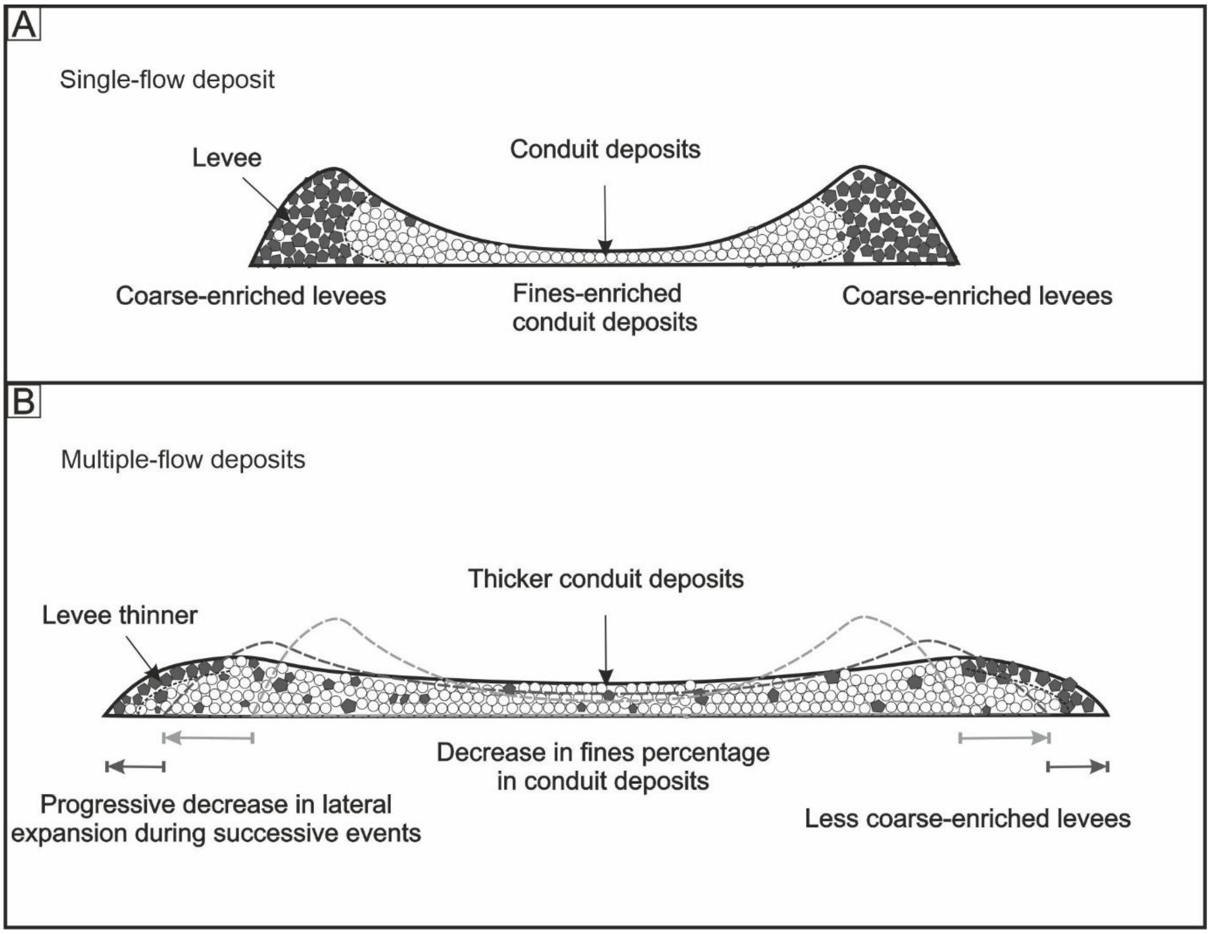

Figure 6-19: Schematic upslope cross-section of (A) the single-flow deposit, and (B) the multiple-flow deposits. The composite deposit of multiple flows results in thinner levees with a lower coarse percentage than in the single flow, albeit they remain coarse-enriched. The conduit deposit thickens, with a lower fines percentage than in the single flow deposits. The lateral expansion of the deposit decrease during successive events. The light grey dashed lines in Figure 6-19B represents the deposits from the initial flow (i.e., single flow deposit), and the dark grey dashed line in Figure 6-19B represent intermediate flow deposits. Light circle marks the finer, higher sphericity particles, and the dark pentagons mark the coarser, lower sphericity particles.

(2) Downslope segregation and particle redeposition

In the downslope, the flows enter the downslope narrowing conduit at high velocities, and undergo pronounced lateral expansion, which causes a downstream decrease in velocity. This is evidenced in the second run of multiple 30 vol.% experiments, where velocity decreases beyond ~73 cm (Figure 6-11A), coinciding with marked flow expansion, widening from ~2 times at 75 cm to >3 times at 100 cm, much higher than upslope positions (no more than 1.3 increase across the initial 50 cm; Figure 6-10A and Figure 6-12A). Decreasing flow velocity explains the weakening substrate erosion in the downslope, allowing segregation to become dominant in the downstream. The slower flow, combined with higher coarse fraction from upslope remobilisation, promotes the re-distribution of remobilised coarse particles and the formation of thicker levees downslope, as shown in Figure 6-9D to 7G. Observations from photographs suggest that, during successive flows, upslope levee deposits are progressively eroded during flow widening, and the remobilised particles from upslope entrainment are redeposited further downslope (e.g., Runs 1-3 in Figure 6-10A). This repeated redistribution during successive events promotes downslope levee progradation, causing the location of thickest levees to migrate progressively downslope, and eventually beyond the slope length (e.g., Runs 4-6 in Figure 6-10A).

This flow-deposit interaction progressively lengthens the runout with successive events, causing the location of the thickest levee (mid-slope) to migrate downstream. In turn, these processes help to explain the long run-out distance of multiple, or pulsed, debris flows in submarine settings.

The laboratory experiments presented here were not designed as dynamically scaled replicas of nature-scale submarine debris-flow deposits. Given the large scale of natural cases in submarine settings (e.g., tens of km long debris flow in Chapter 5), a true scaled modelling approach is untenable in laboratory subaqueous experiments, and purely ‘analogue’ models must be employed (Peakall et al., 1996; Paola et al., 2009; Choi et al., 2023). The unscaled experiments in this study are therefore regarded as process-based analogue models (e.g., Kokelaar et al., 2014). Their relevance to large natural deposits lies in the comparison of process and morphology, rather than in the direct upscaling of flow velocity, duration, deposit thickness or runout distance. The most appropriate comparisons are therefore based on scale-independent or normalised characteristics, including the development of lateral levees/enrichment of coarser particles in lateral margins, the enrichment of finer particles in deposit conduit, and relative flow mobility (i.e., velocity and runout) with varying composition. In this sense, the experiments provide a basis for evaluating whether particle segregation occurs in subaqueous settings, and how the segregation-driven self-confinement processes influence the morphology of large-scale granular flow deposits and flow mobility, rather than a quantitative reconstruction of natural examples. On a purely practical basis, any attempt at scaling, irrespective of the broader modelling approach identified above, would be greatly hampered by the inability to measure the flow thickness and internal flow velocity (rather than the head velocity) which mean that key dimensionless variables such as Froude, flow Reynolds, and Shields numbers, cannot be calculated in the models (Peakall et al., 1996). Therefore, any upscaling for comparison against real world flows would be very limited.

6.7 Conclusions

This study uses physical experiments of subaqueous granular flows with different mixtures of two sediment types (i.e., coarser carborundum and finer ballotini), to advance understanding of particle segregation in submarine debris flows, and dynamic flow-substrate interactions. Novel multiple flow experiments are designed to examine the role of flow-deposit interactions to provide insights into flow mobility and evolution (e.g., velocity, width, runout distance) of self-confined debris-flows. I show flows self-channelize through the establishment of coarse-enriched levees and fine-enriched conduit deposits. This occurs in single and multiple subaqueous experimental granular flows and across all mixtures.

The systematic contrast between low-sphericity coarse-enriched lateral levees and high-sphericity fines-enriched conduit deposits suggests that particle segregation in subaqueous flows is controlled by the combination of size- and shape-relevant particle mobility. Compared with equivalent subaerial single flow experiments, subaqueous single flows exhibit higher mobility and narrower flow widths. The presence of interparticle fluid in the subaqueous experiment and the fine-grained flow-contact zones, reduces basal friction, thereby limiting basal shearing and promoting higher flow velocities, which contribute to longer runout and narrower flow width in the subaqueous flows. The maximum flow velocity attained in mixtures containing 60-70 vol.%.

The thickest levees in single flows form at intermediate downslope positions, such as the single 30 vol. % experiments, which increase 67% relative to the thickness of the upstream levees. As the flow propagates downslope, low-sphericity coarse particles are transported to the advancing head, leading to the formation of the bulbous morphology of flow head. Following the passage of the bulbous head, these coarse particles are displaced laterally and deposited along the flow margins, acting as the source to generate self-confining levees behind the head. Thus, levees are thickest where the flow head is thickest, corresponding to maximum accumulation of coarse particles within flow front. Increased fines fraction leads to thinner levees, consistent with less coarse supply to thinner flows heads, and thinner levees.

In multiple experiments, the levees after six runs are thinner than in single-flow experiments. Furthermore, the fines percentage decreases in the conduit deposits and increases in the levee deposits. During successive events, the composite deposits progressively widen, and flow velocity increases relative to the initial flow, with the maximum velocity occurring in the second or third runs. The evolution of subaqueous multiple granular flows is a dynamic flow-deposit process, involving upslope particle remobilisation and downslope redeposition during channel widening. The initial deposit establishes an erodible confined substrate through effective particle segregation. The presence of the lateral levees and the pre-deposited fines-enriched conduit deposits leads to the increased velocity of subsequent flows, thereby enhancing the substrate erosion and particle remobilisation in the upslope area. In the downslope area, the flows undergo pronounced lateral expansion, causing a downstream decrease in the velocity and the increase in segregation that promotes the re-distribution of remobilised coarse particles and the formation of thicker levees. This flow-deposit interaction acts against particle segregation. Nonetheless, over multiple flows, the composite deposit progressive lengthens the runout distance, and causes the location of thickest levee (mid-slope) to migrate downstream, which can help explain the long run-out distance of multiple, or pulsed, debris flows in submarine settings.

Chapter 7 Synthesis and future work

This chapter addresses the research questions that were raised in Chapter 1 within the context of the findings presented in Chapters 4-6 (Figure 7-1). This synthesis integrates evidence from seismic-well-tie, seismic interpretation and subaqueous physical experiments, to develop a comprehensive understanding of how flow-substrate interactions (i.e., lubrication, deposition and erosion) influence flow evolution processes and flow mobility in deep-water systems.

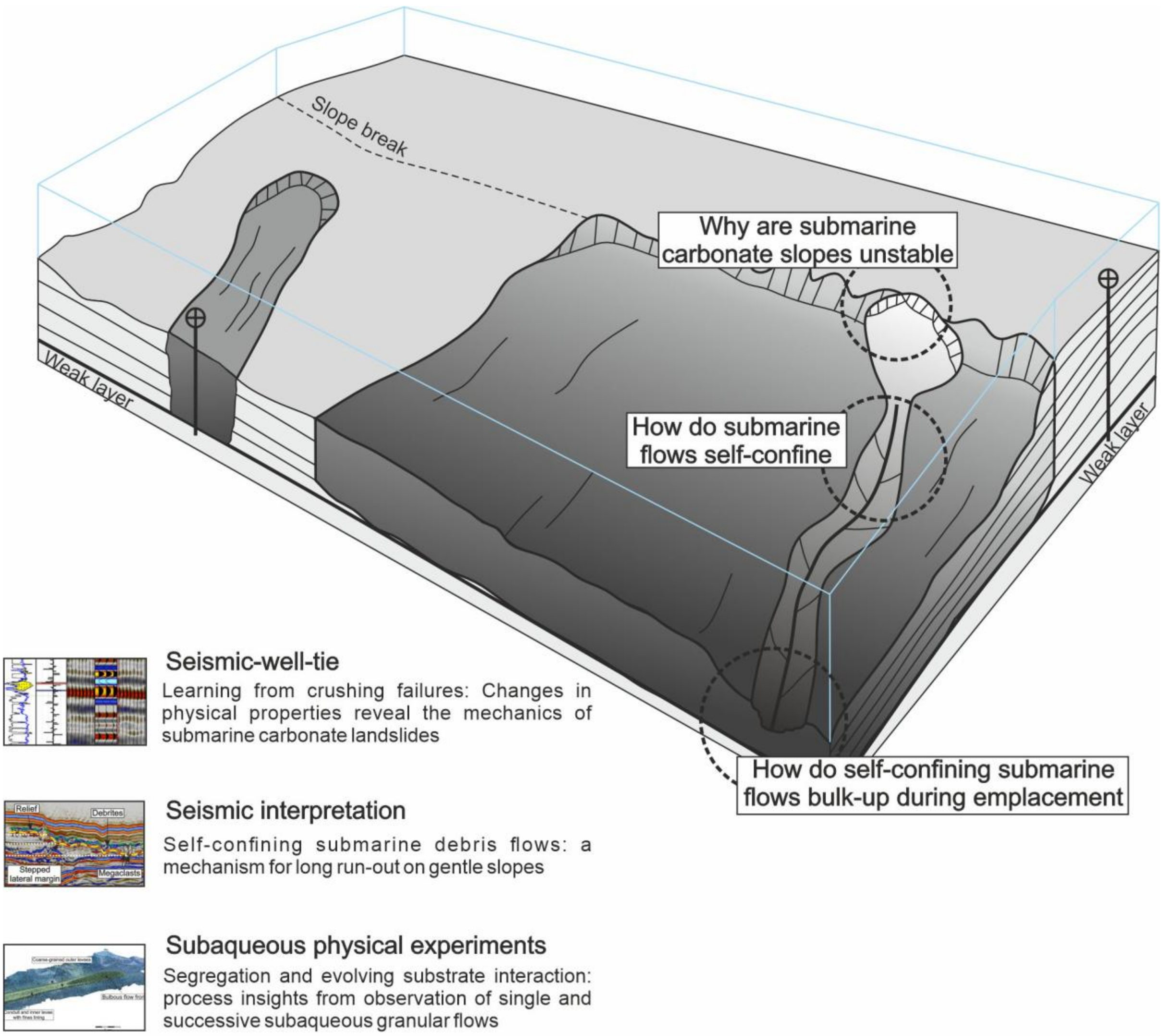

Figure 7-1: Schematic diagram showing the linkages between the research questions posed, and the different methods used in this thesis.

The synthesis demonstrates that large-scale slope instability on gentle carbonate slopes is fundamentally controlled by sediment composition (notably the presence of foraminifera), which governs sediment physical properties. The synthesis demonstrates that subaqueous debris flows and granular flows can become self-confined through lateral depositional relief and/or substrate incision. The positive feedback between flow confinement, substrate incision and flow bulking facilitates flow mobility even on gentle slopes. This synthesis provides a process-based model for better understanding flow initiation, evolution and mobility in subaqueous settings.

7.1 What causes instability on low gradient carbonate submarine slopes?

7.1.1 Preconditioning of submarine failures on gentle carbonate slopes

Numerous submarine landslides developed on the Exmouth Plateau, offshore NW Australia, with a cumulative mapped area exceeding 6000 km^2 (Scarselli et al., 2013, 2019; Wu et al., 2023). Chapters 4 and 5 show how large-scale carbonate submarine failures on gentle slopes are fundamentally controlled by the development of weak layers and enhanced submarine landsliding. Results from this work show how preconditioning for submarine failures through changes in physical properties controlled by sediment composition has implications for understanding how gentle carbonate slopes fail.

Previous studies have recognised the importance of weak layers as a key preconditioning factor for submarine landslides (Berndt et al., 2012; L'Heureux et al., 2012; Locat et al., 2014; Urlaub et al., 2015; Elger et al., 2018; Krastel et al., 2019; Gatter et al., 2021). However, the role of sediment composition in controlling physical properties has remained poorly constrained. This knowledge gap has been addressed by analysing the relationship between sediment composition and physical properties in a carbonate succession, providing new insights into the compositional control on preconditioning of submarine failures on gentle carbonate slopes. In Chapter 4, analysis using seismic-to-well ties demonstrates that the basal shear zone of large-scale submarine landslides and their stepped lateral margins can be traced into adjacent undisturbed sediments, where they coincide with three clay-capped foraminifera-rich successions, characterised by high water content and high porosity (Figure 4-6A). These physical properties are closely related to sediment composition, where foraminifera-rich intervals can store excess water within the intraskeletal void space in the tests of foraminifera (e.g., Hairabian et al., 2014; Beemer et al., 2019).

The basal weak layer contains a greater concentration of foraminifera than the two shallower weak layers (Figure 4-7A; Haq et al., 1990), which explains its higher water content. The correlation between sediment composition and physical properties demonstrates that the water content and properties of carbonate sediment are controlled by foraminifera abundance.

These water-rich carbonate layers are interpreted to have developed party in response to control exerted by the overlying clay-rich layers, which act as permeability barriers that trap fluids within weak layers. This leads to the development of elevated pore pressures within these intervals, thereby facilitating weak layer formation and promoting submarine landslides on carbonate slopes (see 'Section 4.6.1.1' for more details). Chapter 4 demonstrates that the same clay-capped foraminifera-rich successions, when incorporated into the basal shear zone, exhibit markedly reduced water content, porosity and foraminifera content. The mechanism identified to explain the porosity loss and water release is contractive shearing driven by failure, and the decrease in foraminifera abundance is explain by crushing during shearing. The dynamics and evolution of submarine landslides are closely linked to the changes in physical properties of sediments during failure, highlighting the importance of stratigraphic composition. Here, the abundance of foraminifera-clay successions, results in the development of stratal units characterised by elevated pore pressures and reduced shear strengths. These variations in the physical properties of stratal units that are influenced by composition provides a new framework for understanding slope failures on gentle carbonate slopes.

7.1.2 Flow initiation on gentle carbonate slopes

Flow-substrate interaction is a dynamic process that is controlled by substrate rheology, including shear strength and basal friction force (e.g., Ortiz-Karpf et al., 2017; Roelofs et al., 2023). Here, a new framework is presented in which flow initiation on gentle slopes is controlled by elevated pore pressure within the substrate, leading to decreased basal friction and enhanced flow mobility. This synthesis helps to develop new insights into how substrate rheology influences flow evolution.

Chapters 4 and 5 demonstrate that two stages of submarine landslides are recognised in the same area, including a deeper buried, large-scale submarine landslide (Slide 8 in Chapter 4), and a shallow submarine debris flow (Slide 9 in Chapter 5). Seismic-well-tie analysis in Chapter 4 demonstrates that the initiation of Slide 8 is controlled by the variation in physical properties of the substrate, including decreases in foraminifera and porosity associated with water release. These changes in physical properties during failure reflect compaction and fluid redistribution in the substrate (Iverson et al., 2000; Peakall et al., 2020; Roelofs et al., 2023). During failure, the basal weak layer undergoes contractive shearing driven by the overriding landslide, which leads to rapid compaction, crushing of foraminifera, and fluid expulsion (see '*Section 4.6.1.3'* for more details). Confined by a low permeability layer below and an overlying high-density submarine landslide mass, the water squeezed from the weak layers is trapped, which leads to the generation of elevated pore pressure and a natural lubricating layer that reduces substrate friction, thus enhancing the mobility of the overlying landslide.

In contrast to the weak-layer-controlled Slide 8 (Chapter 4), the pre-conditioning of the submarine debris flow (Slide 9) in Chapter 5 is influenced by gas release. Observations from seismic sections, and variance and seafloor maps reveal a strong spatial and stratigraphic relationship between Slide 9 and blocks updip of the Slide 9 headwall (Figure 7-2). The youngest layer incised by Slide 9 corresponds to the youngest layer cut by pockmarks (H1 in Figure 7-3). This relationship suggests that Slide 9, and the pockmarks, developed on the same stratigraphic horizon. This observation is consistent with a previous study in the same study area (Paganoni et al., 2019), which suggests the shallow mass-transport deposits (Slide 9) are triggered by deep thermogenic gas migration. Gas migration can generate localised overpressure (e.g., Brothers et al., 2014), which would increase pore pressure and decrease shear strength (Trincardi et al., 2004). Slide 9 would incise this gas-bearing substrate that is characterised by low shear strength. The substrate blocks adjacent to the headwall region would detach and be transported downslope within the main debris flow (e.g., Jackson, 2011; Alves, 2015; Gamboa and Alves, 2015; Li et al., 2023), generating basal grooves on the basal shear surface observed in Chapter 5. The gas-bearing substrate would provide the preconditioning conditions for slope failure initiation and block entrainment, although the formation mechanism of the blocks remains unclear (see '*Section 7.4.1*' in future research direction).

Despite the different preconditioning mechanisms (i.e., water-rich weak layers in Slide 8, and gas release in Slide 9), this synthesis demonstrates that the initiation of both Slide 8 and Slide 9 was controlled by substrate rheology and fluid distribution, characterised by elevated pore pressure and low shear strength. This synthesis highlights the importance of substrate rheology for analysing the initiation of submarine failures, particularly on gentle carbonate slopes.

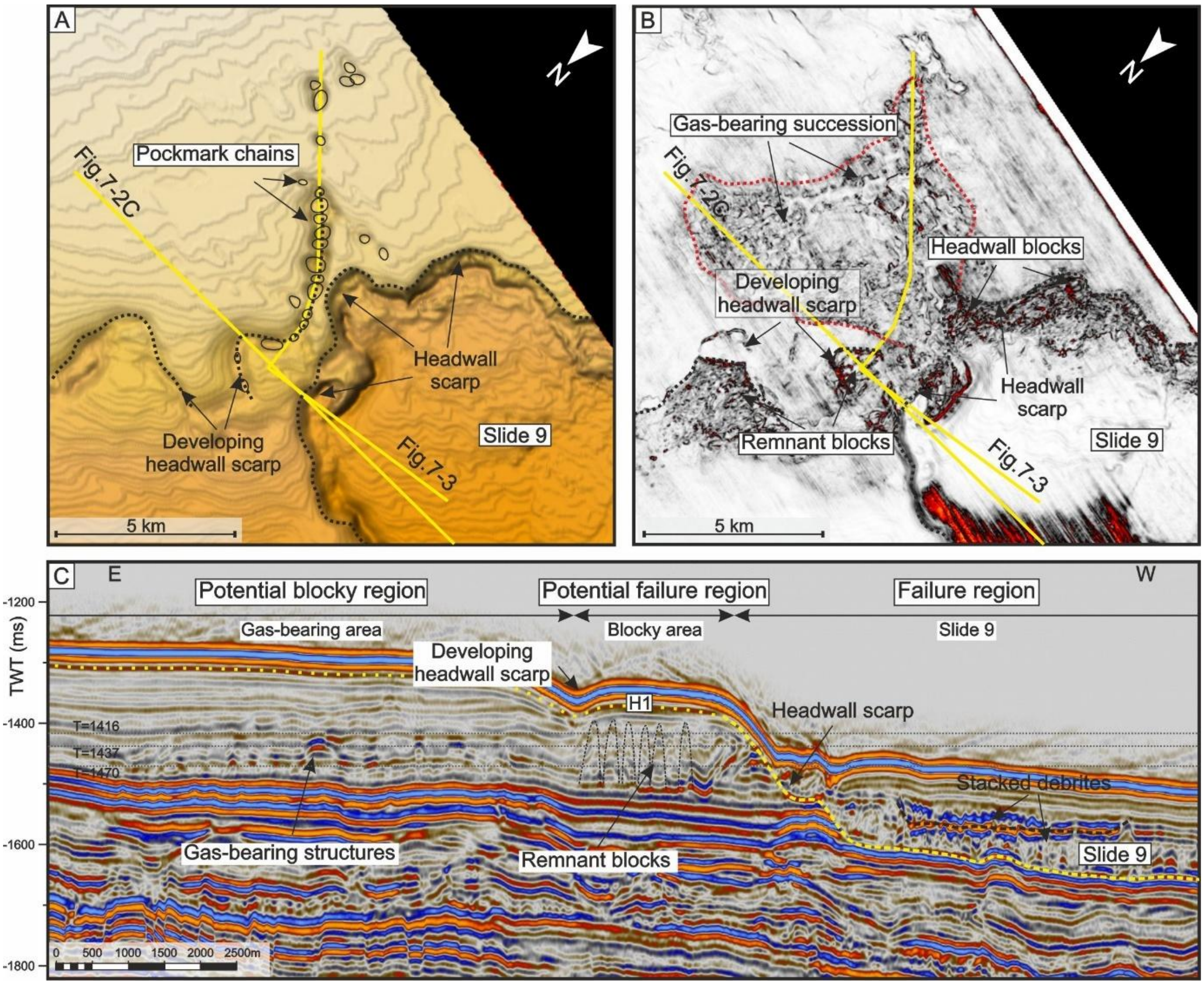

Figure 7-2: (A) The seabed map, showing the seabed expression of the headwall of Slide 9 and the pockmarks near the headwall region of the Slide 9; (B) The variance map (T= 1470 ms), showing the gas charged structure, and the blocky area near the headwall of Slide 9. (C) E-W seismic section, showing Slide 9 (failure region), the blocky area (potential failure region), and the gas charged area (potential blocky region). The location of Section 7-2C is shown in Figure 7-2A and Figure 7-2B.

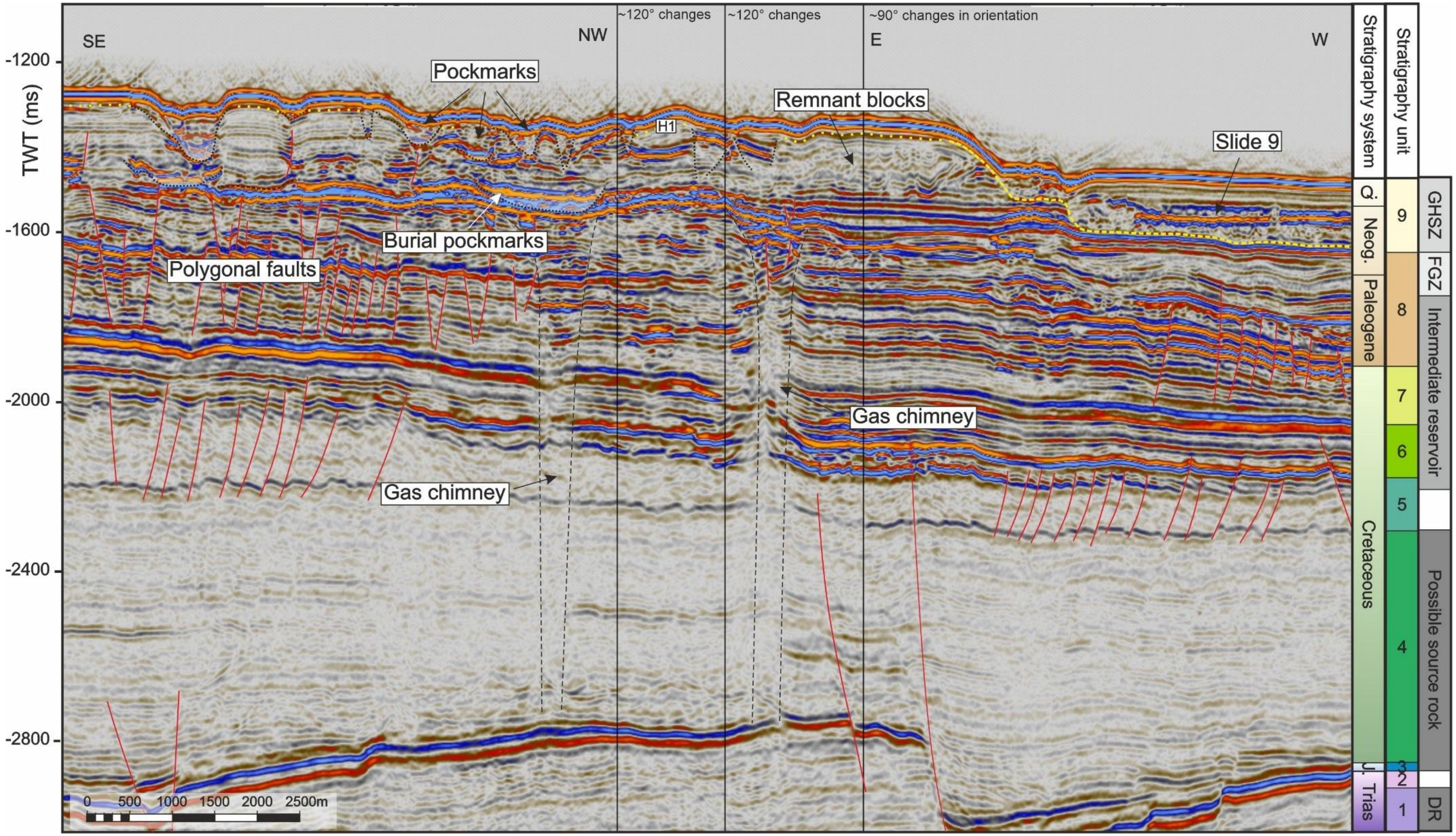
SE
NW
~120° changes
~120° changes
~90° changes in orientation
E
W
TWT (ms)
-1200
-1600
-2000
-2400
-2800
Pockmarks
H1
Remnant blocks
Slide 9
Burial pockmarks
Polygonal faults
Gas chimney
Gas chimney
0 500 1000 1500 2000 2500m
Stratigraphy system
Q.
Neog.
Paleogene
Cretaceous
J.
Trias
Stratigraphy unit
9
8
7
6
5
4
3
2
1
GHSZ
FGZ
Intermediate reservoir
Possible source rock
DR

Figure 7-3: E-W seismic section, showing Slide 9, the pockmarks, and the interpretation of the stratigraphy system, the stratigraphic units and the petroleum system elements. The correlation with stratigraphy system and the interpretation of petroleum system elements are modified from Paganoni et al. (2019). The correlation with stratigraphic units is modified from von Rad et al. (1992). GHSZ = gas hydrate stability zone. FGZ = free gas zone. DR = Deep reservoirs. The location of Section 7-3 is shown in Figure 7-2A and Figure 7-2B.

7.2 How do subaqueous flows self-confine?

Chapters 5 and 6 propose a self-confinement processes that can be applied to explain enhanced flow mobility even on gentle slopes. Confinement restricts lateral flow spreading, maintains flow thickness and sustains downslope flow momentum, thereby facilitating longer runout distances (Major, 1997; Major and Iverson, 1999; Iverson et al., 2010; Johnson et al., 2012). In submarine environments, confinement can be imposed by pre-existing seafloor topography, such as depositional relief and active or inherited tectonic relief near basin margins (e.g., Gee et al., 2001; Talling et al., 2013; Krastel et al., 2016; Ortiz-Karpf et al., 2018; Ward et al., 2018; Li et al., 2020; Nwoko et al., 2020a, 2020b). However, self-confinement, whereby flows generate their own confining topography during emplacement, remains poorly constrained in submarine settings. Existing models on self-confinement are derived from subaerial settings (Major, 1997; Major and Iverson, 1999; Deboeuf et al., 2006; Iverson et al., 2010; Johson et al., 2012; Kokelaar et al., 2014; De Haas et al., 2015, 2016; Rocha et al., 2019), with limited equivalent work in subaqueous environments. Chapters 5 and 6 address this gap by documenting, for the first time, the development and evolution of self-confinement in subaqueous mass flows through field-scale observations and subaqueous physical experiments. The arising insights into the evolution of self-confinement in subaqueous settings, support development of a new mechanism to explain long runout of submarine mass flows on gentle slopes.

7.2.1 Development of self-confinement through depositional relief

Self-confinement in submarine mass flows can develop through the construction of depositional relief. Substantial depositional relief has been observed in submarine debrites (e.g., Prior et al., 1984; Masson et al., 1993; Laberg and Vorren, 1995), yet its role in controlling flow confinement, and thus enhancing flow mobility, has not been fully recognised. Understanding the mechanism by which depositional relief controls flow confinement is crucial for explaining long runout distances of submarine debris flows on gentle slopes, and for reconstructing dynamic flow-deposit interactions in deep-water settings.

Lateral depositional relief has been documented in subaerial mass flows, that facilitate flow runout through lateral confinement (Iverson et al., 2010; Gray and Kokelaar, 2010; Johnson et al., 2012; Kokelaar et al., 2014). However, the role of the depositional relief in enhancing flow mobility has not been fully addressed in submarine settings. Seismic interpretation in Chapter 5 demonstrates that the depositional relief of debrite lobes increases from an initial 6 m in the upstream to 15 m in the mid-slope. As the flow evolves, fed by retrogressive headwall failures, it becomes more confined by existing depositional relief, resulting in the overall basinward progradation of successive debrite lobes (Figure 6-15). The down-dip topography provided by the stacking of debris flow deposits progressively increases the confinement on the flow pathway. The flow behaviour in Chapter 5 demonstrates that submarine debris flows can be steered by its evolving depositional topography, initially forming a confined pathway, thereby facilitating flow mobility.

Observations from subaqueous granular-flows experiments, in Chapter 6, demonstrate how lateral depositional relief can be generated through particle segregation as the flow evolves downslope. During the evolution of subaqueous granular flows presented in Chapter 6, the coarser blocky particles are preferentially transported to the advancing flow head and form coarse-enriched lateral levees (Figure 6-2). This particle segregation in subaqueous settings is consistent with subaerial observations (e.g., Savage and Lun, 1988; Johnson et al., 2012; Kokelaar et al., 2014; Gray, 2018). The comparison between subaqueous and equivalent subaerial experiments in Chapter 6 demonstrates that segregating granular flows in subaqueous settings are more mobile than in subaerial settings, as evidenced by the high velocities, the longer runout distances and the narrower flow widths of the experimental subaqueous single granular flows (Figure 6-3 and Figure 6-5). The enhanced mobility is attributed to the reduced basal friction due to the presence of interparticle fluid (e.g., Iverson et al., 2010), thereby promoting higher flow velocities. These observations in Chapter 6 provide experimental evidence for the evolution of self-confinement through particle segregation in subaqueous settings. This has implications for establishing evolution process models of segregation in submarine environments.

In summary, the flow-deposit interactions presented in Chapters 5 and 6 show how an evolving depositional relief can provide confining boundaries that increase flow momentum and mobility. Therefore, flow-deposit interactions should be taken into consideration in prediction of flow runout distances.

7.2.2 Development of self-confinement through substrate entrainment

Results from Chapters 4 and 5 also demonstrate that self-confinement in submarine mass flows can develop through substrate entrainment and incision, and the formation of negative seafloor topography that confines subsequent flow pathways. Submarine landslides have strong erosional capacity, and can entrain the substrate along their paths (e.g., Gee et al., 2006; Dakin et al., 2013; de Haas et al., 2016; Brooks et al., 2018; Krastel et al., 2019; Martínez-Doñate et al., 2021). Chapters 4 and 5 demonstrate that pronounced substrate incision can occur on gentle slopes, with slope gradients <1°.

As shown in Chapter 4, the stepped basal surface in the headwall region and the lateral margins observed in Slide 8 provide key evidence for substrate incision of up to ~90 m on a gentle slope (Figure 4-3A and Figure 4-5A). The stepped morphology of headwall scarps is commonly interpreted as an indicator of retrogressive headwall collapses (e.g., Bryn et al., 2005; Kvalstad et al., 2005; Sawyer et al., 2009; Barrett et al., 2021). Unlike typical retrogressive headwall scarps, the steps in Slide 8 exhibit extensive lateral continuity (up to 30 km long), far longer than the step-back distance to the headwall (no more than 5 km; Figure 7-4). Seismic-well-tie analysis in Chapter 4 shows that these steps correspond to weak layers (i.e., clay-capped foraminifera-enriched layers) that are characterised by elevated water content, high porosity and low velocity before failure (Figure 4-3, Figure 4-5 and Figure 4-7). The correlation between the steps and weak layers indicates that the stepped morphology of the basal shear surface in Slide 8 is controlled by laterally continuous weak layers, rather than discrete collapse events. During failure, these weak layers are interpreted to undergo contractive shearing, generating elevated pore pressure and reducing friction and shear strength (Kvalstad et al., 2005; Stoecklin et al., 2017; Gatter et al., 2021). As a result, the submarine landslide preferentially localised along the weak layers where the friction is lower, forming the stepped incision surface (Figure 7-4). Chapter 4 demonstrates that substrate incision in weak layer systems is strongly controlled by the distribution and mechanical properties of weak layers, providing new insight into the formation of self-confinement through substrate incision and the development of stepped negative topography.

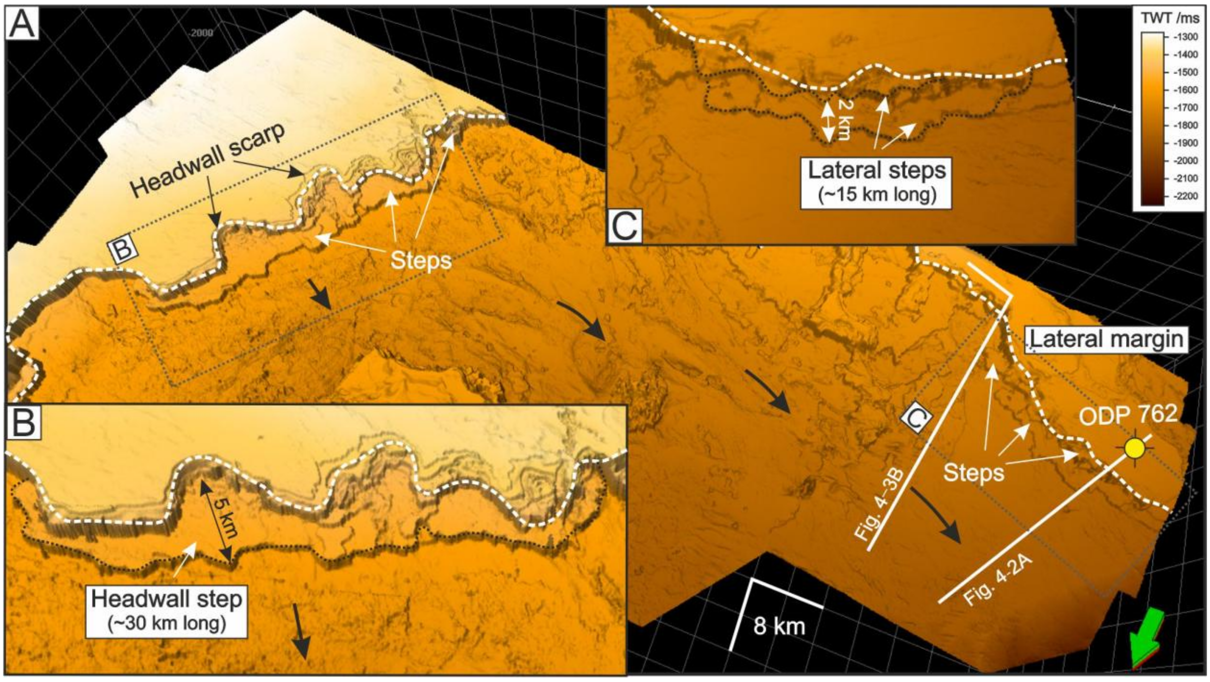

Figure 7-4: The 3D view of the basal shear surface of Slide 8, showing the stepped headwall and lateral margins, and the location of ODP Site 762 used in Chapter 4. The green arrow indicates the north direction. The black arrows indicate the sliding direction of Slide 8.

Chapter 5 provides an example of self-confinement through a combination of depositional relief and substrate incision controlled by pre-existing depositional relief. Mapping shows up to ~82 m of substrate incision with lateral gradients of ~5°, despite the gentle regional slope outside the incision (ca. 0.89°; Figure 5-2, Figure 5-3A, Figure 5-4 and Figure 5-5A). Chapter 5 demonstrates that substantial substrate incision can occur on gentle slopes through positive feedback between depositional relief and flow confinement. The early debris flow built up depositional relief that confines subsequent flows, causing flow to become narrower and thicker. Narrowing and deepening would cause increased momentum, enhanced velocity, and greater basal shear stresses, leading to substrate incision (30-40 m deep; Figure 6-9) as the flow evolved even on a gentle slope (cf. Whipple and Dunne, 1992; de Haas et al., 2016, for subaerial debris flows, albeit on one to three orders of magnitude smaller scales). Chapter 5 demonstrates that confinement driven by depositional relief can cause substrate incision under low-gradient conditions, which can be accentuated by the presence of inherited seabed relief, as with the presence of a diapir on the flow pathway of Slide 9.

In summary, self-confinement can develop through substrate incision, controlled either by weak layers as demonstrated in Chapter 4 or by depositional relief as demonstrated in Chapter 5. This synthesis highlights the importance of substrate incision on the development of self-confinement, even where slope gradients are low (<1°).

7.2.3 Feedbacks between substrate entrainment and flow confinement

Subaerial physical experiments show that debris flows can develop self-confinement through the construction of lateral depositional relief (e.g., Iverson et al., 2010; Johnson et al., 2012; de Haas et al., 2015, 2016), or substrate incision (e.g., de Haas et al., 2016). Here, the concept of self-confinement by debris-flows is extended to submarine settings, and demonstrates that flow self-confinement can develop through the construction of lateral depositional relief, substrate incision, or a combination of both (Chapters 4-6). The stepped geomorphology of the basal shear surface in Chapter 5 demonstrates a positive feedback between flow confinement by depositional relief and substrate incision, which provides new insight into the mechanism of substrate incision and enhanced flow mobility on gentle slopes. The axial deepening of substrate truncation, from 12 m, to 25 m and 35 m deep downslope (Figure 6-13), reveals the progressive increase in confinement and erosive capacity of the debris flow through time. Increased confinement limits lateral flow spreading, increases flow thickness, and results in faster and more efficient transport (Iverson et al., 2010; Johnson et al., 2012; Kokelaar et al., 2014; de Haas et al., 2015, 2016). The stepped basal shear surface further indicates that the debris flow became progressively confined through time (Figure 5-11). Chapter 5 demonstrates the debris flow establishes a positive feedback, whereby self-confinement through lateral depositional relief drives substrate incision and the development of the stepped basal shear surface, which in turn enhances flow confinement (see ‘Section *5.6.1*’ for more details).

The synthesis demonstrates that the self-confinement acts as a key mechanism for long-runout submarine mass flows on gentle carbonate slopes. Self-confinement develops through the construction of lateral depositional relief and/or substrate incision, establishing a positive dynamic flow-substrate feedback that facilitates flow mobility. These findings are crucial for understanding long-runout flow mobility, reconstructing deep-water sediment transport processes, and assessing submarine geohazards.

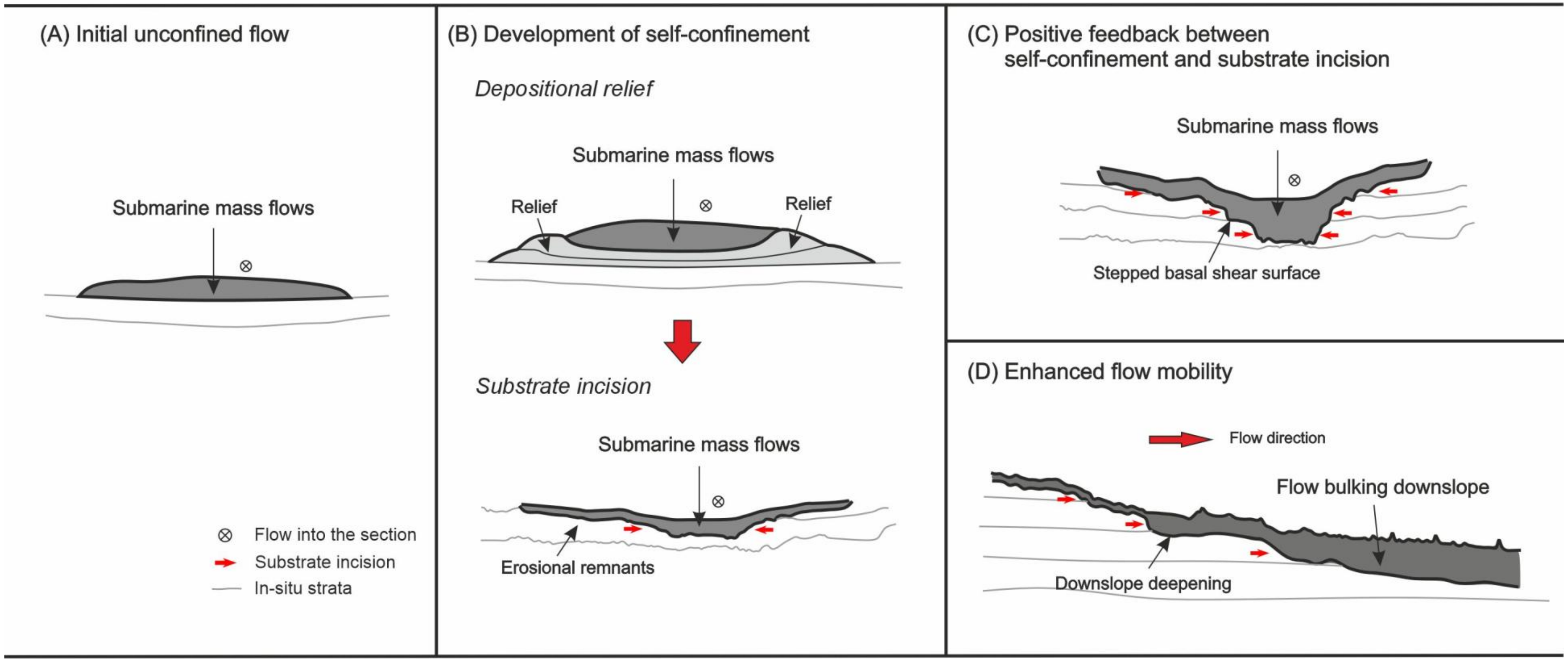

Figure 7-5: Conceptual model showing the evolution of self-confinement in subaqueous settings, including (A) initial unconfined flows, (B) the development of self-confinement through depositional relief and substrate incision, (C) positive feedback between flow confinement and substrate incision, leading to the development of stepped basal shear surface, and (D) enhanced flow mobility and increasing substrate truncation.

7.3 How do self-confining subaqueous flows bulk-up during emplacement?

This thesis demonstrates that self-confining subaqueous mass flows can bulk-up during dynamic flow-substrate interactions, thereby influencing flow mobility. Evidence for flow bulking is demonstrated by the approximately threefold increase in submarine debrite volume in Chater 5, and by the observation that upslope levees after multiple subaqueous flows are thinner than single-flow levees in Chapter 6. The synthesis of Chapters 4-6 provides new insights into how submarine flow bulk-up during emplacement through flow-substrate interactions.

7.3.1 Influence of composition on flow mobility and entrainment

Chapter 6 demonstrates that there is a close relationship between flow composition and mobility in subaqueous settings. Flow composition plays an important role in flow evolution by controlling flow mobility, including velocity, volume and runout distances (e.g., Elverhøi et al., 2010; Iverson et al., 2010; Kokelaar et al., 2014), and therefore influences flow bulking processes during emplacement. Subaqueous single-flow experiments in Chapter 6 demonstrate that flow velocity initially increases with fines fraction, from 0.63 cm/s in the 30 vol.% fines experiment to 1.13 cm/s in the 70 vol.% fines experiment, and then progressively decreases to 0.66 cm/s in the 100 vol.% fines within the initial 120 s and 110 cm of runout (Figure 6-5; Table 6-1). This trend is consistent with equivalent subaerial single granular-flow experiments, where flows containing 60-70 vol.% fines exhibit the longest runout distance (Kokelaar et al., 2014).

The synthesis of Chapters 5 and 6 demonstrates that mobility is influenced by the development of lateral levees, which governs the degree of flow confinement. Chapter 5 demonstrates that there is a downslope increase in depositional relief, from an initial 6 m in the upstream to 15 m in the mid-slope. The increase in lateral relief increases flow confinement and promotes flow mobility (see '*Section 5.1*' for more details). Chapter 6 further demonstrates that, levee thickness and morphology are controlled by flow composition (i.e., coarse percentage and coarse volume), as shown in both subaqueous single- and multiple- flow experiments (Figure 6-7 and Figure 6-13). The subaqueous single-flow experiments in Chapter 6 demonstrate that an increase in the fraction of coarse particles in flows can enhance segregation at the flow front and increase the supply of coarse particles to the flow margins, resulting in thicker levees. Increasing the fines fraction reduces the friction between particles, thereby enhancing flow mobility. Therefore, the observed enhanced mobility of 60-70 vol.% fines flows in single-flow experiments in the subaqueous setting in Chapter 6 and the subaerial setting in Kokelaar et al. (2014) reflects a balance between segregation-driven levee development that promotes flow confinement, and fines-related internal friction, thus influencing flow mobility.

This synthesis of observations in Chapters 5 and 6 demonstrates that flow mobility is controlled by a combination of lateral relief and flow composition. Flow bulking can directly modify flow composition, and thereby influences flow mobility.

7.3.2 Substrate entrainment and mechanism of flow bulking

Chapters 4-6 demonstrate that substrate entrainment is the primary mechanism driving flow bulking during flow self-confinement. Substantial flow bulking is evidenced by the approximate three times increase in debrite volume (Chapter 5), upslope net erosion observed in subaqueous multiple-flow experiments (Chapter 6), and the stepped morphology of the basal shear surface (Chapter 4). These observations demonstrate that submarine mass flows can substantially increase in volume during emplacement through substrate entrainment (e.g., Prior et al., 1984; Gee et al., 1999, 2006; McCoy et al., 2012; Hodgson et al., 2019; Nugraha et al., 2022; Böttner et al., 2024; Valdez Buso et al., 2024).

However, the evolution of substrate entrainment during self-confinement remains poorly understand. Chapter 6 addresses this gap, through multiple-flow experiments, demonstrating how subaqueous granular flows entrain pre-existing deposits, and proposes a new segregation model that captures the dynamic flow-substrate interaction in subaqueous settings. Net profile changes in Chapter 6 demonstrate upslope net erosion and downslope net deposition, indicating that substrate entrainment mainly occurs upslope. Previous experimental and conceptual models have primarily focused on segregation-driven processes on fixed substrates (e.g., Savage and Lun, 1988; Major, 1997; Major and Iverson, 1999; Gray and Thornton, 2005; Iverson et al., 2010; Gray and Kokelaar, 2010; Johnson et al., 2012; Kokelaar et al., 2014; de Haas et al., 2015, 2016), and therefore do not capture the role of entrainment of a mobile substrate in modifying confinement during the evolution process. Chapter 6 addresses this by presenting the evolution process of self-confinement from subaqueous physical experimental models designed as an analogue for submarine flow-substrate interactions in unconfined settings. Observations of subaqueous multiple-flow experiments, in Chapter 6, demonstrate that during successive runs, subsequent flows remobilise pre-deposited particles, leading to the progressive downslope increase in flow volume (bulking) of subsequent flows, and export of material beyond the slope. Chapter 6, for the first time, reveals the complex interactions of substrate entrainment with segregation processes through the subaqueous multiple-flow experiments, highlighting the dynamic nature of flow-deposit interactions.

Chapter 4 demonstrates that flow bulking in weak layer-controlled systems is achieved by confined lubrication, which enhances substrate entrainment ahead of the bulldozing slide through weakening the substrate ahead of the landslide, thereby enabling more entrainment and bulking up of the flow, and thus allowing the landslide to propagate farther into the basin. Chapter 5 presents evidence that substrate entrainment by the submarine debris flows likely further increased flow momentum and velocity. Together, Chapters 4 and 5 demonstrate that substrate entrainment can be enhanced on carbonate substrates, which experience a greater loss of shear strength compared to siliciclastic substrates, which is related to less clay particles (Gaudin and White, 2009; White et al., 2013). This marked loss in strength implies that carbonate slopes are particularly susceptible to incision following failure (cf. Nugraha et al., 2022), thereby facilitating the development of substrate entrainment and long runout distance on carbonate slopes, despite the low slope gradient.

Overall, the synthesis of field-scale seismic observations (Chapters 4 and 5) and physical experiments (Chapter 6) demonstrates that flow bulking in self-confinement is a complicated relationship between the physical properties of the substrate and the evolution of depositional relief, which controls flow mobility, incision and thereby flow volume and runout distances.

7.3.3 Interaction between flow bulking and self-confinement

Chapter 6 demonstrates that flow bulking in self-confining subaqueous flows is a systematic upslope-to-downslope redistribution of particulate material through erosion and deposition during successive flows. The multiple flow experiments show that flow bulking is expressed by net upslope erosion and downslope particle remobilisation and segregation. The mechanism of flow bulking is governed by the dynamic feedback between substrate entrainment and flow confinement. Chapter 6 demonstrates that flow bulking in self-confining subaqueous granular flows is initiated by enhanced velocity within pre-existing confined conduits, where lateral confinement and low-friction conduit deposits together increase flow velocity. The levee-controlled velocity enhancement is consistent with subaerial granular models (e.g., Elverhøi et al., 2010; Gray and Kokelaar, 2010; Iverson et al., 2010; Johnson et al., 2012; Kokelaar et al., 2014). The increase in flow mobility resulting from fines lining the conduit has been proposed in subaerial settings (e.g., Edwards et al., 2023), while the subaqueous multiple experiments, in Chapter 6, demonstrate similar mechanisms during self-confinement processes. The resulting increase in velocity enhances the erosive capacity of flows, leading to pronounced substrate entrainment, as presented in Chapter 6 by thinner multiple-flow levees relative to single-flow levees (Figure 6-7 and Figure 6-13). Following upslope particle remobilisation, flow bulking leads to a higher coarse percentage within flow head. The bulking causes re-mixing of particle size distribution in the flow head (e.g., Johnson et al., 2012), which has direct implications for levee thickness and the lateral confinement of subsequent flows. The coarse enrichment from upstream remobilisation promotes the re-distribution of remobilised coarse particles and the formation of thick levees in the downslope (Figure 6-7 and Figure 6-13). An additional complication is that through time the initial ratio of the particles deposited will change through preferential export of finer grains (Figure 6-14 and Figure 6-15), showing the complex interactions of flow composition and evolving relief even under controlled conditions.

The role of flow bulking in flow confinement is further presented by the observations of substantial debrite volume increase through substrate entrainment in Chapter 5. Such bulking-up can substantially influence flow dynamics through increasing flow volume (McCoy et al., 2012; Hodgson et al., 2019; Nugraha et al., 2022; Böttner et al., 2024), thereby controlling flow momentum and mobility. A similar positive feedback between substrate erosion and flow confinement exists in weak layer-controlled systems (Chapter 4). The confined lubrication mechanism may be self-reinforcing, with contractive shearing generating elevated basal pore water pressures, thereby reducing basal friction and increasing flow velocity. This could promote basal erosion, and enhance the bulldozing and sediment entrainment at the front of the landslide, and in turn increase the efficacy of subsequent contractive shearing.

The synthesis demonstrates that the interaction between flow bulking and confinement is a dynamic process, between evolving substrate entrainment, particle segregation and flow mobility. Analysing the volume increase and physical properties of the flow and the substrate is important to understanding the role of bulk-up processes in self-confining debris flows, albeit a complicated and dynamic process interaction. Enhanced confinement promotes substrate erosion and further increases flow confinement, thereby increasing the run-out distance on gentle slopes.

7.4 Future research directions

Addressing the research questions carried through this thesis has highlighted the requirements for further work to develop a deeper understanding of the topics discussed here and how the self-confinement model can be applied to different deep-marine systems.

7.4.1 Evaluating the role of gas-related preconditioning in submarine slope failures

Blocks or megaclasts are common components of submarine landslides and debrites (e.g., Gee et al., 1999; Jackson, 2011; Alves, 2015; Ortiz-Karpf et al., 2017; Soutter et al., 2018; Hodgson et al., 2019; Nwoko et al., 2020a; Li et al., 2022). The blocks and associated tool marks are used to interpret palaeoflow directions (Nissen et al., 1999; Gee et al., 2005; Jackson, 2011; Ortiz-Karpf et al., 2017; Soutter et al., 2018; Li et al., 2022), and for the analysis of palaeohydraulics and substrate rheology (Peakall et al., 2020).

This thesis suggests that gas-related processes probably play an important role in preconditioning the failure and megaclast size of Slide 9. Seismic sections, variance maps and seafloor mapping show a clear spatial correlation between the failure unit (Slide 9), the block developed area, and the gas-bearing stratigraphic successions adjacent to the headwall region of Slide 9 (Figure 7-2 and Figure 7-5). The same stratigraphic unit that contains the megaclasts can be traced upslope into a gas-bearing unit (Figure 7-3 and Figure 7-5), suggesting a potential correlation between gas migration, block development and subsequent failure initiation.

Gas migration can generate localised overpressure (Trincardi et al., 2004), which reduces sediment shear strength (Brothers et al., 2014). However, how gas influences the physical properties of the sedimentary succession remains unclear, thus its role in the formation of blocks is still uncertain. It is not yet known whether gas-related overpressure and migration directly weakens the unit, promoting local extension and block formation, or whether other processes facilitate block formation.

Future work should evaluate the physical properties of the gas-bearing succession, and the depositional structures of the gas-bearing area and the block area. These could be addressed through integrated seismic interpretation, attribute map analysis, and stratigraphic correlation. Evaluating the role of gas-related preconditioning in submarine slope failures would help the understanding of block formation, slope instability and substrate entrainment in gas-bearing area. Even then, the chemistry of the gas, reactions with the carbonate ooze, and changes in physical properties can only be inferred without targeted coring.

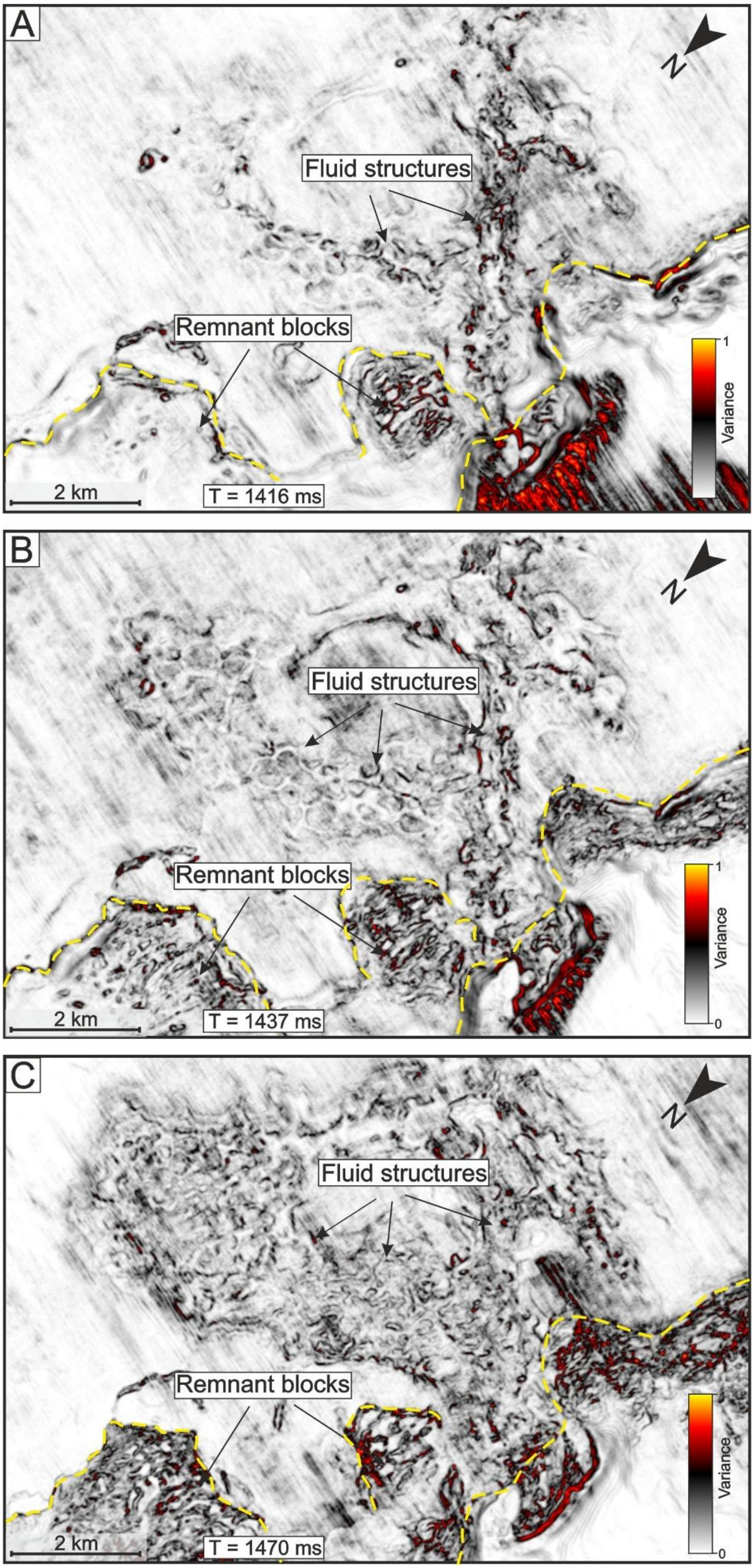
A
Fluid structures
Remnant blocks
Variance
1
2 km
T = 1416 ms
B
Fluid structures
Remnant blocks
Variance
1
0
2 km
T = 1437 ms
C
Fluid structures
Remnant blocks
Variance
0
2 km
T = 1470 ms
N

Figure 7-6: Variance maps at (A) 1416 ms, (B) 1437 ms, and (C) 1470 ms adjacent to the headwall region of Slide 9 on Exmouth Plateau, offshore NW Australia, demonstrating the blocky fluid-related structures in the gas-bearing succession and the adjacent block area. The locations of the variance maps are shown in Figure 7-2C.

7.4.2 Application of proposed self-confinement model to other deep-marine systems

The proposed new model in Chapter 5, demonstrates submarine debris flows can develop self-confinement through the construction of depositional relief and/or substrate incision. The model provides an opportunity to re-evaluate documented examples of long runout debris flows on gentle slopes, particular those with depositional relief, and thus assess the importance of self-confinement in deep-water settings.

Comparable self-confining behaviour has been documented in a range of subaerial mass flows (Iverson, 1997; Major, 1997; Major and Iverson, 1999; Iverson et al., 2010; Johnson et al., 2012). In submarine settings, the accumulation of coarse particles at flow fronts can generate blocky frontal edge flow (Prior et al., 1984; Talling et al., 2010; Hunt et al., 2021), suggesting the segregation-relevant confinement may have a broad application in deep-water system. Depositional relief has already been documented in submarine debrites, including lateral relief, blocky flow fronts, and rafted sediment blocks. Examples includes the Saharan debris flow deposits and debris flow deposits on the Bear Island Trough Mouth Fan (Masson et al., 1993; Laberg and Vorren, 1995). The physical experimental model in Chapter 6 further demonstrates that lateral levees can develop through particle segregation. However, previous studies only describe the observed relief as ‘depositional structures’ (e.g., Masson et al., 1993; Laberg and Vorren, 1995), regardless of the important role of blocky edges on flow confinement.

Submarine debris flows can travel tens to hundreds of kilometres on low gradient slopes, in some cases where slopes decrease to near flat conditions (e.g., Embley, 1976; Prior et al., 1984; Masson et al., 1997; Gee et al., 1999; Talling et al., 2007; Tang et al., 2022). The new model presented in Chapter 5 documents that submarine flows can become self-confined through the construction of depositional relief and substrate incision, and this self-confinement acts as a key mechanism for enhanced flow mobility. During emplacement, self-confinement is dynamically coupled with substrate entrainment (i.e., bulking), generating positive feedbacks between confinement and flow mobility. This self-confinement evolution model provides new insights to re-evaluate existing process models for the long runout debris flows on gentle slopes. Chapter 6 shows that an additional factor to flow mobility is the changing composition of the flow through flow-substrate interactions. Debris-flows have been shown to preferentially entrain different sediment types (e.g. Ortiz-Karpf et al., 2017) making prediction of flow-substrate interactions and their impact on flow dynamics, very challenging.

Future work should therefore pay attention to the role of depositional relief in facilitating flow mobility particularly on gentle slopes, as well as the composition of the flow and substrate. Lateral depositional relief may serve as a confining boundary for subsequent flows, reducing lateral spreading and therefore enhancing upslope incision and flow mobility.

7.4.3 Numerical modelling of self-confining granular flows and confinement-enhanced entrainment

The physical models described in Chapter 6 provide the first subaqueous experimental evidence for the evolution of self-confinement through particle segregation in both single and multiple granular flows. In particular, the multiple-flow experiments demonstrate that self-confinement is dynamically coupled with flow-substrate interaction, whereby subsequent flows can remobilise pre-deposited sediments, reshape lateral levees, and progressively bulk up during downslope propagation.

However, the internal mechanics of particle segregation processes remain poorly constrained. Existing numerical and conceptual models of segregation are developed from subaerial single flows on fixed beds (e.g., Deboeuf et al., 2006; Thornton et al., 2006; Thornton and Gray, 2008; Gray and Ancey, 2009; Iverson et al., 2010; Gray and Kokelaar, 2010; Johnson et al., 2012; Kokelaar et al., 2014; Rocha et al., 2019). These models focus primarily on levee formation, flow-head recirculation and segregation-mobility feedbacks without mass exchange between flow and substrate (Savage and Lun, 1988; Major, 1997; Major and Iverson, 1999; Gray and Thornton, 2005; Iverson et al., 2010; Gray and Kokelaar, 2010; Johnson et al., 2012; Kokelaar et al., 2014; de Haas et al., 2015, 2016; Edwards et al., 2023). As a result, the existing models did not fully capture the role of substrate entrainment in modifying confinement, segregation and flow evolution in subaqueous settings.

Future work should develop numerical models of subaqueous self-confining granular flows that capture substrate entrainment during segregation. Such numerical work would help the understanding of particle trajectories, flow-head recirculation, remobilisation of pre-deposited particles during successive events, and changes in flow and substrate composition in subaqueous settings. The subaqueous experiments in Chapter 6 are designed to examine the role of flow-deposit interactions to provide insights into flow mobility and evolution (e.g., velocity, width, runout distance) of self-confined debris-flows. The experimental results provide a dataset for further numerical modelling of subaqueous segregation. An additional measure to aid validation of the numerical models would be quantification of the material exported from the experiments as these are not closed systems, and the final ratio of particles might be quite different to the starting ratio.

Chapter 8 Conclusions

This thesis has examined the effects of flow-relief and flow-substrate interactions on sediment failure, subsequent evolution, and flow mobility on gentle slopes. The main conclusions relating to the research questions addressed throughout this thesis are listed below.

1) What causes instability on low gradient carbonate submarine slopes?

- The instability of gentle submarine carbonate slopes is fundamentally controlled by sedimentary composition. The abnormal high water content that can be reached within weak layers in carbonate successions is attributed to the presence of foraminifera, which can provide space within chambered foraminifera shells to preserve water. The clay-capped foraminifera-rich successions provided permeability barriers to promote the high water content, and the formation of weak layers to be exploited during failure.

- During failure, weak-layer-controlled substrates are interpreted to undergo contractive shearing, resulting in compaction, crushing of foraminifera, and water release, leading to pore pressure increasing rapidly. As the substrate sediments were overridden by the landslide, the trapped water released from the substrate would elevate pore pressure in the substrate, and generate a water-rich layer/water film that acts as a confined lubricating layer at the top of the underlying weak layer and/or below the basal shear surface, resulting in a decrease in friction and shear strength.

- Although the preconditioning mechanisms differ between the weak-layer-controlled landslides and gas-related debris flows, the initiation of both cases is controlled by a low shear strength substrate, where fluid expulsion and/or pore-pressure can reduce basal friction and enhance flow mobility on gentle slopes.

2) How do subaqueous flows self-confine?

- This study demonstrates that self-confinement of debris flows and granular flows occurs in submarine environments, which provides new insights for the understanding of flow enhanced mobility and long runout on gentle slopes.

- Self-confinement can develop through the production of depositional relief, as shown in submarine debris flows from debrite lobes. Subaqueous granular-flows experiments further demonstrate that lateral depositional relief can be generated through particle segregation, during which coarser blocky particles are preferentially transported to the advancing flow head and form coarse-enriched lateral levees behind the flow head.

- Self-confinement can also develop through substrate incision, driven by depositional relief or the presence of weak layers in the substrate. Such substrate incision generates a negative topography, which can confine subsequent flow pathways.

- The self-confining process establishes a positive feedback where flow spreading is restricted and confinement increases, which drives increases in flow velocity and basal shear stress, leading to substrate incision, further increasing flow confinement, thereby increasing run-out distances.

- A better understanding of the evolution of flow self-confinement provides a new mechanism to explain the long runout distances documented for submarine debris-flows, despite their occurrence on low gradient slopes, with important implications for predicting debris-flow mobility and seafloor erosion.

3) How do self-confining subaqueous flows bulk-up during emplacement?

- Self-confining submarine debris flows can bulk-up substantially even on low gradient slopes. The pre-deposited lateral levees and fines-enriched conduit deposits increase the velocity of subsequent flows, thereby enhancing the entrainment of substrate and remobilisation of particles downslope.

- Flow bulking in self-confining subaqueous multiple experiments shows a dynamic interaction between successive granular flows and pre-existing deposits, through upslope entrainment (i.e., particle remobilisation) and downslope redeposition, and export from the open system.

- Bulking can influence the confinement through dynamic changes in flow composition, which control the thickness of confining levees and flow mobility. Levee thickness decreases with higher fines percentage in both single and multiple flow experiments.

- Submarine entrainment is the primary mechanism of flow bulking, as pre-existing deposits and underlying substrate are progressively incorporated into overriding flows. Substrate entrainment is pronounced on carbonate substrates, which in part is attributed to the lack of attractive forces (electrostatic bonding) from clay particles, which facilitates substrate entrainment on carbonate slopes, despite the low slope gradient.

- The interaction between flow (self-)confinement and bulking-up is a positive feedback, in which confinement enhances the flow volume through substrate entrainment, and substrate incision by entrainment in turn influences flow confinement.

- In nature, there will be a complicated and dynamic relationship between the evolving composition of the flow and the composition of deposits and substrate incorporated in the flow, which will change the flow dynamics in time and space.

Based on field-scale seismic observations and physical experimental results, this thesis demonstrates how flow self-confinement processes may act to influence the long runout distances of submarine debris flows. The dynamic flow-substrate interactions can increase flow confinement through formation of lateral relief, either levees and/or lobes, which can drive substrate incision that further enhances flow confinement, thereby enhancing flow mobility and runout even on low gradient slopes. The study highlights the need to account for flow-substrate interactions when assessing slope instability and flow mobility else hazard area and magnitude may be under-estimated. Consequently this understanding can be applied to improve hazard assessment for seafloor infrastructure, including submarine cables and pipelines (cf. Liu et al., 2026), and the tsunamigenic potential of a submarine slope (cf. Harbitz et al., 2014).

References

Acosta, E. A., Tibana, S., de Almeida, M. D. S., & Saboya, F. (2017). Centrifuge modeling of hydroplaning in submarine slopes. Ocean Engineering, 129, 451-458. http://dx.doi.org/10.1016/j.oceaneng.2016.10.047

Allen, C., Gomis‐Cartesio, L. E., Hodgson, D. M., Peakall, J., & Milana, J. P. (2022). Channel incision into a submarine landslide on a Carboniferous basin margin, San Juan, Argentina: Evidence for the role of knickpoints. The Depositional Record, 8(2), 628-655. https://doi.org/10.1002/dep2.178

Alsop, G. I., & Marco, S. (2011). Soft-sediment deformation within seismogenic slumps of the Dead Sea Basin. Journal of Structural Geology, 33(4), 433-457. https://doi.org/10.1016/j.jsg.2011.02.003

Alves, T. M. (2015). Submarine slide blocks and associated soft-sediment deformation in deep-water basins: A review. Marine and Petroleum Geology, 67, 262-285. https://doi.org/10.1016/j.marpetgeo.2015.05.010

Alves, T. M., & Cartwright, J. A. (2009). Volume balance of a submarine landslide in the Espirito Santo Basin, offshore Brazil: Quantifying seafloor erosion, sediment accumulation and depletion. Earth and Planetary Science Letters, 288(3-4), 572-580. https://doi.org/10.1016/j.epsl.2009.10.020

Ash-Mor, A., Almogi-Labin, A., Bouchet, V. M. P., Seuront, L., Guy-Haim, T., Ben-Avraham, Z., & Bookman, R. (2021). Going with the flow: Experimental simulation of sediment transport from a foraminifera perspective. Sedimentology, 69(3), 1231-1251. https://doi.org/10.1111/sed.12945

Audley-Charles, M., Ballantyne, P., & Hall, R. (1988). Mesozoic-Cenozoic rift-drift sequence of Asian fragments from Gondwanaland. Tectonophysics, 155(1-4), 317-330.

Awad, M., Aldaood, A., & Alkiki, I. (2022). Development of a compressibility prediction model based on soil index properties and area under/bounded by consolidation and rebound curves. Geotechnical and Geological Engineering, 40(9), 4787-4807. https://doi.org/10.1007/s10706-022-02184-9

Baas, J. H., Tracey, N. D., & Peakall, J. (2021). Sole marks reveal deep-marine depositional process and environment: Implications for flow transformation and hybrid event bed models. Journal of Sedimentary Research, 91, 986-1009. https://doi.org/10.2110/jsr.2020.104

Bachman, R. T. (1984). Intratest porosity in foraminifera. Journal of Sedimentary Research, 54, 0257-0262.

Baker, M. L., Baas, J. H., Malarkey, J., Jacinto, R. S., Craig, M. J., Kane, I. A., & Barker, S. (2017). The effect of clay type on the properties of cohesive sediment gravity flows and their deposits. Journal of Sedimentary Research, 87(11), 1176-1195. https://doi.org/10.2110/jsr.2017.63

Barrett, R. S., Bellwald, B., Talling, P. J., Micallef, A., Gross, F., Berndt, C., Planke, S., Myklebust, R., & Krastel, S. (2021). Does retrogression always account for the large volume of submarine megaslides? Evidence to the contrary from the Tampen Slide, Offshore Norway. Journal of Geophysical Research: Solid Earth, 126(2), e2020JB020655. https://doi.org/10.1029/2020jb020655

Barron, E.J., Dean, W. E., Schallreuter, R., & Stow, D. A. V. (1984). Lithology classification section in the introduction and explanatory notes, deep sea drilling project leg 75). In Hay et al. (Eds.), Initial Reports of the Deep Sea Drilling Project (Vol. 75). Washington (U.S. Government Printing Office), pp. 12-15.

Beemer, R.D., Sadekov, A., Lebrec, U., Shaw, J., Bandini-Maeder, A., Cassidy, M.J. (2019). Impact of biology on particle crushing in offshore calcareous sediments, in: Meehan et al. (Eds.), Geo-Congress 2019: Geotechnical Materials, Modeling, and Testing (GSP 310). American Society of Civil Engineers, Philadelphia, pp. 640-650. https://doi.org/10.1061/9780784482124.065

Berger, W. H., & Johnson, T. C. (1976). Deep-sea carbonates: dissolution and mass wasting on Ontong-Java Plateau. Science, 192, 785-787. https://doi.org/10.1126/science.192.4241.785

Berger, W. H., & Wefer, G. (2009). Marine biogenic sediments. In Gornitz, V. (Eds.), Encyclopedia of Paleoclimatology and Ancient Environments. Springer,

Dordrecht, Heidelberg, London, New York, 525-533. https://doi.org/10.1007/978-1-4020-4411-3_131
Berndt, C., Costa, S., Canals, M., Camerlenghi, A., de Mol, B., & Saunders, M. (2012). Repeated slope failure linked to fluid migration: The Ana submarine landslide complex, Eivissa Channel, Western Mediterranean Sea. Earth and Planetary Science Letters, 319, 65-74. https://doi.org/10.1016/j.epsl.2011.11.045
Bernhardt, A., Stright, L., & Lowe, D. R. (2012). Channelized debris‐flow deposits and their impact on turbidity currents: The Puchkirchen axial channel belt in the Austrian Molasse Basin. Sedimentology, 59(7), 2042-2070. https://doi.org/10.1111/j.1365-3091.2012.01334.x
Bilal, A., & McClay, K. (2022). Tectonic and stratigraphic evolution of the central Exmouth Plateau, NW Shelf of Australia. Marine and Petroleum Geology, 136, 105447.
Bjørlykke, K., & Høeg, K. (1997). Effects of burial diagenesis on stresses, compaction and fluid flow in sedimentary basins. Marine and Petroleum Geology, 14(3), 267-276. https://doi.org/10.1016/S0264-8172(96)00051-7
Booth, J.S., O'Leary, D.W., Popenoe, P., & Danforth, W.W. (1993). US Atlantic continental slope landslides: their distribution, general attributes, and implications. In: Schwab, W.C., Lee, H.J. & Twichell, D.C. (Eds.), Submarine Landslides: Selected Studies in the US Exclusive Economic Zone. U.S. Geological Survey Bulletin, 2002, pp. 14-22.
Böttner, C., Stevenson, C.J., Englert, R., Schönke, M., Pandolpho, B.T., Geersen, J., Feldens, P., Krastel, S. (2024). Extreme erosion and bulking in a giant submarine gravity flow. Science Advances 10, eadp2584. https://doi.org/10.1126/sciadv.adp2584
Bouma, A. H. (1962). Sedimentology of Some Flysch Deposits: A Graphic Approach to Facies Interpretation, Elsevier, Amsterdam.
Bowler, J. M. (1976). Aridity in Australia: age, origins and expression in aeolian landforms and sediments. Earth-Science Reviews, 12(2-3), 279-310.
Boyd, R., Williamson, P., & Haq, B.U. (1993). Seismic stratigraphy and passive‐margin evolution of the southern Exmouth plateau. In: Posamentier et al. (Eds.), Sequence Stratigraphy and Facies Associations. Wiley, Oxford, pp. 581-603. https://doi.org/10.1002/9781444304015.ch29
Brooks, H. L., Hodgson, D. M., Brunt, R. L., Peakall, J., & Flint, S. S. (2018). Exhumed lateral margins and increasing flow confinement of a submarine landslide complex. Sedimentology, 65(4), 1067-1096. https://doi.org/10.1111/sed.12415
Broster, B. E., & Hicock, S. R. (1985). Multiple flow and support mechanisms and the development of inverse grading in a subaquatic glacigenic debris flow. Sedimentology, 32(5), 645-657. https://doi.org/10.1111/j.1365-3091.1985.tb00479.x
Brothers, D. S., Ruppel, C., Kluesner, J. W., ten Brink, U. S., Chaytor, J. D., Hill, J. C., Andrews, B. D., & Flores, C. (2014). Seabed fluid expulsion along the upper slope and outer shelf of the U.S. Atlantic continental margin. Geophysical Research Letters, 41(1), 96-101. https://doi.org/10.1002/2013gl058048
Brothers, D. S., Haeussler, P. J., Liberty, L., Finlayson, D., Geist, E., Labay, K., & Byerly, M. (2016). A submarine landslide source for the devastating 1964 Chenega tsunami, southern Alaska. Earth and Planetary Science Letters, 438, 112-121. https://doi.org/10.1016/j.epsl.2016.01.008
Bryn, P., Berg, K., Forsberg, C. F., Solheim, A., & Kvalstad, T. J. (2005). Explaining the Storegga Slide. Marine and Petroleum Geology, 22(1-2), 11-19. https://doi.org/10.1016/j.marpetgeo.2004.12.003
Bull, S., Cartwright, J., & Huuse, M. (2009). A review of kinematic indicators from mass-transport complexes using 3D seismic data. Marine and Petroleum Geology, 26(7), 1132-1151. https://doi.org/10.1016/j.marpetgeo.2008.09.011
Cardona, S., Wood, L. J., Dugan, B., Jobe, Z., & Strachan, L. J. (2020). Characterization of the Rapanui mass-transport deposit and the basal shear zone: Mount Messenger Formation, Taranaki Basin, New Zealand. Sedimentology, 67(4), 2111-2148. https://doi.org/10.1111/sed.12697
Carter, G. D., Cooper, R., Gafeira, J., Howe, J. A., & Long, D. (2020). Morphology of small-scale submarine mass movement events across the northwest United Kingdom. Geomorphology, 365, 107282.

https://doi.org/10.1016/j.geomorph.2020.107282
Casagrande, J., Hodgson, D.M., & Peakall, J. (2024). A salty snapshot: extreme variations in basal erosion patterns preserved in a submarine channel. Journal of the Geological Society of London, 181, jgs2023-006. https://doi.org/10.1144/jgs2023-006
Casas, D., Ercilla, G., Baraza, J. (2006). Physical properties and their relationship to texture and consolidation effects in Pliocene-Quaternary sediments from Madeira Abyssal Plain. Marine Georesources & Geotechnology 24(4), 265-286. https://doi.org/10.1080/10641190600788437
Choi, C. E., Yu, J., & Zhang, J. (2024). Review of the missing link between field and modeled submarine debris flows: Scale effects of physical modeling. Earth-Science Reviews, 258, 104911. https://doi.org/10.1016/j.earscirev.2024.104911
Clare, M. A., Talling, P. J., Challenor, P., Malgesini, G., & Hunt, J. (2014). Distal turbidites reveal a common distribution for large (> 0.1 km^3) submarine landslide recurrence. Geology, 42(3), 263-266. https://doi.org/10.1130/G35160.1
Counts, J. W., Jorry, S. J., Vazquez-Riveiros, N., Amy, L. A., Dennielou, E., & Jouet, G. (2021). Sedimentology and distribution of late quaternary calciturbidites and calcidebrites in the Mozambique Channel (Southwest Indian Ocean). Facies, 67(2), 17. https://doi.org/10.1007/s10347-021-00624-1
Coussot, P., & Meunier, M. (1996). Recognition, classification and mechanical description of debris flows. Earth-Science Reviews, 40(3-4), 209-227. https://doi.org/10.1016/0012-8252(95)00065-8
Couvin, B., Georgiopoulou, A., & Amy, L. A. (2024). A guide to recognising slow-moving subaqueous landslides in seismic and bathymetry datasets. Earth-Science Reviews, 252, 104749. https://doi.org/10.1016/j.earscirev.2024.104749
Crimes, T. (1973). From limestones to distal turbidites: A facies and trace fossil analysis in the Zumaya flysch (Paleocene—Eocene), North Spain. Sedimentology, 20(1), 105-131.
Crutchley, G. J., Elger, J., Kuhlmann, J., Mountjoy, J. J., Orpin, A., Georgiopoulou, A., Carey, J., Dugan, B., Cardona, S., Han, S., Cook, A., Screaton, E. J., Pecher, I. A., Barnes, P., & Huhn, K. (2022). Investigating the Basal Shear Zone of the Submarine Tuaheni Landslide Complex, New Zealand: A Core-Log-Seismic Integration Study. Journal of Geophysical Research: Solid Earth, 127(1), e2021JB021997. https://doi.org/10.1029/2021jb021997
Dakin, N., Pickering, K., Mohrig, D., & Bayliss, N. (2013). Channel-like features created by erosive submarine debris flows: field evidence from the Middle Eocene Ainsa Basin, Spanish Pyrenees. Marine and Petroleum Geology, 41, 62-71. https://doi.org/10.1016/j.marpetgeo.2012.07.007
De Blasio, F. V., Engvik, L., Harbitz, C. B., & Elverhøi, A. (2004a). Hydroplaning and submarine debris flows. Journal of Geophysical Research: Oceans, 109(C1), C01002. https://doi.org/10.1029/2002jc001714
De Blasio, F. V., Ilstad, T., Elverhøi, A., Issler, D., & Harbitz, C. B. (2004b). High mobility of subaqueous debris flows and the lubricating-layer model. In: Offshore Technology Conference (OTC-16564-MS), Houston, Texas. https://doi.org/10.4043/16747-MS
De Blasio, F. V., Elverhøi, A., Engvik, L. E., Issler, D., Gauer, P., & Harbitz, C. (2006). Understanding the high mobility of subaqueous debris flows. Norwegian Journal of Geology, 86(3), 275-284.
Dean, W. E., Leinen, M., & Stow, D. A. V. (1985). Classification of deep-sea, fine-grained sediments. Journal of Sedimentary Research, 55, 0250-0256. https://doi.org/10.1306/212F868E-2B24-11D7-8648000102C1865D
de Haas, T., Braat, L., Leuven, J. R. F. W., Lokhorst, I. R., & Kleinhans, M. G. (2015). Effects of debris flow composition on runout, depositional mechanisms, and deposit morphology in laboratory experiments. Journal of Geophysical Research: Earth Surface, 120(9), 1949-1972. https://doi.org/10.1002/2015jf003525
de Haas, T., van den Berg, W., Braat, L., & Kleinhans, M. G. (2016). Autogenic avulsion, channelization and backfilling dynamics of debris-flow fans. Sedimentology, 63(6), 1596-1619. https://doi.org/10.1111/sed.12275
Deboeuf, S., Lajeunesse, E., Dauchot, O., & Andreotti, B. (2006). Flow rule, self-

channelization, and levees in unconfined granular flows. Physical review letters, 97(15), 158303. https://doi.org/10.1103/PhysRevLett.97.158303
Demars, K. R. (1982). Unique engineering properties and compression behavior of deep-sea calcareous sediments. ASTM International. In: Demars and Chaney (Eds), Geotechnical Properties, Behaviour, and Performance of Calcareous Soils. ASTM International, STP777-EB, pp. 97-112.
Deptuck, M. E., Mosher, D. C., Campbell, D. C., Hughes-Clarke, J. E., & Noseworthy, D. (2007). Along slope variations in mass failures and relationships to major Plio-Pleistocene morphological elements, SW Labrador Sea. In: Lykousis et al. (Eds.), Submarine Mass Movements and Their Consequences. Springer, Dordrecht, 27, pp. 37-45. https://doi.org/10.1007/978-1-4020-6512-5_5
Dijkstra, J., Gaudin, C., & White, D. J. (2013). Comparison of failure modes below footings on carbonate and silica sands. International Journal of Physical Modelling in Geotechnics, 13(1), 1-12. https://doi.org/10.1680/ijpmg.12.00004
Direen, N., Stagg, H., Symonds, P., & Colwell, J. (2008). Architecture of volcanic rifted margins: new insights from the Exmouth–Gascoyne margin, Western Australia. Australian Journal of Earth Sciences, 55(3), 341-363.
Driscoll, N. W., & Karner, G. D. (1998). Lower crustal extension across the Northern Carnarvon basin, Australia: Evidence for an eastward dipping detachment. Journal of Geophysical Research: Solid Earth, 103(B3), 4975-4991.
Dong, Y., Wang, D., & Randolph, M. F. (2017). Runout of submarine landslide simulated with material point method. Journal of Hydrodynamics, Ser. B, 29(3), 438-444. https://doi.org/10.1016/S1001-6058(16)60754-0
Dumoulin, J. A. (1992). Lower cretaceous smarl turbidites of the Argo Abyssal Plain, Indian Ocean. In: Gradstein et al. (Eds), Proc. ODP, Sci. Results, 123. College Station, TX (Ocean Drilling Program), pp. 111-135.
Dutkiewicz, A., Muller, R.D., O'Callaghan, S., Jonasson, H. (2015). Census of seafloor sediments in the world's ocean. Geology 43(9), 795-798. https://doi.org/10.1130/G36883.1
Dutkiewicz, A., Judge, A. & Muller, R.D. (2020). Environmental predictors of deep-sea polymetallic nodule occurrence in the global ocean. Geology 48(3), 293-297. https://doi.org/10.1130/G46836.1
Edwards, A. N., Rocha, F. M., Kokelaar, B. P., Johnson, C. G., & Gray, J. M. N. T. (2023). Particle-size segregation in self-channelized granular flows. Journal of Fluid Mechanics, 955. https://doi.org/10.1017/jfm.2022.1089
Elger, J., Berndt, C., Rupke, L., Krastel, S., Gross, F., & Geissler, W. H. (2018). Submarine slope failures due to pipe structure formation. Nat Commun 9, 715. https://doi.org/10.1038/s41467-018-03176-1
Elverhøi, A., Issler, D., De Blasio, F. V., Ilstad, T., Harbitz, C. B., & Gauer, P. (2005). Emerging insights into the dynamics of submarine debris flows. Natural Hazards and Earth System Sciences, 5(5), 633-648. https://doi.org/10.5194/nhess-5-633-2005
Elverhøi, A., Breien, H., De Blasio, F. V., Harbitz, C. B., & Pagliardi, M. (2010). Submarine landslides and the importance of the initial sediment composition for run-out length and final deposit. Ocean Dynamics, 60(4), 1027-1046. https://doi.org/10.1007/s10236-010-0317-z
Embley, R. W. (1976). New evidence for occurrence of debris flow deposits in the deep sea. Geology, 4(6), 371-374. https://doi.org/10.1130/0091-7613(1976)4<371:NEFOOD>2.0.CO;2
Embley, R. W. (1982). Anatomy of some Atlantic margin sediment slides and some comments on ages and mechanisms. In : Saxov, S., & Nieuwenhuis, J.K. (Eds), Marine Slides and Other Mass Movements. NATO Conference Series, Springer, Boston, MA, vol 6., pp. 189-213. https://doi.org/10.1007/978-1-4613-3362-3_11
Enos, P. (1969). Anatomy of a flysch. Journal of Sedimentary Research, 39(2), 680-723. https://doi.org/10.1306/74D71CF8-2B21-11D7-8648000102C1865D
Eruteya, O. E., Niyazi, Y., Omosanya, K. O., Ierodiaconou, D. & Moscariello, A. (2020). Evolution and morphology of rafted blocks in an ancient deepwater mass-transport complex (Exmouth Plateau, offshore North West Australia). Interpretation, 8(4), SV31-SV50. https://doi.org/10.1190/INT-2020-0067.1

Evans, D., Harrison, Z., Shannon, P., Laberg, J., Nielsen, T., Ayers, S., Holmes, R., Hoult, R., Lindberg, B., Haflidason, H. & Long, D., Kuijpers, A., Andersen, E.S., & Bryn, P. (2005). Palaeoslides and other mass failures of Pliocene to Pleistocene age along the Atlantic continental margin of NW Europe. Marine and Petroleum Geology, 22(9-10), 1131-1148. https://doi.org/10.1016/j.marpetgeo.2005.01.010

Exon, N., Haq, B. & Von Rad, U. (1992). Exmouth Plateau revisited: scientific drilling and geological framework, in: von Rad, U., Haq, B.U. (Eds.), Proceedings of the Ocean Drilling Program, Scientific Results, 122. TX (Ocean Drilling Program), Texas, pp. 3-20.

Feng, Y., & Owen, D. (2014). Discrete element modelling of large scale particle systems—I: exact scaling laws. Computational Particle Mechanics, 1(2), 159-168. https://doi.org/10.1007/s40571-014-0010-y

Fine, I. V., Rabinovich, A. B., Bornhold, B., Thomson, R., & Kulikov, E. A. (2005). The Grand Banks landslide-generated tsunami of November 18, 1929: preliminary analysis and numerical modeling. Marine Geology, 215(1-2), 45-57. https://doi.org/10.1016/j.margeo.2004.11.007

Frey-Martínez, J., Cartwright, J., James, D. (2006). Frontally confined versus frontally emergent submarine landslides: A 3D seismic characterisation. Marine and Petroleum Geology 23(5), 585-604. https://doi.org/10.1016/j.marpetgeo.2006.04.002

Gales, J.A., Talling, P.J., Cartigny, M.J., Hughes Clarke, J., Lintern, G., Stacey, C. & Clare, M.A. (2019). What controls submarine channel development and the morphology of deltas entering deep‐water fjords? Earth Surface Processes and Landforms, 44(2), 535-551. https://doi.org/10.1002/esp.4515

Gales, J.A., McKay, R.M., De Santis, L., Rebesco, M., Laberg, J.S., Shevenell, A.E., Harwood, D., Leckie, R.M., Kulhanek, D.K., King, M., Patterson, M., Lucchi, R.G., Kim, S., Kim, S., Dodd, J., Seidenstein, J., Prunella, C., Ferrante, G.M., IODP Expedition 374 Scientists. (2023). Climate-controlled submarine landslides on the Antarctic continental margin. Nature Communications 14(1), 2714. https://doi.org/10.1038/s41467-023-38240-y

Gamboa, D., Alves, T. & Cartwright, J. (2011). Distribution and characterization of failed (mega)blocks along salt ridges, southeast Brazil: Implications for vertical fluid flow on continental margins. Journal of Geophysical Research-Solid Earth, 116(B8), 1-20. https://doi.org/10.1029/2011JB008357

Gamboa, D., Alves, T. & Cartwright, J. (2012). Seismic-scale rafted and remnant blocks over salt ridges in the Espírito Santo Basin, Brazil. In: Yamada et al. (Eds), Submarine Mass Movements and Their Consequences, Advances in Natural and Technological Hazards Research. Springer, Dordrecht, 31, pp. 629-638. https://doi.org/10.1007/978-94-007-2162-3_56

Gamboa, D., & Alves, T. M. (2015). Three-dimensional fault meshes and multi-layer shear in mass-transport blocks: Implications for fluid flow on continental margins. Tectonophysics, 647, 21-32. https://doi.org/10.1016/j.tecto.2015.02.007

Gartrell, A. (2000). Rheological controls on extensional styles and the structural evolution of the Northern Carnarvon Basin, North West Shelf, Australia. Australian Journal of Earth Sciences, 47(2), 231-244.

Gatter, R., Clare, M.A., Kuhlmann, J., Huhn, K. (2021). Characterisation of weak layers, physical controls on their global distribution and their role in submarine landslide formation. Earth-Science Reviews 223, 103845. https://doi.org/10.1016/j.earscirev.2021.103845

Gaudin, C., & White, D. (2009). New centrifuge modelling techniques for investigating seabed pipeline behaviour. In: Hamza et al. (Eds), Proceedings of the 17th International Conference on Soil Mechanics and Geotechnical Engineering. IOS Press, 1, pp. 448-451. https://doi.org/10.3233/978-1-60750-031-5-448

Gee, M. J. R., Masson, D. G., Watts, A. B., & Allen, P. A. (1999). The Saharan debris flow: an insight into the mechanics of long runout submarine debris flows. Sedimentology, 46(2), 317-335. https://doi.org/10.1046/j.1365-3091.1999.00215.x

Gee, M. J., Masson, D. G., Watts, A. B., & Mitchell, N. C. (2001). Passage of debris flows and turbidity currents through a topographic constriction: seafloor erosion and deflection of flow pathways.

Sedimentology, 48(6), 1389-1409. https://doi.org/10.1046/j.1365-3091.2001.00427.x
Gee, M. J. R., Gawthorpe, R. L., & Friedmann, J. S. (2005). Giant striations at the base of a submarine landslide. Marine Geology, 214(1-3), 287-294. https://doi.org/10.1016/j.margeo.2004.09.003
Gee, M. J. R., Gawthorpe, R. L., & Friedmann, S. J. (2006). Triggering and evolution of a giant submarine landslide, offshore Angola, revealed by 3D seismic stratigraphy and geomorphology. Journal of Sedimentary Research, 76(1-2), 9-19. https://doi.org/10.2110/jsr.2006.02
Gee, M. J. R., Uy, H. S., Warren, J., Morley, C. K., & Lambiase, J. J. (2007). The Brunei slide: A giant submarine landslide on the North West Borneo Margin revealed by 3D seismic data. Marine Geology, 246(1), 9-23. https://doi.org/10.1016/j.margeo.2007.07.009
Georgiopoulou, A., Masson, D. G., Wynn, R. B., & Krastel, S. (2010). Sahara Slide: age, initiation, and processes of a giant submarine slide. Geochemistry, Geophysics, Geosystems, 11(7), Q07014. https://doi.org/10.1029/2010GC003066
Gibbons, A. D., Barckhausen, U., vanden Bogaard, P., Hoernle, K., Werner, R., Whittaker, J. M., & Müller, R. D. (2012), Constraining the Jurassic extent of Greater India: Tectonic evolution of the West Australian margin, Geochem. Geophys. Geosyst., 13, Q05W13, https://doi.org/10.1029/2011GC003919
Gray, J. M. N. T. (2018). Particle Segregation in Dense Granular Flows. Annual Review of Fluid Mechanics, 50(1), 407-433. https://doi.org/10.1146/annurev-fluid-122316-045201
Gray, J., & Thornton, A. (2005). A theory for particle size segregation in shallow granular free-surface flows. Proceedings of the Royal Society A: Mathematical, Physical and Engineering Sciences, 461(2057), 1447-1473. https://doi.org/10.1098/rspa.2004.1420
Gray, J. N. T., & Ancey, C. (2009). Segregation, recirculation and deposition of coarse particles near two-dimensional avalanche fronts. Journal of Fluid Mechanics, 629, 387-423. https://doi.org/10.1017/S0022112009006466
Gray, J., & Kokelaar, B. (2010). Large particle segregation, transport and accumulation in granular free-surface flows. Journal of Fluid Mechanics, 652, 105-137. https://doi.org/10.1017/S002211201000011X
Gray, J. M. N. T., Gajjar, P., & Kokelaar, P. (2015). Particle-size segregation in dense granular avalanches. Comptes Rendus Physique, 16(1), 73-85. http://dx.doi.org/10.1016/j.crhy.2015.01.004
Grilli, S. T., Taylor, O. D. S., Baxter, C. D. P., & Maretzki, S. (2009). A probabilistic approach for determining submarine landslide tsunami hazard along the upper east coast of the United States. Marine Geology, 264(1-2), 74-97. https://doi.org/10.1016/j.margeo.2009.02.010
Grilli, S. T., Tappin, D. R., Carey, S., Watt, S. F. L., Ward, S. N., Grilli, A. R., Engwell, S. L., Zhang, C., Kirby, J. T., Schambach, L., & Muin, M. (2019). Modelling of the tsunami from the December 22, 2018 lateral collapse of Anak Krakatau volcano in the Sunda Straits, Indonesia. Sci Rep, 9(1), 11946. https://doi.org/10.1038/s41598-019-48327-6
Gross, F., Mountjoy, J. J., Crutchley, G. J., Bottner, C., Koch, S., Bialas, J., Pecher, I., Woelz, S., Dannowski, A., Micallef, A., Huhn, K., & Krastel, S. (2018). Free gas distribution and basal shear zone development in a subaqueous landslide - Insight from 3D seismic imaging of the Tuaheni Landslide Complex, New Zealand. Earth and Planetary Science Letters, 502, 231-243. https://doi.org/10.1016/j.epsl.2018.09.002
Grousset, F. E., Biscaye, P. E., Revel, M., Petit, J.-R., Pye, K., Joussaume, S., & Jouzel, J. (1992). Antarctic (Dome C) ice-core dust at 18 ky BP: Isotopic constraints on origins. Earth and Planetary Science Letters, 111(1), 175-182.
Grützner, J., & Mienert, J. (1999). Physical Property Changes as a Monitor of Pelagic Carbonate Diagenesis: an Empirically Derived Diagenetic Model for Atlantic Ocean Basins. AAPG bulletin, 83(9), 1485-1501. https://doi.org/10.1306/E4FD41ED-1732-11D7-8645000102C1865D
Guiastrennec-Faugas, L., Gillet, H., Jacinto, R.S., Dennielou, B., Hanquiez, V., Schmidt, S., Simplet, L. & Rousset, A. (2020). Upstream migrating knickpoints and related sedimentary processes in a submarine canyon from a rare 20-year

morpho-bathymetric time-lapse (Capbreton submarine canyon, Bay of Biscay, France). Marine Geology, 423, 106143. https://doi.org/10.1016/j.margeo.2020.106143
Guiastrennec-Faugas, L., Gillet, H., Peakall, J., Dennielou, B., Gaillot, A. & Jacinto, R.S. (2021). Initiation and evolution of knickpoints and their role in cut and fill processes in active submarine channels. Geology, 49, 314– 319. https://doi.org/10.1130/G48369.1
Haflidason, H., Sejrup, H. P., Nygard, A., Mienert, J., Bryn, P., Lien, R., Forsberg, C. F., Berg, K., & Masson, D. (2004). The Storegga Slide: architecture, geometry and slide development. Marine Geology, 213(1-4), 201-234. https://doi.org/10.1016/j.margeo.2004.10.007
Haflidason, H., Lien, R., Sejrup, H. P., Forsberg, C. F., & Bryn, P. (2005). The dating and morphometry of the Storegga Slide. Marine and Petroleum Geology, 22(1-2), 123-136. https://doi.org/10.1016/j.marpetgeo.2004.10.008
Haq, B.U., Von Rad, U., O'Connell, S., Bent, A., 1990. Proceedings of the Ocean Drilling Program: Initial Reports, 122, TX (Ocean Drilling Program), Texas.
Hairabian, A., Fournier, F., Borgomano, J., & Nardon, S. (2014). Depositional facies, pore types and elastic properties of deep-water gravity flow carbonates. Journal of Petroleum Geology, 37(3), 231-249. https://doi.org/10.1111/jpg.12581
Hamilton, E. L. (1976). Variations of density and porosity with depth in deep-sea sediments. Journal of Sedimentary Research, 46(2), 280-300. https://doi.org/10.1306/212F6F3C-2B24-11D7-8648000102C1865D
Hampton, M.A. (1970). Subaqueous Debris Flow and Generation of Turbidity Currents. Unpublished doctoral dissertation, Stanford University, California, 180 pp.
Hampton, M. A., Lee, H. J., & Locat, J. (1996). Submarine landslides. Reviews of Geophysics, 34(1), 33-59. https://doi.org/10.1029/95RG03287
Harbitz, C. B., Løvholt, F., & Bungum, H. (2014). Submarine landslide tsunamis: how extreme and how likely?. Natural Hazards, 72(3), 1341-1374. https://doi.org/10.1007/s11069-013-0681-3
Haughton, P., Davis, C., McCaffrey, W., & Barker, S. (2009). Hybrid sediment gravity flow deposits–classification, origin and significance. Marine and Petroleum Geology, 26(10), 1900-1918. https://doi.org/10.1016/j.marpetgeo.2009.02.012
Heijnen, M.S., Clare, M.A., Cartigny, M.J.B., Talling, P.J., Hage, S., Lintern, D.G., Stacey, C., Parsons, D.R., Simmons, S.M., Chen, Y., Sumner, E.J., Dix, J.K. & Hughes Clarke, J.E. (2020). Rapidly-migrating and internally-generated knickpoints can control submarine channel evolution. Nature Communications, 11, 3129.
Hengesh, J. V., Dirstein, J. K., & Stanley, A. J. (2013). Landslide geomorphology along the Exmouth Plateau continental margin, north west shelf, Australia. Australian Geomechanics, 48, 71-92.
Hodgson, D.M., Brooks, H.L., Ortiz-Karpf, A., Spychala, Y., Lee, D.R., & Jackson, C.A.L. (2019). Entrainment and abrasion of megaclasts during submarine landsliding and their impact on flow behaviour. In: Lintern et al. (Eds.), Subaqueous Mass Movements and Their Consequences: Assessing Geohazards, Environmental Implications and Economic Significance of Subaqueous Landslides. Geological Society, London, Special Publications, 477(1), pp. 223-240. https://doi.org/10.1144/sp477.26
Hodgson, D. M., Miramontes, E., Kane, I. A., & Jackson, C. A.-L. (2026). 12. Deep-Water Detrital Systems. In: Lovell (Ed.), Reading's Sedimentary Environments: Processes, Facies and Stratigraphy (4th ed.). WILEY, Blackwell, pp. 1039-1113.
Hoffman, P. F., & Hartz, E. H. (1999). Large, coherent, submarine landslide associated with Pan-African foreland flexure. Geology, 27(8), 687-690. https://doi.org/10.1130/0091-7613(1999)027<0687:LCSLAW>2.3.CO;2
Hu, F., & Xiao, X. (2025). Grain Shape Variation of Different Sand-Sized Particles and Its Implication for Discriminating Sedimentary Environment. Geosciences, 15(11), 412. https://doi.org/10.3390/geosciences15110412
Hunt, J. E., Tappin, D. R., Watt, S. F. L., Susilohadi, S., Novellino, A., Ebmeier, S. K., Cassidy, M., Engwell, S. L., Grilli, S. T., Hanif, M., Priyanto, W. S., Clare, M. A., Abdurrachman, M., & Udrekh, U. (2021). Submarine landslide megablocks

show half of Anak Krakatau island failed on December 22nd, 2018. Nat Commun, 12(1), 2827. https://doi.org/10.1038/s41467-021-22610-5
Hussein, A.A.A., Zhao, L., Al-Masgari, A.A.S.A., Handoyo, H. (2024). Shear strength characteristics of marine sediments: the influences of lithofacies and sedimentological environment. Marine Geophysical Research 45(3), 14. https://doi.org/10.1007/s11001-024-09545-4
Ikehara, K., Irino, T., Usami, K., Jenkins, R., Omura, A., & Ashi, J. (2014). Possible submarine tsunami deposits on the outer shelf of Sendai Bay, Japan resulting from the 2011 earthquake and tsunami off the Pacific coast of Tohoku. Marine Geology, 358, 120-127. https://doi.org/10.1016/j.margeo.2014.11.004
Ilstad, T., Elverhøi, A., Issler, D., & Marr, J. G. (2004a). Subaqueous debris flow behaviour and its dependence on the sand/clay ratio: a laboratory study using particle tracking. Marine Geology, 213(1-4), 415-438. https://doi.org/10.1016/j.margeo.2004.10.017
Ilstad, T., De Blasio, F. V., Elverhøi, A., Harbitz, C. B., Engvik, L., Longva, O., & Marr, J. G. (2004b). On the frontal dynamics and morphology of submarine debris flows. Marine Geology, 213(1-4), 481-497. https://doi.org/10.1016/j.margeo.2004.10.020
Ilstad, T., Marr, J. G., Elverhøi, A., & Harbitz, C. B. (2004c). Laboratory studies of subaqueous debris flows by measurements of pore-fluid pressure and total stress. Marine Geology, 213(1-4), 403-414. https://doi.org/10.1016/j.margeo.2004.10.016
Imran, J., Harff, P., & Parker, G. (2001). A numerical model of submarine debris flow with graphical user interface. Computers & Geosciences, 27(6), 717-729. https://doi.org/10.1016/S0098-3004(00)00124-2
Iverson, R. M. (1997). The physics of debris flows. Reviews of Geophysics, 35(3), 245-296. https://doi.org/10.1029/97RG00426
Iverson, R. M. (2005). Regulation of landslide motion by dilatancy and pore pressure feedback. Journal of Geophysical Research: Earth Surface, 110(F2). https://doi.org/10.1029/2004jf000268
Iverson, R.M. (2012). Elementary theory of bed-sediment entrainment by debris flows and avalanches, Journal of Geophysical Research 117, F03006. https://doi.org/10.1029/2011JF002189
Iverson, R. M., & Vallance, J. W. (2001). New views of granular mass flows. Geology, 29(2), 115-118. https://doi.org/10.1130/0091-7613(2001)029<0115:NVOGMF>2.0.CO;2
Iverson, R. M., Reid, M. E., & LaHusen, R. G. (1997). Debris-flow mobilization from landslides. Annual Review of Earth and Planetary Sciences, 25(1), 85-138. https://doi.org/10.1146/annurev.earth.25.1.85
Iverson, R.M., Reid, M.E., Iverson, N.R., LaHusen, R.G., Logan, M., Mann, J.E., Brien, D.L. (2000). Acute sensitivity of landslide rates to initial soil porosity. Science 290(5491), 513-516. https://doi.org/10.1126/science.290.5491.513
Iverson, R. M., Logan, M., LaHusen, R. G., & Berti, M. (2010). The perfect debris flow? Aggregated results from 28 large-scale experiments. Journal of Geophysical Research: Earth Surface, 115, F03005. https://doi.org/10.1029/2009JF001514
Iverson, R. M., Reid, M. E., Logan, M., LaHusen, R. G., Godt, J. W., & Griswold, J. P. (2011). Positive feedback and momentum growth during debris-flow entrainment of wet bed sediment. Nature Geoscience, 4(2), 116-121. https://doi.org/10.1038/ngeo1040
Jackson, C. A. L. (2011). Three-dimensional seismic analysis of megaclast deformation within a mass transport deposit; implications for debris flow kinematics. Geology, 39(3), 203-206. https://doi.org/10.1130/G31767.1
Johnson, C., Kokelaar, B., Iverson, R. M., Logan, M., LaHusen, R., & Gray, J. (2012). Grain-size segregation and levee formation in geophysical mass flows. Journal of Geophysical Research: Earth Surface, 117, F01032. https://doi.org/10.1029/2011JF002185
Kaitna, R., Palucis, M. C., Yohannes, B., Hill, K. M., & Dietrich, W. E. (2016). Effects of coarse grain size distribution and fine particle content on pore fluid pressure and shear behavior in experimental debris flows. Journal of Geophysical Research:

Earth Surface, 121(2), 415-441. https://doi.org/10.1002/2015jf003725
Kastens, K.A. (1984). Earthquakes as a triggering mechanism for debris flows and turbidites on the Calabrian Ridge. Mar. Geol., 55, 13-33.
Kawakita, S., Asahina, D., Takemura, T., Hosono, H., Kitajima, K. (2020). Effect of hydraulic and mechanical characteristics of sediment layers on water film formation in submarine landslides. Progress in Earth and Planetary Science 7 (62), 1-12. https://doi.org/10.1186/s40645-020-00375-7
Kleinhans, M. G., van Dijk, W. M., van de Lageweg, W. I., Hoyal, D. C., Markies, H., van Maarseveen, M., ... & Cheshier, N. (2014). Quantifiable effectiveness of experimental scaling of river-and delta morphodynamics and stratigraphy. Earth-Science Reviews, 133, 43-61. https://doi.org/10.1016/j.earscirev.2014.03.001
Kokelaar, B., Graham, R., Gray, J., & Vallance, J. W. (2014). Fine-grained linings of leveed channels facilitate runout of granular flows. Earth and Planetary Science Letters, 385, 172-180. https://doi.org/10.1016/j.epsl.2013.10.043
Kokusho, T. (1999). Water film in liquefied sand and its effect on lateral spread, in: O'Sullivan et al. (Eds.), Journal of Geotechnical and Geoenvironmental Engineering. ASCE, pp. 817–826. https://doi.org/10.1061/(ASCE)1090-0241(1999)125:10(817)
Kokusho, T., Kojima, T. (2002). Mechanism for postliquefaction water film generation in layered sand, in: O'Sullivan et al. (Eds.), Journal of Geotechnical and Geoenvironmental Engineering. ASCE, Reston, pp. 129-137. https://doi.org/10.1061/(ASCE)1090-0241(2002)128:2(129)
Krastel, S., Wynn, R. B., Feldens, P., Schürer, A., Böttner, C., Stevenson, C., Cartigny, M. J., Hühnerbach, V., & Unverricht, D. (2016). Flow behaviour of a giant landslide and debris flow entering Agadir Canyon, NW Africa. In: Lamaeche et al. (Eds), Submarine Mass Movements and their Consequences: 7th International Symposium. Springer, Cham, 41, pp. 145-154. https://doi.org/10.1007/978-3-319-20979-1_14
Krastel, S., Li, W., Urlaub, M., Georgiopoulou, A., Wynn, R., Schwenk, T., Stevenson, C., & Feldens, P. (2019). Mass wasting along the NW African continental margin. In: Lintern et al. (Eds), Subaqueous Mass Movements and Their Consequences: Assessing Geohazards, Environmental Implications and Economic Significance of Subaqueous Landslides. Geological Society, London, Special Publications, 477(1), pp. 151-167. https://doi.org/10.1144/SP477.36
Kuenen, P. H. (1957). Sole markings of graded graywacke beds. The Journal of Geology, 65(3), 231-258.
Kumar, P. C., Omosanya, K. O., Eruteya, O. E., & Sain, K. (2021). Geomorphological characterization of basal flow markers during recurrent mass movement: A case study from the Taranaki Basin, offshore New Zealand. Basin research, 33(4), 2358-2382. https://doi.org/10.1111/bre.12560
Kvalstad, T.J., Andresen, L., Forsberg, C.F., Berg, K., Bryn, P., Wangen, M. (2005). The Storegga slide: evaluation of triggering sources and slide mechanics, Marine and Petroleum Geology 22, 245-256. https://doi.org/10.1016/j.marpetgeo.2004.10.019
Laberg, J., & Vorren, T. (1995). Late Weichselian submarine debris flow deposits on the Bear Island Trough mouth fan. Marine Geology, 127(1-4), 45-72. https://doi.org/10.1016/0025-3227(95)00055-4
Laberg, J., & Vorren, T. (2000). The Trænadjupet Slide, offshore Norway—morphology, evacuation and triggering mechanisms. Marine Geology, 171(1-4), 95-114. https://doi.org/10.1016/S0025-3227(00)00112-2
Lamarche, G., Joanne, C., & Collot, J. Y. (2008). Successive, large mass-transport deposits in the south Kermadec fore-arc basin, New Zealand: The Matakaoa submarine instability complex. Geochemistry Geophysics Geosystems, 9(4), Q04001. https://doi.org/10.1029/2007GC001843
Lamas, F., Irigaray, C., & Chacón, J. (2002). Geotechnical characterization of carbonate marls for the construction of impermeable dam cores. Engineering Geology, 66(3-4), 283-294. https://doi.org/10.1016/S0013-7952(02)00048-0
Le Houedec, S., Meynadier, L., & Allègre, C. J. (2012). Nd isotope systematics on ODP Sites 756 and 762 sediments reveal major volcanic, oceanic and climatic change s in South Indian Ocean over the last 35Ma.

Earth and Planetary Science Letters, 327-328, 29-38. https://doi.org/10.1016/j.epsl.2012.01.019
Lee, H. (1982). Bulk Density and Shear Strength of Several Deep-Sea Calcareous. In: Demars and Chaney (Eds), Geotechnical Properties, Behavior, and Performance of Calcareous Soils. ASTM International, pp. 1-25. https://doi.org/10.1520/STP28910S
L'Heureux, J.-S., Glimsdal, S., Longva, O., Hansen, L., & Harbitz, C. (2011). The 1888 shoreline landslide and tsunami in Trondheimsfjorden, central Norway. Marine Geophysical Research, 32(1), 313-329. https://doi.org/10.1007/s11001-010-9103-z
L'Heureux, J.-S., Longva, O., Steiner, A., Hansen, L., Vardy, M. E., Vanneste, M., Haflidason, H., Brendryen, J., Kvalstad, T. J., Forsberg, C. F., Chand, S., Kopf, A. (2012). Identification of weak layers and their role for the stability of slopes at Finneidfjord, Northern Norway, in: Yamada et al. (Eds.), Submarine mass movements and their consequences. Advances in Natural and Technological Hazards Research, Springer, Dordrecht, 31, pp. 321-330. https://doi.org/10.1007/978-94-007-2162-3_29
Li, J., Li, W., Alves, T. M., Rebesco, M., Zhan, W. H., Sun, J., Mitchell, N. C., & Wu, S. G. (2019). Different origins of seafloor undulations in a submarine canyon system, northern South China Sea, based on their seismic character and relative location. Marine Geology, 413, 99-111. https://doi.org/10.1016/j.margeo.2019.04.007
Li, W., Alves, T. M., Wu, S. G., Volker, D., Zhao, F., Mi, L. J., & Kopf, A. (2015). Recurrent slope failure and submarine channel incision as key factors controlling reservoir potential in the South China Sea (Qiongdongnan Basin, South Hainan Island). Marine and Petroleum Geology, 64, 17-30. https://doi.org/10.1016/j.marpetgeo.2015.02.043
Li, W., Alves, T. M., Urlaub, M., Georgiopoulou, A., Klaucke, I., Wynn, R. B., Gross, F., Meyer, M., Repschlager, J., Berndt, C., & Krastel, S. (2017). Morphology, age and sediment dynamics of the upper headwall of the Sahara Slide Complex, Northwest Africa: Evidence for a large Late Holocene failure. Marine Geology, 393, 109-123. https://doi.org/10.1016/j.margeo.2016.11.013
Li, W., Alves, T. M., Rebesco, M., Sun, J., Li, J., Li, S., & Wu, S. (2020). The Baiyun Slide Complex, South China Sea: A modern example of slope instability controlling submarine-channel incision on continental slopes. Marine and Petroleum Geology, 114, 104231. https://doi.org/10.1016/j.marpetgeo.2020.104231
Li, W., Li, Y., Omosanya, K. O., Alves, T. M., Jing, S., Wang, X., Wu, N., & Zhan, W. (2023). Quantitative and geomorphologic parameterization of megaclasts within mass-transport complexes, offshore Taranaki Basin, New Zealand. GSA Bulletin, 135(7-8), 1828-1843. https://doi.org/10.1130/B36446.1
Li, W., Jing, S., Urlaub, M., & Rebesco, M. (2025). Sea-level variations influence weak layer formation and submarine landslides on a low-latitude continental margin. Communications Earth & Environment, 6(1), 950. https://doi.org/10.1038/s43247-025-02949-z
Liu, H., Yuan, F., Jiang, Y., Zhao, M., Chen, K., Guo, Z., Wang, Y. (2019). Mechanisms for overpressure generated by the undercompaction of paleogene strata in the Baxian depression of Bohai Bay Basin, China. Marine and Petroleum Geology 99, 337-346. https://doi.org/10.1016/j.marpetgeo.2018.10.001
Liu, X., Wei, S., Meng, X., Xie, B., Chen, X., & Guo, X. (2026). A global dataset of impact forces from submarine landslides on pipelines and cables. Scientific Data, 13, 285. https://doi.org/10.1038/s41597-026-06629-1
Locat, J. (1995). On the development of microstructure in collapsible soils, in: Derbyshire et al. (Eds.), Genesis and Properties of Collapsible Soils. NATO ASI Series, Springer, Dordrecht, pp. 93-128. https://doi.org/10.1007/978-94-011-0097-7_6
Locat, J., & Lee, H. J. (2002). Submarine landslides: advances and challenges. Canadian Geotechnical Journal, 39(1), 193-212. https://doi.org/10.1139/T01-089
Locat, J., Leroueil, S., Locat, A., & Lee, H. (2014). Weak Layers: Their Definition and Classification from a Geotechnical Perspective. In: Krastel et al. (Eds), Submarine Mass Movements and Their Consequences, Advances in Natural and

Technological Hazards Research. Springer, Cham, 37, pp. 3-12. https://doi.org/10.1007/978-3-319-00972-8_1

Longley, I., Buessenschuett, C., Clydsdale, L., Cubitt, C., Davis, R., Johnson, M., Marshall, N., Murray, A., Somerville, R., & Spry, T. (2002). The North West shelf of Australia–a woodside perspective. The sedimentary basins of Western Australia, 3, 27-88.

Løvholt, F., Harbitz, C. B., & Haugen, K. B. (2005). A parametric study of tsunamis generated by submarine slides in the Ormen Lange/Storegga area off western Norway. Marine and Petroleum Geology, 22(1-2), 219-231. https://doi.org/10.1016/j.marpetgeo.2004.10.017

Lowe, D. R. (1976). Subaqueous liquefied and fluidized sediment flows and their deposits. Sedimentology, 23(3), 285-308. https://doi.org/10.1111/j.1365-3091.1976.tb00051.x

Lowe, D. R. (1982). Sediment gravity flows; II, Depositional models with special reference to the deposits of high-density turbidity currents. Journal of Sedimentary Research, 52(1), 279-297. https://doi.org/10.1306/212F7F31-2B24-11D7-8648000102C1865D

Lüdmann, T., Betzler, C., Lindhorst, S., Lahajnar, N., Hübscher, C. (2022). Submarine landsliding in carbonate ooze along low-angle slopes (Inner Sea, Maldives). Marine and Petroleum Geology 136, 105403. https://doi.org/10.1016/j.marpetgeo.2021.105403

Mac McGilvery, T., Haddad, G., & Cook, D. (2004). Seafloor and shallow subsurface examples of mass transport complexes, offshore Brunei. In: McGilvery et al. (Eds), Offshore Technology Conference. Houston, Texas, pp. OTC-16780-MS. https://doi.org/10.4043/16780-MS

Major, J. J. (1997). Depositional processes in large-scale debris-flow experiments. The Journal of Geology, 105(3), 345-366.

Major, J.J. (2000). Gravity-driven consolidation of granular slurries: implications for debris-flow deposition and deposit characteristics. Journal of Sedimentary Research 70(1), 64-83. https://doi.org/10.1306/2DC408FF-0E47-11D7-8643000102C1865D

Major, J. J., & Iverson, R. M. (1999). Debris-flow deposition: Effects of pore-fluid pressure and friction concentrated at flow margins. Geological Society of America Bulletin, 111(10), 1424-1434. https://doi.org/10.1130/0016-7606(1999)111<1424:DFDEOP>2.3.CO;2

Martin, H. (2006). Cenozoic climatic change and the development of the arid vegetation in Australia. Journal of arid Environments, 66(3), 533-563.

Martínez-Doñate, A., Privat, A. M. J., Hodgson, D., Jackson, C. A., Kane, I., Spychala, Y., Duller, R. A., Stevenson, C., Keavney, E., & Schwarz, E. (2021). Substrate entrainment, depositional relief, and sediment capture: impact of a submarine landslide on flow process and sediment supply. Frontiers in Earth Science, 9, 757617. https://doi.org/10.3389/feart.2021.757617

Masson, D. G., Huggett, Q. J., & Brunsden, D. (1993). The surface texture of the Saharan Debris Flow deposit and some speculations on submarine debris flow processes. Sedimentology, 40(3), 583-598. https://doi.org/10.1111/j.1365-3091.1993.tb01351.x

Masson, D., Van Niel, B., & Weaver, P. (1997). Flow processes and sediment deformation in the Canary debris flow on the NW African continental rise. Sedimentary Geology, 110(3-4), 163-179. https://doi.org/10.1016/S0037-0738(96)00089-9

Masson, D. G., Canals, M., Alonso, B., Urgeles, R., & Huhnerbach, V. (1998). The Canary Debris Flow: source area morphology and failure mechanisms. Sedimentology, 45(2), 411-432. https://doi.org/10.1046/j.1365-3091.1998.0165f.x

Masson, D. G., Watts, A. B., Gee, M. J. R., Urgeles, R., Mitchell, N. C., Le Bas, T. P., & Canals, M. (2002). Slope failures on the flanks of the western Canary Islands. Earth-Science Reviews, 57(1-2), 1-35. https://doi.org/10.1016/S0012-8252(01)00069-1

Masson, D., Harbitz, C., Wynn, R., Pedersen, G., & Løvholt, F. (2006). Submarine landslides: processes, triggers and hazard prediction. Philosophical Transactions of the Royal Society A: Mathematical, Physical and Engineering Sciences, 364(1845), 2009-2039. https://doi.org/10.1098/rsta.2006.1810

McArthur, A. D., Tek, D. E., Poyatos-Moré, M., Colombera, L., & McCaffrey, W. D. (2024). Deep-ocean channel-wall collapse order of magnitude larger than any other documented. Communications Earth &

Environment, 5(1), 143. https://doi.org/10.1038/s43247-024-01311-z
McCoy, S.W., Kean, J.W., Coe, J.A., Tucker, G.E., Staley, D.M., Wasklewicz, T.A. (2012). Sediment entrainment by debris flows: In situ measurements from the headwaters of a steep catchment. Journal of Geophysical Research: Earth Surface 117, F03016. https://doi.org/10.1029/2011JF002278
McGowan, D., Salian, A., Baas, J. H., Peakall, J., & Best, J. (2024). On the origin of chevron marks and striated grooves, and their use in predicting mud bed rheology. Sedimentology, 71(2), 687-708. https://doi.org/10.1111/sed.13148
Micallef, A., Berndt, C., Masson, D. G., & Stow, D. A. V. (2008). Scale invariant characteristics of the Storegga Slide and implications for large-scale submarine mass movements. Marine Geology, 247(1-2), 46-60. https://doi.org/10.1016/j.margeo.2007.08.003
Middleton, G. V., & Hampton, M. A. (1973). Part I. Sediment gravity flows: mechanics of flow and deposition. In: Bouma (Ed), Turbidity and Deep Water Sedimentation. SEPM, pp.1-38.
Miller, N., & Henderson, J. (2010). Quantifying sand particle shape complexity using a dynamic, digital imaging technique. Agronomy Journal, 102(5), 1407-1414. https://doi.org/10.2134/agronj2010.0097
Milliken, K. (2014). A Compositional Classification For Grain Assemblages In Fine-Grained Sediments and Sedimentary Rocks. Journal of Sedimentary Research, 84(12), 1185-1199. https://doi.org/10.2110/jsr.2014.92
Miramontes, E., Sultan, N., Garziglia, S., Jouet, G., Pelleter, E., & Cattaneo, A. (2018). Altered volcanic deposits as basal failure surfaces of submarine landslides. Geology 46(7), 663-666. https://doi.org/10.1130/G40268.1
Mohrig, D., Ellis, C., Parker, G., Whipple, K. X., & Hondzo, M. (1998). Hydroplaning of subaqueous debris flows. Geological Society of America Bulletin, 110(3), 387-394. https://doi.org/10.1130/0016-7606(1998)110<0387:HOSDF>2.3.CO;2
Moore, D. G. (1961). Submarine slumps. Journal of Sedimentary Research, 31(3), 343-357. https://doi.org/10.1306/74D70B78-2B21-11D7-8648000102C1865D
Moore, J. G., Bryan, W. B., Beeson, M. H., & Normark, W. R. (1995). Giant blocks in the South Kona landslide, Hawaii. Geology, 23(2), 125-128. https://doi.org/10.1130/0091-7613(1995)023<0125:GBITSK>2.3.CO;2
Morse, J. W. (2003). Formation and diagenesis of carbonate sediments. In: Mackenzie et al. (Eds), Treatise on Geochemistry. Elsevier, 7, pp.67-85. https://doi.org/10.1016/B0-08-043751-6/07093-6
Moscardelli, L., & Wood, L. (2008). New classification system for mass transport complexes in offshore Trinidad. Basin research, 20(1), 73-98. https://doi.org/10.1111/j.1365-2117.2007.00340.x
Moscardelli, L., & Wood, L. (2016). Morphometry of mass-transport deposits as a predictive tool. Geological Society of America Bulletin, 128(1-2), 47-80. https://doi.org/10.1130/B31221.1
Moscardelli, L., Wood, L., & Mann, P. (2006). Mass-transport complexes and associated processes in the offshore area of Trinidad and Venezuela. AAPG bulletin, 90(7), 1059-1088. https://doi.org/10.1306/02210605052
Mosher, D. C., Mayer, L. A., Shipley, T. H., Winterer, E. L., Hagen, R. A., Marsters, J. C., Bassinot, F., Wilkens, R., & Mayer, L. A. (1993). 3. Seismic stratigraphy of the Ontong Java Plateau. In: Berger et al. (Eds), Proceedings of the Ocean Drilling Program, Scientific Results (vol. 130). College Station, TX (Ocean Drilling Program), 130, pp. 33-49.
Mosher, D., Xu, Z., & Shimeld, J. (2010). The Pliocene Shelburne mass-movement and consequent tsunami, western Scotian Slope. In: Mosher (eds), Submarine Mass Movements and Their Consequences. Springer, Dordrecht, 28, pp. 765-775. https://doi.org/10.1007/978-90-481-3071-9_62
Mulder, T., & Alexander, J. (2001). The physical character of subaqueous sedimentary density flows and their deposits. Sedimentology, 48(2), 269-299. https://doi.org/10.1046/j.1365-3091.2001.00360.x
Mulia, I. E., Watada, S., Ho, T. C., Satake, K., Wang, Y. C., & Aditiya, A. (2020). Simulation of the 2018 Tsunami Due to the Flank Failure of Anak Krakatau Volcano and Implication for Future Observing Systems. Geophysical Research Letters, 47(14),

e2020GL087334. https://doi.org/10.1029/2020GL087334
Nemec, W. (1990). Aspects of sediment movement on steep delta slopes. In Colella & Prior (Eds.), Coarse-grained deltas. Spec. Publs int. Ass. Sediment, vol. 10, pp. 29-73.
Nugraha, H. D., Jackson, C. A. L., Johnson, H. D., Hodgson, D. M., & Clare, M. A. (2022). Extreme erosion by submarine slides. Geology, 50(10), 1130-1134. https://doi.org/10.1130/G50164.1
Nwoko, J., Kane, I., & Huuse, M. (2020a). Megaclasts within mass-transport deposits: their origin, characteristics and effect on substrates and succeeding flows. In: Georgiopoulou et al. (Eds), Subaqueous Mass Movements and their Consequences: Advances in Process Understanding, Monitoring and Hazard Assessments. Geological Society, London, Special Publications, 500(1), 515-530. https://doi.org/10.1144/sp500-2019-146
Nwoko, J., Kane, I., & Huuse, M. (2020b). Mass transport deposit (MTD) relief as a control on post-MTD sedimentation: Insights from the Taranaki Basin, offshore New Zealand. Marine and Petroleum Geology, 120, 104489. https://doi.org/10.1016/j.marpetgeo.2020.104489
Omira, R., Baptista, M. A., Quartau, R., Ramalho, R. S., Kim, J., Ramalho, I., & Rodrigues, A. (2022). How hazardous are tsunamis triggered by small-scale mass-wasting events on volcanic islands? New insights from Madeira – NE Atlantic. Earth and Planetary Science Letters, 578, 117333. https://doi.org/10.1016/j.epsl.2021.117333
Omosanya, K. O., & Alves, T. M. (2013). A 3-dimensional seismic method to assess the provenance of Mass-Transport Deposits (MTDs) on salt-rich continental slopes (Espirito Santo Basin, SE Brazil). Marine and Petroleum Geology, 44, 223-239. https://doi.org/10.1016/j.marpetgeo.2013.02.006
Ortiz-Karpf, A., Hodgson, D. M., & McCaffrey, W. D. (2015). The role of mass-transport complexes in controlling channel avulsion and the subsequent sediment dispersal patterns on an active margin: The Magdalena Fan, offshore Colombia. Marine and Petroleum Geology, 64, 58-75. https://doi.org/10.1016/j.marpetgeo.2015.01.005
Ortiz-Karpf, A., Hodgson, D. M., Jackson, C. A. L., & McCaffrey, W. D. (2017). Influence of seabed morphology and substrate composition on mass-transport flow processes and pathways: insights from the Magdalena Fan, Offshore Colombia. Journal of Sedimentary Research, 87(3), 189-209. https://doi.org/10.2110/jsr.2017.10
Ortiz-Karpf, A., Hodgson, D. M., Jackson, C. A. L., & McCaffrey, W. D. (2018). Mass-transport complexes as markers of deep-water fold-and-thrust belt evolution: insights from the southern Magdalena fan, offshore Colombia. Basin research, 30(S1), 65-88. https://doi.org/10.1111/bre.12208
Paganoni, M., King, J. J., Foschi, M., Mellor-Jones, K., & Cartwright, J. A. (2019). A natural gas hydrate system on the Exmouth Plateau (NW shelf of Australia) sourced by thermogenic hydrocarbon leakage. Marine and Petroleum Geology, 99, 370-392. https://doi.org/10.1016/j.marpetgeo.2018.10.029
Palmer-Julson, A., & Rack, F. (1992). The relationship between sediment fabric and planktonic microfossil taphonomy: how do plankton skeletons become pelagic ooze? Palaios 7(2), 167-177. https://doi.org/10.2307/3514927
Peakall, J., Ashworth, P., & Best, J. (1996). Physical modelling in fluvial geomorphology: principles, applications and unresolved issues. In: Rhoads and Thorn (Eds). The Scientific Nature of Geomorphology. John Wiley & Sons, Chichester, 221-253.
Peakall, J., McCaffrey, W. D., & Kneller, B.C. (2000). A process model for the evolution, morphology and architecture of sinuous submarine channels. Journal of Sedimentary Research, 70, 434-448. https://doi.org/10.1306/2DC4091C-0E47-11D7-8643000102C1865D
Peakall, J., Ashworth, P. J., & Best, J. L. (2007). Meander-bend evolution, alluvial architecture, and the role of cohesion in sinuous river channels: a flume study. Journal of Sedimentary Research, 77(3), 197-212. https://doi.org/10.2110/jsr.2007.017
Peakall, J., Best, J., Baas, J. H., Hodgson, D. M., Clare, M. A., Talling, P. J., Dorrell, R. M., & Lee, D. R. (2020). An integrated process-based model of flutes and tool marks in deep-water environments: Implications for palaeohydraulics, the

Bouma sequence and hybrid event beds. Sedimentology, 67(4), 1601-1666. https://doi.org/10.1111/sed.12727
Peakall, J., Best, J. L., Baas, J. H., Wignall, P. B., Hodgson, D. M., & Łapcik, P. (2024). Flow-induced interfacial deformation structures (FIDS): Implications for the interpretation of palaeocurrents, flow dynamics and substrate rheology. Sedimentology, 71(6), 1709-1743. https://doi.org/10.1111/sed.13219
Pereira, G., & Cleary, P. (2017). Segregation due to particle shape of a granular mixture in a slowly rotating tumbler. Granular Matter, 19(2), 23. https://doi.org/10.1007/s10035-017-0708-7
Pett, J. W., & Walker, R. G. (1971). Relationship of flute cast morphology to internal sedimentary structures in turbidites. Journal of Sedimentary Research, 41(1), 114-128. https://doi.org/10.1306/74D721FD-2B21-11D7-8648000102C1865D
Piper, D., Pirmez, C., Manley, P., Long, D., Flood, R., Normark, W., & Showers, W. (1997). Mass-transport deposits of the Amazon Fan. In: Flood et al. (Eds), Proceedings of the Ocean Drilling Program, Scientific Results, Vol. 155. College Station, TX (Ocean Drilling Program), pp. 109-146.
Piper, D. J. W., Cochonat, P., & Morrison, M. L. (1999). The sequence of events around the epicentre of the 1929 Grand Banks earthquake: initiation of debris flows and turbidity current inferred from sidescan sonar. Sedimentology, 46(1), 79-97. https://doi.org/10.1046/j.1365-3091.1999.00204.x
Piper, D., Mosher, D., & Campbell, D. (2012). Controls on the distribution of major types of submarine landslides. In: John & Stead (Eds), Landslides Types, Mechanisms and Modeling. Cambridge University Press Cambridge. pp. 95-107.
Pittenger, A., Taylor, E., Bryant, W.R. (1989). The influence of biogenic silica on the geotechnical stratigraphy of the Voring Plateau, Norwegian Sea, in: Eldholm et al. (Eds.), Proceedings of the Ocean Drilling Program, Scientific Results, 122. TX (Ocean Drilling Program), Texas, pp. 923-940.
Posamentier, H. W. (2003). Depositional elements associated with a basin floor channel-levee system: case study from the Gulf of Mexico. Marine and Petroleum Geology, 20(6-8), 677-690. https://doi.org/10.1016/j.marpetgeo.2003.01.002
Posamentier, H., & Martinsen, O. (2011). The Character and Genesis of Submarine Mass-Transport Deposits: Insights from Outcrop and 3D Seismic Data. In: Shipp et al. (Eds.), Mass-Transport Deposits in Deepwater Settings, SEPM Special Publication, vol. 96, pp. 7–38. https://doi.org/10.2110/sepmsp.096.007
Principaud, M., Mulder, T., Gillet, H., & Borgomano, J. (2015). Large-scale carbonate submarine mass-wasting along the northwestern slope of the Great Bahama Bank (Bahamas): Morphology, architecture, and mechanisms. Sedimentary Geology, 317, 27-42. https://doi.org/10.1016/j.sedgeo.2014.10.008
Prior, D. B., Bornhold, B., & Johns, M. (1984). Depositional characteristics of a submarine debris flow. The Journal of Geology, 92(6), 707-727.
Pudasaini, S. P., & Mergili, M. (2019). A multi-phase mass flow model. Journal of Geophysical Research: Earth Surface, 124(12), 2920-2942. https://doi.org/10.1029/2019JF005204
Puga-Bernabéu, Á., Webster, J. M., Beaman, R. J., & Guilbaud, V. (2011). Morphology and controls on the evolution of a mixed carbonate–siliciclastic submarine canyon system, Great Barrier Reef margin, north-eastern Australia. Marine Geology, 289(1-4), 100-116. https://doi.org/10.1016/j.margeo.2011.09.013
Puga-Bernabéu, Á., Webster, J. M., Beaman, R. J., Thran, A., López-Cabrera, J., Hinestrosa, G., & Daniel, J. (2020). Chapter 19 Submarine Landslides Along the Mixed Siliciclastic-Carbonate Margin of the Great Barrier Reef (Offshore Australia). In: Ogata et al. (eds), Submarine Landslides: Subaqueous Mass Transport Deposits from Outcrops to Seismic Profiles, Geophysical Monograph. American Geophysical Union, 246, pp, 313-337. https://doi.org/10.1002/9781119500513.ch19
Puga-Bernabéu, Á., López-Cabrera, J., Webster, J. M., & Beaman, R. J. (2022). Submarine landslide morphometrics and slope failure dynamics along a mixed carbonate-siliciclastic margin, north-eastern Australia. Geomorphology, 403, 108179.

https://doi.org/10.1016/j.geomorph.2022.108179
Purkis, S. J., Ward, S. N., Shernisky, H., Chimienti, G., Sharifi, A., Marchese, F., Benzoni, F., Rodrigue, M., Raymo, M. E., & Abdulla, A. (2022). Tsunamigenic Potential of an Incipient Submarine Landslide in the Tiran Straits. Geophysical Research Letters, 49(4). https://doi.org/10.1029/2021gl097493
Rack, F.R., Bryant, W.R., Julson, A.P. (1993). Microfabric and physical properties of deep-sea high latitude carbonate oozes, in: Rezak, R., Lavoie, D.L. (Eds.), Carbonate Microfabrics. Frontiers in Sedimentary Geology. Springer, New York, pp. 129–147. https://doi.org/10.1007/978-1-4684-9421-1_10
Rashid, H., MacKillop, K., Sherwin, J., Piper, D. J. W., Marche, B., & Vermooten, M. (2017). Slope instability on a shallow contourite-dominated continental margin, southeastern Grand Banks, eastern Canada. Marine Geology, 393, 203-215. https://doi.org/10.1016/j.margeo.2017.01.001
Rea, D. K. (1994). The paleoclimatic record provided by eolian deposition in the deep sea: The geologic history of wind. Reviews of Geophysics, 32(2), 159-195.
Reijmer, J. J. G., Palmieri, P., Groen, R., & Floquet, M. (2015). Calciturbidites and calcidebrites: Sea-level variations or tectonic processes? Sedimentary Geology, 317, 53-70. https://doi.org/10.1016/j.sedgeo.2014.10.013
Ribó, M., Mountjoy, J.J., Mitchell, N., Watson, S.J., Hoffman, J.J.L. & Woelz, S. (2025). New insights on gravity flow dynamics during submarine canyon flushing events. Geology, 53, 34-39.
Rocha, F., Johnson, C., & Gray, J. (2019). Self-channelisation and levee formation in monodisperse granular flows. Journal of Fluid Mechanics, 876, 591-641. https://doi.org/10.1017/jfm.2019.518
Roelofs, L., Nota, E.W., Flipsen, T.C., Colucci, P., de Haas, T. (2023). How bed composition affects erosion by debris flows—An experimental assessment. Geophysical Research Letters 50(14), e2023GL103294. https://doi.org/10.1029/2023GL103294
Ruano, P., Bohoyo, F., Galindo-Zaldivar, J., Perez, L. F., Hernandez-Molina, F. J., Maldonado, A., Garcia, M., & Medialdea, T. (2014). Mass transport processes in the southern Scotia Sea: Evidence of paleoearthquakes. Global and Planetary Change, 123, 374-391. https://doi.org/10.1016/j.gloplacha.2014.06.009
Sammartini, M., Moernaut, J., Kopf, A., Stegmann, S., Fabbri, S. C., Anselmetti, F. S., & Strasser, M. (2021). Propagation of frontally confined subaqueous landslides: Insights from combining geophysical, sedimentological, and geotechnical analysis. Sedimentary Geology, 416, 105877. https://doi.org/10.1016/j.sedgeo.2021.105877
Savage, S., & Lun, C. (1988). Particle size segregation in inclined chute flow of dry cohesionless granular solids. Journal of Fluid Mechanics, 189, 311-335. https://doi.org/10.1017/S002211208800103X
Sawyer, D.E., Hodelka, B. (2016). Tiny fossils, big impact: the role of foraminifera-enriched condensed section in arresting the movement of a large retrogressive submarine landslide in the Gulf of Mexico, in: Lamarche et al. (Eds.), Submarine Mass Movements and their Consequences. Advances in Natural and Technological Hazards Research, Springer, Cham, pp. 479-486. https://doi.org/10.1007/978-3-319-20979-1_48
Sawyer, D. E., Flemings, P. B., Dugan, B., & Germaine, J. T. (2009). Retrogressive failures recorded in mass transport deposits in the Ursa Basin, Northern Gulf of Mexico. Journal of Geophysical Research-Solid Earth, 114, B10102. https://doi.org/10.1029/2008jb006159
Scarselli, N. (2020). Chapter 16 - Submarine landslides - architecture, controlling factors and environments. A summary. In: Scarselli et al. (Eds.), Regional Geology and Tectonics (Second Edition). Elsevier, pp. 417-439. https://doi.org/10.1016/B978-0-444-64134-2.00015-8
Scarselli, N., McClay, K., & Elders, C. (2013). Submarine slide and slump complexes, Exmouth Plateau, NW Shelf of Australia. In: Keep, M. & Moss, S.J. (Eds.), The Sedimentary Basins of Western Australia 4: Proceedings of Petroleum Exploration Society of Australia Symposium. Perth, WA, pp. 1-19.
Scarselli, N., McClay, K., Elders, C. (2019). Seismic examples of composite slope failures (offshore North West Shelf,

Australia). in: Ogata et al. (Eds.), Submarine Landslides: Subaqueous Mass Transport Deposits from Outcrops to Seismic Profiles, Geophysical Monograph Series. Wiley, Washington, pp. 261-276. https://doi.org/10.1002/9781119500513.ch16

Scarselli, N., McClay, K., & Elders, C. (2020). Seismic examples of composite slope failures (Offshore North West Shelf, Australia). In: Ogata et al. (Eds), Submarine Landslides: Subaqueous Mass Transport Deposits from Outcrops to Seismic Profiles. Geological Society of London, Special Publications, 246, pp. 261-276. https://doi.org/10.1002/9781119500513.ch16

Seed, R. B., Cetin, K. O., Moss, R. E., Kammerer, A. M., Wu, J., Pestana, J. M., Riemer, M. F., Sancio, R. B., Bray, J. D., & Kayen, R. E. (2003). Recent advances in soil liquefaction engineering: a unified and consistent framework. In Proceedings of the 26th Annual ASCE Los Angeles Geotechnical Spring Seminar. Long Beach, CA, pp. 1-71.

Shanmugam, G. (2020). Gravity flows: Types, definitions, origins, identification markers, and problems. The Journal of The Indian Association of Sedimentologists, 37(2), 61-90. https://doi.org/10.51710/jias.v37i2.117

Shanmugam, G., Lehtonen, L. R., Straume, T., Syvertsen, S. E., Hodgkinson, R. J., & Skibeli, M. (1994). Slump and Debris-Flow Dominated Upper Slope Facies in the Cretaceous of the Norwegian and Northern North Seas (61-67-Degrees-N) - Implications for Sand Distribution. AAPG Bulletin, 78(6), 910-937. https://doi.org/10.1306/A25FE3E7-171B-11D7-8645000102C1865D

Shepard, F. P. (1955). Delta-front valleys bordering the Mississippi distributaries. Geological Society of America Bulletin, 66(12), 1489-1498. https://doi.org/10.1130/0016-7606(1955)66[1489:DVBTMD]2.0.CO;2

Silva, A. J., & Booth, J. S. (1984). Creep behavior of submarine sediments. Geo-Marine Letters, 4(3), 215-219. https://doi.org/10.1007/BF02281709

Smith, R. C., Hill, J., Collins, G. S., Piggott, M. D., Kramer, S. C., Parkinson, S. D., & Wilson, C. (2016). Comparing approaches for numerical modelling of tsunami generation by deformable submarine slides. Ocean Modelling, 100, 125-140. https://doi.org/10.1016/j.ocemod.2016.02.007

Sobiesiak, M.S., Kneller, B., Alsop, G.I., & Milana, J.P. (2018). Styles of basal interaction beneath mass transport deposits. Marine and Petroleum Geology 98, 629-639. https://doi.org/10.1016/j.marpetgeo.2018.08.028

Sola, F., Puga-Bernabeu, A., Aguirre, J., & Braga, J. C. (2018). Origin, evolution and sedimentary processes associated with a late Miocene submarine landslide, southeast Spain. Sedimentary Geology, 364, 351-366. https://doi.org/10.1016/j.sedgeo.2017.09.005

Soutter, E. L., Kane, I. A., & Huuse, M. (2018). Giant submarine landslide triggered by Paleocene mantle plume activity in the North Atlantic. Geology, 46(6), 511-514. https://doi.org/10.1130/G40308.1

Stagg, H.M.J., & Colwell, J.B. (1994). Structure of the offshore Canning Basin: First impressions from a new regional deep-seismic data set. In: Purcell, P.G., Purcell, R.R. (Eds.), The Sedimentary Basins of Western Australia. Petrol. Expl. Soc. Aust., Perth, pp. 757-768. https://archives.datapages.com/data/petroleum-exploration-society-of-australia/conferences/012/012001/pdfs/757.htm

Stoecklin, A., Friedli, B., & Puzrin, A. M. (2017). Sedimentation as a Control for Large Submarine Landslides: Mechanical Modeling and Analysis of the Santa Barbara Basin. Journal of Geophysical Research-Solid Earth, 122(11), 8645-8663. https://doi.org/10.1002/2017jb014752

Stow, D. A. V. (1984). Turbidite facies, associations, and sequences in the southeastern angola basin. In: Hay et al. (Eds), Init. Repts. DSDP, 75. Washington (U.S. Govt. Printing Office), pp: 785-799.

Stow, D. A. V., & Piper, D. J. W. (1984). Deep-water fine-grained sediments: facies models. Geological Society, London, Special Publications, 15, 611-646. https://doi.org/10.1144/GSL.SP.1984.015.01.3

Sultan, N., Cochonat, P., Canals, M., Cattaneo, A., Dennielou, B., Haflidason, H., Laberg, J., Long, D., Mienert, J., Trincardi, F., Urgeles, R., Vorren, T. O., & Wilson, V. (2004). Triggering mechanisms of slope instability processes and sediment failures on continental margins:

a geotechnical approach. Marine Geology, 213(1-4), 291-321. https://doi.org/10.1016/j.margeo.2004.10.011
Sultan, N., Jouet, G., Riboulot, V., Terzariol, M., Garziglia, S., Cattaneo, A., Giraudeau, J., Jorry, S. J. (2023). Sea-level fluctuations control the distribution of highly liquefaction-prone layers on volcanic-carbonate slopes. Geology 51(4), 402-407. https://doi.org/10.1130/g50785.1
Sun, Q., Alves, T. M., Lu, X., Chen, C., & Xie, X. (2018). True volumes of slope failure estimated from a Quaternary mass-transport deposit in the northern South China Sea. Geophysical Research Letters, 45(6), 2642-2651. https://doi.org/10.1002/2017GL076484
Talling, P. J. (2013). Hybrid submarine flows comprising turbidity current and cohesive debris flow: Deposits, theoretical and experimental analyses, and generalized models. Geosphere, 9(3), 460-488. https://doi.org/10.1130/GES00793.1
Talling, P.J., Amy, L.A., Wynn, R.B., Peakall, J., & Robinson, M. (2004) Beds comprising debrite sandwiched within co-genetic turbidite: origin and widespread occurrence in distal depositional environments. Sedimentology, 51, 163-194.
Talling, P. J., Wynn, R. B., Masson, D. G., Frenz, M., Cronin, B. T., Schiebel, R., Akhmetzhanov, A. M., Dallmeier-Tiessen, S., Benetti, S., Weaver, P. P., Georgiopoulou, A., Zuhlsdorff, C., & Amy, L. A. (2007). Onset of submarine debris flow deposition far from original giant landslide. Nature, 450(7169), 541-544. https://doi.org/10.1038/nature06313
Talling, P. J., Wynn, R. B., Schmmidt, D. N., Rixon, R., Sumner, E., & Amy, L. (2010). How did thin submarine debris flows carry boulder-sized intraclasts for remarkable distances across low gradients to the far reaches of the Mississippi Fan? Journal of Sedimentary Research, 80(10), 829-851. https://doi.org/10.2110/jsr.2010.076
Talling, P. J., Masson, D. G., Sumner, E. J., & Malgesini, G. (2012a). Subaqueous sediment density flows: Depositional processes and deposit types. Sedimentology, 59(7), 1937-2003. https://doi.org/10.1111/j.1365-3091.2012.01353.x
Talling, P.J., Malgesini, G., Sumner, E.J., Amy, L.A., Felletti, F., Blackbourn, G., Nutt, C., Wilcox, C., Harding, I.C., & Akbari, S. (2012b). Planform geometry, stacking pattern, and extra-basinal origin of low strength and intermediate strength cohesive debris flow deposits in the Marnoso-arenacea Formation, Italy. Geosphere, 8, 1207-1230.
Talling, P. J., Paull, C. K., & Piper, D. J. (2013). How are subaqueous sediment density flows triggered, what is their internal structure and how does it evolve? Direct observations from monitoring of active flows. Earth-Science Reviews, 125, 244-287. https://doi.org/10.1016/j.earscirev.2013.07.005
Tang, Q., Geersen, J., Düring, A., Unverricht, D., Schneider von Deimling, J., Lenz, K. F., Li, W., & Krastel, S. (2022). Sequence of multiple slope failures in the headwall area of the giant Sahara slide complex at the NW African continental margin. Geochemistry, Geophysics, Geosystems, 23, e2021GC010283. https://doi.org/10.1029/2021gc010283
Thornton, A., & Gray, J. (2008). Breaking size segregation waves and particle recirculation in granular avalanches. Journal of Fluid Mechanics, 596, 261-284. https://doi.org/10.1017/S0022112007009445
Thornton, A. R., Gray, J., & Hogg, A. (2006). A three-phase mixture theory for particle size segregation in shallow granular free-surface flows. Journal of Fluid Mechanics, 550, 1-25. https://doi.org/10.1017/S0022112005007676
Tingay, M.R., Hillis, R.R., Swarbrick, R.E., Morley, C.K., Damit, A.R. (2009). Origin of overpressure and pore-pressure prediction in the Baram province, Brunei. AAPG Bulletin 93(1), 51-74. https://doi.org/10.1306/08080808016
Tournadour, E., Mulder, T., Borgomano, J., Hanquiez, V., Ducassou, E., & Gillet, H. (2015). Origin and architecture of a Mass Transport Complex on the northwest slope of Little Bahama Bank (Bahamas): Relations between off-bank transport, bottom current sedimentation and submarine landslides. Sedimentary Geology, 317, 9-26. https://doi.org/10.1016/j.sedgeo.2014.10.003
Tournadour, E., Mulder, T., Borgomano, J., Gillet, H., Chabaud, L., Ducassou, E., Hanquiez, V., & Etienne, S. (2017). Submarine canyon morphologies and evolution in modern carbonate settings: The northern slope of Little Bahama Bank,

Bahamas. Marine Geology, 391, 76-97. https://doi.org/10.1016/j.margeo.2017.07.014
Tozer, B., Sandwell, D. T., Smith, W. H., Olson, C., Beale, J., & Wessel, P. (2019). Global bathymetry and topography at 15 arc sec: SRTM15+. Earth and Space Science, 6(10), 1847-1864. https://doi.org/10.1029/2019EA000658
Trincardi, F., Cattaneo, A., Correggiari, A., & Ridente, D. (2004). Evidence of soft sediment deformation, fluid escape, sediment failure and regional weak layers within the late Quaternary mud deposits of the Adriatic Sea. Marine Geology, 213(1-4), 91-119. https://doi.org/10.1016/j.margeo.2004.10.003
Trofimovs, J., Fisher, J. K., Macdonald, H. A., Talling, P. J., Sparks, R. S. J., Hart, M. B., Smart, C. W., Boudon, G., Deplus, C., Komorowski, J.-C., Le Friant, A., Moreton, S. G., & Leng, M. J. (2010). Evidence for carbonate platform failure during rapid sea-level rise; ca 14 000 year old bioclastic flow deposits in the Lesser Antilles. Sedimentology, 57(3), 735-759. https://doi.org/10.1111/j.1365-3091.2009.01117.x
Urlaub, M., Talling, P. J., Zervos, A., & Masson, D. (2015). What causes large submarine landslides on low gradient (<2°) continental slopes with slow (~0.15 m/kyr) sediment accumulation? Journal of Geophysical Research: Solid Earth, 120(10), 6722-6739. https://doi.org/10.1002/2015jb012347
Urlaub, M., Geersen, J., Krastel, S., Schwenk, T. (2018). Diatom ooze: crucial for the generation of submarine mega-slides? Geology 46(4), 331-334. https://doi.org/10.1130/g39892.1
Valdez Buso, V., Kneller, B., da Silva Reis Assis, V., Farias Vesely, F. & Milana, J.P. (2024) Incorporation of substrate blocks into mass transport deposits: Insights from subsurface and outcrop studies. The Depositional Record, 10, 708–719. https://doi.org/10.1002/dep2.283
Van Dijk, W. M., Van de Lageweg, W. I., & Kleinhans, M. G. (2012). Experimental meandering river with chute cutoffs. Journal of Geophysical Research: Earth Surface, 117, F03023. https://doi.org/10.1029/2011JF002314
Vardy, M. E., L'Heureux, J. S., Vanneste, M., Longva, O., Steiner, A., Forsberg, C. F., Haflidason, H., & Brendryen, J. (2012). Multidisciplinary investigation of a shallow near-shore landslide, Finneidfjord, Norway. Near Surface Geophysics, 10(4), 267-277. https://doi.org/10.3997/1873-2012022
von Rad, U., Exon, N.F., Haq, B.U. (1992). 46. Rift-to-drift history of the Wombat Plateau, Northwest Australia: Triassic to Tertiary Leg 122 Results, in: von Rad et al. (Eds.), Proceedings of the Ocean Drilling Program, Sci. Results, 122. TX (Ocean Drilling Program), Texas, pp. 765-800.
Vorren, T. O., Laberg, J. S., Blaume, F., Dowdeswell, J. A., Kenyon, N. H., Mienert, J., Rumohr, J., & Werner, F. (1998). The Norwegian–Greenland Sea continental margins: morphology and late Quaternary sedimentary processes and environment. Quaternary Science Reviews, 17(1-3), 273-302. https://doi.org/10.1016/S0277-3791(97)00072-3
Wang, X., Maselli, V., Flessati, L., Wang, H., Sun, Z., Wang, Q., Chen, J., Li, Q., Alberti, S., Kienast, M. (2025). Preconditioning of sediment failure by astronomically paced weak-layer deposition. Nat Commun 16(1), 7244. https://doi.org/10.1038/s41467-025-62493-4
Wang, X. Z., Shan, H. G., Wu, Y., Meng, Q. S., & Zhu, C. Q. (2020). Factors affecting particle breakage of calcareous soil retrieved from South China Sea. Geomechanics and Engineering, 22(2), 173-185. https://doi.org/10.12989/gae.2020.22.2.173
Ward, N. I. P., Alves, T. M., & Blenkinsop, T. G. (2018). Submarine sediment routing over a blocky mass-transport deposit in the Espirito Santo Basin, SE Brazil. Basin Research, 30(4), 816-834. https://doi.org/10.1111/bre.12282
Watson, S. J., Whittaker, J. M., Lucieer, V., Coffin, M. F., & Lamarche, G. (2017). Erosional and depositional processes on the submarine flanks of Ontong Java and Nukumanu atolls, western equatorial Pacific Ocean. Marine Geology, 392, 122-139. https://doi.org/10.1016/j.margeo.2017.08.006
Waythomas, C. F., Watts, P., Shi, F. Y., & Kirby, J. T. (2009). Pacific Basin tsunami hazards associated with mass flows in the Aleutian arc of Alaska. Quaternary Science Reviews, 28(11-12), 1006-1019.

https://doi.org/10.1016/j.quascirev.2009.02.019
Webster, J. M., George, N. P. J., Beaman, R. J., Hill, J., Puga-Bernabéu, Á., Hinestrosa, G., Abbey, E. A., & Daniell, J. J. (2016). Submarine landslides on the Great Barrier Reef shelf edge and upper slope: A mechanism for generating tsunamis on the north-east Australian coast? Marine Geology, 371, 120-129. https://doi.org/10.1016/j.margeo.2015.11.008
Weimer, P. (1990). Sequence stratigraphy, facies geometries, and depositional history of the Mississippi Fan, Gulf of Mexico. AAPG Bulletin, 74(4), 425-453. https://doi.org/10.1306/0C9B2321-1710-11D7-8645000102C1865D
Weltje, G. J., & Prins, M. A. (2007). Genetically meaningful decomposition of grain-size distributions. Sedimentary Geology, 202(3), 409-424. https://doi.org/10.1016/j.sedgeo.2007.03.007
Wessel, P., Luis, J., Uieda, L., Scharroo, R., Wobbe, F., Smith, W. H., & Tian, D. (2019). The generic mapping tools version 6. Geochemistry, Geophysics, Geosystems, 20(11), 5556-5564. https://doi.org/10.1029/2019GC008515
Whipple, K. X., & Dunne, T. (1992). The influence of debris-flow rheology on fan morphology, Owens Valley, California. Geological Society of America Bulletin, 104(7), 887-900. https://doi.org/10.1130/0016-7606(1992)104<0887:TIODFR>2.3.CO;2
White, D., Boylan, N., & Levy, N. (2013). Geotechnics offshore Australia-beyond traditional soil mechanics. Australian Geomechanics Journal, 48(4), 25-47.
White, D.J., Randolph, M.F., Gaudin, C., Boylan, N.P., Wang, D., Boukpeti, N., Zhu, H., Sahdi, F. (2016). The Impact of submarine slides on pipelines: outcomes from the COFS-MERIWA JIP, in: Fowler, J. (Eds.), Offshore Technology Conference 2016. Offshore Technology Conference, Houston, pp. OTC-27034-MS. https://doi.org/10.4043/27034-MS
Winterwerp, J.C., van Kesteren, W.G.M., van Prooijen, B., Jacobs, W. (2012). A conceptual framework for shear flow-induced erosion of soft cohesive sediment beds. Journal of Geophysical Research: Oceans, 117(C10), C10020. https://doi.org/10.1029/2012jc008072
Wu, N., Jackson, C. A.-L., Johnson, H., Hodgson, D. M., & Nugraha, H. D. (2020). Mass-transport complexes (MTCs) document minibasin subsidence patterns and diapir evolution in the northern Gulf of Mexico. Basin Research, 32(6), 1300-1327. https://doi.org/10.1111/bre.12429
Wu, N., Jackson, C. A. L., Johnson, H. D., Hodgson, D. M., Clare, M. A., Nugraha, H. D., & Li, W. (2021). The formation and implications of giant blocks and fluid escape structures in submarine lateral spreads. Basin Research, 33(3), 1711-1730. https://doi.org/10.1111/bre.12532
Wu, N., Jackson, C. A. L., Clare, M. A., Hodgson, D. M., Nugraha, H. D., Steventon, M. J., & Zhong, G. (2023). Diagenetic priming of submarine landslides in ooze-rich substrates. Geology, 51(1), 85-90. https://doi.org/10.1130/g50458.1
Yang, G., Jing, L., Kwok, C., & Sobral, Y. (2020). Pore-scale simulation of immersed granular collapse: Implications to submarine landslides. Journal of Geophysical Research: Earth Surface, 125(1), e2019JF005044. https://doi.org/10.1029/2019JF005044
Zampetti, V., Schlager, W., van Konijnenburg, J. H., & Everts, A. J. (2004). 3-D seismic characterization of submarine landslides on a Miocene carbonate platform (Luconia Province, Malaysia). Journal of Sedimentary Research, 74(6), 817-830. https://doi.org/10.1306/040604740817
Zhang, X., Oñate, E., Torres, S. A. G., Bleyer, J., & Krabbenhoft, K. (2019). A unified Lagrangian formulation for solid and fluid dynamics and its possibility for modelling submarine landslides and their consequences. Computer Methods in Applied Mechanics and Engineering, 343, 314-338. https://doi.org/10.1016/j.cma.2018.07.043
Zulkifli, Z., Clare, M.A., Heijnen, M., Lintern, D.G., Stacey, C., Talling, P.J., Cartigny, M.J.B., Minshull, T.A., Moreno, H.M., Peakall, J., & Darby, S. (2024). A threshold in submarine channel curvature explains erosion rate and type. Earth and Planetary Science Letters, 646, 118953.